Quantitative Raman spectroscopy of gases related to KATRIN.

James, Timothy M

Quantitative Raman spectroscopy of gases related to KATRIN

Timothy M. James MPhys
Department of Physics
Swansea University

Swansea University
Prifysgol Abertawe

Submitted to Swansea University in fulfilment
of the requirements for the Degree of Doctor of Philosophy

February 2013

Summary

The overall aim of this thesis was to improve the laser Raman system of the Karlsruhe Tritium Neutrino (KATRIN) experiment and enable the extracted Raman intensity data to be quantified. This was achieved by improving the signal-to-noise ratio of the system and accurately measuring the depolarisation ratios of all six hydrogen isotopologues. This measurement was required to verify whether the polarisability tensors, a and γ, found in the literature can be inserted into the Raman intensity to produce a theoretical intensity curve, which is needed to extract compositions from the measured Raman intensity with a known accuracy.

A procedure has been developed to accurately measure the depolarisation ratio of all six hydrogen isotopologues and the depolarisation ratios of the Q_1-branch agree with the theoretical values, calculated by LeRoy, with a 1σ confidence level. This procedure has also been applied to some of the atmospheric gases.

In addition, a Raman system beyond the scope of the KATRIN experiment has been developed, to increase the signal-to-noise ratio of the system further. The selected setup makes use of a hollow metal-coated glass fibre as the Raman cell and is referred to as "capillary Raman spectroscopy". The initial test measurements have shown that capillary Raman spectroscopy produces Raman signals that are a factor of 170 higher than single-pass 90° Raman spectroscopy. Due to increased fluorescence, as a result of the observation of Raman light in the same direction as the laser excitation, the increase in the signal-to-noise ratio is between a factor of 9 and 24. As a result of these successful measurements the capillary Raman system will be tested with tritium in the near future.

Declaration

This work has not previously been accepted in substance for any degree and is not being concurrently submitted in candidature for any degree.

Signed ..... (candidate)
Date .....6/3/13.....

Statement 1

This thesis is the result of my own investigations, except where otherwise stated. Other sources are acknowledged by giving explicit references in the form of a bibliography.

Signed ..... (candidate)
Date .....6/3/13.....

Statement 2

I hereby give consent for my thesis, if accepted, to be available for photocopying and for inter-library loan, and for the title and summary to be made available to outside organisations.

Signed ..... (candidate)
Date .....6/3/13.....

Contents

Acknowledgements

I would like to thank my supervisor, Professor Helmut Telle, for his guidance and support throughout my PhD.

I would like the thank former members of the KATRIN LARA group at Swansea, Ahmed Alshahrie and Richard Lewis, for there assistance and discussions at the start of my PhD research when I was introduced to the KATRIN LARA system.

I would like to thank our colleagues of the KATRIN LARA group at Tritium Laboratory Karlsruhe (TLK), who contributed to areas of this research, were pleasant and good natured when I visited TLK. In particular Magnus Schlösser, Sebastian Fischer and Beate Bornschein.

I would like to thank the Karlsruhe House of Young Scientists (KHYS) for providing a studentship that enabled my extended visit to TLK to take place in Autumn/Winter 2011. This research period improved efficiency and the collaboration between myself and Magnus Schlösser enabled sections of this work to be completed more quickly.

Finally, I would like to thank the technical staff at Swansea University, Julian Kivell and Hugh Thomas for there assistance with part manufacture when required and Dave Payne for I.T support, specifically maintaining the shared server between Swansea and KIT.

Chapter 1

Introduction

The results of neutrino oscillation experiments showed neutrino mixing among the neutrino generations ([Fuk98], [Egu03]); this implies that the neutrino is not massless. If the neutrino is a massive particle, finding its mass is an important problem in particle physics due to its influence on cosmological and particle physics research. The neutrino detection experiments and investigations into the oscillations (e.g. Super-Kamiokande Collaboration [Fuk98]) have produced results of the mass differences. To determine the absolute mass of the neutrino, direct mass measurements need to be completed.

1.1 Direct neutrino mass measurements

1.1.1 Tritium beta decay

One of the most accurate ways of determining the mass of the electron-neutrino is to study the kinematics of the tritium β^- decay.

$$^3\mathrm{H} \rightarrow {}^3\mathrm{He}^+ + \mathrm{e}^- + \bar{\nu}_\mathrm{e} \tag{1.1}$$

The energy Q_{β^-} of the beta decay is expressed as

$$\begin{aligned} Q_{\beta^-} &= [m(Z,A) - Zm_e]c^2 - [m(Z+1,A) - (Z+1)m_e]c^2 \\ &= [m(Z,A) - m(Z+1,A) - m_e]c^2 \end{aligned} \tag{1.2}$$

where: Z is the atomic number of the decaying nucleus, A is the atomic mass of the decaying nucleus, $m(Z,A)$ is the mass of the neutral atom, and m_e is the mass of the electron.

The important equation in neutrino mass measurements is the beta spectrum of an allowed β^- decay, which is [Wei05]

$$\frac{d^2N}{dt\,dE} = CM_{\text{nucl}}^2 F(E, Z+1)p(E+m_e)\epsilon \sum_i U_{ei}^2 \sqrt{\epsilon^2 - m^2(\nu_i)}\ominus(\epsilon - m(\nu_i)) \qquad (1.3)$$

where E, m_e and p are the kinetic energy, mass and the momentum of the electron; ϵ is the energy difference given by $\epsilon = E_0 - E$; E_0 is the total decay energy; $m(\nu_i)$ is the neutrino mass state; F is the Fermi function accounting the Coulomb interaction of the outgoing β electron with the remaining daughter nucleus of charge $Z+1$; M_{nucl} is the nuclear matrix element; $\ominus(\epsilon - m(\nu_i))$ is included for energy conservation; and C is given by

$$C = \frac{G_f^2}{2\pi^3\hbar^7}\cos^2(\theta_c) \qquad (1.4)$$

where G_f is the Fermi constant and θ_c is the Cabibbo angle. Please note that in equations (1.3) and (1.4) the speed of light has been set to unity.

In figure 1.1 this spectrum is plotted with respect to the energy difference, ϵ, and viewed close to the end-point, E_0, where the neutrino mass is set to $m(\nu_i) = 0\,\text{eV}$ and $m(\nu_i) = 1\,\text{eV}$.

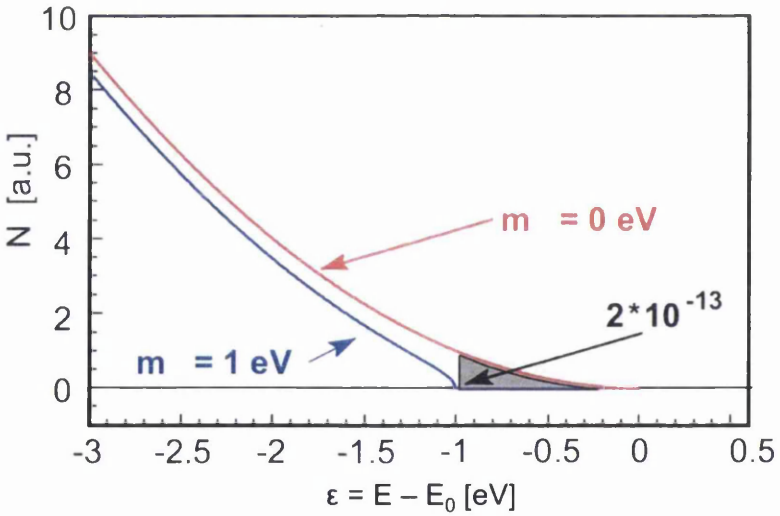

Figure 1.1: The electron spectrum of tritium β-decay, zoomed in on the end-point region. The spectrum is displayed for neutrino masses of 0 eV and 1 eV. From Bornschein [Bor05]

The figure shows that if the neutrino has a mass the spectrum is distorted near the energy end-point. This distortion would occur for all of the individual neutrino mass eigenstates, $m(\nu_i)$. However, the observed neutrino mass in experiments, at the current sensitivity, is an average of neutrino mass eigenstates, due to the small differences of the neutrino mass differences observed in oscillation experiments. This average is referred

to as the electron neutrino mass given by

$$m^2(\nu_e) = \sum_i U_{ei}^2 m^2(\nu_i) \tag{1.5}$$

where U_{ei}^2 is the neutrino complex mixing matrix. For more details the reader is referred to Weinheimer [Wei05] and the references therein.

The β^- decay of tritium is considered the best choice for direct measurements of the mass of the electron neutrino because it has a short half life of 12.3 years and the smallest endpoint energy of all allowed β^- decays of 18.6 keV. The short half life leads to tritium having a high activity and it minimises inelastic processes of β-electrons within the tritium source. The low end-point energy is advantageous because the fraction of decays in the end-point region is proportional to $(1/E_0)^3$. This means that β-emitters with higher end-point energies would have a lower fraction of decays in the end-point (measurement) region.

Tritium being used as a β-emitter has other advantages, these being

- The nuclear matrix element is electron-energy independent. This means that the dependence of the spectral shape on the neutrino mass is given by the phase space.
- The electronic shell configuration of tritium and the decay daughter-nucleus $^3He^+$ are simple, which enables the final state spectrum to be precisely calculated. These calculations are performed in Doss *et al* [Dos06] and will not be discussed further here.

1.1.2 The Mainz and Troitsk experiments

Various tritium direct neutrino mass measurements have been reported in the literature. The latest of these in the 1990s were an experiment in Mainz, Germany and an experiment in Troitsk, Russia. These two experiments had similar detection methods using MAC-E-Filters (Magnetic Adiabatic Collimation combined with an Electrostatic Filter). This method is also used in the KATRIN experiment and will be discussed in section 1.2.1 below. The tritium source used in the two experiments was different. In the Mainz experiment, the source consisted of a film of molecular tritium quench-condensed onto graphite or aluminium substrates. For more details see Kraus *et al* [Kra05] and references therein. In the Troitsk experiment, a windowless gaseous tritium source was used [Bel95]. This type of source is also utilised in the KATRIN experiment and is discussed in section 1.2.2.

The Mainz and Troitsk experiments did not detect the mass of the neutrino within their energy resolution, so the published results were upper limits for the neutrino mass of $m_{\nu_e} < 2.30eV/c^2$ (95% C.L) and $m_{\nu_e} < 2.05eV/c^2$ (95% C.L) respectively [Kra05] and [Lob03].

1.2 KATRIN experiment

The Karlsruhe Tritium Neutrino (KATRIN) mass experiment is the next generation neutrino mass experiment under construction at Karlsruhe Institute of Technology (KIT). KATRIN is designed to improve the sensitivity of measurement of the neutrino mass down to $m_{\nu_e} < 0.2eV/c^2$; an order of magnitude reduction in the upper limit of m_{ν_e} given by the Mainz and Troitsk experiments [Ott08]. This will be achieved by measuring the shape of the β-spectrum of tritium near its end-point with a higher resolution. This involves increasing the source intensity, improving the energy resolution to $\Delta E \approx 1\,\text{eV}$ at the tritium β end-point of 18.6 keV and reducing the background level.

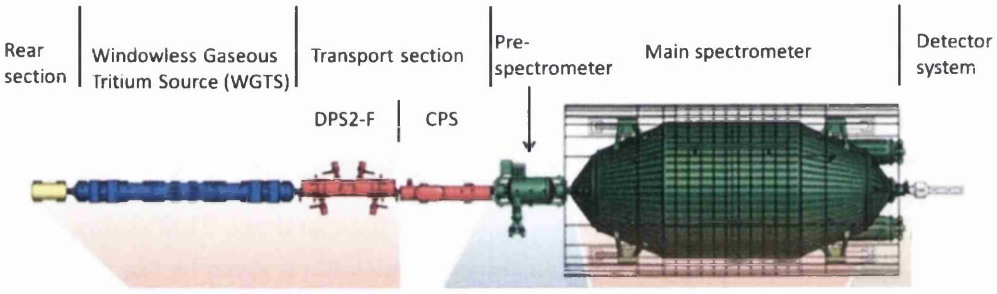

Figure 1.2: Diagram of the KATRIN setup (adapted from [Kat12]).

The KATRIN setup is made up of five main sections (see figure 1.2). The Windowless Gaseous Tritium Source (WGTS), the transport system, the pre-spectrometer, the main spectrometer (Mac-E-Filter) and the detector system. The MAC-E-Filter and WGTS will be discussed in more detail below. The transport system adiabatically guides the β-decay electrons from the source to the spectrometer using a series of superconducting solenoids with a 5.6 T magnetic field. The transport system also contains the DPS2-F and CPS pumping sections, which reduces the amount of tritium between the source and spectrometer by a factor of 10^7. The pre-spectrometer acts as a low energy electron rejection filter. It will be run at a retarding energy 200 eV below the β-endpoint, to reject all but the high energy electrons. After the MAC-E-Filter a large array of PIN photodiodes acts as the electron detector. For more details on the KATRIN components the reader is directed to the latest publications from the individual section groups [Bab12], [Pra12], [Wue10] [Val10] and the KATRIN webpage [Kat12].

1.2.1 MAC-E-Filter

The MAC-E-Filter (Magnetic Adiabatic Collimation combined with an Electrostatic Filter) was used in previous direct neutrino mass measurements in the 1990s ([Bel95], [Kra05]). The principle of operation of a MAC-E-Filter is shown in figure 1.3. It

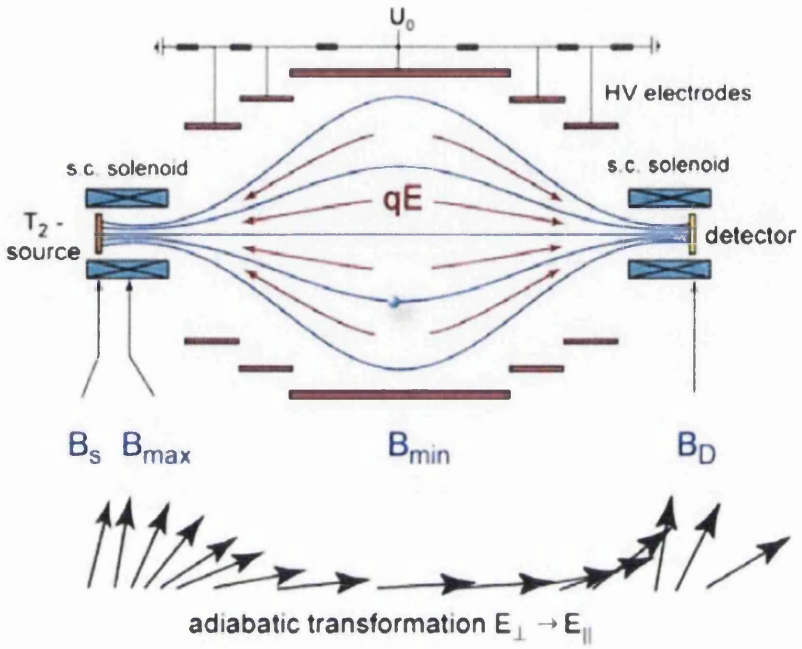

Figure 1.3: Principle of the operation of the MAC-E-Filter. From [Bor05]

consists of two superconducting solenoids, which produce an inhomogeneous magnetic field between the two. The magnetic field lines guide the decay electrons from the tritium source, through the spectrometer using cyclotron motion with a full forward acceptance solid angle of up to 2π. As the magnetic field passes through the spectrometer, it drops by several orders of magnitude. The magnetic gradient force transforms the majority of the cyclotron energy into longitudinal motion. This leads to the β-decay electrons being adiabatically transformed into a broad beam of electrons moving almost parallel to the magnetic field lines. The electrons can be energetically analysed by applying an electrostatic potential, produced by a set of cylindrical electrodes. The potential enables high energy electrons to pass through and reflects the lower energy electrons, thus it acts as a high-energy pass filter.

The KATRIN MAC-E-Filter is about 23 m long with a 10 m diameter. This allows the tritium β-decay endpoint to be scanned at a resolution of $\Delta E = 0.93\,\text{eV}$ [Wei05]. For more details on the MAC-E-Filter technique the reader is referred to Prall *et al* [Pra12].

1.2.2 Windowless Gaseous Tritium Source (WGTS)

The WGTS (used in the Troitsk experiment) was chosen over a frozen tritium source (used in the Mainz experiment), as KATRIN requires a source activity of 10^{11} Bq. If a frozen tritium source was used it would have to have a column density of 5×10^{17} molecules cm^{-1}, which corresponds to a 500 monolayer source thickness; this would generate a voltage of 10 V across the frozen film, which would reduce the energy resolution of the experiment. More details can be found in Otten and Weinheimer [Ott08].

The WGTS consists of a 10 m long cylindrical tube with a diameter of 90 mm, filled with molecular tritium gas; this has an isotopic purity of $> 95\%$ and is kept at a temperature of 27K. It is combined with the DPS2-F (differential pumping section) and the CPS (cryogenic pumping system) to form the STS (source and transport system) in KATRIN. The principle of the WGTS is shown in figure 1.4

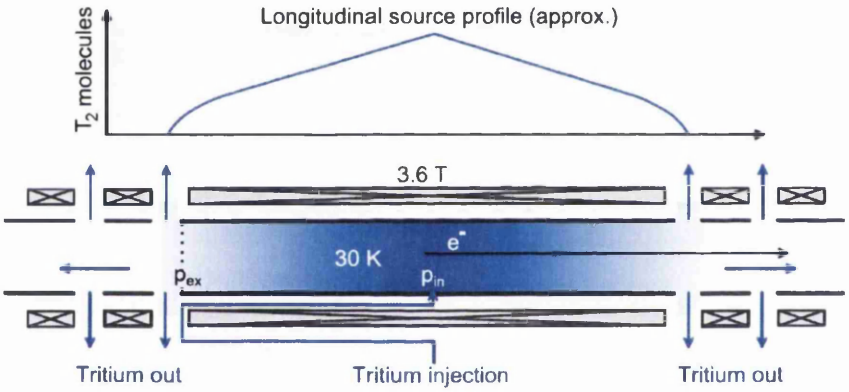

Figure 1.4: Principle of the WGTS. Tritium is continuously injected in the centre and pumped out at both ends to maintain a constant density profile. From Babutzka *et al* [Bab12].

The WGTS source tube will be surrounded by a chain of superconducting solenoids, which generate a homogeneous magnetic field of 3.6 T. The magnetic field will adiabatically guide the electrons, produced in the β^--decay, to the tube ends. The tritium gas mixture is injected near the centre of the source tube at a pressure, $p_{in} = 3.368 \times 10^{-3}$ mbar, and is pumped out at both ends with a pressure of approximately $0.03 - 0.05 p_{in}$. For more details on the operating parameters and current status of the WGTS, the reader is directed towards Babutzka *et al* [Bab12] and the references therein.

To achieve the required sensitivity on the neutrino mass measurement, the column density and isotopic purity of the tritium source gas are vitally important. The column density will not be considered further here. For more information the reader is directed towards Babutzka *et al* [Bab12]. Due to the the natural low abundance of the iso-

topologue T_2, and the design of the WGTS's tritium injection and gas circulation loop, T_2, HT and DT will be encountered in the system. The β spectrum and final state distributions of HT and DT are slightly different to that of T_2. Thus, the proportion of these isotopologues needs to be known, to achieve the required accuracy of the KATRIN experiment. This means that a monitoring procedure is required that measures the composition of the gas mixture with a high precision, in-line and as close to real time as is practicably achievable.

1.3 Laser Raman Spectroscopy in KATRIN

Laser Raman spectroscopy was identified as the most practical method to achieve the KATRIN design requirements for monitoring the tritium gas being injected into the WGTS. Foremost, the method had to be able to measure the individual hydrogen isotopologue components and dynamic changes within the mixture to the order of $\pm 0.1\%$ precision, with a trueness of better than 10%. The integration time of an individual measurement needs to be as short as possible, so that it is compatible with the KATRIN measurement interval.

Laser Raman spectroscopy has the advantage over other techniques as it is a non-contact and in-line analysis method based on inelastic Raman scattering. The theory behind Raman scattering is discussed in detail in chapters 2 and 3. Raman scattering is also sensitive to possible contaminant gases of nitrogen or tritiated methanes. These are not expected to be injected into the WGTS. However, tritiated methanes were detected in test measurements of the KATRIN tritium loop [Fis11] and were attributed to exchange reactions between tritium and carbon in the stainless steel vessels and tubes.

1.3.1 Previous Raman measurements at KIT

In past measurements by Lewis *et al* [Lew08] and Sturm *et al* [Stu09], a Raman system was demonstrated that met the KATRIN design requirements with 3σ measurement sensitivities of 5×10^{-3}, 7×10^{-3} and 25×10^{-3}mBar for T_2, DT and HT respectively. In the latter tests all six hydrogen isotopologues were observed, with an accumulation time of 1000 s, and a measured composition accuracy of $\pm 0.1\%$.

Even though the design requirements of the KATRIN experiment have been met, these measurements only monitor the relative intensities of the hydrogen isotopologues. Ideally, KATRIN would be supplied with absolute composition data for each isotopologue, with a trueness of better than 10%. The acquisition time of 1000 s can also be reduced by improving the signal-to-noise ratio of the Raman system.

Alongside the main LARA setup, which will be used for the KATRIN experiment at KIT, duplicate setups have also been constructed at KIT and Swansea, so that procedures can be developed and tested in parallel. In total, at the point of writing, there are

three LARA systems at the Tritium Laboratory Karlsruhe (TLK) in KIT and the one system in Swansea, which was used for the majority of the research described in this thesis.

1.4 Goals of this work

Raman spectroscopy of the hydrogen isotopologues has evolved over the previous five years, where four Raman spectroscopy systems have been built at KIT and Swansea. To enable the continuous monitoring of the gas composition for a period of up to 60 days, the stability and sensitivity of the system are important. Calibration techniques are also required to convert the measured intensities to absolute compositions. As a result of these requirements, the following will be considered here in this work:

1. Improvements to the sensitivity and stability of the Swansea LARA system were required. The reason behind this is to increase its sensitivity so that it is closer to that of the systems in KIT. Some of the sensitivity improvements may also be applicable to all systems, if they are shown to further enhance the system sensitivity. The improvement test measurements will be discussed in chapter 5.

2. To convert the measured Raman intensities to absolute concentrations, some form of system calibration was required. The method considered here involves creating theoretical Raman spectra from the Raman polarisability tensors (transition probabilities) and the systems spectral efficiency. However, there is no indication of the accuracy of the theoretical polarisability tensors. To verify the theoretical values, depolarisation measurements of all six hydrogen isotopologues are performed in chapter 6. As a result of these measurements (and some of the improvements discussed in chapter 5), an accurate calibration of the KATRIN LARA system has been performed by Schlösser *et al* [Sch12b]. This compares two calibration methods: the first using the verified theoretical values, performed in this work, with an accurate spectral sensitivity calibration; and the second based on accurate gas samples. A comparison of the non-radioactive isotopologues (H_2, HD and D_2) resulted in an agreement of better than 2% in the relative response function, which exceeds the trueness requirements of the KATRIN experiment of 10%. These measurements are beyond the scope of this work, so will not be discussed any further here.

3. As a result of developing a technique to accurately determine the depolarisation ratio of gas mixtures, this method is applied to atmospheric gases in chapter 7. These measurements are beyond the scope of the KATRIN experiment. However, there is a lack of accurate depolarisation measurements of these gases in the literature. The measurement also shows that the depolarisation measurement technique

can be applied to a number of gases beyond the hydrogen isotopologues. Note also that, in particular, methane isotopologues were observed in some extended-time scale measurements at LOOPINO in TLK [Fis11].

4. The KATRIN experiment requires a certain precision. However, beyond the scope of this experiment, improving the sensitivity of the Raman setup would enable the method to be applied to other tritium accountancy projects at TLK. This could prove to be particularly useful in monitoring injection gases in research linked to the ITER experiment [Shu12]. With this in mind, a technique called capillary Raman spectroscopy is investigated in chapter 8 to determine the potential increase in the signal-to-noise ratio over standard 90° Raman spectroscopy. The setup is based on the work of Okita *et al* [Okit10] and Buric *et al* [Bur10].

5. As part of the required KATRIN LARA package software, routines have been developed that enable full on-line analysis, in the form of a fully automated procedure for post-acquisition data treatment of (Raman) spectra and analysis of spectral line peaks. This is discussed in detail in [Jam13], [SJLc], [SJLd], and appendix A.6.

6. As the Raman spectra of all six hydrogen isotopologues are measured in this work, the line positions (Raman shift) of the isotopologues can be compared with different theoretical methods. In chapter 6, the measurement and comparison is made for the non-tritiated isotopologues H_2, HD and D_2. The intent is to accurately perform the measurement for all six isotopologues in the near future.

A long-term run of the KATRIN loop system was performed by Fischer *et al* [Fis11], before the improvements discussed in chapter 5 were implemented. Even though this demonstrated that all six hydrogen isotopologues could be monitored simultaneously, for a period of > 21 days, with a precision of 0.1% (an individual accumulation time of 250 s and a 5 W laser power), the improvements would reduce the accumulation time further.

Chapter 9 summarises the results of this work and discusses the future work that is planned. This includes a planned repeat long term measurement run with the KATRIN LARA system, to verify that all the improvements have been successful.

Chapter 2

The Raman effect

2.1 Chapter overview

In this chapter the basic aspects of Raman scattering are discussed and links to the polarisability tensor and the time dependent induced electric dipole vector are provided. Note that, a full quantum mechanical treatment is needed for real world quantitative analysis of Raman spectra. This allows one to differentiate between the hydrogen isotopologues (H_2, D_2, T_2, HD, HT and DT). For a full treatment of Raman scattering the reader is directed towards Long [Lon02].

The selection rules for Raman scattering of diatomic molecules are summarised along with the equations required to calculate the Raman line positions of diatomic molecules with unperturbed electronic states.

The concept of non-linear Raman spectroscopy is introduced as a potential enhancement over normal Raman scattering. Our first experimental tests of a form of stimulated Raman scattering called PARS are beyond the scope of the work in this thesis, and are not described here, but will be looked at in detail by other members of the KATRIN LARA group.

2.2 The Raman effect

When a beam of monochromatic radiation, with a frequency ω_1, is focussed into a sample, some of the light will interact with the sample. When the light interacts it will be reflected, absorbed or scattered. The reflected and absorption interactions will not be discussed here. When investigating the spectrum of the scattered radiation, scattered light with exactly the same frequencies as the incident light is found. This effect is called Rayleigh scattering. However, one will also find some weak additional lines that do not appear in the spectrum of the incident light source. This phenomenon is commonly known as the Raman effect (or Raman scattering).

Each of the Rayleigh lines in the scattered spectrum is accompanied by one or more Raman lines, where the displacements from the Rayleigh lines (in cm^{-1}) are independent of the (excitation) frequency of the Rayleigh lines. This implies that, if an alternative light source (with a different emission spectrum) is used with the same scattering substance, other Raman lines are obtained but their displacements from the Rayleigh lines are the same. If the scattering substance is changed the displacement has a different magnitude. Thus the displacement of the Raman lines from the Rayleigh lines is a characteristic of the scattering substance used. Consequently, the Raman effect can be used to determine the nature of the scattering substance.

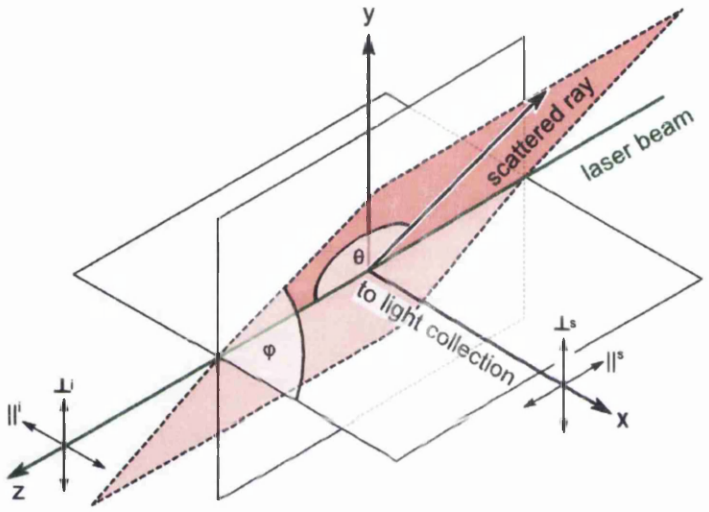

Figure 2.1: Generalised light scattering experiment. The laser beam moves along the z-axis and the angles define the direction of the scattered light. The scattering point is at the axis origin.

Figure 2.1 shows a generalised, incoherent light scattering experiment. The figure includes the angles θ and φ, which define the direction of the scattered light. These will be discussed in more detail in chapter 3. From a practical (spectroscopy) point of view, one would like to know how the relationship, between incident and scattered radiation's properties, is determined by the material's system-properties and the illumination-observation geometry.

2.2.1 Stokes and anti-Stokes Raman scattering

The energy level diagrams of non-resonant Rayleigh and Raman scattering via an intermediate state, $|\, r\rangle$, are shown in figure 2.2. $|\, r\rangle$ is not a real state but a state combining a photon with an initial molecular quantum state, when they are both in close proximity i.e. a so called "dressed" state. As can be seen in the figure, Raman scattering is split

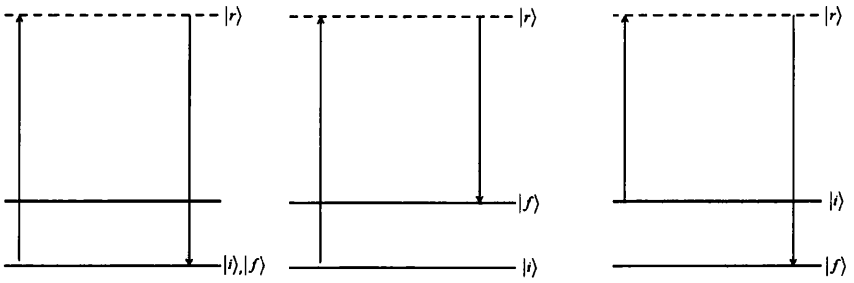

Figure 2.2: Schematic energy level diagrams for non resonant-photon excitation: a) Rayleigh scattering, b) Stokes Raman scattering and c) anti-Stokes Raman scattering.

into two types. These being when the photon frequency of the Raman scattered light is less than the frequency of incident radiation ($\omega_s = \omega_i - \omega_m$), this is called Stokes Raman scattering; when the photon frequency of Raman scattered light is more than the frequency of the incident radiation ($\omega_s = \omega_i + \omega_m$), this is called anti-Stokes Raman scattering. In this work we are only interested in the Stokes Raman scattered lines and block the anti-Stokes lines using an Edge filter.

2.2.2 Raman intensities

The intensity is defined as the time averaged power per unit solid angle radiated by an oscillating electric dipole, p_0, which is induced in a molecule due to incident electromagnetic radiation. Classically, the intensity is given by

$$I = k'_\omega \omega_s^4 p_0^2 \sin^2 \theta_o \tag{2.1}$$

where ω_s is the angular frequency of the scattered radiation, θ_o is the angle between the observation direction and the axis of the induced dipole (not the same as θ in figure 2.1) and k'_ω is defined as:

$$k'_\omega = \frac{1}{32\pi^2 \epsilon_0 c_0^3} \tag{2.2}$$

where ϵ_0 is the permittivity of free space and c_0 is the speed of light in a vacuum.

This can be reformulated for the wavenumber $\tilde{\nu}$ using the substitution

$$\omega_s = 2\pi c_0 \tilde{\nu}_s \tag{2.3}$$

producing

$$I = k' \tilde{\nu}^4 p_0^2 \sin^2 \theta_o \tag{2.4}$$

with

$$k'_\nu = \frac{\pi^2 c_0}{2\epsilon_0} \tag{2.5}$$

Both equations are included as angular frequency is usually used in theoretical treatments, while in real world spectra the band position in the spectrum is the main interest. Raman spectra are also normally represented in terms of wavenumber shifts, rather than wavelength or frequency, as the wavenumber shift is invariant if the wavelength of the monochromatic excitation radiation is changed.

The wavenumber $\tilde{\nu}$ in vacuum is defined as

$$\tilde{\nu}(\mathrm{cm}^{-1}) = \frac{1}{\lambda(\mathrm{cm})} \tag{2.6}$$

However, in reality Raman measurements are performed in a medium. Therefore, the refractive index needs to be taken into account. This changes the wavenumber $\tilde{\nu}$ to

$$\tilde{\nu}(\mathrm{cm}^{-1}) = \frac{\mathrm{n}}{\lambda(\mathrm{cm})} \tag{2.7}$$

where n is the refractive index of the medium. The wavenumber shift of the Raman lines is then $\tilde{\nu}_s = \tilde{\nu}_0 - \tilde{\nu}_{\mathrm{v,J}}$ (Stokes) and $\tilde{\nu}_s = \tilde{\nu}_0 + \tilde{\nu}_{\mathrm{v,J}}$ (anti-Stokes).

Raman intensity expressions will be discussed in more detail in chapter 3.

2.2.3 Raman spectroscopy in KATRIN

The KATRIN monitoring system (LARA) will focus on vibration-rotation lines, as the operating temperature of the inner loop in the WGTS is low enough that the strongest pure rotation tritium lines would be cut-off by the laser edge filter, meaning they would no longer be visible. Intensities are also needed as they show a strong dependence on Raman scattering with respect to the polarisation. This means that the quantum mechanical treatment of the Raman effect is essential as the classical treatment does not provide a full analysis of the vibration rotation lines.

2.2.4 Resonant Raman scattering

A type of Raman scattering exists where the frequency of the incident radiation, ω_i, approaches and surpasses a molecular transition frequency ω_{ri}; this process is called resonance Raman scattering. This can be split into three distinct types where i) $\omega_i \rightarrow \omega_{\mathrm{ri}}$ pre-resonance Raman scattering, ii) $\omega_i = \omega_{\mathrm{ri}}$ resonance Raman scattering and iii) ω_i is in the range of dissociative continuum levels which is called continuum resonance Raman scattering. The intensity of resonance Raman scattering is expected to be orders of magnitude higher than normal Raman scattering as the denominator of the Raman transition probability of the terms $\omega_{\mathrm{ri}} - \omega_i - i\Gamma_r$ [Lon02] tends to $-i\Gamma_r$ for the state $|r>$

and these terms dominate in the transition probability.

Other than an increased intensity, resonance Raman spectroscopy has the advantage that detailed information about the states and their lifetimes can be extracted from the measured spectra. For more information the reader is directed to [Lon02].

An application of resonance Raman scattering is Gonzálvez and Ureña [Gon12], where they combine resonance Raman scattering with a technique called transmission Raman spectroscopy to analyse β-carotene in carrots. They have observed an enhancement in sensitivity of several orders of magnitude of the resonant Raman signal compared with non-resonant Raman spectroscopy. This enhancement enables a detection sensitivity of the order of hundreds of picograms in solid samples.

Even though resonant Raman spectroscopy would lead to an increased intensity it is not feasible for the hydrogen isotopologues as it would require Raman excitation at UV wavelengths, which is not easily possible.

2.3 Raman scattering: theoretical principles

In the theoretical treatment of Raman Scattering, the scattered radiation is seen to be produced by the oscillating electric (or magnetic) multipole moments of the incident electromagnetic radiation. The dynamic electric field $\boldsymbol{E}$, is a time dependent electric field vector, which is a monochromatic plane wave of frequency ω_1.

The theory of Raman scattering can be considered using a classical or quantum mechanical treatment. The classical theory can be used to consider Rayleigh scattering and vibration Raman scattering if the frequency dependencies are required only. However, in this work the Raman line positions and intensities need to be quantified. Therefore, the quantum mechanical treatment will only be considered.

2.3.1 Quantum mechanical theory

Looking at the quantum mechanical treatment, the electromagnetic radiation is treated as a classical field and the scattering molecule is treated quantum mechanically (to enable a full quantitative analysis of the scattering process). The theory can be interpreted as a series of small perturbations on the state vectors of the scattering molecule by the electromagnetic fields. The properties of these perturbations are then investigated using time independent perturbation theory.

In this quantum mechanical process, the scattering transitions are interpreted as the allowed transitions between the states of the molecule whilst the molecule is being perturbed by the classical electromagnetic fields.

The aim of the quantum mechanical treatment is to derive expressions for the transition dipole moment tensor and the transition polarisability tensor, as they can be (in principle) linked quantitatively to the molecular properties of the scattering molecule.

The quantum mechanical total induced electric dipole vector $(\boldsymbol{p})_{fi}$ can be written as a sum of the time-dependent induced electric dipole moment vectors

$$(\boldsymbol{p})_{fi} = (\boldsymbol{p}^1)_{fi} + (\boldsymbol{p}^2)_{fi} + (\boldsymbol{p}^3)_{fi} + \dots \tag{2.8}$$

Each term increases the order of its dependence on the electric field $\boldsymbol{E}$: $(\boldsymbol{p}^{(1)})_{fi}$ is linear in $\boldsymbol{E}$, $(\boldsymbol{p}^{(2)})_{fi}$ is quadratic in $\boldsymbol{E}$, $(\boldsymbol{p}^{(3)})_{fi}$ is cubic etc. With appropriate definitions of the total induced electric dipole vector and the wavefunctions within the relationship between the electric field $\boldsymbol{E}$, the polarisability tensor and the time dependent induced transition electric dipole vector can be derived. This leads to the expressions

$$(p_\rho^{(1)})_{fi} = \frac{1}{2}(p_{\rho_0}^{(1)})_{fi}\{\exp(-i\omega_s t) + \exp(i\omega_s t)\} \tag{2.9}$$

with

$$(p_{\rho_0}^{(1)})_{fi} = (\alpha_{\rho\sigma})_{fi} E_{\sigma_0}(\omega_1) \tag{2.10}$$

For a complete derivation of these equations the reader is directed towards Lewis [Lew07] or Long [Lon02]. The definition of the time dependent induced transition electric dipole vector is used in chapter 3 to obtain a complete expression for the Raman intensity of the hydrogen isotopologues (diatomic molecules).

2.3.2 Selection rules for diatomic molecules

The branch labelling notation used here is the same as that used previously by Lewis [Lew07]. This notation is the same as Long [Lon02] with the addition of subscripts indicating the value of Δv. The change in the vibrational quantum number v for diatomic molecules is $\Delta v = 0, \pm 1, (\pm 2$ overtones $<<$ intensity). The addition of the subscript notation means that a '0' subscript identifies the pure rotation branch and a '1' subscript identifies the vibration-rotation branch. The subscript notation states the vibrational level at the end of the transition. For example a Q_1-branch starts in $v'' = 0$ and ends in $v' = 1$. The simplified branch names of S_0, S_1, Q_1 and O_1 are implemented for diatomic molecules.

The S_0-branch is the pure rotational transition and the O_1-, Q_1- and S_1-branches are the three vibration-rotation transitions. Also, the notation for the wavenumber (or Raman) shift is taken as $S_0(J)$ etc. In a more general case (like in Long [Lon02]) the Raman shift is taken as $S(J); |\Delta\tilde{\nu}|$ and the sign of the $\Delta\tilde{\nu}$ is clarified by the context $(J = J'')$.

Looking at the definition of $\Delta J = J' - J''$, the double prime refers to the lower energy level and the single prime refers to the higher energy level. This applies if J' is in the same rotational manifold as J'', or they are members of a manifold of a different electronic or vibrational state. However, the J parameter in the Raman shift symbol

Table 2.1: Values of the experimental constants used to model the line positions of the hydrogen isotopologues (from Lewis [Lew07]). * means value is interpolated. The uncertainty (when stated) is in the final digit.

	Constant / cm^{-1}					
	H_2	HD	HT	D_2	DT	T_2
B_0	59.339(5)	44.668(5)	40.055*	29.911(5)	24.331*	20.0386(5)
D_0	0.0460(3)	0.0259(3)	0.0205*	0.0113(3)	0.0071*	0.00499(4)
$H_0(\times 10^{-6})$	52(5)	22(5)	14 *	4(5)	2 *	1.2(8)
$\tilde{\nu_{vib}}$	4161.14	3632.05	3445.68*	2993.56	2723.46*	2464.324(1)
B_1	56.36(1)	42.74(1)	38.39*	28.85(1)	23.66*	19.4530(7)
D_1	0.043(1)	0.026(1)	0.021*	0.011(1)	0.007*	0.00470(5)

and rotational energy is always taken to be J'' for all diatomic Stokes Raman transitions that are being considered in this work.

The simplified branch names of S_0, S_1, Q_1 and O_1 of the diatomic molecules correspond to the following energy level changes

- $\Delta J = +2$ and $\Delta v = 0$ the branch name is S_0.
- $\Delta J = -2$ and $\Delta v = 1$ the branch name is O_1.
- $\Delta J = 0$ and $\Delta v = 1$ the branch name is Q_1.
- $\Delta J = +2$ and $\Delta v = 1$ the branch name is S_1.

For a more rigorous derivation of the selection rules for Raman spectra see Long [Lon02] or an equivalent book on the Raman effect.

Please note that for polyatomic molecules the notation becomes more complex. For measurements of atmospheric gases (included in chapter 7) the appropriate line naming convention and selection rules will be discussed briefly.

2.3.3 Raman Line Positions

The position of the Raman lines is being measured in the KATRIN LARA setup. Therefore, the expected positions of the Raman lines need to be known as these are used to determine the scattering sample from the measured spectrum. The line positions can be determined using theoretical calculations or by approximations from experimentally determined spectroscopic constants. The method of determining the line positions using experimental constants has been considered previously by Lewis [Lew07] and the final results will only be included here. The experimental constants used in [Lew07] are collated in table 2.1.

Table 2.2: Raman (wavenumber) shifts for the first ten lines of the Stokes S_0-branch for the six hydrogen isotopologues (from Lewis [Lew07]).

	Raman Shift $S_0(J)$ / cm^{-1}					
J''	H_2	HD	HT	D_2	DT	T_2
0	354.389	267.080	239.597	179.060	145.732	120.052
1	587.039	443.092	397.708	297.535	242.323	199.689
2	814.407	616.096	553.426	414.672	338.074	278.733
3	1034.640	785.000	705.865	529.956	432.662	356.953
4	1246.151	948.822	854.212	642.893	525.770	434.122
5	1447.686	1106.725	997.744	753.014	617.099	510.024
6	1638.406	1258.044	1135.852	859.881	706.366	584.451
7	1817.958	1402.319	1268.062	963.094	793.306	657.206
8	1986.549	1539.330	1394.051	1062.298	877.680	728.105
9	2145.024	1669.126	1513.672	1157.185	959.274	796.980

To enable a better understanding of the constants in the table the generic formula for vibration-rotation energy levels (assuming the electronic energy is zero) is

$$E_{v,J} = G_v + F_{v,J} \tag{2.11}$$

where

$$(G_1 - G_0) = \tilde{\nu_{\text{vib}}} \tag{2.12}$$

$$F_{v,J} = B_v J(J+1) - D_v J^2(J+1)^2 + \ldots \tag{2.13}$$

Pure rotational transitions The pure rotational wavenumber shift for diatomic molecules is

$$S_0(J) = (4B_0 - 6D_0 + \frac{27}{4}H_0)(J+\frac{3}{2}) - (8D_0 - 34H_0)(J+\frac{3}{2})^3 + 12H_0(J+\frac{3}{2})^5 \tag{2.14}$$

where B_0 is a constant of proportionality, D_0 is a small positive centrifugal stretching constant and H_0 is a very small positive correction to the line position.

The model that was produced by R.J Lewis in [Lew07] obtained appropriate values of B_0, D_0 and H_0 for the hydrogen isotopologues from different texts cited in the work (summarised in table 2.1) and by an interpolation procedure for the HT and DT values. A *National Instruments* LabVIEW program was written in Lewis [Lew07] that calculates the Raman shift for the first ten lines of each branch. The values calculated using this code are shown in table 2.2.

These Raman shifts are subtracted from the absolute wavenumber value of the exciting radiation. The absolute wavenumber value of the scattered radiation is given by

$$\tilde{\nu}_s = \tilde{\nu}_i - S_0(J) \tag{2.15}$$

where $\tilde{\nu}_i$ is the absolute wavenumber of the incident radiation.

Vibration-rotation transitions The expressions for the positions of the vibration-rotation branches are

$$\begin{aligned} S_1(J) = \tilde{\nu}_{vib} &+ 6B_1 + (5B_1 - B_0)J + (B_1 - B_0)J^2 \\ &- \frac{9}{16}(D_1 - D_0) - \frac{3}{2}(D_1 + D_0)(2J+3) - \frac{11}{8}(D_1 - D_0)(2J+3)^2 \\ &- \frac{1}{2}(D_1 + D_0)(2J+3)^3 - \frac{1}{16}(D_1 - D_0)(2J+3)^4 \end{aligned} \tag{2.16}$$

with $J = J'' = 0, 1, 2, \ldots,$

$$\begin{aligned} O_1(J) = \tilde{\nu}_{vib} &+ 2B_1 - (3B_1 + B_0)J + (B_1 - B_0)J^2 \\ &- \frac{9}{16}(D_1 - D_0) + \frac{3}{2}(D_1 + D_0)(2J-1) - \frac{11}{2}(D_1 - D_0)(2J-1)^2 \\ &+ \frac{1}{2}(D_1 + D_0)(2J-1)^3 - \frac{1}{16}(D_1 - D_0)(2J-1)^4 \end{aligned} \tag{2.17}$$

with $J = J'' = 2, 3, 4, \ldots,$

$$Q_1(J) = \tilde{\nu}_{vib} + (B_1 - B_0)J(J+1) + (D_1 - D_0)J^2(J+1)^2 \tag{2.18}$$

with $J = J'' = 0, 1, 2, \ldots.$

The definitions and values of the constants B_0, D_0, B_1, D_1 and the vibrational band offset ($\tilde{\nu}_{vib}$) for the hydrogen isotopologues can be found in Lewis [Lew07] (and in table 2.1). Again, the aforementioned LabVIEW routine was applied to calculate the first ten lines of each branch of the S_1, O_1 and Q_1 branches (see table 2.3).

Combining these with the first ten S_0-branch shifts leads to a complete set of Stokes Raman lines for the hydrogen isotopologues.

Theoretical calculations The Raman line positions can also be determined from theoretical calculations of the energy levels [LRoy88]. The line position is then determined from the energy level difference. The line positions of the first ten Raman lines for each branch of the hydrogen isotopologues analogous to those in table 2.3 have been calculated using the theoretical energy levels from LeRoy [Roy12]. These line positions are collated in table 2.4. Note that the pure rotational transitions have not been recalculated as they are too close to the laser line to be completely observed.

Table 2.3: Raman (wavenumber) shifts for the first ten lines of the Stokes S_1-, Q_1- and O_1-branches for the six hydrogen isotopologues (from Lewis [Lew07]).

	Raman Shift $S_1(J)$ / cm^{-1}					
J''	H_2	HD	HT	D_2	DT	T_2
0	4497.752	3887.554	3675.264	3166.264	2865.168	2580.873
1	4712.774	4051.954	3823.308	3278.399	2957.738	2657.026
2	4916.762	4209.374	3965.486	3387.101	3048.129	2731.452
3	5107.796	4358.564	4100.768	3491.855	3136.007	2803.939
4	5284.028	4498.266	4228.106	3592.156	3221.043	2874.283
5	5443.682	4627.224	4346.445	3687.504	3302.907	2942.286
6	5585.054	4744.178	4454.715	3777.407	3381.274	3007.756
7	5706.512	4847.864	4551.833	3861.381	3455.817	3070.511
8	5806.496	4937.020	4636.705	3938.947	3526.215	3130.373
9	5883.518	5010.376	4708.225	4009.636	3592.145	3187.172

	Raman Shift $Q_1(J)$ / cm^{-1}					
J''	H_2	HD	HT	D_2	DT	T_2
0	4161.140	3632.050	3445.680	2993.560	2723.460	2464.324
1	4155.194	3628.194	3442.348	2991.439	2722.118	2463.154
2	4143.374	3620.478	3435.670	2987.205	2719.437	2460.821
3	4125.824	3608.900	3425.624	2980.871	2715.419	2457.339
4	4102.760	3593.450	3412.170	2972.46	2710.071	2452.728
5	4074.470	3574.120	3395.261	2962.000	2703.399	2447.017
6	4041.314	3550.898	3374.835	2949.527	2695.414	2440.240
7	4003.724	3523.768	3350.817	2935.085	2686.125	2432.440
8	3962.204	3492.716	3323.121	2918.723	2675.547	2423.664
9	3917.330	3457.720	3291.649	2900.500	2663.693	2413.969

	Raman Shift $O_1(J)$ / cm^{-1}					
J''	H_2	HD	HT	D_2	DT	T_2
2	3803.669	3363.102	3204.574	2813.709	2577.225	2343.934
3	3556.093	3177.863	3038.803	2690.820	2477.836	2262.140
4	3297.582	2985.642	2867.150	2564.507	2376.270	2178.628
5	3026.216	2785.186	2688.582	2434.257	2272.195	2093.187
6	2740.147	2575.240	2502.055	2299.564	2165.279	2005.613
7	2437.599	2354.546	2306.512	2159.927	2055.195	1915.706
8	2116.868	2121.845	2100.882	2014.856	1941.615	1823.278
9	1776.322	1875.873	1884.083	1863.864	1824.215	1728.142
10	1414.401	1615.367	1655.022	1706.476	1702.672	1630.124
11	1029.617	1339.058	1412.591	1542.220	1576.663	1529.053

Table 2.4: Theoretical Raman (wavenumber) shifts for the first ten lines of the Stokes S_1-, Q_1- and O_1-branches for the six hydrogen isotopologues (calculated from energy levels in LeRoy [Roy12]).

	Raman Shift $S_1(J)$ / cm^{-1}					
J''	H_2	HD	HT	D_2	DT	T_2
0	4497.820	3887.662	3663.017	3166.35	2888.114	2581.099
1	4712.887	4052.177	3810.325	3278.513	2982.410	2657.277
2	4916.990	4209.942	3952.093	3387.252	3074.177	2731.705
3	5108.388	4359.923	4087.487	3492.084	3163.070	2804.158
4	5285.577	4501.194	4215.754	3592.556	3248.767	2874.423
5	5447.324	4632.952	4336.229	3688.258	3330.970	2942.299
6	5592.675	4754.532	4448.345	3778.827	3409.405	3007.600
7	5720.963	4865.404	4551.641	3863.942	3483.833	3070.157
8	5831.790	4965.179	4645.758	3943.342	3554.044	3129.816
9	5925.008	5053.604	4730.441	4016.812	3619.858	3186.446

	Raman Shift $Q_1(J)$ / cm^{-1}					
J''	H_2	HD	HT	D_2	DT	T_2
0	4161.147	3632.143	3434.846	2993.606	2743.324	2464.498
1	4155.234	3628.287	3431.608	2991.497	2741.715	2463.342
2	4143.447	3620.593	3425.146	2987.283	2738.500	2461.033
3	4125.855	3609.096	3415.486	2980.979	2733.688	2457.575
4	4102.565	3593.850	3402.667	2972.604	2727.291	2452.976
5	4073.717	3574.922	3386.742	2962.184	2719.326	2447.245
6	4039.478	3552.398	3367.774	2949.75	2709.812	2440.393
7	4000.044	3526.376	3345.837	2935.338	2698.775	2432.436
8	3955.630	3496.967	3321.016	2918.994	2686.241	2423.388
9	3906.472	3464.295	3293.406	2900.763	2672.240	2413.268

	Raman Shift $O_1(J)$ / cm^{-1}					
J''	H_2	HD	HT	D_2	DT	T_2
2	3806.774	3365.074	3196.975	2814.539	2593.710	2344.432
3	3568.202	3185.206	3036.769	2693.963	2492.993	2263.640
4	3329.022	3004.501	2875.720	2572.635	2391.614	2182.304
5	3091.184	2824.095	2714.741	2451.079	2289.944	2100.662
6	2856.466	2645.054	2554.687	2329.798	2188.336	2018.946
7	2626.437	2468.346	2396.350	2209.264	2087.131	1937.382
8	2402.433	2294.833	2240.445	2089.917	1986.648	1856.181
9	2185.553	2125.267	2087.602	1972.159	1887.182	1775.547
10	1976.654	1960.280	1938.364	1856.350	1789.006	1695.667
11	1776.373	1800.384	1793.187	1742.805	1692.364	1616.715

When comparing the calculated Raman line positions using the two methods significant discrepancies can be noted. In chapter 6 the line positions for the non-tritiated have been measured and are compared to these calculations from first principles and based on spectroscopic constants.

2.4 Non-linear Raman scattering

Raman signals can be enhanced by either using clever signal amplification and collection techniques (see chapters 5 and 8 and/or Pearman *et al* [Pea08]) or by looking into non-linear Raman spectroscopy. In normal Raman spectroscopy, with the theory described in the sections above, the incident radiation consisted of one monochromatic wave for frequency ω_1. In non-linear Raman spectroscopy, the incident radiation comprises two overlapping beams of frequencies ω_1 and ω_2. If ω_2 is varied whilst keeping ω_1 constant, the intensity of the scattered radiation increases dramatically when $\omega_1 - \omega_2 = \omega_m$, where ω_m is the molecular frequency from Raman scattering. This condition is called the Raman resonance and can be satisfied in a couple of ways, and thus splits non-linear Raman spectroscopy into two main groups, namely

1. Stimulated Raman (gain or loss) spectroscopy (SRS)
2. Coherent anti-stokes (or stokes) Raman scattering (CARS)

Below, each of these methods is briefly sketched individually.

2.4.1 Stimulated Raman spectroscopy

In SRS $\omega_1 > \omega_2$ with the Raman resonance condition $\omega_1 - \omega_2 = \omega_m$ and $\omega_s = \omega_2 = \omega_1 - \omega_m$. This situation can be visualised as the interaction of the radiation within the sample material, resulting in the annihilation of a photon of energy $\hbar\omega_1$ and the creation of a photon of energy $\hbar\omega_2$. This means that, if before the interaction the radiation consisted of n_1 photons of ω_1 and ω_2, it now consists of $(n_1 - 1)$ photons of energy $\hbar\omega_1$ and $(n_2 + 1)$ photons of energy $\hbar\omega_2$. The process is a Stokes Raman process like in normal Raman scattering. However, it is stimulated under the presence of radiation of frequency $\omega_2 = \omega_1 - \omega_m$ and produces a gain in intensity of frequency ω_2. It should be noted that, the gain in intensity can be exponential and that the gain in ω_2 corresponds directly to a loss in ω_1. Also the opposite (anti-Stokes) process can occur where a photon of energy $\hbar\omega_2$ is annihilated and a photon of energy $\hbar\omega_1$ is created. It should also be noted that as the number of photons of frequency ω_2 goes to zero, SRS tends to normal Raman spectroscopy. The energy level diagram for stimulated Raman scattering is shown in figure 2.3 i.

The main disadvantage of SRS is that the probe beam is mixed with the scattered radiation as the amplification only occurs in the direction of the probe beam. This

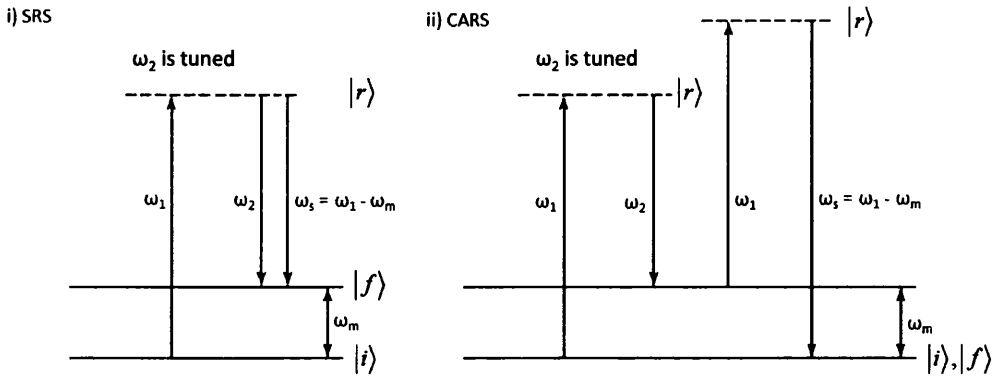

Figure 2.3: Energy level diagrams for non-linear scattering: (i)Coherent anti Stokes Raman scattering (CARS) and (ii) stimulated Raman scattering (SRS)

means different methods are needed to remove the probe beam and obtain the scattered signal on its own.

The SRS process has been extensively studied for solids, liquids and gases (See e.g. Owyoung [Owy78] and Eckhardt [Eck62]). A variety of different methods of experimentally achieving SRS have been developed over the years; some examples are given below

- In 1978 Owyoung [Owy78] took measurements of the Q_1 branch in hydrogen, with a gas pressure of 266.64 mbar with a 450 mW pump beam and a 15 mW probe beam. The detection method was using a silicon photodiode. Owyoung reports that SRS enables high resolution Raman spectra to be taken in the presence of background fluorescence and luminescence. It also states that the sensitivity is not reduced by increasing the resolution of the measured spectra. The quoted detection limit for a 1 W pump beam and 10 mW probe beam with a 3 s integration time for H_2 is 4.67 mbar

- Multiple authors ([Plo07], [McCam03] and [Witt00] and others) have used high powered, pulsed beams as the pump and probe beams, which leads to very large amplifications of the Raman signal. McCammant *et al* [McCam03] compare their measured femtosecond SRS (FSRS) spectra with 90° Raman. They state that to obtain a signal-to-noise ratio of 100 using rhodamine 6G as the scattering substance requires an acquisition time of 11 s for FSRS. For 90° Raman an acquisition time of 180 s is required. This corresponds to an order of magnitude gain in the system sensitivity.

- An innovative variant of SRS was developed by Barrett *et al* [Bar79] and [Bar85] called photoacoustic Raman spectroscopy (PARS). The excitation process is the

same as for SRS. However, the difference is in the method of observing the signal. In SRS the amplification is observed in the same way as normal Raman i.e. observing the scattered light. In PARS during or following stimulated Raman scattering, collisional relaxation of the excited molecules produces a pressure change in the sample medium. This pressure change is then detected by a microphone. At least one of either the pump or probe beam needs to be pulsed or modulated. Chopped continuous wave (cw) laser beams can be used, although the overall enhancement is lower. In Barrett [Bar85] sensitivity limits (signal-to-noise ratio of 1) for a variety of gases are reported with an observed sensitivity limit of 1 ppm of CH_4 in 1 bar N_2 buffer gas using 50 and 14.5 mJ pulses of the pump and probe beam respectively. When a CW source was used a signal-to-noise ratio of approximately 30 is observed for 1066.58 mbar of methane. The authors do not state an exact gain when using pulsed sources. However, a calculation is performed that shows for low power CW PARS the Stokes gain is of the order of 10^{-5} per cm. For high power pulsed sources the Stokes gain is of the order of 5 per cm. This is an increase of 5 orders of magnitude.

Of the experimental methods of achieving stimulated Raman scattering, PARS seemed the most interesting. While first attempts at PARS were undertaken by our group, the research is beyond the scope of this work, but will be looked into in more detail by other members of the KATRIN LARA group in the future.

2.4.2 Coherent anti Stokes Raman scattering

In CARS $\omega_1 > \omega_2$ with the Raman resonance condition $\omega_1 - \omega_2 = \omega_m$ and $\omega_s = 2\omega_1 - \omega_2 = \omega_1 + (\omega_1 - \omega_2) = \omega_1 + \omega_m$. This situation can be visualised, if we consider the frequency combination of $2\omega_1 - \omega_2$ and vary ω_2 as above until the Raman resonance condition is satisfied. A CARS spectrum is obtained by varying ω_2 over the desired range of ω_m and the CARS spectrum is superimposed on a background of week non-resonant scattering given by $2\omega_1 - \omega_2$. The energy level diagram for CARS is shown in figure 2.3 ii.

CARS will not be discussed further as the CARS resonance is much more difficult to tune than SRS, even though others in the literature have found that it may be slightly more sensitive [Oki99] in favourable cases.

CARS is mostly used by research groups investigating solid samples in biomedical applications (for e.g. see [Eva05], [Bon09] or [Dow01]).

Chapter 3

Theory of Raman intensities and depolarisation ratio measurements

3.1 Chapter overview

In this chapter the theory behind Raman intensities is described. Specifically, the angular dependence of the line strength function is calculated, so that a full integral intensity description over the solid collection angle is obtained.

The solid angle is parameterised by setting the integration limits appropriately. This has been calculated for the collection angle, which is governed by two separate apertures; this is the case in the KATRIN LARA systems and any system where a cell is used to hold the gas mixture. The second aperture becomes important when scattering from an extended source is taken into account. The integration limits have been defined for situations where the window radius r_w is greater than the focal lens radius r_f and visa versa.

The intensity theory is applied to depolarisation measurements and the theory is used in the analysis of depolarisation measurements for the hydrogen isotopologues and atmospheric gases. This is discussed further in chapters 6 and 7. It is also discussed in [SJLa] and [SJLb] in the form of the DepolTools analysis software.

The theory is needed to calculate the intensity of the scattered light. The measured intensities can be used to determine the composition of the gas mixture. The theory discussed here is a condensed form of the more thorough treatment used in Long [Lon02].

3.2 Raman intensities

3.2.1 Aims of theoretical discussion

The aim of this section is to produce a full theoretical description of the intensity of Raman scattered light for diatomic molecules. This involves extending equation (2.4) to produce quantities that can be defined from an experimental point of view and considering the individual terms such as the wavelength dependence. During this derivation certain approximations are needed, which are valid for discussions relating specifically to the hydrogen isotopologues.

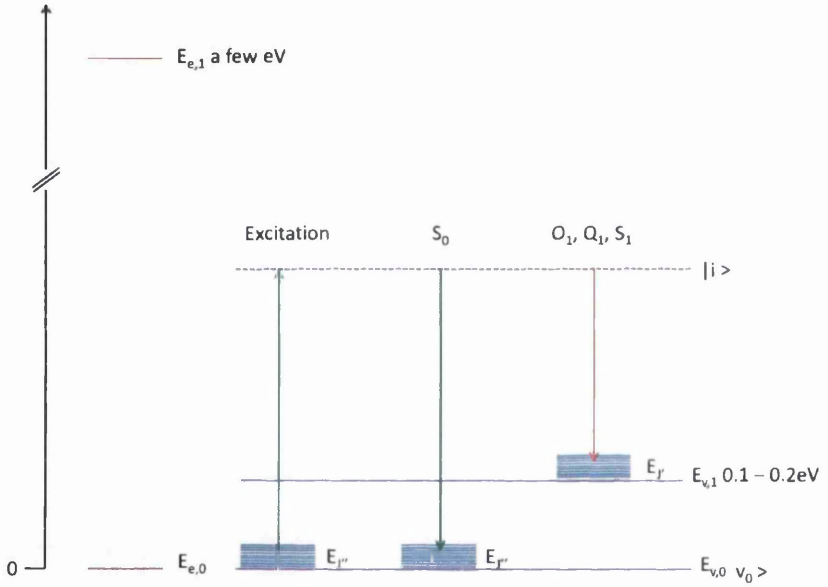

Figure 3.1: Sketch highlighting the energy levels and scattering diagram considered for the Raman intensity derivation. E_e are the electronic energy levels, E_v are the vibrational energy levels and E_J are the rotational energy levels.

Figure 3.1 contains the energy levels found in a diatomic molecule. The notation uses the selection rules discussed in chapter 2. The figure shows that in hydrogen isotopologues (as for many other gaseous inorganic and organic molecules) one finds $E_e > E_v > E_J$, which means that only $E_{e,0}$ and $E_{v,0}$ contribute to the Raman intensity and a range of E_J levels are observed. The influence this has on the Raman intensity is discussed in section 3.2.5.

The scattering geometry is also considered as it is needed when the line strength function is derived using the relationship between the electric field and the electric dipole moment from chapter 2. This derivation is then performed in section 3.3.

3.2.2 Introduction to Raman intensity

Provided the transition polarisability tensor is symmetric, the intensity of Raman scattered light is given as

$$I(\theta; p^s, p^i) = k_{\tilde{\nu}} \tilde{\nu_0} (\tilde{\nu_0} - \tilde{\nu}_{v,J})^3 g_i N_i \Phi(a^2, \gamma^2, \theta) \mathcal{I} \tag{3.1}$$

where θ is the angle defining the observation direction relative to the incident radiation; p^i and p^s define the polarisation of the incident and scattered light respectively; $k_{\tilde{\nu}}$ is a constant defined in equation (3.2); $\tilde{\nu_0}$ is the wavenumber of the excitation radiation; $\tilde{\nu_{v,J}}$ is the wavenumber of the Raman shift; g_i is the overall statistical weight of the initial state; N_i is a population factor where the definition is dependent on the transition involved. $\mathcal{I}$ is the irradiance of the incident radiation and $\Phi(a^2, \gamma^2, \theta)$ is the line strength function, which is parameterised by the polarisability tensor components a and γ and is dependent on the angle scattering geometry. This intensity equation is calculated from equation (2.4) given in chapter 2 using the time-induced electric dipole vector. This calculation leads to the line strength function. The line strength function will be discussed in more detail, as the polarisability tensor components are dependent on the transition and can greatly influence the scattered light intensity.

The constant $k_{\tilde{\nu}}$ is related to the permittivity of free space, ϵ_0, by

$$k_{\tilde{\nu}} = \frac{\pi^2}{\epsilon_0^2} \tag{3.2}$$

Experimentally this constant is embedded with the spectral efficiency of the detector as a separate constant $K = k_{\tilde{\nu}} \times \mathrm{S_E}$ where $\mathrm{S_E}$ is the spectral efficiency. K is the measured value when the spectral efficiency of the detector system is calculated. This changes equation (3.1) to

$$I(\theta; p^s, p^i) = K \tilde{\nu_0} (\tilde{\nu_0} - \tilde{\nu}_{v,J})^3 g_i N_i \Phi(a^2, \gamma^2, \theta) \mathcal{I} \tag{3.3}$$

The individual terms of the Raman intensity will now be discussed.

3.2.3 Irradiance

The irradiance, $\mathcal{I}$, is directly proportional to the power of the excitation light source. For most of the measurements in this work the source is a $\mathrm{TEM_{00}}$ output from a Nd:YAG laser (see chapter 4). This can be approximated as a Gaussian beam, given by

$$\mathrm{I(r,z)} = \mathrm{I_0} \left(\frac{\omega_0}{\omega[\mathrm{z}]} \right)^2 \exp\left(\frac{-2\mathrm{r}^2}{(\omega[\mathrm{z}])^2} \right) \tag{3.4}$$

where ω_o is the beam waist and r is the beam radius. Gaussian beam propagation is discussed in a little more detail in chapter 4. To obtain the irradiance of the beam, an integral over the scattering volume needs to be performed. The scattering volume of LARA related measurements is discussed in more detail in chapter 4, relating directly to depolarisation measurements in section 3.4.

3.2.4 Wavelength dependence

The wavelength dependence of the Raman intensity is usually described in the literature as $I \propto \tilde{\nu}^4$. $\tilde{\nu}$ is the wavenumber of the scattered radiation, which is equal to $\tilde{\nu_0} - \tilde{\nu_J}$ where $\tilde{\nu_0}$ is the wavenumber of the exciting radiation and $\tilde{\nu_J}$ is the Raman shift of the scattered radiation, which is the invariant for the scattering substance.

At this point we would like to make an important comment: the $I \propto \tilde{\nu}^4$ relationship is only an approximation for small Raman shifts. The correct proportionality of the intensity with respect to wavelength is shown in equation (3.3) and is

$$I \propto \tilde{\nu_0}(\tilde{\nu_0} - \tilde{\nu_{v,J}})^3 \tag{3.5}$$

This change in relationship was noticed during spectral calibration measurements at KIT [Sch13] that using $\tilde{\nu}^4$ lead to a disagreement between the theoretical and measured intensities. However, when the $\tilde{\nu_0}(\tilde{\nu_0} - \tilde{\nu_{v,J}})^3$ notation was used the experimental and theoretical intensities matched. McCreery [McC02] argues that the $\tilde{\nu}^4$ agreement is valid for intensity measurements in W/s, whereas the $(\tilde{\nu_0} - \tilde{\nu_{v,J}})^3$ relationship is valid for measurements in photon/s (such as a CCD detector). This argument may not be completely correct however, the $(\tilde{\nu_0} - \tilde{\nu_{v,J}})^3$ relationship comes out of the the Einstein coefficients, which is also dependent to the third power.

Note that if $\tilde{\nu_J} << \tilde{\nu_0}$ the $\tilde{\nu}^4$ approximation is valid. However, as the Raman shift of the vibration-rotation lines of interest in the hydrogen isotopologues is between 2000 and 4000 cm^{-1} the wavelength relationship cannot be expressed this way and leads to a disagreement between experiment and theory as stated above. Therefore in all intensity equations in this work the $\tilde{\nu_0}(\tilde{\nu_0} - \tilde{\nu_{v,J}})^3$ wavelength dependence relationship will be used.

3.2.5 State population N

If the scattering substance is considered as a system of N molecules in thermal equilibrium, the number of irradiated molecules, N_i, in the initial energy level i with energy, E, and degeneracy, g_i, is given by

$$N_i = \frac{N g_i \exp(-E_i/kT)}{Q} \tag{3.6}$$

where k is the Boltzmann constant, T is the temperature of the irradiated molecules and Q is the molecular partition function and is given by

$$Q = \sum_j g_j \exp(-E_j/kT) \tag{3.7}$$

where g_j is the statistical weight of the energy level E_j.

To determine N_i, Q needs to be determined. The molecular partition function Q can be approximated (reduced) to a product of three independent, individual partition functions, for the electronic (Q_e), vibrational (Q_v) and rotational (Q_R) terms as [Lon02]

$$Q = Q_e Q_v Q_R \tag{3.8}$$

where the individual partition functions are given as

$$Q_e = \sum_j g_{ej} \exp(-\tilde{T_{ej}} hc_0/kT) \tag{3.9}$$

$$Q_v = \sum_j g_{vj} \exp(-\tilde{G_j} hc_0/kT) \tag{3.10}$$

$$Q_R = \sum_j g_{Rj} \exp(-\tilde{F_j} hc_0/kT) \tag{3.11}$$

in all the equations h is Planck's constant and c_0 is the speed of light in a vacuum. $\tilde{T_{ej}}$ is the electronic energy term, $\tilde{G_j}$ is the vibrational energy term and $\tilde{F_j}$ is the rotational energy term.

In this work, all the Raman transitions considered are in the same electronic energy level; the ground electronic energy level. This means it can be assumed that $\tilde{T_{ej}} = \tilde{T_{ej}}' = \tilde{T_{ej}}'' = 0$ which means $Q_e = 1$. This is valid as most excited electronic energy levels are $> 1\,\text{eV}$ c.f $E_{\text{laser}} = 2.33\,\text{eV}$.

For the vibrational partition function it can be assumed that the molecule is undergoing simple harmonic motion, see Long [Lon02]. Then for diatomic molecules, with a vibrational wavenumber $\tilde{\nu}$:

$$\tilde{G}(\text{v}) = (\text{v} + \frac{1}{2})\tilde{\nu} \tag{3.12}$$

where $\text{v} \geq 0$ and an integer. If we choose to measure all energies from the zero-point energy level, defining $\tilde{G_0}(\text{v})$ and substituting for $\tilde{G}(\text{v})$ gives

$$\tilde{G_0}(\text{v}) = \tilde{\text{G}}(\text{v}) - \tilde{\text{G}}(0) = (\text{v} + \frac{1}{2})\tilde{\nu} - \frac{1}{2}\tilde{\nu} = \text{v}\tilde{\nu} \tag{3.13}$$

If we then substitute $\tilde{G_0}(\text{v})$ for $\tilde{G_J}(\text{v})$ in equation (3.10) and assuming that the vibra-

tional energy levels are non degenerate by setting $g_{vj} = 1$ leads to

$$Q_v = \sum_{\nu} \exp(-\mathrm{v}\tilde{\nu}\mathrm{hc_0/kT}) \tag{3.14}$$

As long as $\tilde{\nu}$ is sufficiently large, all the exponential terms where v > 0 in equation (3.14) can be neglected, which simplifies Q_v to $Q_v = 1$. A point to emphasise is that this simplification can be used for the hydrogen isotopologues since the related $\tilde{\nu}$ is large. However, the effect of this term is observed in the Raman spectra of polyatomic molecules as "hot bands" i.e. Raman excitation from the $\nu'' = 1$ to $\nu' = 2$.

The rotational partition function cannot be simplified in the same manner. The rotational degeneracy, g_R, for a symmetric top molecule is a product of the nuclear spin degeneracy (g_n) and the rotational degeneracy (g_{jk}). In this work we mainly deal with diatomic molecules. In the case where a diatomic molecule is treated as a rigid rotor, Q_R becomes

$$Q_R = \sum_{j} g_n(2J+1)\exp(-\tilde{F}_j hc_0/kT) \tag{3.15}$$

Comparing this equation with equation (3.11) implies that $g_{Rj} = g_n(2J+1)$. $2J+1$ is the rotational degeneracy as there are $2J+1$ energy levels with the same energy.

The individual partition functions can be substituted into equation (3.8) and then substituting for Q into equation (3.6) gives a full expression for N_i as

$$N_i = \frac{N g_n(2J+1)\exp(-\tilde{F}_j hc_0/kT)}{\sum_j g_n(2J+1)\exp(-\tilde{F}_j hc_0/kT)} \tag{3.16}$$

This equation can now be used with the appropriate values of the nuclear spin degeneracy inserted for each rotational quantum number J. This will not be discussed in any more detail here. However, a point to note is that the nuclear spin degeneracy is different for odd and even values of J for the heteronuclear diatomic molecules. For more details on this the reader is directed to for example the textbook by Herzberg [Her50].

3.2.6 Scattering geometry

To understand the notation, when discussing Raman intensities, the figure showing a generalised light scattering experiment, from the previous chapter, is repeated for clarity as figure 3.2. The figure shows the angles θ and φ, which define the direction of the scattered light. θ also defines the illumination-observation geometry. In practice the observation plane is usually at

- $\theta = 0$ (forward Raman),
- $\theta = n\pi/2$ where n is an odd number (90° Raman)

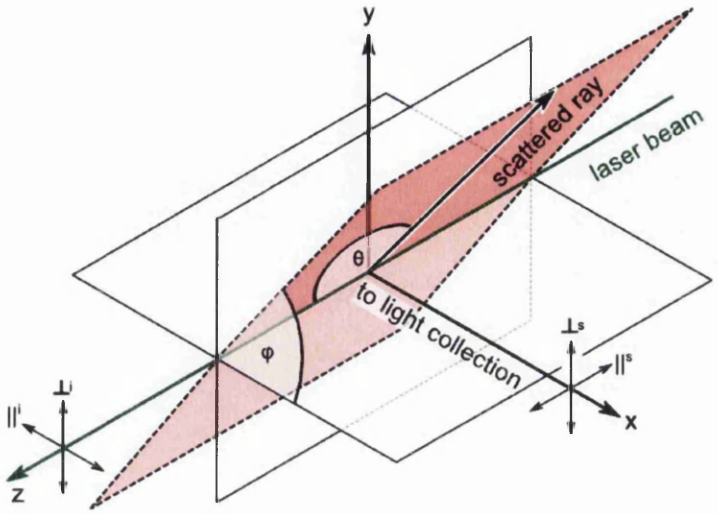

Figure 3.2: Generalised light scattering experiment. The laser beam propagates along the z-axis and the angles define the direction of the scattered light. The scattering point is at the axis origin.

- or $\theta = \pi$ (backwards Raman).

As is visualised in the figure, the laser beam propagates along the z-axis, θ is the angle between the z-axis and the scattered ray and φ is the angle between the scattered ray and the x-axis. The scattered ray has the unit vector $\boldsymbol{n}_0^s$, defining its direction of propagation and the incident radiation has the unit vector $\boldsymbol{n}_0^i$, defining its direction of propagation. In this work, the unit vector $\boldsymbol{n}_0^i = e_z$.

Using this scattering geometry with the laser beam moving along the z-axis, it is useful to define a separate coordinate system defined by a,b and c, with the unit vectors $\boldsymbol{e}_a$, $\boldsymbol{e}_b$ and $\boldsymbol{e}_c$, to obtain angular-dependent equations for the terms in equation (3.1). In theoretical situations, of non-divergent incident and scattered beams, $\varphi = 0$; this is referred to as the single-point, zero solid-angle (SP0SA) approximation of the collection geometry. In this approximation, the coordinate system is defined such that $\boldsymbol{n}_0^s = \boldsymbol{e}_a$, which lies in the scattering plane defined by the x and z-axis, $\boldsymbol{e}_c$ is perpendicular to $\boldsymbol{e}_a$ but also lies in the scattering plane defined by the x and z-axis and $\boldsymbol{e}_b$ is perpendicular to this scattering plane. Then the unit vectors are defined as

$$\boldsymbol{n}_0^s = \boldsymbol{e}_a = \boldsymbol{e}_x \sin\theta + \boldsymbol{e}_z \cos\theta \tag{3.17}$$

$$\boldsymbol{e}_b = \boldsymbol{e}_y \tag{3.18}$$

$$\boldsymbol{e}_c = -\boldsymbol{e}_x \cos\theta + \boldsymbol{e}_z \sin\theta \tag{3.19}$$

However, in real measurements, the divergent scattered radiation is collected over a finite solid angle to increase the signal of the measured light. In this situation, φ and θ are varied to define the collection solid angle. As a consequence the coordinate system needs to be redefined for different unit vectors $\boldsymbol{e}_{\underline{a}}$, $\boldsymbol{e}_{\underline{b}}$ and $\boldsymbol{e}_{\underline{c}}$. These unit vectors have an additional angular dependence in terms of φ and are defined such that $\boldsymbol{n}_0^s = \boldsymbol{e}_{\underline{a}}$ which is the scattered ray in figure 3.2 and $\boldsymbol{e}_{\underline{a}} = \boldsymbol{e}_a$, $\boldsymbol{e}_{\underline{b}} = \boldsymbol{e}_b$ and $\boldsymbol{e}_{\underline{c}} = \boldsymbol{e}_c$ when $\varphi = 0$ then the unit vectors are

$$\boldsymbol{n}_0^s = \boldsymbol{e}_{\underline{a}} = \boldsymbol{e}_x \cos\varphi \sin\theta + \boldsymbol{e}_y \sin\varphi \cos\theta + \boldsymbol{e}_z \cos\theta \tag{3.20}$$

$$\boldsymbol{e}_{\underline{b}} = -\boldsymbol{e}_x \sin\varphi + \boldsymbol{e}_y \cos\varphi \tag{3.21}$$

$$\boldsymbol{e}_{\underline{c}} = -\boldsymbol{e}_x \cos\varphi \cos\theta - \boldsymbol{e}_y \sin\varphi \cos\theta + \boldsymbol{e}_z \sin\theta \tag{3.22}$$

One last geometry definition is related to the polarisation of the incident and scattered radiation. In this work, the polarisation of the incident excitation radiation is always linear and the polarisation is defined with respect to the scattering plane. The scattering plane is usually the plane parameterised by the x-axis and z-axis (as is shown in figure 3.2).

- $\perp^i$ defines incident radiation where the polarisation direction is perpendicular to the scattering plane,
- $\|^i$ defines incident radiation where the polarisation direction is parallel to the scattering plane,
- $\perp^s$ defines scattered radiation where the polarisation direction is perpendicular to the scattering plane
- and $\|^s$ defines scattered radiation where the polarisation direction is parallel to the scattering plane.

It should be noted that, combining this notation with the unit vectors above, the vectors $\boldsymbol{e}_{\underline{b}}$ and $\boldsymbol{e}_b$ are the $\|^s$ component and $\boldsymbol{e}_{\underline{c}}$ and $\boldsymbol{e}_c$ are the $\perp^s$. Also that $\|^i$ corresponds to the y-axis and $\perp^i$ corresponds to the x-axis.

In most theoretical considerations, the SP0SA approximation is followed as it eliminates integrations over potentially complicated solid angles in the collection path. When the line strength function is discussed in section 3.3, the SP0SA approximation will be used initially and then expanded to the extended source, non-zero solid angle (ESSA) approximation that will lead to actual, experimental intensities that need to be integrated over the solid angle.

3.3 The line strength function

To derive the line strength function, it proves useful to define equation (2.10) in chapter 2 as three time-dependent linear equations

$$(p_{x0}) = (\alpha_{xx})E_{x0} + (\alpha_{xy})E_{y0} + (\alpha_{xz})E_{z0} \tag{3.23}$$

$$(p_{y0}) = (\alpha_{yx})E_{x0} + (\alpha_{yy})E_{y0} + (\alpha_{yz})E_{z0} \tag{3.24}$$

$$(p_{z0}) = (\alpha_{zx})E_{x0} + (\alpha_{zy})E_{y0} + (\alpha_{zz})E_{z0} \tag{3.25}$$

These terms can then be appropriately substituted into equation (2.1) in chapter 2 with definitions of the electric field vectors given by the restricted polarisation of the incident and scattered beams as described above.

3.3.1 Single point, zero solid angle (SP0SA) approximation

First we define the line strength function with the scattering geometry such that $\varphi = 0$ i.e. the SP0SA approximation. There are four intensity configurations to be considered for linearly polarised incident radiation; these are $I(\theta; \perp^s, \perp^i)$, $I(\theta; \perp^s, \|^i)$, $I(\theta; \|^s, \|^i)$ and $I(\theta; \|^s, \perp^i)$. These configurations have been selected as they are the simplest logical limiting cases to describe the polarisation. For diatomic molecules, vertical and horizontal polarisations of the excited beam describe the maximum and minimum situations, as the molecule is axio-symmetric. For complex polyatomic molecules, this selection of perpendicular and parallel components may be insufficient to describe the dipole moment of a system completely. This would mean that a complete map of the Raman intensity dependence would need to be performed.

The derivation of the intensity components is included in appendix A.1.1. The values for the four intensity configurations are just stated here:

$$I(\theta; \|^s, \perp^i) = k_{\tilde{\nu}}\tilde{\nu_0}(\tilde{\nu_0} - \tilde{\nu}_{v,J})^3 g_i N_i \langle(\alpha_{xy})^2\rangle \mathcal{I} \tag{3.26}$$

$$I(\theta; \perp^s, \perp^i) = k_{\tilde{\nu}}\tilde{\nu_0}(\tilde{\nu_0} - \tilde{\nu}_{v,J})^3 g_i N_i \langle(\alpha_{yy})^2\rangle \mathcal{I} \tag{3.27}$$

$$I(\theta; \perp^s, \|^i) = k_{\tilde{\nu}}\tilde{\nu_0}(\tilde{\nu_0} - \tilde{\nu}_{v,J})^3 g_i N_i \langle(\alpha_{yx})^2\rangle \mathcal{I} \tag{3.28}$$

and

$$I(\theta; \|^s, \|^i) = k_{\tilde{\nu}}\tilde{\nu_0}(\tilde{\nu_0} - \tilde{\nu}_{v,J})^3 g_i N_i \Big(\langle(\alpha_{xx})^2\rangle \cos^2\theta + \langle(\alpha_{zx})^2\rangle \sin^2\theta \Big) \mathcal{I} \tag{3.29}$$

for the SP0SA approximation.

3.3.2 Extended source, non-zero solid angle (ESSA) approximation

To bring the theory into line with a real measurement setup the line strength function will now be defined where φ and θ are both allowed to vary i.e. the ESSA approximation. The four intensity configurations for linearly polarised incident radiation are the same as for the SP0SA approximation. The notation is changed to also include the dependence on φ. The derivation of the intensity components is included in the appendix A.1.2. The values of the four intensity configurations are just stated here:

$$I(\theta,\varphi;\|^s,\perp^i) = k_{\tilde{\nu}}\tilde{\nu_0}(\tilde{\nu_0}-\tilde{\nu}_{v,J})^3 g_i N_i \Big(\langle(\alpha_{xy})^2\rangle \cos^2\varphi\cos^2\theta + \langle(\alpha_{yy})^2\rangle \sin^2\varphi\cos^2\theta + \langle(\alpha_{zy})^2\rangle \sin^2\theta\Big)\mathcal{I} \tag{3.30}$$

$$I(\theta,\varphi;\perp^s,\perp^i) = k_{\tilde{\nu}}\tilde{\nu_0}(\tilde{\nu_0}-\tilde{\nu}_{v,J})^3 g_i N_i \Big(\langle(\alpha_{yy})^2\rangle - (\langle(\alpha_{yy})^2\rangle - \langle(\alpha_{xy})^2\rangle)\sin^2\varphi\Big)\mathcal{I} \tag{3.31}$$

$$I(\theta,\varphi;\perp^s,\|^i) = k_{\tilde{\nu}}\tilde{\nu_0}(\tilde{\nu_0}-\tilde{\nu}_{v,J})^3 g_i N_i \Big(\langle(\alpha_{xx})^2\rangle \sin^2\varphi + \langle(\alpha_{yx})^2\rangle \cos^2\varphi\Big)\mathcal{I} \tag{3.32}$$

and

$$I(\theta,\varphi;\|^s,\|^i) = k_{\tilde{\nu}}\tilde{\nu_0}(\tilde{\nu_0}-\tilde{\nu}_{v,J})^3 g_i N_i \Big(\langle(\alpha_{xx})^2\rangle \cos^2\varphi\cos^2\theta + \langle(\alpha_{yx})^2\rangle \sin^2\varphi\cos^2\theta + \langle(\alpha_{zx})^2\rangle \sin^2\theta\Big)\mathcal{I} \tag{3.33}$$

for the ESSA approximation.

To complete the discussion, the isotropic averages included in the intensity equations will be discussed and defined in the following.

3.3.3 Isotropic averages

Two isotropic averages of transition polarisability components are required to determine the intensity and polarisation components of the scattered radiation. These isotropic averages are used in the line strength functions embedded in the intensity equations derived above. For all measurements in this work linearly polarised light is used. The isotropic averages for linearly polarised light are (from Long [Lon02])

$$\langle(\alpha_{xx})^2\rangle = \langle(\alpha_{yy})^2\rangle = \langle(\alpha_{zz})^2\rangle = \frac{1}{(2J^i+1)}\left\{\frac{1}{3}(g^{(0)})_{fi} + \frac{2}{15}(g^{(2)})_{fi}\right\} \tag{3.34}$$

$$\langle(\alpha_{xy})^2\rangle = \langle(\alpha_{yz})^2\rangle = \langle(\alpha_{zx})^2\rangle = \frac{1}{(2J^i+1)}\left\{\frac{1}{10}(g^{(2)})_{fi}\right\} \tag{3.35}$$

where i and f are the initial and final state respectively and $g^{(j)}$ are the Placzek invariants, which are

$$g^{(j)}_{v^f J^f K^f M^f : v^i J^i K^i M^i} = (2J^i + 1) b^j_{J^f K^f M^f : J^i K^i M^i} |\langle v^f | \alpha^{(j)}_{\Delta K} | v^i \rangle|^2 \tag{3.36}$$

in their most general form. b^j are the Placzek-Teller b-factors.

For diatomic molecules this can be simplified as a diatomic molecule can be regarded as a special case of a symmetric top with $K = 0$ and $\Delta K = 0$. This reduces the definitions of $g^{(0)}_{fi}$ and $g^{(2)}_{fi}$ to (for the complete derivation see Long [Lon02])

$$g^{(0)}_{v^f J^f : v^i J^i} = 3(2J^i + 1) |\langle v^f | a | v^i \rangle|^2 \tag{3.37}$$

with $\Delta J = 0$ i.e. $J^f = J^i$, $a^2 = \frac{1}{3}|\alpha^{(0)}_0|^2$ and

$$g^{(2)}_{v^f J^f : v^i J^i} = (2J^i + 1) b^2_{J^f 0 : J^i 0} \frac{2}{3} |\langle v^f | \gamma | v^i \rangle|^2 \tag{3.38}$$

with $\Delta J = 0, \pm 2$ i.e. $J^f = J^i, J^i \pm 2$ and $\gamma^2 = \frac{3}{2}|\alpha^{(2)}_0|^2$. For diatomic molecules the $b^2_{J^f 0 : J^i 0}$ factors for the three vibration-rotation branches Q_1, O_1 and S_1 are:
for $\Delta J = 0$ (Q_1)

$$b^2_{J^i 0 : J^i 0} = \frac{J(J+1)}{(2J-1)(2J+3)} \tag{3.39}$$

for $\Delta J = +2$ (S_1)

$$b^2_{J^i+2, 0 : J^i 0} = \frac{3(J+1)(J+2)}{2(2J+1)(2J+3)} \tag{3.40}$$

and for $\Delta J = -2$ (O_1)

$$b^2_{J^i-2, 0 : J^i 0} = \frac{3J(J-1)}{2(2J-1)(2J+1)} \tag{3.41}$$

Equation (3.37) implies that $g^{(0)}_{v^f J^f : v^i J^i} = 0$ when $\Delta J = \pm 2$.

Substituting equations (3.37) and (3.38) into equations (3.34) and (3.35) gives

$$\langle (\alpha_{xx})^2 \rangle = \langle (\alpha_{yy})^2 \rangle = \langle (\alpha_{zz})^2 \rangle = \left\{ |\langle v^f | a | v^i \rangle|^2 + \frac{4}{45} b^2_{J^f 0 : J^i 0} |\langle v^f | \gamma | v^i \rangle|^2 \right\} \tag{3.42}$$

$$\langle (\alpha_{xy})^2 \rangle = \langle (\alpha_{yz})^2 \rangle = \langle (\alpha_{zx})^2 \rangle = \left\{ \frac{1}{15} b^2_{J^f 0 : J^i 0} |\langle v^f | \gamma | v^i \rangle|^2 \right\} \tag{3.43}$$

These are the complete expressions of the isotropic averages, which can be used to determine the line strength functions for both SP0SA and ESSA approximations.

3.3.4 Complete line strength function

The full intensity equations (and hence the line strength functions) can now be determined for the SP0SA and ESSA approximations, by substituting equations (3.42) and

Table 3.1: Table showing the full θ dependent line strength functions of the SP0SA approximation and the general θ and φ dependent line strength functions of the ESSA approximation for diatomic molecules.

SP0SA approximation	
p^s, p^i	$\Phi(\theta; p^s, p^i)$
$\perp^s, \perp^i$	$\lvert\langle v^f\rvert a\rvert v^i\rangle\rvert^2 + \frac{4}{45} b^2_{Jf0:Ji0} \lvert\langle v^f\rvert \gamma\rvert v^i\rangle\rvert^2$
$\parallel^s, \perp^i$	$\frac{1}{15} b^2_{Jf0:Ji0} \lvert\langle v^f\rvert \gamma\rvert v^i\rangle\rvert^2$
$\perp^s, \parallel^i$	$\frac{1}{15} b^2_{Jf0:Ji0} \lvert\langle v^f\rvert \gamma\rvert v^i\rangle\rvert^2$
$\parallel^s, \parallel^i$	$\frac{1}{45}(45\lvert\langle v^f\rvert a\rvert v^i\rangle\rvert^2 + 4b^2_{Jf0:Ji0}\lvert\langle v^f\rvert \gamma\rvert v^i\rangle\rvert^2)\cos^2\theta + 3b^2_{Jf0:Ji0}\lvert\langle v^f\rvert \gamma\rvert v^i\rangle\rvert^2 \sin^2\theta)$
ESSA approximation	
p^s, p^i	$\Phi(\theta, \varphi; p^s, p^i)$
$\perp^s, \perp^i$	$\lvert\langle v^f\rvert a\rvert v^i\rangle\rvert^2 \cos^2\varphi + \frac{\lvert\langle v^f\rvert \gamma\rvert v^i\rangle\rvert^2}{45} b^2_{Jf0:Ji0}(4 - \sin^2\varphi)$
$\parallel^s, \perp^i$	$\lvert\langle v^f\rvert a\rvert v^i\rangle\rvert^2 \sin^2\varphi\cos^2\theta + \frac{\lvert\langle v^f\rvert \gamma\rvert v^i\rangle\rvert^2}{45} b^2_{Jf0:Ji0}(3 + \sin^2\varphi\cos^2\theta)$
$\perp^s, \parallel^i$	$\lvert\langle v^f\rvert a\rvert v^i\rangle\rvert^2 \sin^2\varphi + \frac{\lvert\langle v^f\rvert \gamma\rvert v^i\rangle\rvert^2}{45} b^2_{Jf0:Ji0}(3 + \sin^2\varphi\ )$
$\parallel^s, \parallel^i$	$\lvert\langle v^f\rvert a\rvert v^i\rangle\rvert^2 \cos^2\varphi\cos^2\theta + \frac{\lvert\langle v^f\rvert \gamma\rvert v^i\rangle\rvert^2}{45} b^2_{Jf0:Ji0}(3 + \cos^2\varphi\cos^2\theta)$

(3.43) into the appropriate intensity equations in sections 3.3.1 and 3.3.2 above.

The resultant line strength function equations for the SP0SA approximation for diatomic molecules, are shown in table 3.1. The appropriate selection rules would need to be applied to obtain the individual branch line strength functions, as for certain transitions some terms are zero as can be seen in equation (3.37) above.

To obtain the line strength function equations for the ESSA approximation for diatomic molecules, a few extra lines of calculation will be helpful for the four polarisation configurations $I(\theta, \varphi; \parallel^s, \perp^i)$, $I(\theta, \varphi; \perp^s, \perp^i)$, $I(\theta, \varphi; \parallel^s, \parallel^i)$ and $I(\theta, \varphi; \parallel^s, \parallel^i)$. This is included in appendix A.1.3. The line strength functions for the ESSA approximation can be extracted from the final equations for each polarisation regime derived in the appendix and are collated in table 3.1.

The complete line strength functions can now be used when depolarisation measurements are discussed in the next section. However, there are a few additional considerations that are needed to completely match the theory with experimental data. The first of these is the effect of optics in the beam path on the polarisation of the incident and scattered radiation. Then the integration of the intensity over the real solid angle will be considered.

3.3.5 Effects induced by optical components

To obtain a direct comparison between the purely theoretical SP0SA description of Raman measurements, the theory of the line strength function has already been extended to the ESSA approximation; however, in real experimental situations the exciting radiation and scattered radiation pass through optical components on their way into and out of the scattering region.

When polarisation of a light beam is considered theoretically, it is assumed to be perfect. However, in reality there will always be a small "impurity" left over in the perpendicular component. This is usually quoted as a ratio (e.g. for a Glan-Taylor polariser this is typically $10^5 : 1$) and when using a polariser the "impurity" is usually low. If the beam then passes through optical components, the "impurity" in the laser beam may increase due to birefringence in the optic. The "impurity" then needs to be taken into account in the theoretical description of the polarisation dependent components of the Raman intensity i.e. the line strength function.

Mathematically, the admixture can be taken into account by using an associated parameter $\xi = \cos^2 \alpha$, where α is the angular deviation of the polarisation from the vertical ($\perp^i$) polarisation direction. Using this description,

- $\xi = 1$ would correspond to perfect vertical (linear) polarisation,
- $\xi = 0.5$ where its $\perp^i$- and $\|^i$-polarisation components are of equal magnitude
- and a value of $\xi = 0$ corresponds to a perfect horizontal (linear) polarisation.

The parameter ξ will be referred to as the laser beam (polarisation) cleannness (at the scattering centre).

In chapter 5, reasons are given for inserting a sheet polariser into the collection path of the scattered radiation. This reduces the number of possible line strength function components from four to two and an effective line strength function ($\Phi_{\text{effective}}$) can be determined. If an analyser (polariser) that only allows the $\perp^s$-polarised light component to pass, is inserted into the light collection path, the line strength function becomes an effective line strength function, $\Phi_{\text{effective}}$, which is

$$\Phi_{\text{effective}}(\varphi, \theta) = \xi \Phi_{\perp^s, \perp^i}(\varphi, \theta) + (1 - \xi) \Phi_{\perp^s, \|^i}(\varphi, \theta) \tag{3.44}$$

The effect of the optics in the collection path are measured and discussed in chapter 6 and in Schlösser *et al* [Sch12a]. As a result of these discussions, the additional effects of the optics in the collection path can be neglected and the required theory will not be discussed in this chapter.

A full description of the measured Raman intensity is obtained by inserting equation (3.44) into equation (3.3).

As this full Raman intensity description is dependent on the collection angle, the intensity would need to be integrated over the scattering solid angle to obtain the true theoretical form of the measured Raman intensities for diatomic molecules. This changes equation (3.3) to

$$\begin{aligned} I(\theta; p^s, p^i) &= K\tilde{\nu_0}(\tilde{\nu_0} - \tilde{\nu}_{v,J})^3 g_i N_i \mathcal{I} \iiint_{\varphi,z,\theta} \Phi(a^2, \gamma^2, \theta) \sin\theta d\theta dz d\varphi \\ &= K\tilde{\nu_0}(\tilde{\nu_0} - \tilde{\nu}_{v,J})^3 g_i N_i \mathcal{I} \iiint_{\varphi,z,\theta} \Phi_{\text{effective}}(\varphi, \theta) \sin\theta d\theta dz d\varphi \end{aligned} \tag{3.45}$$

Note that the solid angle of the collection system needs to be defined accurately to ensure the integration is performed correctly.

3.3.6 Solid angle parameterisation

The solid angle influences the integration by defining the limits of the individual φ, θ and z integrals. A complete derivation of the solid angle in this work is shown in appendix A.1.4.

The integration is parameterised for a solid angle governed by two apertures, such that all the parameterisations are dependent on φ. A sketch of the collection optics and solid angle for the ESSA approximation is shown in figure 3.3. The parameterisations are set as the integration limits for the intensity integral. This leads to the full integral for the Raman intensity with limits

$$\begin{aligned} I(\theta; p^s, p^i) = 2A \int_0^{\varphi_{\max}} 2\Bigg(& \int_0^{\eta(\varphi)} \int_{\theta_{\min}(z,\varphi)}^{\theta_{\max}(z,\varphi)} \Phi_{\text{effective}}(\varphi, \theta) \sin\theta d\theta dz d\varphi \\ & + \int_{\eta(\varphi)}^{r_w} \int_{\theta_{\min}(z,\varphi)}^{\theta_{\max}(z,\varphi)} \Phi_{\text{effective}}(\varphi, \theta) \sin\theta d\theta dz d\varphi \\ & + \int_{r_w}^{z_{max}(\varphi)} \int_{\theta_{\min}(z,\varphi)}^{\theta_{\max}(z,\varphi)} \Phi_{\text{effective}}(\varphi, \theta) \sin\theta d\theta dz d\varphi \Bigg) \end{aligned} \tag{3.46}$$

with the appropriate change of η to $\bar{\eta}$ when changing between $r_f > r_w$ and $r_w > r_f$ and A is the collated terms outside of the integral, given by

$$A = K\tilde{\nu_0}(\tilde{\nu_0} - \tilde{\nu}_{v,J})^3 g_i N_i \mathcal{I}$$

These parameterisations are not limited to two apertures as, even if the solid angle appears to be more complicated, an additional aperture can be inserted in front of the collection lens. The size of this aperture can then be adjusted to ensure that the solid angle can be determined by these two apertures. This is the case with the depolarisation measurements in this work, as described in chapters 6 and 7; where the reasons for inserting this additional aperture are described in more detail.

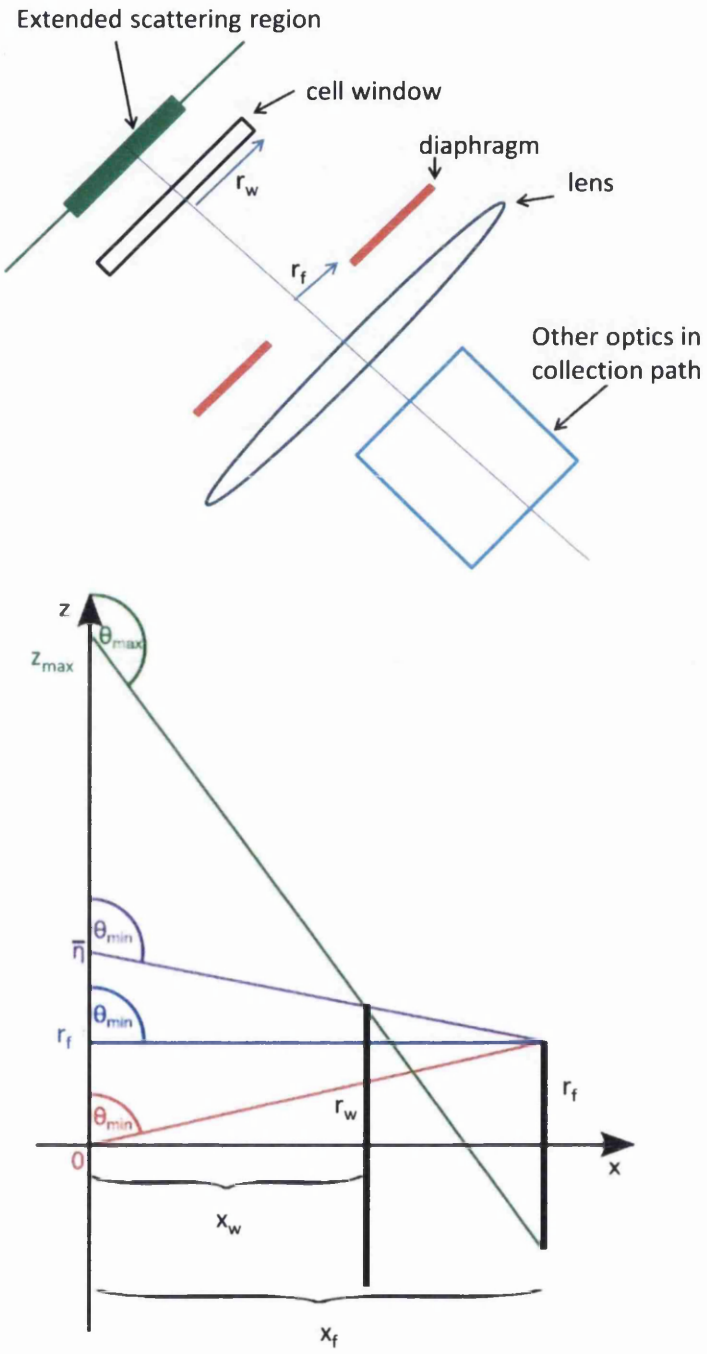

Figure 3.3: Sketch of the collection optics demonstrating the ESSA approximation and the limits used in the solid angle parameterisation. The top panel identifies the collection optics and the bottom panel identifies the integration limits.

Now that the solid angle has been defined to give integration limits, the integral can be solved numerically and applied to depolarisation measurements.

3.4 Depolarisation measurements

To determine the composition of the gas mixture, using Raman spectroscopy, the measured intensity needs to be fitted to a theoretical intensity curve. This may be obtained using a combination of the following:

- spectral resolution,
- spectral efficiency,
- transition probabilities embedded in the line strength function as the polarisability tensors,
- known laser and Raman shift positions,
- state population N.

The spectral resolution and laser and Raman shift positions are obtained experimentally with relative ease. However, obtaining the spectral efficiency is not trivial. Methods of measuring the spectral efficiency in the LARA system have/are being investigated by other members of the KATRIN LARA group in Rupp [Rup12] and Napoli [Nap12]. The state populations can be calculated as is shown above in section 3.2.5.

The transition probabilities (polarisability tensors) have been derived from *ab initio* calculations [LRoy88] and [Roy12]. However, to verify whether these are correct an experimental comparison using the Raman setups of the LARA group is needed for several reasons. First, the theoretical values will only apply for the SP0SA approximation. With the ESSA extension, plus optics corrections (see section 3.3.5) that have been applied to the theory, we would need to verify that these are behaving as we expect. Second, there is no indication in the theory about how accurate the calculations are. The numbers have varied in the literature, as improvements to the calculations are made ([LRoy88] and [Hun84]). Thus, an experimental verification would give an upper limit to the uncertainty of these values.

It is not easy to obtain the average polarisability and anisotropy directly from LARA measurements, as all the terms outside of the line strength function would need to be known to a high degree of accuracy. However, measuring the depolarisation ratio has become a relatively common method to verify the matrix elements.

3.4.1 Depolarisation ratio

The phenomenon of depolarisation is associated with the change in the intensity, of the perpendicular and parallel components of the Raman scattered irradiation; either

by changing the polarisation of the incident exciting radiation (for a fixed intensity component), or by measuring the intensity of the perpendicular and parallel components of the scattered radiation (for a fixed incident exciting radiation polarisation). The ratio between the two components (in either case) is referred to as the depolarisation ratio, ρ.

In this work, the depolarisation ratio is measured for a fixed scattered polarisation, $\perp^s$, and the depolarisation ratio is given as

$$\rho_{\text{obs}} = \frac{I_{\perp^s,\parallel^i}(\theta,\varphi)}{I_{\perp^s,\perp^i}(\theta,\varphi)} = \frac{\Phi_{\perp^s,\parallel^i}(\theta,\varphi)}{\Phi_{\perp^s,\perp^i}(\theta,\varphi)} \tag{3.47}$$

ρ_{obs} is referred to as the observed (measured) depolarisation ratio. The theoretical description of the intensities within this ratio is obtained using the ESSA approximation, with the addition of optics effects (polarisation aberrations) as described in section 3.3.5. The depolarisation ratio referred to in the literature is the same as the SP0SA approximation and this depolarisation ratio is given by

$$\rho_{\text{SP0SA}} = \frac{I_{\perp^s,\parallel^i}(\theta=\pi/2,\varphi=0)}{I_{\perp^s,\perp^i}(\theta=\pi/2,\varphi=0)} = \frac{3b^2_{Jf0:Ji0}|\langle v^f|\gamma|v^i\rangle|^2}{45|\langle v^f|a|v^i\rangle|^2 + 4b^2_{Jf0:Ji0}|\langle v^f|\gamma|v^i\rangle|^2} \tag{3.48}$$

This can be calculated from the literature values of LeRoy [Roy12] (collated in appendix A.4.1).

Following the theory described earlier in the chapter, the full expression for the depolarisation ratio (ESSA plus optics effect) is

$$\rho_{\text{calc}} = \frac{\xi A + (1-\xi)B}{\xi B + (1-\xi)A} \tag{3.49}$$

where

$$A = \iiint_{\varphi,z,\theta} I_{\perp^s,\parallel^i}(\theta,\varphi)\sin\theta d\theta dz d\varphi \tag{3.50}$$

$$B = \iiint_{\varphi,z,\theta} I_{\perp^s,\perp^i}(\theta,\varphi)\sin\theta d\theta dz d\varphi \tag{3.51}$$

and the integrals are parameterised over the collection solid angle as described in section 3.3.6. A method is required that utilises the integration definition in ρ_{calc} to calculate ρ_{SP0SA} from the measured ρ_{obs}. Recall that ξ is the cleanness for the polarisation of the incident laser beam at the scattering centre.

The reason that the depolarisation ratio enables verification of the polarisability tensors, is that the ratio of intensities of different polarisations (of the same Raman line) is equivalent to the ratio of line strength functions, as all other terms in the intensity equation are independent of the polarisation of the incident laser beam. For definitions

of other depolarisation ratio scenarios the reader is directed to Allemand [All70] or Long [Lon02].

3.4.2 Solving the integral

A dedicated software suite has been written to solve the integrals over the solid angle called DepolTools ([SJLb], [SJLa] and [Sch12a]). The software solves the integral for the intensity for a solid angle that is parameterised, as in section 3.3.6. A known depolarisation ratio [e.g. diatomic molecules $Q_1(J = 0)$ has a theoretical depolarisation ratio of 0] is required, along with a range of cleanness values, (ξ), to calculate ρ_{calc}. The software outputs a set of depolarisation ratios for each value of ξ within the specified range. This enables a fit of ρ_{calc} vs. ξ to be produced, allowing the laser beam cleanness, ξ, to be calculated using the measured depolarisation ratio of this known line. This beam cleanness is input into the second part of the program, along with the other measured depolarisation ratios, and the program calculates corrected depolarisation ratios, ρ_{SPOSA}, which can then be compared with the theory. This method will be described in more detail in chapter 6, with direct application to the hydrogen isotopologues.

The theory described in this chapter has been applied to depolarisation measurements of the hydrogen isotopologues and some of the atmospheric gases. The full experimental procedure and results of these measurements are described in chapters 6 and 7, and are published in two publications [Jam12a] and [Sch12a].

Chapter 4

Equipment for Raman spectroscopy experiments

4.1 Chapter overview

In this chapter the main equipment used in the spectroscopy research for this thesis is described. First, the equipment used in the laser Raman configurations is summarised with particular emphasis on the excitation sources, guiding optics, collection optics, laser Raman (LARA) cell and the capillary Raman cell. Spectrometers and the CCD detectors will be discussed separately in more detail. Finally, the other components used are summarised with half-wave plates, photo detectors, analogue to digital (A/D) converters and beam position monitors (modified web cameras).

The theory behind Raman scattering was discussed in the previous chapters, 2 and 3, where the parameters that directly affect the Raman intensity are discussed. Two Raman configurations (90° and 0°) are employed in this work, however, the majority of the components used are the same, just the transportation optics are changed.

The main excitation source is a frequency-doubled 2W continuous wave (CW) *Laser Quantum* Excel Nd:YAG laser. In the main LARA system at Tritium Laboratory Karlsruhe (TLK) that will be used for the KATRIN experiment a more powerful Nd:YAG laser produced by the same manufacturer *Laser Quantum*, the 5W CW Finesse laser system, is used.

The scattering medium for KATRIN related measurements is a tritium gas mixture. Measurements have also been performed using atmospheric gases, liquid water and ethanol (for alignment). The cell used for the KATRIN Raman measurements was designed to meet the radiation safety requirements so it can be used in a tritium gas flow line. This was done previously by Taylor *et al* [Tay01]. While this design is optimised for 90° Raman scattering, the loses are not too excessive for 0° (forward) Raman. The cell for capillary Raman was designed based on the work by Okita *et al* [Okit10] and

other test measurements to reduce fluorescence in the scattered spectrum.

The standard spectrometer used for the majority of measurements is the *Acton* Spectra Pro-500 spectrometer, in both Swansea and Karlsruhe Institute of Technology (KIT). The CCD detectors used are either a front illuminated open electrode CCD (Synapse) or a back illuminated open electrode (PIXIS) device.

A typical setup for laser Raman scattering is shown in figure 4.1.

The setup can be split into 7 main sections, namely

- excitation sources,
- guiding optics,
- scattering region,
- collection optics,
- spectrometer,
- detector,
- other components.

The equipment used for each section is discussed separately. For this, a general description is given of how the device works and the specific examples used in this work.

4.2 Excitation sources

The standard excitation source for modern Raman spectroscopy is a laser. A laser is an optical device that amplifies light, producing a directional, high intensity coherent beam. The beams wavelength is usually very pure i.e. the wavelength region is very narrow. The light emission from a laser is either continuous (continuous wave lasers) or pulsed. In this work, a continuous wave laser was used; a frequency doubled Nd:YAG laser that outputs light at 532 nm, which is the second harmonic of the fundamental 1064 nm emission of the laser. The types of Nd:YAG laser in use are *Laser Quantum* 2W Excel and 5W Finesse laser systems.

4.2.1 Nd:YAG

A Nd:YAG laser is a standard laser system discussed in many textbooks. For more information on the theory of a Nd:YAG laser the reader is directed to e.g. Silfvast [Sil04]. Nd:YAG lasers can be lamp- or diode-pumped. In this work all Nd:YAG lasers in use are diode pumped (DPSS).

The output lasing emission of a Nd:YAG laser is 1064 nm. To convert the lasing emission to the required visible wavelength of 532 nm an intracavity frequency doubling

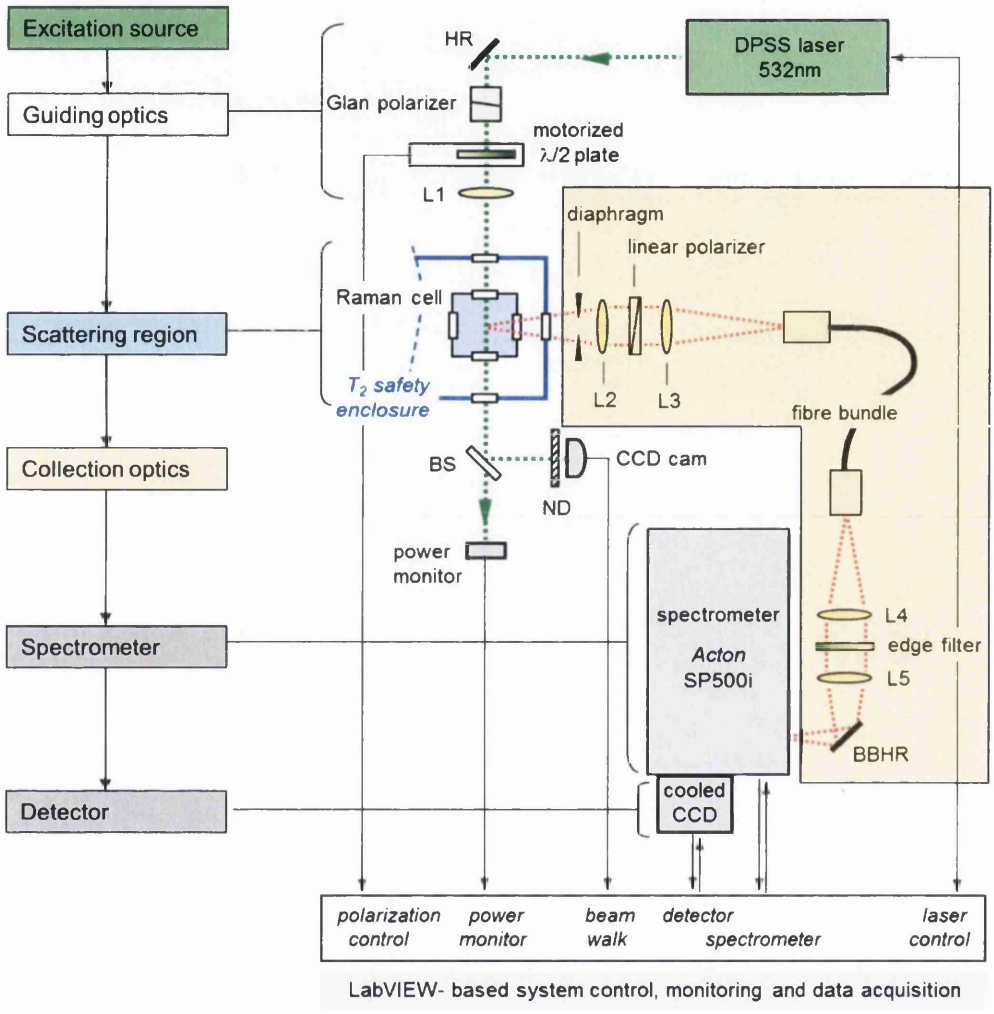

Figure 4.1: Diagram of a standard Raman setup. The left hand side shows a flow diagram of the component sections. The right hand side shows the setup for 90° Raman measurements. Key: HR and BBHR = highly reflective broadband mirror, $\lambda/2$ plate = half-wave plate, BS = beam sampler, ND = neutral density plates and L1 to L5 = lenses (plano-convex or achromats).

crystal is used. This is a non-linear crystal designed to double the incident 1064 nm to 532 nm as it passes through the crystal. The cavity of the diode pumped Nd:YAG lasers used in this work come in two configurations, end pumped and fibre pumped as is shown in figure 4.2. The end pumped configuration is used in the lower powered

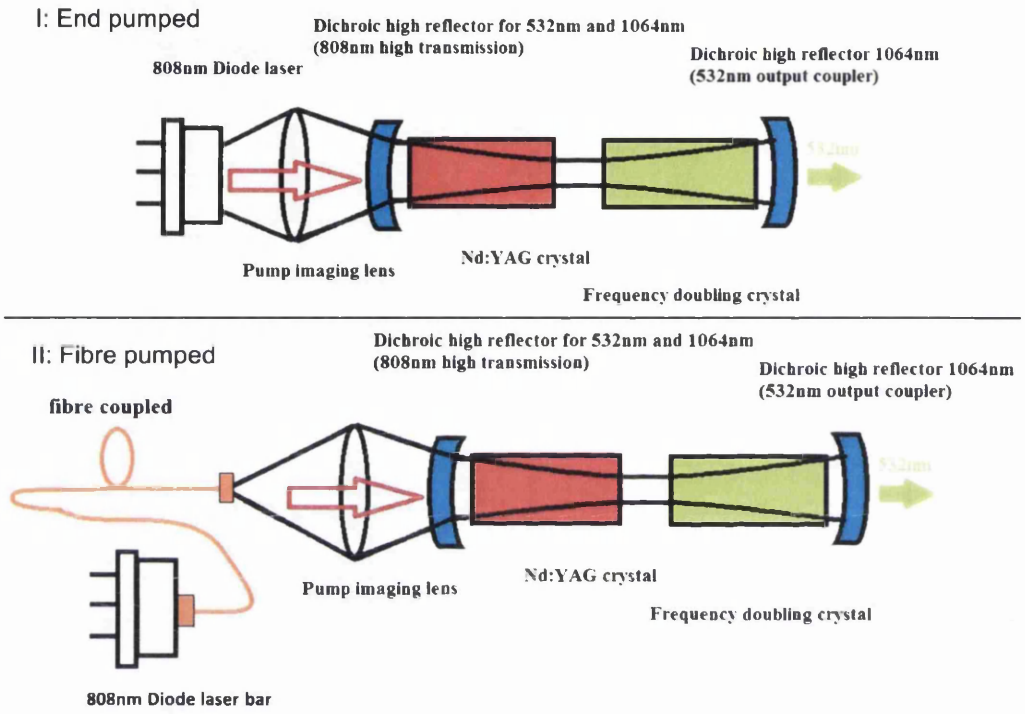

Figure 4.2: Configurations of diode pumped Nd:YAG laser cavity containing the intra-cavity frequency doubling crystal for 532 nm output used in this work. I: End pumped configuration (low powered lasers) and II: Fibre pumped configuration (Excel and Finesse lasers). Adapted from Silfvast [Sil04].

50 mW, 100 mW and 500 mW devices and the fibre pumped configuration is used in the *Laser Quantum* 2W Excel and 5W Finesse laser systems. A point of note is that the diode bar and fibre are contained within the laser head, in the Excel laser, whereas they are situated outside of the laser head, in the Finesse laser system.

As mentioned above, the main types of Nd:YAG laser used in this work are *Laser Quantum* 2W Excel and 5W Finesse laser systems. The design parameters of these lasers are summarised in table 4.1. To achieve (or exceed) the quoted stability of the devices the laser heads need to be cooled to dissipate the heat output by the laser head and to hold the device at a constant temperature. The manufacturer advised against using air cooling and recommended using a water cooling system. The system used with the Excel laser in Swansea is a *Julabo* F34 EH chilling system connected to a custom built (by *Laser Quantum*) water cooling plate. The system used with the Finesse laser

Table 4.1: Design parameters of the *Laser Quantum* Excel and Finesse Nd:YAG laser systems.

Laser model	Excel 2W	Finesse 5W
Wavelength	532 nm	532 nm
Polarisation ratio	> 100 : 1	> 100 : 1
Polarisation orientation	Horizontal	Horizontal
Beam diameter	4.0(5) mm	2.53 mm
Ellipticity	1:1.09	1:1.08
Power (Average)	2328 mW	5000 mW
Stability (24hr)	0.13%	0.04%
RMS noise	0.17%	0.09%
Mode structure	TEM_{00}	TEM_{00}
Internal baseplate temperature	30°C	28°C

in KIT is a *Melcor* MRC 300 connected to a custom built (by *Laser Quantum*) water cooling plate. The cooling test measurements and optimisation for the Excel laser are summarised in chapter 5 and in Alshahrie [Als11]. Lower powered 50 mW, 100 mW and 500 mW devices were also available for characterisation measurements.

The output beam from a green Nd:YAG laser is linearly polarised. In both the Finesse and Excel laser systems the output emission is horizontally polarised. A combination of a Glan-Taylor polariser and a half-wave plate are used between the laser output and the focussing optics to select the polarisation required for the application. These optics will be discussed in section 4.8.

4.3 Guiding optics

The guiding optics in the KATRIN LARA setup consist of the following components:

- broadband mirrors, with a high reflectivity, to guide the laser beam to the scattering region, and to align the beam in the sideways and vertical directions,
- a Glan Taylor polariser to clean up the polarisation of the laser beam,
- a half-wave plate to enable the polarisation of the beam to be changed,
- and relevant lenses to focus the laser beam in the appropriate geometry.

The lens configuration for 0° and 90° Raman are different and are shown in figure 4.3. Please note in the forward Raman configuration that there is an option of monitoring the power of the light reflected off of the Glan-polariser. If this is not monitored the reflected light needs to be dumped for safety reasons

To maximise the intensity of the light, all optics in the laser beam path are AR-coated (anti-reflection) to minimise reflections off the optic surface. The mirrors, lenses

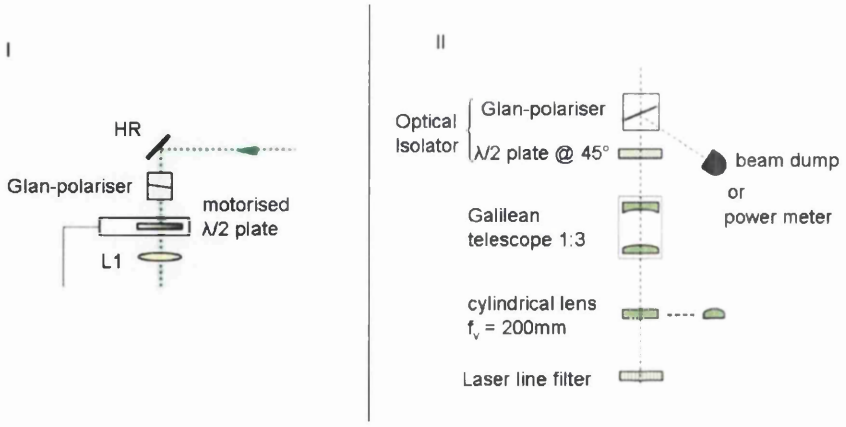

Figure 4.3: Diagram of guiding optics used in Raman setups. I: guiding optics for 90° Raman set up, II: Guiding optics for 0° Raman set up.

and Glan Taylor polariser have broadband coatings with a high anti-reflection region between 400 and 700 nm. As the half-wave plate is a wavelength specific optic the coating is optimised for that specific wavelength.

4.4 Scattering region

The scattering region is where the Raman interaction occurs. If one wishes to perform Raman measurements with samples other than the ambient air, a cell is required to store the gas. Two different cell designs were used.

4.4.1 LARA cell

The main LARA cell was designed by Taylor *et al* [Tay01] for use with the actively stabilised external resonator (ASER) signal enhancement apparatus at Tritium Laboratory Karlsruhe (TLK). It is designed to be used with 90° scattering experiments and a diagram of the cell can be seen in figure 4.4. The laser windows are coated with 532nm V-type anti-reflection coatings and the collection windows are coated with broadband coatings. To avoid damaging the coatings, the power density of the focussed beam needs to be kept as low as possible. To achieve this in the cell design, the laser windows are placed as far apart as possible within the dimension constraints of the TLK glovebox. On the other hand the collection windows are recessed to maximise the 90° collection angle. It turns out that in the current light collection configuration this is not the limiting aperture of the collection system (see chapter 6)

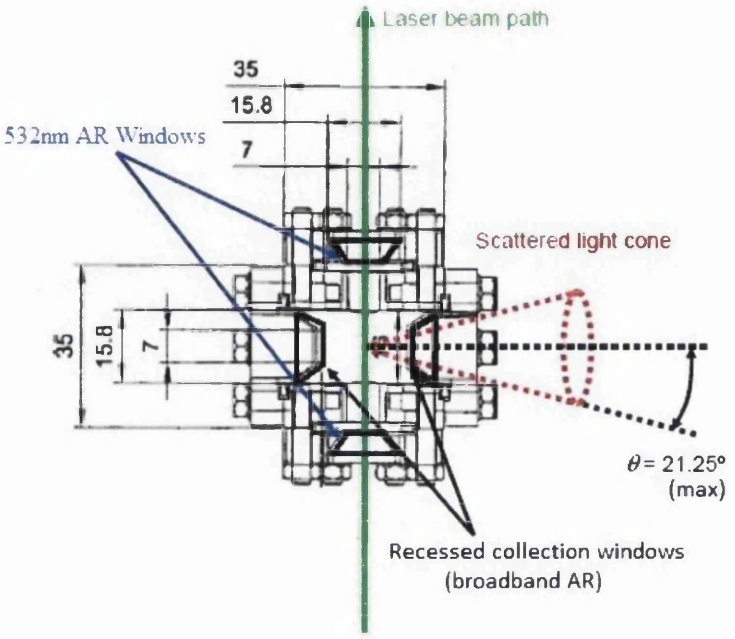

Figure 4.4: The LARA gas cell design used in this work in Swansea and KIT. The figure shows the laser beam path and the scattering collection angle of the cell. Adapted from Lewis [Lew07]

4.4.2 Scattering region geometry

To facilitate the appropriate selection of lenses, the scattering region geometry will be discussed briefly, including how lenses focus Gaussian beams.

When focussing laser beams, the radiation at the focus can no longer be considered as a point like source. The intensity profile of a TEM_{00} mode output from a Nd:YAG laser can be approximated as a Gaussian distribution. The intensity of the Gaussian beam propagating along the z-axis is given by [Lew07]

$$\mathrm{I(r,z)} = \mathrm{I_0}\left(\frac{\omega_0}{\omega[\mathrm{z}]}\right)^2 \exp\left(\frac{-2\mathrm{r}^2}{(\omega[\mathrm{z}])^2}\right) \tag{4.1}$$

r is the radial coordinate, z is the axial coordinate, $\mathrm{I_0}$ is the intensity at the beam centre, $\omega[z]$ is the radius of the beam at point z on the z-axis (it is also referred to as the 'spot size') and ω_0 is the minimum radius of the beam. The standard definition of the beam radius is defined as r when the intensity $\mathrm{I(r,z)} = \frac{1}{e^2}\mathrm{I_{peak}}$.

When focussing a Gaussian beam given in equation (4.1) the minimum radius ω_0 is located at the geometrical focus. This is commonly referred to as the 'beam waist'. The

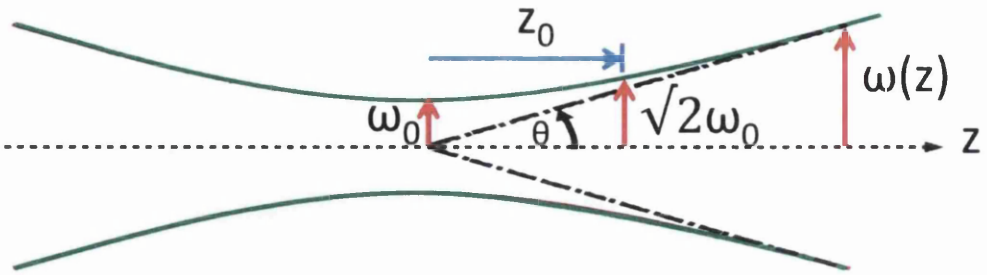

Figure 4.5: A focussed Gaussian beam. The green line represents the beam radius $\omega[z]$, z_0 is the depth of focus and θ is the divergence angle.

beam radius is described by the function (from Demtröder [Dem96])

$$\omega[z] = \omega_0 \sqrt{1 + \left(\frac{\lambda z}{\pi \omega_0^2}\right)^2} \tag{4.2}$$

where the origin of this expression is defined by the beam waist, z_0 is the depth of focus which is defined as the distance from the beam waist at which the radius is equal to $\sqrt{2}\omega_0$. Using this definition in equation (4.2) gives

$$\omega[z_0] = \omega_0 \sqrt{1 + \left(\frac{\lambda z_0}{\pi \omega_0^2}\right)^2} = \sqrt{2}\omega_0 \tag{4.3}$$

this gives the depth of focus as

$$z_0 = \frac{\pi \omega_0^2}{\lambda} \tag{4.4}$$

where λ is the wavelength of the Gaussian radiation. Equation (4.4) can be substituted into equation (4.2) to give

$$\omega[z] = \omega_0 \sqrt{1 + (\frac{z}{z_0})^2} \tag{4.5}$$

The depth of focus also applies when collecting scattered light.

Another term that is sometimes used when referring to the focal region of a Gaussian beam is the confocal parameter b. This is the length over which the beam radius is less than or equal to $\sqrt{2}\omega_0$ therefore based on the definition of the depth of focus $b = 2z_0$.

A useful parameter in spectroscopy is the spot size of a focussed laser beam at ω_0. This can be calculated from the wavelength of the laser beam, its radius at the focussing lens (R) and the focal length of the lens (f). Under the geometrical optics limit ($z >> z_0$) $\omega(z)$ approaches a straight line. Using this approximation, equation (4.5) and the diagram

in figure 4.5 the angle between the beam axis and $\omega(z)$ is obtained as

$$\theta = \tan^{-1}\left(\frac{\omega[z]}{z}\right) = \tan^{-1}\left(\frac{\lambda}{\pi\omega_0}\right) \tag{4.6}$$

This equation can be rearranged to give an expression for ω_0

$$\omega_0 = \frac{\lambda}{\pi \tan\theta} = \frac{\lambda f}{\pi R} \tag{4.7}$$

The focal spot sizes (beam waist) and confocal parameter for a variety of different focal length lenses when focussing the output of the Excel laser are shown in table 4.2. The data shows that the spot size of the laser beam varies between $2\,\mu$m and $42\,\mu$m

Table 4.2: Focal spot size (beam waist ω_0) and confocal parameter of the Excel laser for a range of lens focal lengths. The measured radius at the lens is 2 ± 0.25 mm and the measured laser wavelength is 532.074 ± 0.002 nm. Note the wavelength changes by up to 0.03 nm when it is switched off and back on again.

Focal length (mm)	Focal spot size (μm)	Confocal parameter (mm)
25	2.12	0.0529
50	4.23	0.212
75	6.35	0.476
100	8.47	0.847
150	12.7	1.91
200	16.9	3.38
250	21.2	5.29
300	25.4	7.62
750	42.3	21.2

so the minimum diameter of the beam at the focus is between $4\,\mu$m and $84\,\mu$m. The confocal parameter varies between 0.0529 mm and 21.2 mm. These two parameters are important when considering how the Raman light will be collected in the standard 90° and forward Raman configurations for the selected focal lens. Note that for most of the measurements in this thesis $f = 250$ mm was selected.

4.4.3 Capillary Raman cell

Using a hollow metal-lined capillary (fibre) as a Raman cell has the potential of enhancing the Raman signal as explained in chapter 8 and the work of Buric *et al* [Bur09]. This requires a purpose built cell to house the capillary and enable different gas mixtures to be circulated through it. The selected capillary is a *Doko Engineering* 0.65m, silver-lined, hollow optical fibre VSS 1000/1600 with an inner diameter of $1000\,\mu$m and an outer diameter of $1600\,\mu$m. It transmits wavelengths between 350 and 750 nm. The silver layer is coated with a thin polymer coating to protect the silver from oxidation

when it is exposed to air. The additional polymer does not alter the capillary's transmission properties. The cell design is shown in figure 4.6 top and a photograph of the cell is shown in figure 4.6 bottom. The capillary works as the reflectivity of silver approaches nearly 100% for grazing angles to the silver surface (Buric *et al* [Bur09]). For the grazing matching condition to be maintained along the fibre length, the capillary is kept straight and the focal length of the lens is appropriately chosen. As the laser beam reflects along the capillary, it is similar to it being refocused multiple times. This means that the Raman interaction region is the length of the capillary. The scattered Raman radiation will also be reflected by the capillary walls, so the scattered light over the entire Raman interaction region can be imaged and measured. In this work the capillary is 650 mm long. This is the maximum size based on the space inside of the enclosure in Swansea.

The cell windows are made of calcium fluoride or fused silica and are coated with broadband anti reflection coatings. Calcium fluoride (or fused silica) has been chosen as the substrate to minimise fluorescence within the windows (see chapter 8). A broadband mirror is installed within the cell to reflect the laser beam on a second pass back into the fibre to enhance the signal. The gas connectors on top of the cell are designed so that the cell can be connected to the 6mm *Swagelok* tubing of the gas mixing system in Swansea (described in Alshahrie [Als11] and appendix A.2).

4.5 Collection optics

To maximise the Raman signal captured from the scattering region the scattered light is usually collected with a relatively large solid angle, transported and then focussed into the spectrometer. Two different collection systems have been used in this work for the standard 90° Raman of KATRIN and 0°/180° Raman. The first is a 1:1 imaging of the scattering region onto a fibre bundle, which then transports the scattered light to the spectrometer system. The second does not image the signal 1:1 but uses a combination of cylindrical lenses in the 0°/180° Raman configuration so that the width of the scattering region is the 6mm width of the fibre bundle in use. Alternatively, a dot-to-slit fibre bundle was used during the final stages of the work. The details of these measurements and the new fibre bundle are included in chapter 8.

4.5.1 Lens theory

A variety of different types of lenses have been used in this work. The main types are plano-convex, cylindrical, aspheric, plano-concave and achromatic lenses. The theory behind each lens is briefly summarised below.

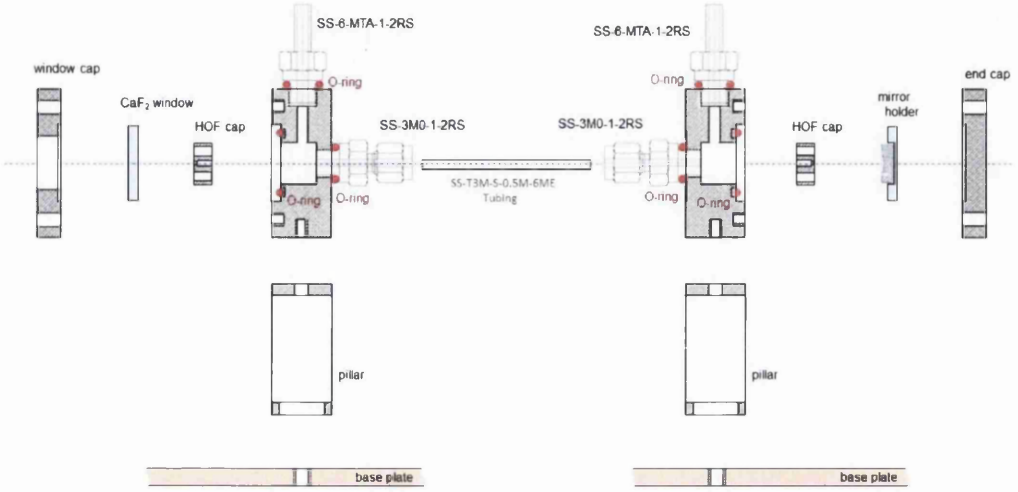

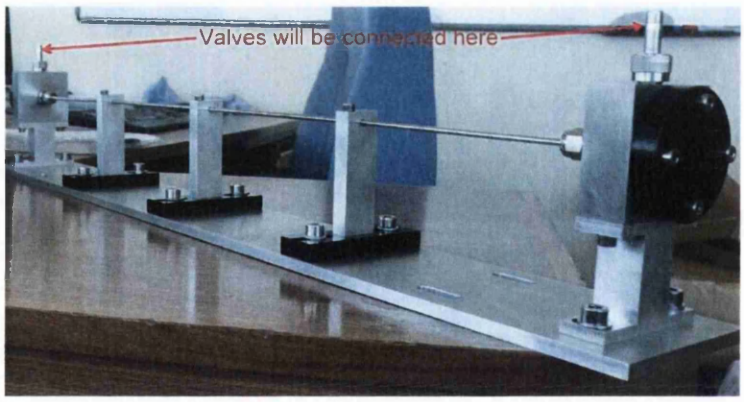

Figure 4.6: Top: The capillary gas cell design used in this work in Swansea. The figure shows an exploded view of each of the individual parts. Bottom: Photograph of the capillary gas cell design used in this work in Swansea. Note: valves will be connected as indicated in the figure. The cell parts were manufactured by the *Machining Centre*.

Plano-convex lenses A plano-convex lens is the standard lens that is used to focus collimated light and to collimate divergent light. It consists of an optical element, which has one flat surface (plano) and one surface where the curvature is convex. They have a positive focal length, which can be calculated if the radius of curvature and refractive index of the optic are known.

Cylindrical lenses A cylindrical lens is designed to focus or expand light in one axis only. It is cylindrical in shape with curvature in one dimension. The collimation of the light for the one axis works in exactly the same way as a plano-convex lens i.e. to collimate light the light needs to strike the flat side of the optic.

Aspheric lenses Aspheric lenses are rotationally symmetric optics whose radius of curvature varies radially from the centre of the optic. They are used to focus or collimate light without introducing spherical aberrations into the wavefront of the light. This is particularly important if one wants to reach the diffraction limit for collimating or focussing monochromatic light. The diffraction limit is the minimum achievable focal spot size.

They can be the best solution when only using a single optical element to collimate the output of a fibre or laser diode. However, the focal length of these lenses is usually quite short (maximum effective focal length of a *Thor Labs* aspheric lens is 18.40 mm). If one wishes to refocus the collimated light with a long focal length lens, geometrical etendue will limit the focal image size, as an invariant across a lens system (in one dimension) is [Ete]

$$h_1\theta_1 = h_2\theta_2 \tag{4.8}$$

where h_i is the focussed image height and θ_i is the one dimensional divergence angle of the light. From this equation it is clear that if $\theta_1 > \theta_2$ then $h_1 < h_2$ and the focal spot size will be limited.

Plano-concave lenses A plano-concave lens is a lens with a negative focal length that is used to diverge collimated light. It consists of an optical element, which has one flat surface and one surface where the curvature is concave. To diverge a collimated beam the curved surface should face the collimated beam. Combining a plano-concave lens with a plano-convex lens will lead to a beam expander, where a collimated beam is expanded and re-collimated.

Achromatic lenses Achromatic lenses are different to a standard lens as they are made of a positive optical element cemented to a negative optical element. The materials for the two elements are chosen to cancel out chromatic aberrations at two well separated

wavelengths. For the *ThorLabs* f = 50 mm AC254 − 050 − A used in this work the two materials are Schott N-BAF10 and SF10 glasses.

The improvement the reduction in chromatic aberrations has on a lens system can be quantified by calculating the wavelength dependent focal length for a plano-convex lens and the equivalent achromatic lens. The focal lengths variation with wavelength can then be compared. The standard lens equation to determine the focal length of a plano-convex lens is

$$\frac{1}{f} = (n-1)\left(\frac{1}{R_1} - \frac{1}{R_2} + \frac{(n-1)d}{nR_1R_2}\right) \tag{4.9}$$

For a plano-convex lens $R_1 = \infty$ and $R_2 = -R$.

Table 4.3: Wavelength dependent focal length comparison between a 1 inch $f = 50$ mm plano-convex lens and a 1 inch $f = 50$ mm achromatic lens. Calculated for *ThorLabs* LA1131-A and AC254-050-A-ML lenses

Wavelength (nm)	PCL Δf (mm)	Achromat Δf (mm)
400	−1.42876	0.06016
412	−1.28827	0.00908
424	−1.16087	−0.02694
436	−1.04303	−0.05178
448	−0.93396	−0.06822
460	−0.83379	−0.07827
472	−0.74168	−0.08345
484	−0.65490	−0.08487
496	−0.57445	−0.08339
508	−0.50040	−0.07966
520	−0.42993	−0.07418
532	−0.36405	−0.06734
544	−0.30279	−0.05943
556	−0.24521	−0.05071
568	−0.19039	−0.04134
580	−0.13835	−0.03148
592	−0.09006	−0.02125
604	−0.04362	−0.01073
616	0.00000	0.00000
628	0.04175	0.01089
640	0.08163	0.02188
652	0.11961	0.03296
664	0.15668	0.04408
676	0.19088	0.05522
688	0.22414	0.06638
700	0.25646	0.07754

For an achromatic doublet the effective focal length of the two lenses f_{eff} is given as

$$\frac{1}{f_{\text{eff}}} = \frac{1}{f_1} + \frac{1}{f_2} - \frac{d}{f_1 f_2} \tag{4.10}$$

where d is the distance between the principle planes of the lenses, f_1 and f_2 are the focal lengths of the individual lenses that make up the doublet, which can be calculated using equation (4.9) and the appropriate parameters for the lens in question. For an appropriate comparison of the focal length dependence on wavelength between a plano-convex lens and an achromatic lens these equations need to be used with appropriate values of the radii of curvature. Both lenses are *ThorLabs* $f = 50\,\text{mm}$; a BK7 plano-convex lens (LA1131-A) and a Schott N-BAF10 and SF10 achromatic doublet (AC254-050-A-ML). The lenses have the following parameters.

- The BK7 plano-convex lens: $R = 25.8\,\text{mm}$,
- The N-BAF10 lens in the achromatic doublet: $R_1 = 33.34\,\text{mm}$, $R_2 = -22.28\,\text{mm}$ and $d = 9\,\text{mm}$,
- and for the SF10 lens in the achromatic doublet: $R_1 = -22.28\,\text{mm}$, $R_2 = -291.07\,\text{mm}$ and $d = 2.5\,\text{mm}$.

The refractive indices of the materials can be calculated from the appropriate Sellmeier equation. For comparison purposes the important parameter is the change in focal length $\Delta f = f(\lambda) - f(\text{fix})$ with respect to a fixed wavelength. As the wavelength range of interest in this work is 600 to 700 nm the wavelength change is calculated with respect to 616 nm. The calculated values are collated in table 4.3. Comparing the focal length differences in the table shows that in the 600 to 700 nm range changing from a plano-convex lens to an achromatic lens reduces the focal length shift from $\approx 0.3\,\text{mm}$ to $\approx 0.08\,\text{mm}$. This is a reduction in shift by approximately a factor of 3.

The influence the chromatic aberration in the plano-convex lenses has on the LARA measurements has been demonstrated from measurements in Swansea and TLK. The measurement show that the maximum intensity of the H_2, HD and D_2 Raman Q-branches occurs at a different collection lens location. This has a knock-on effect in that the systems wavelength dependent spectral response would then change if the lens location is moved. This is not ideal as a stable system is required for the KATRIN related measurements over a long period of time.

Chromatic aberrations also influence the observed line width of the spectral lines. The optimal alignment method of spectrometers in this work is discussed in chapter 5. In this situation the spectrometer slit is not used to define the line width, but the fibre bundle width is used as a 'slit' and the fibre bundle is imaged onto the CCD plane. If normal plano-convex lenses are used to do this the image size on the CCD plane will

change with respect to wavelength. The method of determining the change in image size with focal length is depicted in figure 4.7.

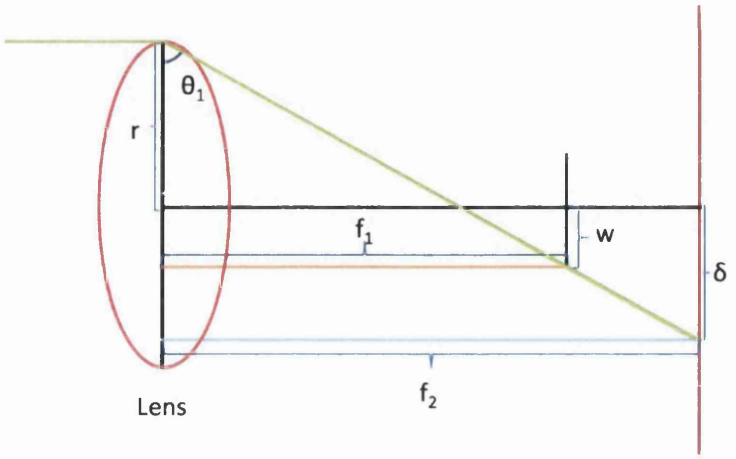

Figure 4.7: Sketch of image size change with focal length. f_2 is the image plane distance which is matched to the focal length for one wavelength.

The figure shows the maximum displacement for an extended image as is the case when imaging an image of length 2w. The parameter of interest is the maximum displacement, δ, as the imaging plane differs from the focal length. This is obtained as

$$\tan\theta_1 = \frac{f_1}{r+w} = \frac{f_2}{r+\delta} \tag{4.11}$$

this can be rearranged to give δ, which is

$$\delta = \frac{f_2(r+w)}{f_1} - r \tag{4.12}$$

This gives the displacement as f_1 differs from f_2.

To obtain the total image at f_2 the light ray propagation would have to be followed for all r values. However, the size of the image can be obtained by finding the maximum values of the displacement from the centre position $\delta_{\max}$. In this case, as the image is extended, a full mapping would have to be performed for all r and w to obtain a full image. At $w \neq 0$ the displacement for each w value is not symmetric so the maximum image size occurs at different w locations. The maximum image size at a given focal length is given by

$$\delta_{\max} = \frac{f_2(r+w_{\max})}{f_2} - r \tag{4.13}$$

when $f_2 > f_1$, which is the case shown in figure 4.7. The second maximum is symmetric to this so the image size at f_2 is still $2\delta_{\max}$ but the intensity distribution would be

smeared.

For $f_2 < f_1$ the maximum image size is given by

$$\delta_{\max} = \frac{f_2(r - w_{\max})}{f_1} - r. \tag{4.14}$$

The image size at f_2 is given by $2\delta_{\max}$ for the same reasons as explained above.

In this work the fibre bundle is being imaged onto the spectrometer plane. The spectrometer is designed such that the image on the entrance slit is imaged onto the detector plane, so the focal lengths in question for the chromatic aberration shift are those of the spectrometer focussing lens, which has a focal length of 50 mm. The change in focal length shift for a 50 mm plano-convex lens and a 50 mm achromatic lens has been performed above. These focal length shift values can be used in equation (4.12) to determine the change in fibre image size on the detector plane, where f_2 has been matched to the focal length of the lenses at 633 nm. 633 nm has been selected as this is the approximate location of the Raman Q-branch of D_2 for 532 nm excitation radiation. The fibre bundle width is 100 μm so the half width is $w_{\max} = 50\,\mu\text{m} = 0.05\,\text{mm}$ (see section 4.5.2 below) and the lens radius is $r = 12.7\,\text{mm}$. The resultant image size $2\delta_{\max}$ with respect to wavelength for the two lenses is shown in figure 4.8. The figure shows

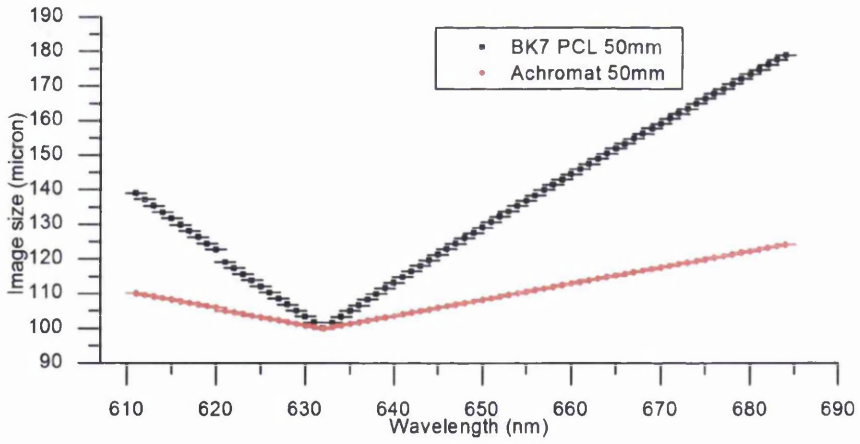

Figure 4.8: Figure showing the dependence of the image size of the fibre bundle on the detector plane with respect to wavelength of the incident light when using a plano-convex lens and an achromatic lens.

that if a simple plano-convex lens is used to image the fibre bundle onto the detector plane the image size varies between 100 μm and 179 μm. This corresponds to an increase in the image size by a factor of 1.79. For the achromatic lens the image size only varies between 100 μm and 124 μm. This constitutes a large improvement as the image size only increases by a factor of 1.24 although it is still far from perfect.

4.5.2 Optical fibre bundle

A standard method of guiding light over a distance is to use an optical fibre. Optical fibres guide light along their length; as the light undergoes total internal reflection as it strikes the walls of fibre core. A fibre consists of a core, cladding and protective jacket. The fibre is constructed such the refractive index of the core (n_1) is larger than the refractive index of the cladding (n_2). This leads to total internal reflection at the cladding core surface, when the angle of incidence of the light is greater than a critical angle (θ_c) and light coupled into the fibre propagates along the fibre core [Tel07]. In standard fibres, manufacturers quote a quantity known as the fibres numerical aperture (NA), which is given by

$$\mathrm{NA} = \sin\theta_{\mathrm{ext}} \approx \frac{\mathrm{D}}{2\mathrm{f}} \tag{4.15}$$

Where

$$\theta_{\mathrm{ext}} = \sin^{-1}((\frac{n_1}{n_0})\sin(\theta_c)) \tag{4.16}$$

θ_{ext} is referred to as the fibre acceptance angle, n_0 is the refractive index of air (≈ 1), D is the diameter and f is the focal length of the lens used to image the light onto the fibre. Note, all angles are measured from the axis of the fibre core. Transmission through a fibre is never 100% due to low level losses caused by absorption, scattering, reflection losses and Fresnel diffraction. The absorption losses occur when the condition for total internal reflection within the fibre is not met and the light passes into the fibre cladding, and as light is absorbed as it passes along the fibre core. A fibre with a constant core refractive index along the entire length is referred to as a step index fibre.

The main factors affecting the total transmission are the size of the fibre and its composition. All fibres used in this work are step index multi-mode fibres. Multi-mode fibres have core diameters between 50 and 400 μm. A multi-mode fibre is a fibre that enables light to propagate through it as multiple light rays. The core diameter limits the maximum energy and power that can be coupled to a fibre, because above a certain power the light will exceed the damage threshold, $\mathrm{P_{damage}}$, of the core material. The transmittable peak power of a fibre is $\mathrm{P_{peak}} < \mathrm{A_{core}P_{damage}}$ where $\mathrm{A_{core}}$ is the area of the fibre core. This can be used as an estimate, as the true thresholds depend on the beam profile and wavelength.

In the case of scattering experiments, coupling the scattered light to the spectrometer with a fibre enables flexibility on where the spectrometer is placed i.e. it does not have to be directly in front of the scattered light. This is particularly useful if space is limited. A standard single core optical fibre has a core size of between 50 and 400 μm. In the 90° Raman setup the scattering length is approximately 6 mm. If a single fibre was used, a large proportion of the scattered light would be lost. To overcome this problem a fibre bundle can be used instead.

A fibre bundle is a cluster of individual fibres, which are mounted and arranged in a configuration of the user/manufacturers choice. The fibre bundles used in this work have a "slit to slit" mounting configuration and consist of 48 single, adjoining, step index multi-mode fibres with a 100μm/125μm core/cladding diameter ratio. The fibre bundle is visualised in figure 4.9. The total length of the fibre slit is 6 mm. The left hand side

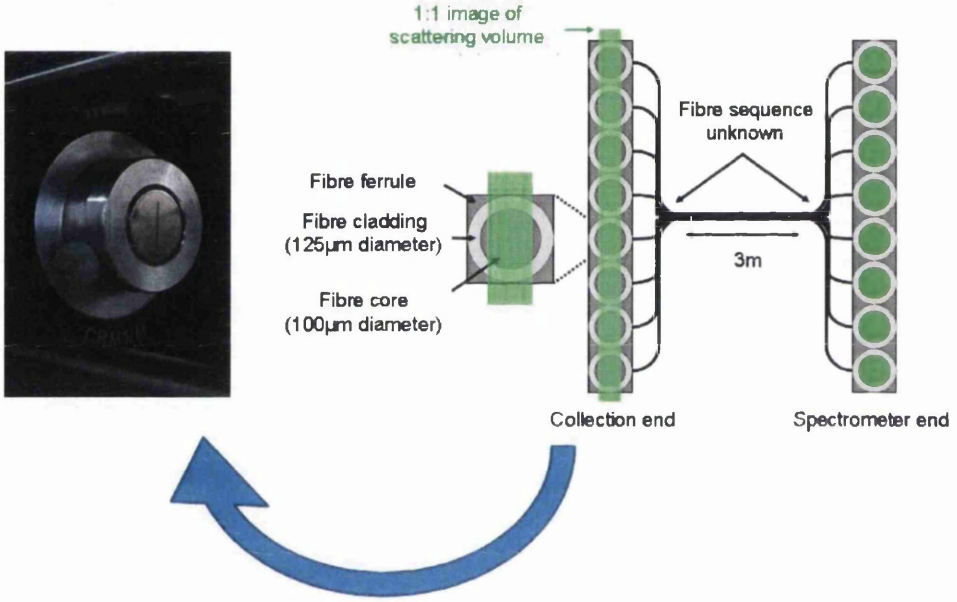

Figure 4.9: Fibre bundle used in this work. The left hand side contains a photograph of the entrance slit of the fibre bundle. On the right hand side 8 of the 48 fibres in the slit to slit configuration are shown. Adapted from Lewis [Lew07]

of the figure shows a photograph of the mounted fibre and the right hand side shows a sketch of 8 of the 48 fibres in the slit to slit configuration. The manufacturer quotes the numerical aperture of the fibre bundle as 0.22 ± 0.02 ([Lew07]). From equations (4.15) and (4.16), the fibre (bundle) acceptance angle can be calculated as

$$\theta_{\text{ext}} = \sin^{-1}(NA) = \sin^{-1}(0.22) = 12.7^{\circ} \tag{4.17}$$

However, test Raman measurements with the depolarisation measurements have shown that the fibre bundle starts to limit the amount of light collected at angles below about 5°. Details of these measurements are shown in chapter 6. This limitation is performed using a diaphragm of constant radius. However, the fibre bundle is 6 mm in length and

100 μm high. Using a diaphragm reduces the amount of light imaged onto the fibre bundle more strongly in the horizontal direction than the vertical direction. This means that this is not an accurate way of determining the fibre bundle numerical aperture. A better indication of the numerical aperture of the fibre bundle would be obtained by limiting the collected light using a slit.

If the light incident on the fibre bundle is polarised, as is the case with Raman measurements, the effect the fibre has on this polarisation needs to be known. It was assumed by Lewis [Lew07] that the scattered Raman light passing through this fibre bundle is essentially depolarised. However, measurements have been performed which have shown that the fibre bundle partly preserves the polarisation of the light that has passed through it (see chapter 5). As a consequence, all the light entering the fibre bundle for 90° Raman measurements will have the polarisation fixed to vertically polarised light by a sheet polariser. This means that the preserved polarisation from the fibre bundle is always the same (as long as the fibre isn't moved too much; note that the polarisation preservation changes slightly with fibre movement).

4.5.3 Edge filter

Edge filters are used in Raman collection systems to remove the really bright Rayleigh line (and laser line in forward Raman) from the measured scattered light. This is particularly important if one wishes to observe the pure rotational Raman lines of the hydrogen isotopologues, many of which have small Raman shifts of (typically) less than 500 cm^{-1}.

An edge filter is designed such that it lets 99% of the light through in the transmitting region, and less than 4×10^{-5} % in the suppression region. The 50% transmission point of the edge filter used in this work occurs at 536 nm (*Semrock* LP03-532RU-25). This corresponds to a Raman shift of 140 cm^{-1} (532 nm excitation), which would mean any pure rotational lines with smaller shifts would be lost. For the hydrogen isotopologues this blocks the $S_0(J = 0)$ line of T_2, which is calculated to occur at 120.052 cm^{-1}. For heavier diatomic molecules, such as nitrogen and oxygen, even more pure rotational lines will be blocked.

A point to note is that an edge filter is designed for a specific optic tilt, laser wavelength and power. As the optic is tilted the wavelength position of the sharp edge shifts, so care should be taken ensuring the tilt remains constant.

4.5.4 Dichroic beam splitter

A dichroic beam splitter works in a similar way to an edge filter. The difference is that an edge filter is designed to block light when the optic is perpendicular to the light propagation. A dichroic beam splitter is designed such that it reflects light (in

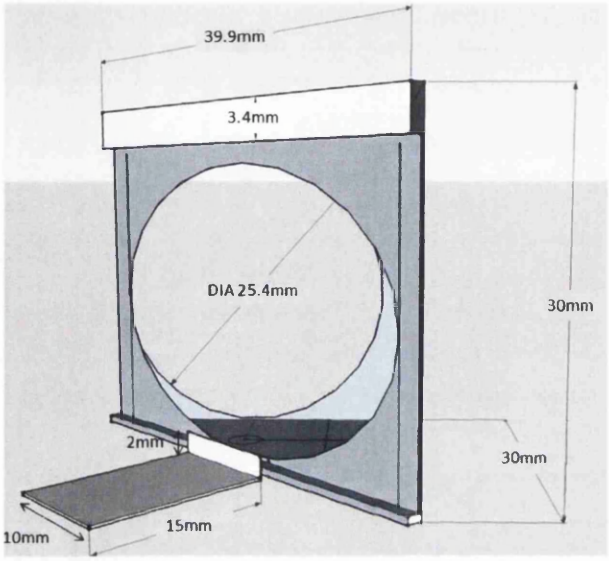

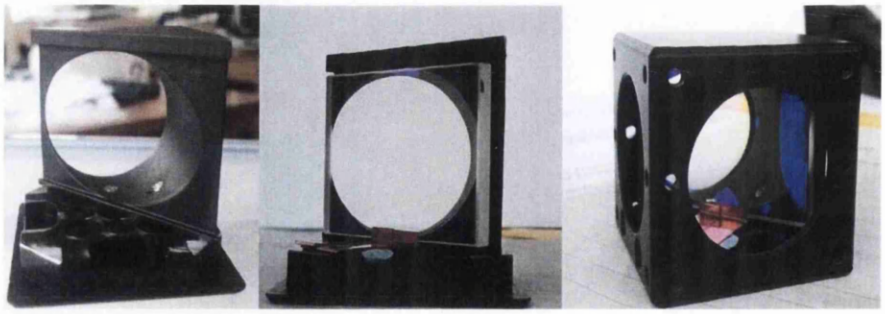

Figure 4.10: Top: Design of the light tight beam splitter housing. Produced using *Google SketchUp*. Bottom: Photograph of the finalised light tight beam splitter. i) Custom made housing, ii)with installed 3 mm thick beam splitter(final version is 1 mm thick) and iii) Complete housing in *Thorlabs* CM1-4E

the suppression region) when the optic is at an angle of 45° to the light propagation direction. The remainder of the light is transmitted in the light propagation direction for both configurations.

As the transmission/reflections of the optic are optimal when it is at an angle of 45° to the light propagation direction, a custom housing has been designed to ensure that the optic is at the correct angle and the collection path remains light-tight. The design is shown in figure 4.10 and a photograph of the housing is shown in the lower part of the figure. The optic included in the figure is the thicker *Semrock* DMLP425R dichroic beam splitter. For the final measurements, a thinner optic (*Semrock* LPD01-532RS-25x36) was purchased which fits into the mount design better. The advantage of this design is that it can be installed into a *Thorlabs* 30mm cage system, which is in use in the collection line in all measurements in this thesis. Cage systems are housing that contain rails allowing optics to be installed using special mounts. They make the setup easier to align correctly, as all movement directions are fixed by the cage system apart from one, which can be adjusted fairly accurately.

4.6 Spectrometers

A spectrometer is an optical instrument that is used to measure the wavelength of light by causing linear dispersion of the wavelength so the spread of the lines is proportional to the wavelength. It does this by forming laterally separated images of the entrance slit. The lateral separation of the images corresponds to the different wavelengths (λ) of the light incident on the entrance slit. This lateral separation is usually referred to as lateral dispersion. The element causing the dispersion is either a prism or a reflective grating; reflective gratings can be plane or concave. All spectrometers used in this work are grating spectrometers.

A spectrometer can either be used as a monochromator or a spectrograph. A spectrograph and monochromator differ in the way that they detect the dispersed light. A monochromator uses a photoelectric device (like a photodiode) to detect small spectral regions, while a spectrograph has a CCD diode array placed in the focal plane of the output mirror of the spectrometer. All spectrometers used in this work are used as spectrographs with two dimensional CCD array detectors. The spectrometer used in Swansea, and one of the devices in KIT, is a SP-500i triple grating spectrograph made by *Acton Research Corporation* (now *Princeton Instruments*). In KIT, the spectrometer, which will be used in KATRIN measurements (and for some work included here), is the HTS high throughput lens spectrometer made by *Acton Research Corporation* (now *Princeton Instruments*). Both of these are grating spectrographs that operate in the same way, using the grating to select the wavelength region to view on the detector plane. However, the HTS only has one grating and the SP-500i has three gratings available,

with different numbers of grooves per mm (gr/mm). This enables the user to change the spectral resolution of the system. High resolution measurements are not needed for Raman measurements in KATRIN. However, high resolution spectra are sometimes needed for offline measurements (see chapter 6 for an example of measurements where this is the case). Also, the light transportation and focussing method is different for each. The SP-500i uses mirrors (Czerny-Turner spectrograph), while the HTS uses lenses (Transmitting optics type spectrograph). To obtain the theory behind gratings the reader is directed towards e.g. Demtröder [Dem96] or other optics textbooks.

The important parameters when using grating spectrometers are the angular dispersion and resolution of the grating. The angular dispersion and resolution of a grating spectrometer are stated here. For the full derivation see Demtröder [Dem96]. The angular dispersion $\frac{d\beta}{d\lambda}$ is

$$\frac{d\beta}{d\lambda} = \frac{\mathrm{m}}{\mathrm{d}\cos\beta} = \frac{\sin\alpha \pm \sin\beta}{\lambda\cos\beta} \tag{4.18}$$

and the resolution R of the grating spectrometer is

$$R = \frac{\mathrm{Nd}(\sin\alpha \pm \sin\beta)}{\lambda} = \mathrm{m}\lambda \tag{4.19}$$

A few additional points need to be kept in mind when using gratings. Firstly, the reflectivity is dependent on the polarisation of the light incident on the grating. This is one of the problems that was encountered and overcome when performing depolarisation measurements in section 6. Secondly, the zeroth reflection off a grating is a non-dispersing reflection i.e. it acts like a mirror. Thirdly, the grating intensity response is wavelength-dependent. This needs to be measured to be able to calibrate a Raman system and is being looked into by other members of the KATRIN LARA group [Rup12].

The two types of grating spectrometer will now be summarised highlighting their differences.

4.6.1 Czerny-Turner spectrometers

A Czerny-Turner spectrometer is a standard grating spectrometer. A set of images are spatially separated at the point of detection. The wavelength centre of this image can be changed by rotating the diffraction grating. This changes the angle of incidence, α, to the grating normal and using the equation for the path difference of light reflected off a grating [Dem96]

$$\mathrm{d}(\sin\alpha \pm \sin\beta) = \mathrm{m}\lambda = \Delta\mathrm{s} \tag{4.20}$$

for the same reflection angle, β, a different wavelength value is obtained. The wavelength range of the spatially separated images is the bandpass. Figure 4.11 shows the general layout of a Czerny-Turner spectrometer.

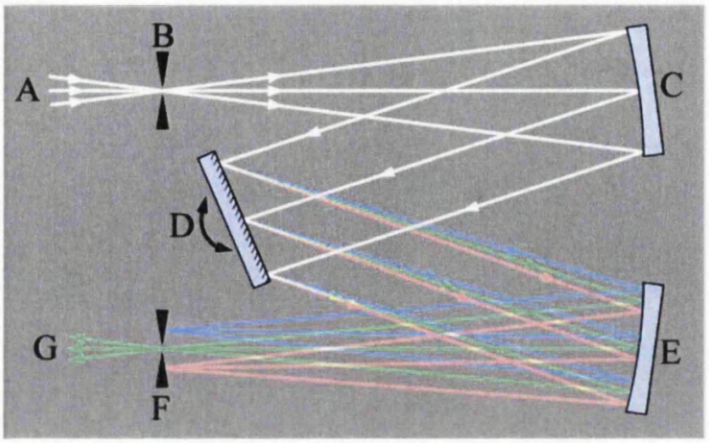

Figure 4.11: Typical grating spectrometer configuration, showing the incident light (A), the entrance slit (B), the spherical mirror (C), the diffraction grating (D), the entrance slit (F) and the bandpass (G).

4.6.2 Transmitting optics type spectrometers

As mentioned above in section 4.6, the difference between a Czerny-Turner spectrometer and a transmitting optics type spectrometer is that the mirrors in the Czerny-Turner are replaced by lenses. This enables the unit's dimensions to be smaller and to utilise a 90° grating illumination geometry. Whereas, a typical Czery-Turner has a 180° illumination geometry and has to be much larger to achieve the same dispersion with the same focal length optics. The transmitting optics type spectrometer in use, the HTS, only has one grating, whereas the SP500i has three gratings which are useable. The short focal length of the lenses in the spectrometer has the advantage that the light collection power is high (f-number equals f/1.8) for a fixed aperture size. The disadvantage of the short focal length is that it leads to strong astigmatism of the entrance slit image, in the detector plane, that needs to be corrected for in post-acquisition procedures. The correction procedure is discussed in Lewis *et al* [Lew08], (or in [SJLd] and [SJLc]). Figure 4.12 shows the layout of a transmitting optics type spectrometer

4.6.3 Alignment

The standard method of imaging light into a spectrometer is by using a lens (system) to focus the light onto the entrance slit. The slit width is reduced to increase the spectral resolution. However, this also reduces the intensity. In this work, the light always passes through an optical fibre bundle before it is focussed into the spectrometer. The fibre core width acts as an additional slit. If the output from the fibre bundle is imaged onto

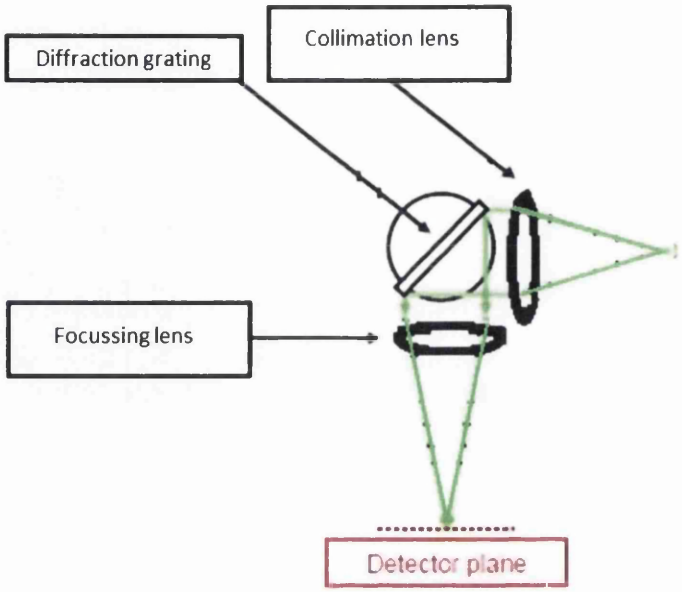

Figure 4.12: Figure showing typical transmitting optics type spectrometer. Adapted from Lewis [Lew07].

the spectrometer slit then the image on the detector is a convolution of the spectrometer slit and the fibre width. When the spectrometer entrance slit width is narrower than the fibre core width, the slit width is the dominating function. As the spectrometer slit width approaches and exceeds that of fibre core (105μm), the fibre width becomes the limiting width. As there are two functions affecting the image, care has to be taken to ensure the slit is centrally illuminated, otherwise distorted line shape profiles occur on the detector plane.

For spectrometer imaging one aperture is required. In this work there are two apertures present therefore, the spectrometer slit can be ignored by setting its width such that it is a lot larger than the fibre core diameter. The optimum position would be in the first minimum of the single slit diffraction pattern of the fibre bundle output. Then the fibre (bundle) is imaged directly onto the detector plane by appropriately adjusting the position of the external imaging lens until the line width on the detector plane is at its narrowest point (to the diffraction limit). This leads to an increase in the observed intensity. It should be noted that the 1:1 imaging geometry of the spectrometer itself is no longer maintained. The fibre bundle height was matched to the detector height of 6 mm, but due to the reduced image size of the fibre bundle in the detector plane the detector chip is no longer fully illuminated. The improvements of this alignment method are shown in chapter 5.

Table 4.4: Characteristics of the SP500i and HTS spectrometers used in this work.

Feature	**Spectrometer**	
	SP500i	HTS
Focal length	500 mm	85 mm
Design	Czerny Turner	Transmitting optics type
Aperture ratio (f/#)	1/6.5	1/1.8
Slits	Micrometer adjustable	Micrometer adjustable
Slit width	10 μm to 3 mm	
Slit adjustment	10 μm steps	
Number of gratings	3 (150, 600) and 2400 gr/mm)	1 (600 gr/mm)
Grating blaze wavelength		
150 gr/mm	500 nm	NA
600 gr/mm	300 nm	500 nm
2400 gr/mm	240 nm	NA
Resolution		
150 gr/mm	$\approx$ 0.337 nm/pixel	NA
600 gr/mm	$\approx$ 0.08 nm/pixel	1 nm (10 μm slit)
2400 gr/mm	0.0094(3) nm/pixel	NA
Wavelength coverage $\Delta\lambda$	(On Synapse CCD)	(over 1" focal plane)
150 gr/mm	345 nm	NA
600 gr/mm	81.5 nm	254 nm
2400 gr/mm	$\approx$ 10 nm	NA
Operating range		
150 grpmm	500 - > 1000 nm	NA
600 grpmm	300 - > 1000 nm	500-750 nm (fixed)
2400 grpmm	240 - 750 nm	NA

4.6.4 Spectrometers used by the KATRIN LARA group

As stated at the beginning of section 4.6 the spectrometers used in this work are a SP-500i triple grating spectrograph made by *Acton Research Corporation* (now *Princeton Instruments*) and a HTS high throughput lens spectrometer made by *Acton Research Corporation* (now *Princeton Instruments*). As a result of the discussions on spectrometer types above the spectrometers have different parameters which are summarised in table 4.4. The table shows that the HTS spectrometer has a lower resolution than is possible with the SP500i spectrometer due to the choice of 3 gratings. The HTS has the main advantage of a better f/# meaning it has a higher light collection power. The other advantage is that the grating blaze wavelength of the HTS is higher than for the SP500i, which means that the grating efficiency is higher at the longer wavelengths of the Raman lines of the hydrogen isotopologues. This means that with a higher efficiency the amount of light throughput is also higher. Overall, this implies that the HTS spectrometer

Table 4.5: Synapse detector characteristics.

Feature	Synapse	PIXIS
CCD grade	Scientific (Grade 1)	Scientific (Grade 1)
ADC precision	16 bit	16 bit
ADC dynamic range	65535 max	65535 max
Data conversion speed	20 kHz and 1 MHz	100 kHz and 2 MHz
Gain settings	High sensitivity	High (3)
	Best dynamic range	Med (2)
	High light	Low (1)
Operating temperature	$-70°C$ @ $T_A = +20°C$	$-75°C$
Readout noise	2.5 - 5 e^- rms	3.5 - 5 5 e^- rms
Nonlinearity	$< 0.4\%$ @ 20 kHz	$< 1\%$ @ 100 kHz
	$< 1\%$ @ 1 MHz	$< 2\%$ @ 2 MHz
Dark current	< 0.005 electrons/pixel/sec	< 0.01 electrons/pixel/sec
Exposure time	0.001s min to 49.71 days max	
Computer interface	USB 2.0	USB 2.0
LabVIEW VIs	Yes	Yes
Built in shutter	Yes	No

is more sensitive than the SP500i. However, the SP500i is needed if high resolution measurements are desired as is the case for the depolarisation measurements of the hydrogen isotopologues and atmospheric gases described in chapters 6 and 7.

4.7 CCD Detector

Charge-Coupled-Devices (CCDs) have been used as detectors in Raman spectroscopy since the mid-1980s. The controlling software for all detectors used by the KATRIN LARA group are custom written *National Instruments* LabVIEW routines.

4.7.1 Detectors used in this work

The detectors used in this work are the *Horiba* Synapse FIOP (front illuminated open electrode) detector in Swansea and *Princeton Instruments* PIXIS 400B back illuminated detector in KIT. Both of these detectors have 2-dimensional chip sets that have a height of 6 mm, the fibre bundles were designed to match the chip height. The pixel configuration is slightly different for both detectors. The PIXIS has 1340×400 pixels, whereas the Synapse has 1024×256 pixels. Both detectors are air cooled using a 4-stage peltier block to bring down the chip temperature to $-75°C$ (PIXIS) and $-70°C$ (Synapse) respectively, to minimise the dark current of the system. The detector characteristics are summarised in table 4.5. Both of these detectors are compared with test measurements in chapter 5.

The main difference between the detectors is the readout noise and the spectral sensitivity.

4.7.2 CCD detector noise

Detector noise needs to be minimised to achieve a high signal-to-noise ratio. The main sources of (residual) noise in a CCD detector are dark current noise and readout noise. When measuring signals, shot-noise is also present.

Dark current noise is a result of spontaneous generation of electrons within the detector when no light is present. The dark current noise is strongly dependent on temperature. Therefore, all modern CCD detectors are cooled to minimise this noise current. Dark current noise can also be reduced by taking multiple readouts of the same data and averaging them. This, however, increases the readout noise.

Readout noise is a result of the conversion of the measured electrons to a digital signal that is recorded by the detector control software. The readout noise is dependent on the number of times the data is sampled, so minimising this will minimise the readout noise. This means that a single data acquisition has the lowest readout noise, but a higher dark current noise than multiple data acquisitions.

Most modern CCDs offer the option of on-chip binning to reduce the readout noise, which otherwise would build up when reading out each individual line of the CCD detector. This is achieved by internally accumulating the signal content of multiple pixel (rows) before the signal is read out. This means that readout noise only contributes once for every readout operation and its influence is greatly reduced if a small number of bins (areas) are selected. The overall readout time of the CCD detector is also shorter.

Front illuminated detectors have the advantage of a lower dark current and readout noise compared to back illuminated detectors. They also do not experience the etaloning phenomenon in the near infra-red (NIR), which leads to a modulation on the observed spectrum in back illuminated CCDs in the NIR region. The reason for this is due to the manufacturing process of back illuminated CCD detectors. Back illuminated CCDs are etched to 15 - 30 μm to collect light through the back surface, reducing loss of light in absorption and reflection and increasing the quantum efficiency. This process leads to the etaloning phenomenon (for more details see [Pri12]). The etching also leads to high concentrations of uncoated dangling bonds in close proximity to the back surface [Wes09]. This could result in the higher dark currents observed in back illuminated CCDs.

Cosmic ray events are also captured by CCD detectors and appear as single pixel signals, where the individual pixel has a much higher intensity than its neighbouring pixels. Cosmic ray events are random and the number increases as the acquisition time increases. Cosmic rays are removed from spectra using post acquisition software routines. These will be discussed in appendix A.6.

The detector's spectral response (quantum efficiency) has an effect on the sensitivity of the detector. It is defined as the conversion rate of photons incident on a CCD pixel into electrons. It is dependent on the wavelength of the light incident on the detector. The detector spectral response needs to be measured, along with the rest of the Raman system, to enable quantification of Raman spectra and to calibrate the system. As mentioned in section 4.6, a method to measure the systems spectral response is being looked into by other members of the KATRIN LARA group [Rup12]. As a rough guide, the quantum efficiency of the PIXIS detector is $> 90\%$ in the 500 nm to 700 nm region whereas the quantum efficiency of the Synapse detector is between 30% and 50% in the same spectral region. This would imply the sensitivity of the PIXIS detector will be considerable higher. The difference in sensitivity of the detectors is checked with test measurements chapter 5.

4.8 Other components

Some of the other system components used in the LARA systems will be briefly summarised below.

4.8.1 Polarisers

In this work, two different types of polariser are used to filter polarisation of light, namely Glan-Taylor and sheet polarisers.

Glan-Taylor polariser

A Glan-Taylor polariser consists of two angled calcite prisms that are constructed with an air gap between the two. It is designed such that it reflects the s-polarisation (ordinary ray) component at the air gap through one of the prism side ports. The p-polarisation (extraordinary ray) component passes straight through the polariser. This is visualised at the top of figure 4.13. Rotating the polariser about the light axis enables the polarisation of the transmitted component to change. The quoted extinction ratio of a Glan-Taylor polariser is greater than $100,000 : 1$. This has been measured for the *Thorlabs* GT10-A polariser used in this work (see chapter 6). The anti-reflection coating of the polariser can be selected for the appropriate wavelength of the laser beam.

Glan-Taylor polarisers are designed for use with collimated beams of light i.e. laser beams. If a beam is incident on the polarisers such that light exceeds the acceptance angle the extinction ratio of the Glan-Taylor polarisers reduces from the quoted value of $100,000 : 1$.

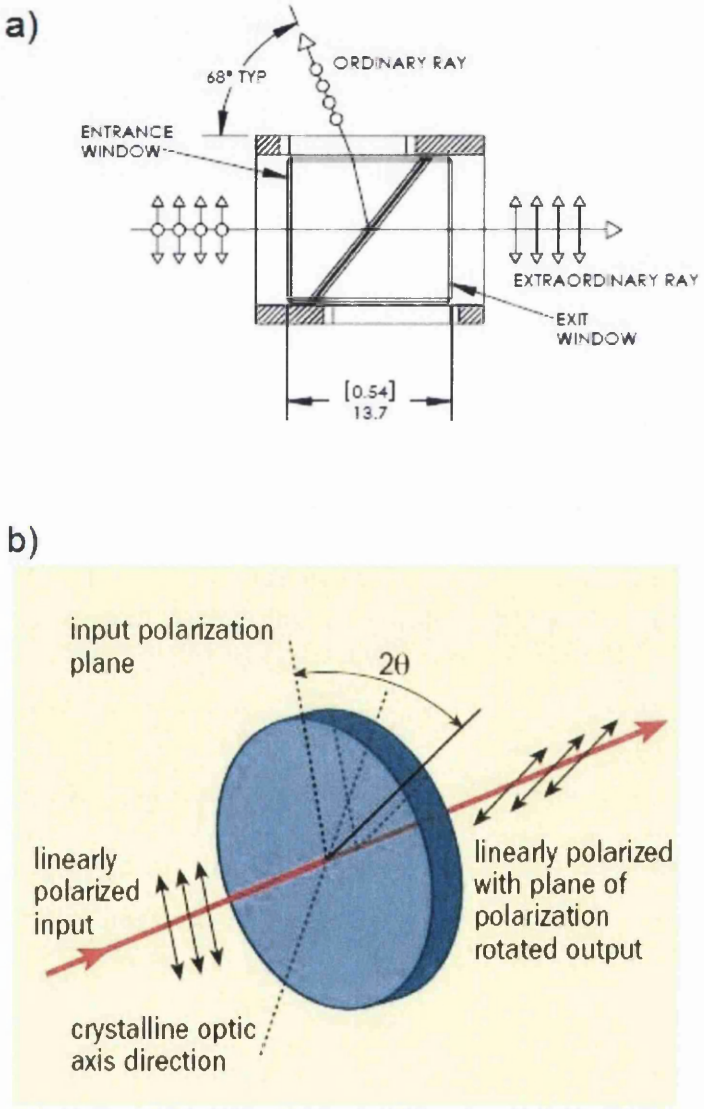

Figure 4.13: Schematic diagrams of a) a Glan-Taylor polariser and b) a half-wave plate.

Sheet polariser

The sheet polarisers used in this work are linear polarising glass filters. Sheet polarisers are optics that are constructed by sandwiching a laminated polymer film between two glass windows.

The filter in use is the *Edmund optics* NT54-926 25.4, mm unmounted linear glass polarizing filter. It has a typical filter transmission of 30% with > 95% polarisation efficiency. It is placed in the collection path for 90° Raman measurements to remove the influence of the polarisation of the detection system (see chapter 5). Similar filters with a much higher transmission will be used in the final KATRIN measurements, so that the sensitivity of the measurements is as high as possible.

4.8.2 Half-wave plates

A schematic diagram of a half-wave plate is shown in the bottom of figure 4.13. A wave plate is a transparent crystalline-structure optic that is used to manipulate the polarisation state of a light beam. This is achieved by generating a phase shift between the two orthogonal polarisation components of the light beam.

A wave plate has mutually perpendicular fast and slow axes, which are perpendicular to the crystal surface. The perpendicular axes are a consequence of linear birefringence within the substrate. The axis with the higher index of refraction is the slow axis because light propagates more slowly along this axis. The axis with the lower index of refraction is the fast axis.

The type of wave plate used in this work is a multi-order half-wave plate ($\lambda/2$). Half-wave plates rotate the polarisation of plane polarised light by twice the angle between the plane of polarisation of the incident light and the fast axis of the crystal. The transmitted electric field, E_2, through a wave plate, is given as [Wav12]

$$E_2 = s(sE_1)e^{i\phi_s} + f(fE_1)e^{i\phi_f} \tag{4.21}$$

s and f are unit vectors along the slow and fast axis respectively and ϕ_s and ϕ_f are the phase shifts of the slow and fast axis. These phase shifts are given by

$$\phi_s = n_s(\omega)\frac{\omega t}{c} = 2\pi\frac{n_s(\lambda)t}{\lambda} \tag{4.22}$$

$$\phi_f = n_f(\omega)\frac{\omega t}{c} = 2\pi\frac{n_f(\lambda)t}{\lambda} \tag{4.23}$$

where t is the thickness of the wave plate and n_s and n_f are the refractive indices of the slow and fast axis respectively. In Raman scattering we are only interested in the beam intensity. This means that one can discard one phase factor in measuring this intensity

and assign the entire phase delay to the slow axis. This leads to

$$E_2 = s(sE_1)e^{i\phi} + f(fE_1) \tag{4.24}$$

where ϕ is

$$\phi = 2\pi\frac{(n_s(\lambda) - n_f(\lambda))t}{\lambda} = 2\pi\frac{\Delta n(\lambda)t}{\lambda} \tag{4.25}$$

$\Delta n(\lambda)$ is the birefringence of the wave plate. This birefringence is an important parameter in wave plate design.

If E_1 is initially polarised along the x-axis then the slow axis of the wave plate is at an angle θ to the x-axis. If the wave plate is placed between two linear parallel and perpendicular polarisers the transmission through the wave plate is given by

$$T_{\parallel} \propto |E_{2x}|^2 = 1 - \sin^2(2\theta)\sin^2(\frac{\phi}{2}) \tag{4.26}$$

$$T_{\perp} \propto |E_{2y}|^2 = \sin^2(2\theta)\sin^2(\frac{\phi}{2}) \tag{4.27}$$

θ is a function of the wave plate rotation angle (orientation), ϕ is a function of the wavelength as given above and the birefringence is a function of the wave plate thickness. For a multi order half wave plate the values are $\phi = (2m + 1)\pi$, $T_{\perp} = \sin^2(2\theta)$ and $T_{\parallel} = \cos^2(2\theta)$. This transmission is the same as if linearly polarised light was rotated through an angle of 2θ. Therefore, a half wave plate can be used to rotate the polarisation of linearly polarised light.

The wave plates used in this work are multi order, half-wave plates designed for 532 nm incident laser radiation. The "cleanness" of the polarisation, with different tilt angles of the 532 nm wave plate, has been tested and the results are discussed later in chapter 6.

4.8.3 Galilean telescope

A Galilean telescope is an optical device used to expand collimated light beams and recollimate them. It consists of a plano-concave lens, followed by a plano-convex lens. The plano-concave lens has a negative focal length, whereas the plano-convex has a positive focal length. The focal lengths of the lenses and the distances between the two are adjusted to change the magnification of the telescope. The lenses used in the Galilean telescope in this work are a $f = -25$ mm plano-concave lens (*Thorlabs* LC1054-A) and a $f = 75$ mm plano-convex lens (*Thorlabs* LA1608-A). The lenses are mounted onto a 30mm cage system and the relative positions of the lenses were adjusted to expand a 4 mm diameter laser beam to the required diameter.

4.8.4 Photo detectors

Photodiodes are a tool used to e.g. measure the power of laser beams; they measure the power as a photovoltage. To convert the measured photovoltage to a photocurrent, J_{PD}, the voltage is read across a resistor and the photocurrent can be calculated using Ohms law. The spectral dependence of the absorption coefficient of the diode is needed to convert the measured current to the optical power of the radiation incident on the diode. This is embedded in the diodes wavelength dependent responsivity, $c(\lambda)$. Photodiodes that have had the measured current calibrated to optical power by the National Institute of Standards and Technology (NIST) can be purchased. Their wavelength dependent responsivity curve, $c(\lambda)$, is provided, where the power P of the incident light can be calculated as

$$P = \frac{J_{PD}}{c(\lambda)} \tag{4.28}$$

This responsivity, $c(\lambda)$, is also temperature dependent. For this reason, photodiode detector heads need to be temperature stabilised to ensure that the measurement of the power remains stable throughout the measurement period.

A Newton plate needs to be inserted in front of the photodiode when the power of coherent light is measured i.e. laser light. The reason for this is to avoid interference in the photodiode window. A Newton plate scrambles the coherence of a light beam.

4.8.5 A/D converter

For flexible computer controlled data acquisition of voltages, current, resistance and temperature a *National Instruments* NI USB-6009 is used. It contains 8 single reference single ended signal inputs or 4 differential signal coupling inputs. The range of the inputs is $\pm 10\,V$ with a maximum sampling rate of 48000 samples per second and a 14 bit dynamic range. The unit integrates seamlessly with LabVIEW to read in the signals as required. The unit has been thoroughly tested as is shown in Alshahrie [Als11].

4.8.6 Webcam - beam position monitoring

For beam position monitoring the simplest and cheapest device to use proved to be a (dismantled) *Logitech* webcam. The webcam was pulled apart and the lens removed to give access to the photosensitive chip. When illuminating the webcam, an appropriate amount of neutral density filters are placed in the beam path to stop the detector from saturating, so that the beam position can be obtained to a reasonable level of accuracy. The advantage of using a webcam is that drivers for computer control are already supplied by the manufacturer. A simple *LabVIEW* routine has been written (see appendix A.6.2) to enable the 2D chip readout to be read and recorded. The beam position is found by:

- Finding the maximum intensity for each row (for the x- and y-directions separately) and output the row number, max index and max value.
- Fit the maximum intensity vs row number with a Gaussian fit. The centre position of this fit is the pixel co-ordinate in that direction.

The saved pixel coordinate enables the beam walk to be monitored. The angle that the beam has deflected by can also be calculated using trigonometry, as long as the pixel dimensions and length of the side arm, the webcam is installed on, is known. In this case the pixel dimensions are approximately $10\,\mu$m.

Chapter 5

Improvements to Swansea's laser Raman (LARA) system

5.1 Chapter overview

In this chapter the accumulative changes to the laser Raman (LARA) system in Swansea are described, leading to improvements in the signal-to-noise ratio (SNR) of the system. Some of the alterations only apply to the Swansea system. However, others can also be implemented for all LARA systems as they will lead to improvements there as well. The improvements are as follows

1. Laser system: Installation of *Laser Quantum* Excel laser system increases the laser power from 500 mW to 2 W, with a power stability of better than 0.4%, wavelength stability of $\Delta\lambda = 0.005nm \approx 0.177\,\mathrm{cm}^{-1}$ and a beam pointing stability of $\Delta q < 10\,\mu\mathrm{m}$ when the water cooled baseplate is held at 24°C. All stability measurements are over a 24 hour period. Equivalent systems have been installed in Swansea and LARA2 in Tritium Laboratory Karlsruhe (TLK) at Karlsruhe Institute of Technology (KIT).

2. CCD detector: Installation of *Horiba* Synapse detector in Swansea. The PIXIS 400B detector used in TLK is ≈ 1.7 times more sensitive than the Synapse detector. On-chip binning leads to an increase in the SNR by about a factor of 5. The Synapse detector will be used in Swansea, and on-chip binning will be used in all LARA systems.

3. Multi-pass experiments: Adding a second pass of the laser beam approximately doubles the Raman signal. The Raman signal is too sensitive to beam-walk off to implement more passes of the laser beam accurately. Two passes of the laser beam through the LARA cell will be used in all LARA systems.

4. Improved spectrometer imaging: By using the fixed width of the fibre bundle as a slit and imaging the light directly onto the detector plane maximises the amount of light collected. This leads to an improvement of between a factor of 4 and 12 to the SNR whilst maintaining a narrow spectral peak width. This imaging method will be implemented in all LARA systems.

5. Sheet polariser introduction: The fibre bundle does not scramble the polarisation of the incident light. To overcome this problem a sheet polariser is inserted into the LARA collection system between the two collection lenses, which fixes the polarisation beyond this point. Any change to the polarisation of the light incident on the polariser is observed as an intensity change only. For the depolarisation measurements, described in chapter 6, a low-cost polariser is used with a transmission of 30%. A sheet polariser with a much higher transmission is required to implement this in all LARA set ups.

In all future measurements in Swansea the items listed will be implemented. There will be occasions where only one pass of the laser beam will be used. When this occurs it will be stated. Overall, the improvements implemented here have vastly increased the sensitivity of the 90° LARA system in Swansea.

At the start of this work, the Swansea system consisted of a 500 mW *Dream* laser [dla] as the excitation source and a *Princeton instruments* IPDA-700/GB detector. For information on the systems at TLK see Schlösser [Sch09] and Schlösser *et al* [Sch11]. As the Swansea system is developed in parallel with the KIT systems, some of the improvements will be compared with the systems in KIT and if there is a further improvement the change will be implemented on all systems.

5.2 Laser Quantum *Excel* laser system

A 2 W *Laser Quantum* Excel laser system [LQu09] has been installed in Swansea's LARA system to bring the power and stability of the excitation closer to the 5 W of the LARA setups at KIT. Test measurements have been completed using the 2W *Laser Quantum* Excel laser system to quantify the optimum operating parameters of the laser when used in the LARA setup in Swansea and are described in detail in Alshahrie [Als11]. The findings will be briefly summarised here with reference to the important parameters, these being the resultant pointing stability, wavelength drift at the optimal temperature set point and power stabilisation.

5.2.1 Measurement summary

Test measurements of various cooling configurations were performed where the following parameters were measured:

1. room temperature,
2. cooling water temperature (when applicable),
3. laser baseplate temperature,
4. laser power,
5. laser wavelength,
6. beam position.

Three cooling configurations were tested:

- No cooling: Laser mounted to the cooling plate, but no cooling in operation.
- Laser mounted to a modified head sink with copper tubing placed between fins. Water is pumped through the fins and cooled using a LC-035 chilling unit by *TE Technology Inc.* [Tec09] and a *XSPC* DDC 18W Ultra pump/reservoir.
- Laser mounted to the water cooling plate supplied by *Laser Quantum.* The water was pumped through the plate and cooled using a *Julabo* F34 refrigerated/heating circulator [Jul09].

The findings of the measurements were that cooling the laser head of the 2W *Laser Quantum* Excel laser system greatly improves the stability of the output parameters of the device. When the *Julabo* F34 refrigerated/heating circulator was used to cool the water, beam walk-off is no longer visible. A laser output power of 2.1W was attainable, which is stable for a chosen temperature set point of 24°C. The wavelength has a drift of $\Delta\lambda = 0.005\,\text{nm} \approx 0.177\,\text{cm}^{-1}$ for the three temperature set points tested, but shifts by 0.03nm between the 24°C and 26°C temperature set points. This is about an order of magnitude larger than the shift if the laser head is kept at a constant temperature.

5.2.2 Important parameters

From the measurements described above, the parameters that are important for spectroscopy measurements are:

- the beam pointing stability,
- output wavelength,
- stability at the chosen temperature set point,
- and the power stabilisation.

These will be considered now.

Beam pointing stability In the temperature stabilised test, there was no observed beam walk-off over time. This means that the pointing stability is better than the accuracy of the beam position measurement using the webcam. The pixel size of the webcam is of the order of 10 μm. The beam walk was measured on a sidearm 150 mm off the initial beam path, which was set to be the same distance from the focal lens as the scattering centre (200 mm). This means that the observed walk-off matches the walk-off at the scattering centre. Therefore, the beam position stability at the scattering centre Δq is less than 10 μm i.e. $\Delta q < 10\,\mu$m.

Wavelength stability In the test measurements, the wavelength of the emitted light from the laser drifts for the first 24 hours of measurement whilst the laser warms up. After this warm up period the wavelength stability is $\Delta\lambda = 0.005\,\text{nm} \approx 0.177\,\text{cm}^{-1} \approx 5\,\text{GHz}$. The absolute wavelength shifts by 0.03 nm between the 24°C and 26°C temperature set points. If the absolute wavelength is required to a high accuracy it should be remeasured each time the laser is switched on. This is the case for the accurate Raman line position measurements in chapter 6. However, the wavelength for a temperature set point of 24°C is 532.070(5) nm, where the uncertainty is determined from the wavelength stability. This drift is well within the specified line width of the Excel laser of 30 GHz.

Power stability In the test measurements, the power of the emitted light from the laser increases quickly to a maximum value of approximately 2 W. A laser output power of 2.1 W, was attainable which is stable for a chosen temperature set point of 24°C. The power stability was found to be 0.00851 W = 8.5 mW $\approx$ 0.4% over a 22 hour period. This means that, over a measurement day, the power is sufficiently stable that corrections for the laser power fluctuation should not be needed. This fluctuation is slightly larger than the quoted stability of the laser. The reason for this could be the accuracy of the power determination or the slight temperature variation of the room, which results in small-scale fluctuations of the cooling water temperature.

5.3 Characterisation of the Horiba *Synapse* detector: FIOP vs back illumination detectors

The Synapse 1024 × 256 FIOP CCD detector (S#: MCD-798B-0310) [Syn09] has been thoroughly tested, in order to assess its functionality and performance in comparison to the *Princeton Instruments* PIXIS400B (back-illuminated) CCD detector [Pix09]. Back illuminated CCD detectors are used in the LARA systems at KIT. They generally have a higher quantum efficiency. However, front illuminated detectors have the advantage of a lower dark current noise and the etaloning phenomenon does not occur at long wavelengths. Etaloning introduces ripple to the measured spectrum. Therefore, the test

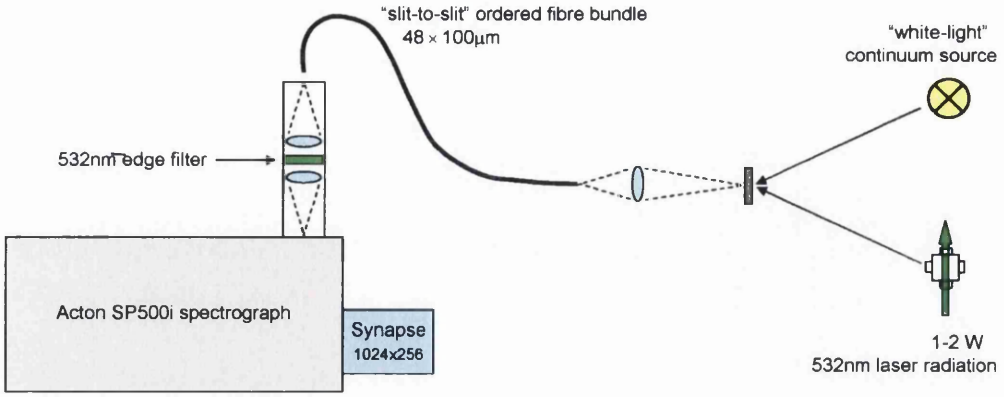

Figure 5.1: Diagram of the setup used for the Synapse test measurements.

is performed to verify which detector leads to higher signal-to-noise ratios (SNRs). In both cases the detector was coupled to a *Princeton Instruments* (formerly *Acton*) SP500i spectrograph (see figure 5.1) with three installed gratings: 150 gr/mm, 600 gr/mm and 2400 gr/mm. The following tests were carried out on the Synapse detector:

- setup and operation using "LabSpec 5" and VIs from the LabVIEW test modules for the Symphony detector;
- dark current measurement to quantify the noise;
- spectral measurements to quantify the quantum efficiency of the detector and to evaluate the SNR in Raman measurements in air.

The results are compared to those obtained by Schlösser [Sch10a] for the PIXIS400B CCD detector.

5.3.1 Installation and software modifications

The Synapse camera was delivered with the software "LabSpec 5" rather than the software package "SynerJY" (as specified in the *Horiba* leaflets for this detector). This caused tremendous problems, which could only be overcome by reverting to a suite of LabVIEW VIs, supplied by *Horiba* on request. The various issues with the LabSpec software are summarised in appendix A.3.1.

LabVIEW VIs and Synapse configuration The detector can be run using *National Instruments* LabVIEW. The LabVIEW VIs for the Symphony CCD detector (version 0.9.4.0) have been modified so that (i) they work with the Synapse detector

Table 5.1: Synapse detector response at different gain levels and read-out noise values for the two read-out speeds (from Test report MCD-798B-0310 24 Jan 2010).

	Specification	Measured	Units
Gain level			
High sensitivity	1.4	1.215	e^- / ADC count
Best dynamic	2.8	2.397	e^- / ADC count
High light	18.7	16.698	e^- / ADC count
Read-out noise			
20 kHz speed	5	3.21	e^- rms
1 MHz speed	25	11.97	e^- rms

and (ii) all the settings can be modified from within the LabVIEW VI. The software has been gradually optimised throughout this work and is discussed in appendix A.6.

As a consequence, some of the problems have been overcome. Note that all the results discussed in the sections below were acquired with the detector running under LabVIEW control.

Note, after the initial tests with the detector, all further measurements with the detector were performed using the modified LabVIEW VIs.

5.3.2 Dark current measurements

As described in chapter 4, any CCD detector has a noise level which needs to be determined before it can be used. This noise arises from three main sources:

- dark current noise,
- readout noise,
- cosmic ray event noise.

The cosmic ray events are not a property of the detector and, normally, they are removed post-acquisition. The post-acquisition data treatment is discussed separately (see appendix A.6). The remaining, measured noise is a combination of dark current noise and readout noise. Dark current noise and readout noise are both dependent on accumulation time and, therefore, the noise measured by the CCD detector will also be time dependent.

Measurement procedure The two main readout modes of the Synapse 1024 × 256 FIOP CCD detector are 20 kHz and 1 MHz. The detector has three different gain settings; "High sensitivity", "Best dynamic range" and "High light mode". These correspond to different settings of the system transfer function, as given by the Synapse

Table 5.2: Noise values for 20 kHz readout mode

Acquisition time (s)	High light	Best dynamic range	High Sensitivity
0.1	0.794	1.646	-
0.5	0.796	1.644	-
1	0.801	1.623	3.050
5	0.818	1.635	3.175
10	0.802	1.632	-
100	0.804	1.682	-
500	0.826	1.761	3.126
1000	0.848	1.981	3.322

manual and summarised in table 5.1. In addition, the readout noise values are also included in the table.

A number of dark acquisitions were recorded using the 20 kHz readout mode only, but for all three gain settings. The acquisition times were chosen to match those used by Schlösser when testing the PIXIS detector at KIT [Sch10a], and were 0.1 s, 0.5 s, 1 s, 5 s, 10 s, 100 s, 500 s and 1000 s.

Results and discussion The dark spectra were analysed using a LabVIEW tool, which calculates the standard deviation of the measured signal. The standard deviation is a measurement of the detector noise. The LabVIEW tool also counts how many pixels are removed associated with cosmic ray events (recognised as pixels with a much higher intensity than the adjacent pixels), as this affects the statistics of the data. The results are shown in table 5.2. There are a few missing entries in the table as some of the data runs produced very "stripey" images. The cause of this was most likely linked to light entering the enclosure during these dark acquisitions. The enclosure wasn't completely light-tight due to incomplete retro-fitting of the panels after the detector exchange; when people were entering the laboratory during measurements light leaked into the room.

When comparing this data with those measured with the KIT setup, one observes that the noise values of the Synapse detector are slightly lower than those recorded for the PIXIS (from [Sch10a]) by a factor of 1.43 (1000 s acquisition PIXIS "gain 3", Synapse "high sensitivity" setting). This isn't too surprising since front-illuminated (open-electrode) chips exhibit slightly lower dark currents than back-illuminated chips (as in the PIXIS 400B). A graph of the noise trend for the Synapse detector is given in figure 5.2. The ratios of the measured noise signals for the three Synapse gain settings (high light, best dynamic range and high sensitivity) at 20 kHz readout are approximately 0.8 : 1.6 : 3.2 which corresponds to a ratio of 1 : 2 : 4.

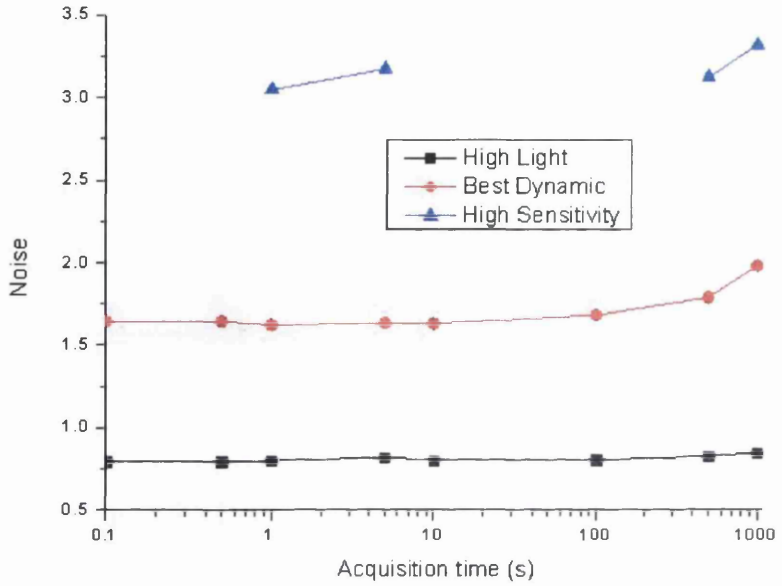

Figure 5.2: The Synapse noise variation with respect to exposure time for 20 kHz readout mode. Note there are no error bars in this graph as the noise is the measured standard deviation of the dark spectrum.

5.3.3 Spectral measurements and determination of SNR

Once the detector noise had been measured, the quantum efficiency and the detector's capabilities of acquiring low level signals were tested.

To be able to compare the SNR to the ones measured in Schlösser [Sch10a], using the PIXIS400B detector, the setup needs to be as similar as possible - see figure 5.1 for the Synapse test setup configuration. Ambient air was therefore used as the scattering medium (removing the cell from the Raman setup) as this can be compared at both locations. The spectral region selected for the test described in this section is shown in figure 5.3.

Measurement procedure The setup and measurement parameters are collated in table 5.3. Note that the measurement parameters are not completely identical to those in Schlösser [Sch10a] (as can be seen in table 5.3) for the following reasons:

- A lens with focal length f=250mm was not available (at the time) in Swansea so the closest available focal length was used.

- The laser power was found to fluctuate (measured as approximately 1W with laser diode current set to its maximum value). This is most likely due to heating in either the laser or the laser power supply, since active cooling (as described in

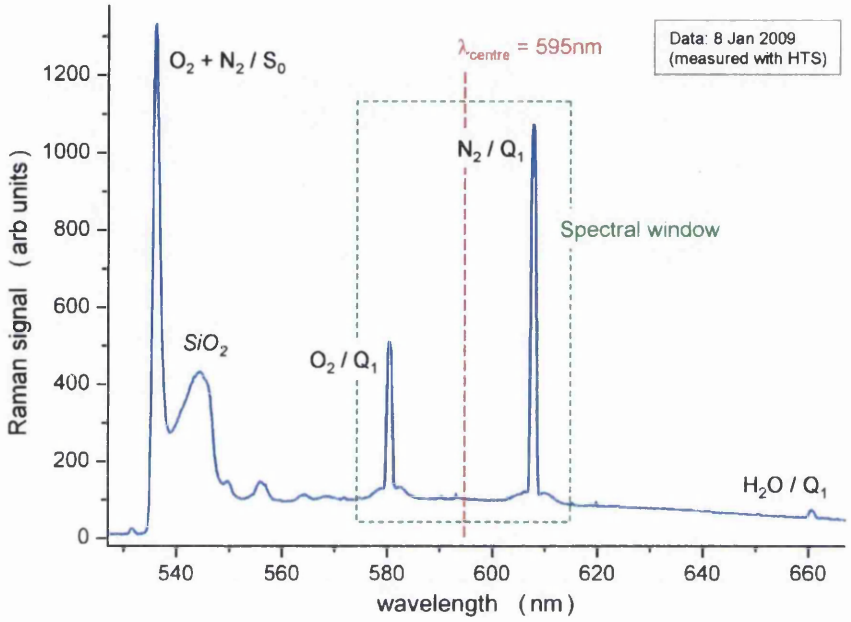

Figure 5.3: Reference spectrum for air (within LARA cell), measured in LARA 1 at KIT, with 1W laser power (1000 s exposure, slit width 127 μm).

Table 5.3: Parameters used in the spectral measurements

Parameter	Synapse measurement value	PIXIS measurement value
Laser power	≈ 1 W	1.488 W
Focussing lens	$f = 200$ mm	$f = 250$ mm
Spectrometer slit width	100 μm	100 μm
Grating	600gr / mm	600gr / mm
Centre wavelength	595 nm	595 nm
Spectral window	≈ 40 nm	≈ 40 nm

section 5.2) was not yet installed into Swansea's LARA system at the time of the test measurements.

The differences will be taken into account when the results for the PIXIS and Synapse detectors are compared further below.

Raman spectra of air were taken using the high sensitivity gain setting of the Synapse detector, with an acquisition time of 100 s and the 20 kHz readout mode.

Results and discussion From the recorded Raman spectra of air, the SNR was calculated for the nitrogen Q_1-branch at 607.245 nm (most intense Raman peak of air from [Jam09], chapter 7 and figure 5.3). The signal is taken as the height of the N_2 Raman peak (above the noise) and the noise as the standard deviation of a "flat" region of the measured spectra. These two values are then used to calculate the SNR.

The resultant SNR was found to be 71.7(34). The laser power was measured as approximately 1 W at the time of this measurement.

Comparison with PIXIS data The SNR of the N_2 Q_1-branch measured using the Synapse detector can now be compared with the equivalent 100 s measurement recorded using the PIXIS detector [Sch10a]. The SNR of N_2 Q_1-branch measured using the PIXIS detector, acquired using gain 3 with an acquisition time of 100 s, is 179.9.

On first observation, the SNR obtained using the PIXIS detector is approximately 2.5 times better than that obtained with the Synapse detector. However, the laser power in each of the two setups is different (approx. 1 W at Swansea and 1.48 W at KIT). This would cause an increase of a factor of approximately 1.5 to the measured Synapse SNR, assuming that the signal scales linearly with laser power. If the high sensitivity 100 s SNR measured using the Synapse detector is multiplied by 1.48 (to correct for the power difference) the PIXIS SNR is about 1.69 times larger than that of the Synapse. The reduction from the expected value of approximately 2 from the values specified in the data sheets is caused by the slightly lower noise levels recorded by the Synapse CCD than the PIXIS.

This data shows that the higher quantum efficiency of the PIXIS detector overcomes the gain of the reduced noise of the Synapse, so it is still about 1.7 times more sensitive.

5.3.4 Detector problems - "dead pixel" phenomenon

During the characterisation and alignment process of the Synapse detector a "dead pixel" was observed. The measurements and identification of this are described in the appendix A.3.3.

After consulting with the manufacturer, they informed us that the CCD-chip used in the Synapse detector is a grade-1 CCD and a grade-1 CCD detector can have 1 dead

Table 5.4: Parameters used in the spectral measurements

Parameter	Value
Laser power	fluctuated
Focussing lens	f = 200 mm
Spectrometer slit width	100 μm
Grating	600gr / mm
Centre wavelength	595nm
Spectral window	$\approx$ 40 nm

pixel when it is manufactured. Therefore, the detector was not repaired. This means that, for all measurements with the Synapse detector, the "dead pixel" data values are replaced with the value from an adjacent pixel.

5.3.5 On-chip binning

On-chip binning is a process most modern spectroscopic CCD's offer, where the signal content is accumulated internally over several pixel (rows) before readout. It has the advantage that readout noise only contributes once per readout operation. Therefore, the noise is reduced with respect to the signal strength, along with dark noise fluctuations averaging out prior to readout. Multiple on-chip binning test measurements have been performed in this work using the Synapse detector. However, these early tests were performed before temperature stabilisation of the laser head was performed and laser power drifts were observed in several of the measurement runs. Therefore, most of the measurement sets have been discarded. The experimental procedure and final results are discussed here.

Experimental setup The setup used was the same as that for the Synapse test measurements (see table 5.4). The measurement parameters will be taken into account when the data is analysed. The on-chip binning was performed using a modified LabVIEW routine (embedded in the modified detector software see appendix A.6) where the 2D-chip could be split up into areas for the on-chip binning to occur. The number of areas could be varied between 1 and 256 (for the Synapse detector). The on-chip binning produces spectra for the number of areas chosen. The spectra were then averaged over the areas to produce one graph for each area setting.

Results and observations Raman spectra of air were recorded for acquisitions of 50s, 100s and 150s. The laser power was set to full and monitored on a side arm of the setup. Spectra were recorded for the following areas: 1, 3, 4, 5, 8, 10, 16, 24, 32, 64, 128 and 256. Note that for this detector 1 = a full chip average and 256 = a no row

Table 5.5: Recorded signal, noise and SNR of the N_2 Raman Q_1 branch. Uncertainty (in brackets) in the last digit.

	50s			100s		
Areas	S	N	SNR	S	N	SNR
1	1249.0(353)	9.36(80)	133(12)	2480.0(498)	11.17(92)	222(19)
3	432.7(120)	3.17(34)	136(15)	804.3(164)	3.40(32)	237(22)
4	324.0(90)	2.60(22)	125(11)	607.0(123)	2.81(27)	216(21)
5	258.2(72)	2.25(20)	115(11)	479.0(98)	2.33(23)	206(21)
8	162.9(45)	1.49(13)	109(10)	288.1(60)	1.83(18)	157(15)
10	131.8(36)	1.26(11)	105(10)	232.2(48)	1.49(16)	156(17)
16	84.4(23)	1.00(10)	85(8)	146.1(30)	0.94(8)	155(13)
24	53.7(15)	0.58(6)	93(9)	90.3(19)	1.24(13)	73(8)
32	41.6(11)	0.58(5)	71(6)	72.4(15)	0.58(7)	125(15)
64	19.1(5)	0.41(3)	46(4)	36.3(8)	0.41(4)	88(10)
128	9.7(3)	0.23(2)	42(4)	17.1(4)	0.26(2)	67(6)
256	4.6(1)	0.19(2)	25(3)	8.5(2)	0.20(2)	43(4)

	150s		
Areas	S	N	SNR
1	3323.0(576)	14.70(160)	226(25)
3	1108.0(192)	4.76(60)	233(30)
4	819.8(143)	4.01(32)	205(17)
5	638.8(113)	3.25(24)	197(15)
8	399.5(71)	1.84(19)	217(23)
10	313.2(56)	1.65(15)	190(18)
16	196.9(35)	1.10(10)	179(16)
24	125.0(23)	0.81(8)	155(16)
32	95.3(17)	0.70(7)	136(14)
64	47.7(9)	0.43(4)	112(9)
128	23.9(4)	0.30(3)	81(9)
256	11.1(2)	0.21(3)	52(6)

average. The signal was taken as the height above the background level of the Raman Q_1-branch of N_2 in air and the noise was the standard deviation of a "flat" region in the spectrum. The measured signal, noise and SNR of the nitrogen Q_1-branch in air are shown in table 5.5.

The observations that can be made are:

- The SNR for 3 area on-chip binning is of the same order as that of 1 area (full chip) on-chip binning. The reason for this is that the signal and noise both reduce by approximately a factor of 3 by averaging over the three spectral regions.
- The SNR of 3 area on-chip binning is approximately a factor of 5 higher than that of 256 area on-chip binning (same as image readout for the 1024 × 256 pixel

Synapse detector).

- Multiple area on-chip binning is needed so that astigmatism corrections can be implemented. This cannot be done if binning is performed over the whole chip.

These measurements show that on-chip binning leads to an enhancement in the SNR of measured spectra. The number of areas should be set appropriately to enable astigmatism correction to be performed. A minimum of 3 areas is required to correct for astigmatism. For measurements with a higher astigmatism the number of areas needs to be increased to 5. The data in table 5.5 above shows that using 3 or 5 area on-chip binning have a SNR of the same order of full on-chip binning (1 area) so sensitivity will not be lost. In this work, for 256 row chips, like in the Synapse detector, 3 area on-chip binning will be used and for 400 or 512 row chips, like the PIXIS detectors in TLK, 5 area on-chip binning will be used. This results in the number of rows per binning region being 80 - 100.

Similar tests have been done with the PIXIS 2KB CCD detector (*Princeton Instruments*) to see if it behaves in the same way. The results from this test are shown in figure 5.4. The figure also contains additional information on the astigmatism. The

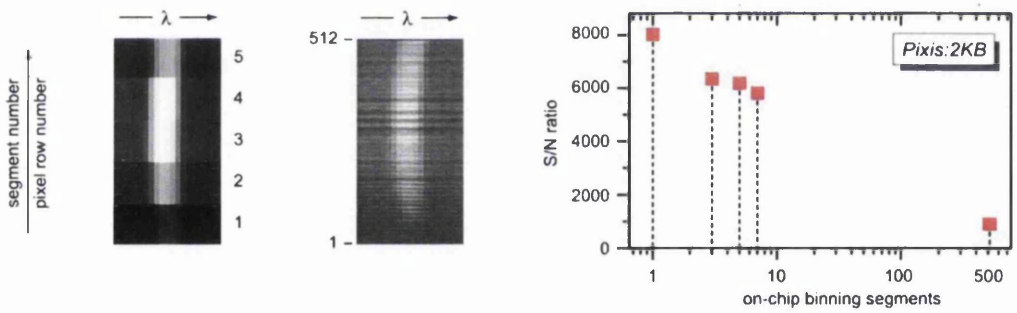

Figure 5.4: SNR of a H_2 Raman line, as a function of binning segments - from complete on-chip binning (1 segment) to no on-chip binning (512 segments) using the *Princeton instruments* PIXIS:2KB detector taken at KIT.

centre-panel contains a 100×500 pixel area of a PIXIS:2KB CCD detector, the left-panel contains the identical spectral region after on-chip binning; the five (vertically-stretched) segments constitute averages over 102 pixel rows. The spectrometer astigmatism in the spectral line is visible in both cases.

The data in the right panel of the figure shows that the SNR of the 3 area and 5 area on-chip binning measurements are very similar, as was the case with the Synapse data. This means that the sensitivity will not be much worse when 5 areas are needed to overcome stronger astigmatism from lens type spectrographs (HTS), as can be seen in the figure. Therefore, to maximise the SNR, 3 or 5 area on-chip binning was implemented for all further LARA measurements in Swansea and KIT.

5.3.6 Conclusions

The Synapse detector has been thoroughly tested and compared with the PIXIS400B. The PIXIS400B (back-illuminated) detector is approximately 1.7 times more sensitive than the Synapse detector. Therefore, back-illuminated CCDs will still be used in any future setups that are built in KIT. The Synapse detector was found to have a "dead pixel", which appears as one pixel with much lower intensity than the surrounding pixels. After consulting with the manufacturer they revealed that 1 dead pixel (column) is within the design specifications of the grade-1 CCD within the Synapse detector.

Full on-chip binning leads to a higher SNR than full chip readout. However, increasing the number of binning areas to 3 or 5 is required to correct for astigmatism from spectrometers. The SNR is not reduced by much from full on-chip binning; so the improvement is not lost. Three or five area on-chip binning was used from here onwards for all LARA measurements at Swansea and KIT to maximise the systems sensitivity. The increase in the number of binning areas is associated with the higher astigmatism of spectrographs used in KIT.

5.4 Multi-pass experiments

In the following section the different signal optimisation experiments that have been carried out to improve the sensitivity of the LARA setup will be discussed.

Theoretically, if a second laser beam, parallel to the incident beam, was to pass through the Raman sample and both beams had the same intensity, then the collected Raman signal should double. The LARA setup in Swansea was modified so that multiple passes of the laser excitation beam through the cell could take place. In the simplest setup, a (rectangular) flat mirror was placed behind the cell; a second focal lens is required to refocus the reflected light back into the cell. A third pass can be implemented by placing a second (rectangular) mirror so that the beam passes back through the cell. Sketches of the two configurations are shown in figures 5.5 (a) and 5.5 (b).

For proof of principle measurements, ethanol was used as the scattering medium. This was chosen because the Raman lines have a high intensity for short acquisition times. An example of the Raman spectrum of ethanol is shown in figure 5.6. This can be used as a reference spectrum, so the positions of the peaks are approximately known.

Ethanol spectra were taken for single-pass, double-pass and triple-pass excitation, for (single) exposure times of 1s, 5s and 10s, respectively. Please note that these measurements were performed before the Synapse detector was installed and the Excel laser was optimised. The intensity of the strongest ethanol peak, at approximately 633 nm, was evaluated for the signal-gain comparison. The recorded intensity values for the three excitation configurations and the different exposure times are collected in table 5.6.

As can be seen, adding a second or third pass approximately doubles and triples

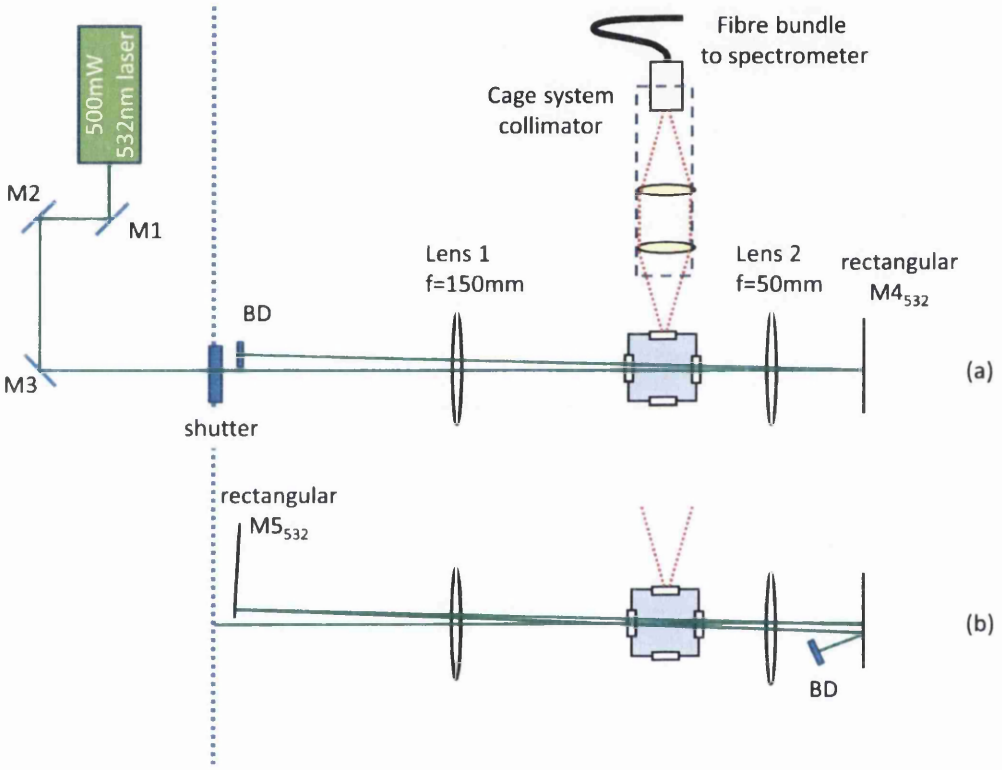

Figure 5.5: Experimental setups for various multi-pass arrangements; (a) double-pass configuration; and (b) triple-pass configuration; M1, M2, M3 = standard high-reflectors (*Thorlabs* E01 coating); M4, M5 = rectangular mirrors with HR 532nm coating; BD = beam dump. In all configurations the rectangular mirrors M4 / M5 were adjusted so that the two / three beams were aligned horizontally (in plane) with the fibre, for the 90 degree collection geometry.

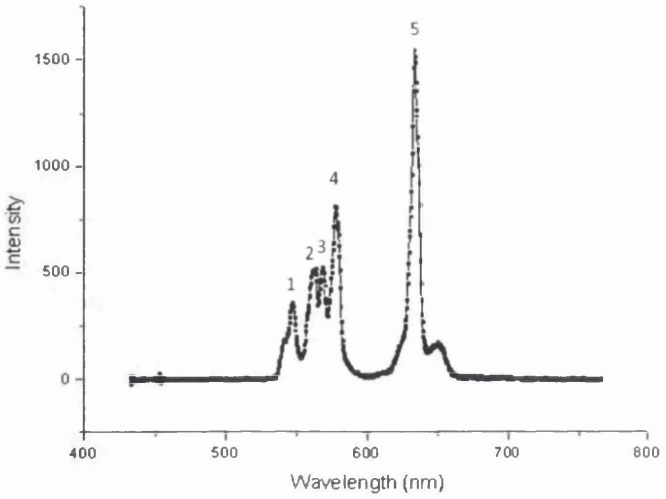

Figure 5.6: An example Raman spectrum of ethanol. The numbers denote the 5 peaks observed

the intensity of the Raman line compared to that of a single pass. Also, the signal improvement for the double pass arrangement is comparable to that of doubling the acquisition time for single pass excitation. This means that, if a second pass is used, the same signal intensity can be achieved within half the acquisition time.

Thus, the proof of principle of modifying the LARA setup to include multiple passes has been successful in that $2\times$ and $3\times$ the Raman signal intensity can be achieved for double and triple passes through the cell.

5.4.1 Effects of beam walk-off on multiple pass setups

Even though beam walk-off from the laser has been minimised, by stabilising the temperature of the laser head, to $\Delta q < 10\,\mu$m in section 5.2, beam walk-off can still occur from temperature fluctuations, resulting in changes to the guiding optics and optical

Table 5.6: Intensities of the main ethanol peak (number "5" at 633nm) for the three different pass setups, for three different exposure times. Uncertainties (in brackets) are in the final digit.

Exposure time	Intensity of main ethanol peak		
	1 pass	2 passes	3 passes
$1 \times$ 1s	1330(36)	2707(52)	4447(67)
$1 \times$ 5s	5731(76)	11729(108)	18930(138)
$1 \times$ 10s	10274(101)	21134(145)	34496(186)

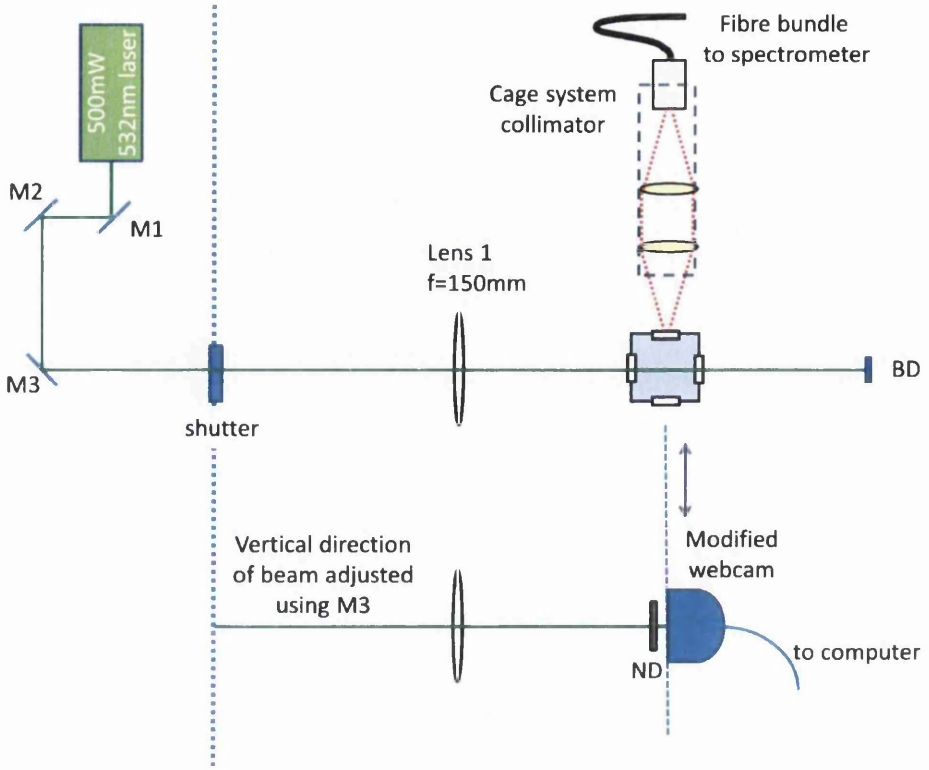

Figure 5.7: Schematic diagram of the setup used to determine the amount of beam displacement of the primary beam.

bench. Therefore, the expected effect of beam walk for the multiple-pass setups needed to be tested, in order to gauge whether the multiple passes would be more severely affected by beam walk-off.

Beam walk is a problem since the excitation volume is imaged onto the fibre bundle with $100\mu m$ core diameter. Any displacement would severely affect the amount of collected light. The beam displacement in the collection (lateral) plane was not tested, as this would only cause the scattering region to walk minimally out of focus. Therefore, the beam was only displaced vertically, and the intensity variation of the main ethanol Raman peak was measured with respect to the displacement of the beam.

The beam displacement was controlled by rotating the vertical control knob on mirror M3 in small increments, marked by the raised dashes. To quantify the actual displacement of each step, a modified webcam was placed at the location of the cell (as shown in figure 5.7). The same rotation procedure of mirror M3 was applied and the beam position (in pixels) for each rotation was recorded (a LabVIEW program had been written, which determines the centre of a laser beam that is incident on the chip of the webcam as described in appendix A.6).

The variation of the main peak intensity, with respect to the incident beam displacement, for the three setups is shown in figure 5.8.

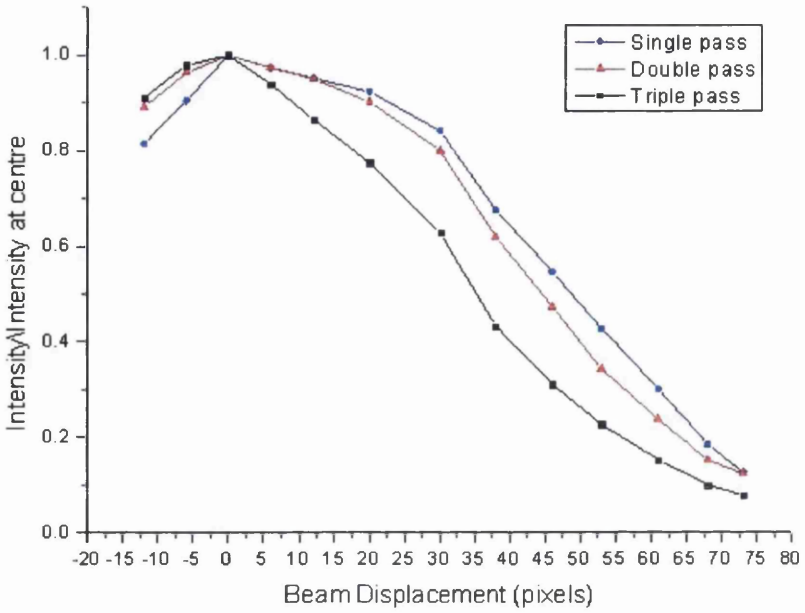

Figure 5.8: Normalised intensity of the main peak of ethanol against the first-beam displacement, in units of pixels.

The displacement in pixels can be converted to μm, if the size of each pixel is known. The pixel size was assumed to be between 6 and $10\mu m$ (the exact pixel specification of the CCD chip was not available at the time of writing). This then enables one to quantify the pixel displacement scale in figure 5.8 in μm.

Every time a pass is added to the system, the beam is reflected off an extra mirror. This means that displacement of the first beam would be amplified in the second and third passes. In the second pass, this doesn't cause too much of an effect on the intensity when the displacement of the incident beam is small. In the third pass, the effect is much more noticeable.

The intensity data for the double- and triple-pass measurements are also affected by the 2nd-pass beam striking the outer rim of the focussing lens after a displacement of approximately 35 pixels of the incident beam. This prevents the 3rd-pass beam from being fully transmitted, and consequently its intensity drops off dramatically.

The tests of beam walk show that the intensity drops of the single- and double-pass setups are similar when beam walk-off occurs. The triple-pass setup, however, results in a faster intensity drop with the same initial-beam displacement. This would mean that for the latter setup to be implemented with the same level of accuracy as the single- and double-pass setups, beam walk-off would have to be lower. Therefore, the double-pass setup was implemented into Swansea's LARA setup. As only a second pass is needed the mirror, M4, in figure 5.5 was replaced with a standard high-reflector (*Thorlabs* E02 coating [tla]).

5.4.2 Multi-pass measurements of gases

Between the ethanol and gas measurements being taken, modifications had been made to the system:

- the 500mW Nd:YAG laser source has been changed with a 2W Nd:YAG laser source (as described in section 5.2),
- the one dimensional IPDA (intensified photodiode array) detector has been replaced with a Synapse 1024 × 256 FIOP (front-illuminated open electrode) CCD detector (as described in section 5.3).

These hardware modifications result in improvements in the SNR. This brings the capabilities of the Swansea LARA system up to approximately those of the second TLK LARA system (LARA2). However, the setups still have slightly different capabilities. This means that direct comparisons between data taken with the different setups are not possible without taking into account the differences. However, other improvements can still be applied to all three setups.

For the double-pass setup to be fully implemented, the improvements need to be verified by test measurements for which the scattering medium is a gas. The gases the system has been tested with are air (cell removed) and hydrogen gas (filled cell approx. 1 bar pressure). The peak intensity values for the N_2 Q-branch and the H_2 $Q_1(J = 3)$ line are collated in table 5.7. As can be seen, adding a second pass approximately doubles the collected Raman signal for a gas. This means this setup can be implemented into all the 90° KATRIN LARA setups.

Table 5.7: Intensities of the N_2 Q branch and the H_2 $Q_1(J = 3)$ branch for one and two pass setups.

Gas used	Exposure time	Peak Intensity	
		1 pass	2 passes
Air (N_2 Q-branch)	1 × 150s	379	752
Hydrogen ($Q_1(J = 3)$)	1 × 200s	404	669

5.5 Improve imaging onto the CCD detector plane

Another way to improve the Raman signal in the LARA setup is to try and optimise the imaging of the scattered light onto the detector plane. In the standard KATRIN LARA configuration, the experimental setup is fixed at an observation angle of 90° and the imaging of the scattered light onto the fibre input is already optimised. As the light is imaged onto the fibre, the fibre output needs to be verified. The setup used to measure

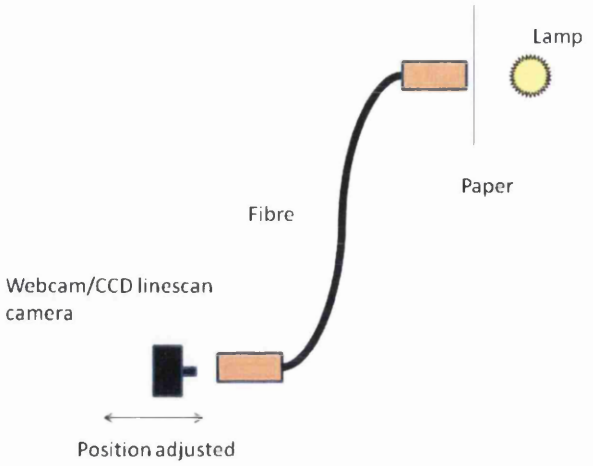

Figure 5.9: Schematic diagram of the setup used to determine the fibre output.

the fibre output is shown in figure 5.9.

A modified webcam was used, as it can be placed as close as possible ($\approx 1\,\text{mm}$ away) to the fibre output, so the light distribution at the fibre output can be determined. As described in chapter 4, the fibre is a slit-to-slit ordered fibre bundle where the slit dimensions are $125\,\mu\text{m} \times 6000\,\mu\text{m}$. $125\,\mu\text{m}$ is width of the cladding; the core width is $100\,\mu\text{m}$. The fibre is orientated such that the longest side is horizontal at the input and vertical at the output. Paper was used to attenuate the white light and ensure the light incident on the fibre was uniform. The webcam chip dimensions are too small to image the complete height. However, the variation of the width of the output can properly be observed.

An appropriate acquisition time was selected, to ensure the webcam did not saturate; the light source was placed at a fixed distance from the fibre input (so the intensity remains constant). The webcam image was recorded for fibre-chip distances of 3, 4, 5, 6 and 7 mm. The recorded images were then binned horizontally, giving an averaged intensity profile across the peak width. The collated binned images are shown in figure 5.10.

As can be seen, the peak profile widens and the intensity reduces and becomes more spread out as the webcam moves further away from the fibre output. More accurate measurements will be needed to determine the profile at the fibre output. This can be done by fixing the webcam to a translational stage and stepping the webcam back in smaller steps. Then one should be able to extrapolate the peak profile and width to the zero-position. The images show that the intensity output from the fibre is approximately Gaussian, but not quite: this is due to the fact that multimode fibres are used whose $100\,\mu\text{m}$ core diameter gives rise to a "hat-top" profile in the far-field. However, this is not problematic since analysis routines have been developed, which use numerical line

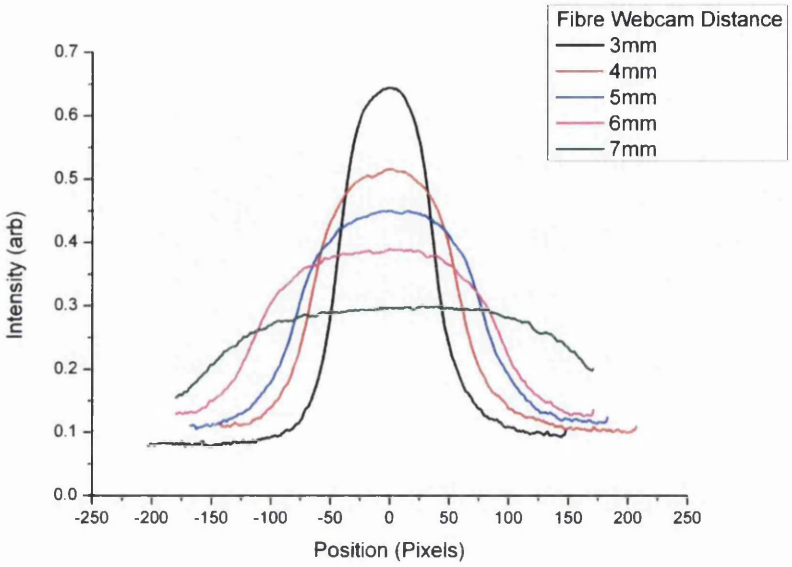

Figure 5.10: Collated graph of the fibre output.

profiles (see ShapeFit in appendix A.6 and [Jam13]). This means that a deviation from a Gaussian line profile can be fully accounted for.

It is worth noting that the measurement data in figure 5.10 can be used to crudely calculate the numerical aperture of the fibre bundle. Taking for example the 5 mm webcam distance plot this has a FWHM of $\approx$ 200 pixels $\approx$ 2 mm (assuming a 10 μm pixel size). This is equivalent to the beam diameter, so the numerical aperture is then NA $\approx \frac{D}{2f} \approx \frac{2}{10} = 0.20(2)$. This agrees with the specified numerical aperture of the fibre bundle NA = 0.22.

5.5.1 Imaging the fibre onto the detector plane

The optical setup, focusing the light output from the fibre through the spectrometer onto the detector plane, is shown in figure 5.11. The setup is built this way to make the system light-tight. The spectrometer has a f-number of f/6.5, which means a focal length lens longer than 50 mm (lens diameter = 25.4 mm) would enable more light to be collected (f-number = 1/2NA = f_{lens}/D_{lens}). To obtain a f-number of 6.5 for D_{lens} = 25.4 mm would require f_{lens} = 165.1 mm. However, it is then difficult to ensure the cage system is completely light-tight. The standard method of imaging ensures that the fibre output is imaged 1:1 onto the spectrometer slit, and the spectral resolution is defined by the slit width. This normal setup is shown in a simplified form in figure 5.12 a. To achieve higher resolution, the slit width needs to be reduced. This results in a substantial loss in the amount of light collected. Overall, the incorrect matching of the fibre numerical aperture with the spectrometer f-number results in a loss of light.

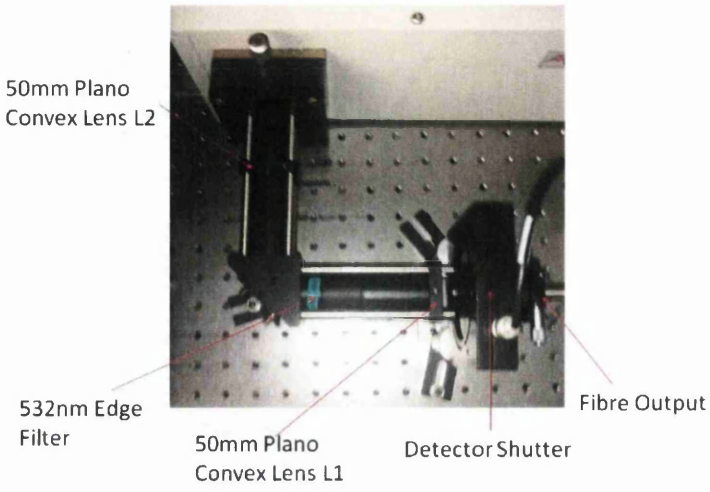

Figure 5.11: Photograph of the spectrometer side of the cage setup

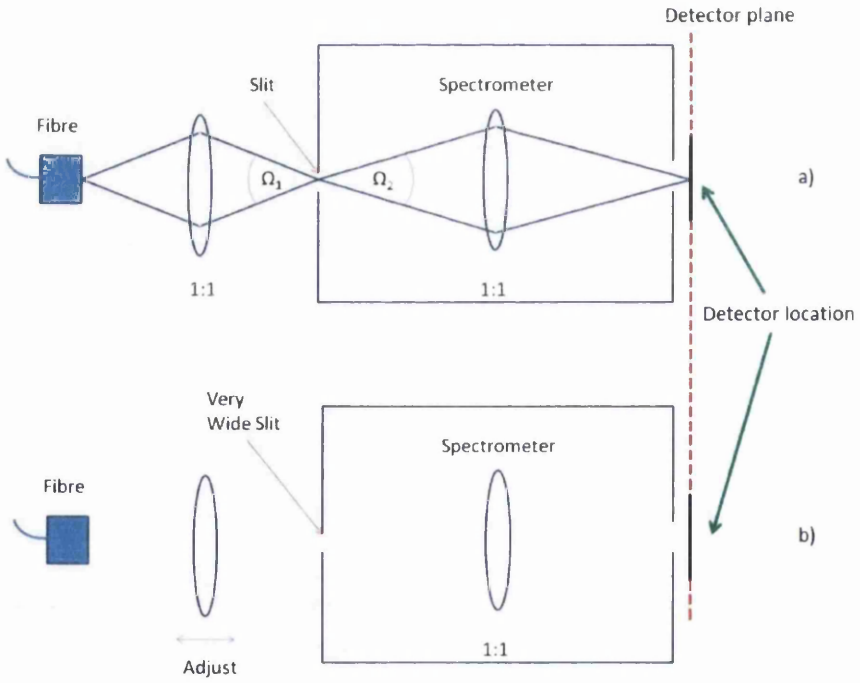

Figure 5.12: Simplified schematic of aligning spectrometer/detector systems. a) Normal setup and b) new idea. Note: In the spectrometer the presence of the dispersing grating has been ignored.

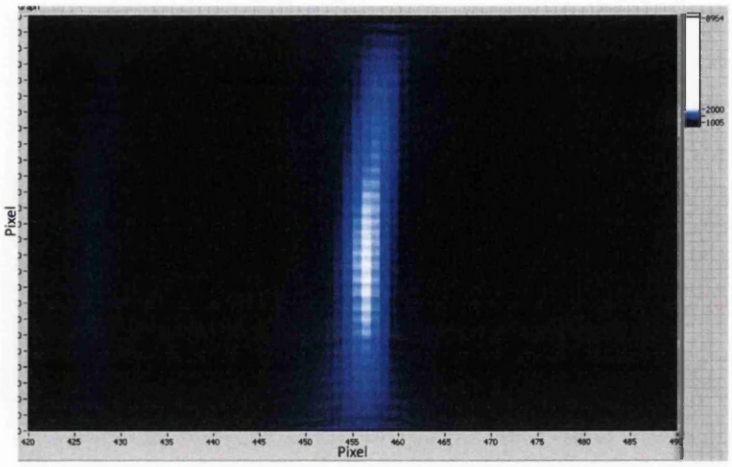

Figure 5.13: Image of the chosen Cs line at 456 pixels $\approx$ 601.049 nm when L2 is at its focal position. Slit width setting = 25 = 350 μm

A different way to image the fibre output onto the detector plane has been suggested to improve on this deficiency. As the fibre bundle has a fixed width the fibre core acts like an additional slit in the setup. The idea is, that if the lens position in the focussing optics is adjusted, the image on the detector plane is a convolution of the fibre core and the spectrometer slit. When the entrance slit width is narrower than the fibre core, the slit is the dominating aperture. When the slit width approaches and exceeds the width of the fibre core (100 μm) the fibre aperture becomes the limiting width. As there is an alignment of two width profiles, care needs to be taken to ensure the fibre image is central on the spectrometer slit, otherwise distorted line profiles occur. This is highlighted in figure 5.15, where the observed profile and intensity of a spectral line are shown as a function of entrance slit setting, for a centred (trace II) and a displaced (trace III) fibre image. Appropriately adjusting the lens position should maximise the amount of light collected whilst maintaining a high resolution spectral image.

To ensure the alignment is correct, and to test the proposed idea, test measurements were performed using a Cs spectral lamp. The position of the lens, L2, was shifted to vary the convolution effect. Here the term "focus" is used to mean highest resolution, and the term "out of focus" means normal imaging of the spectrometer slit . An appropriate acquisition time was selected so that the detector wasn't saturated; the detector was set to 1 MHz readout mode. The spectrometer 600gr/mm grating was selected and centred at 595nm. With the slit adjusted to setting 25 (approximately 350μm), the position of the lens, L2, was adjusted and the spectral line at 456 pixels $\approx$ 601.049 nm was observed. The line width and maximum intensity of the observed line changed as the line approached its focus. Images of the line at the focal point and when the lens is out of focus are shown in figures 5.13 and 5.14 respectively. To achieve the same

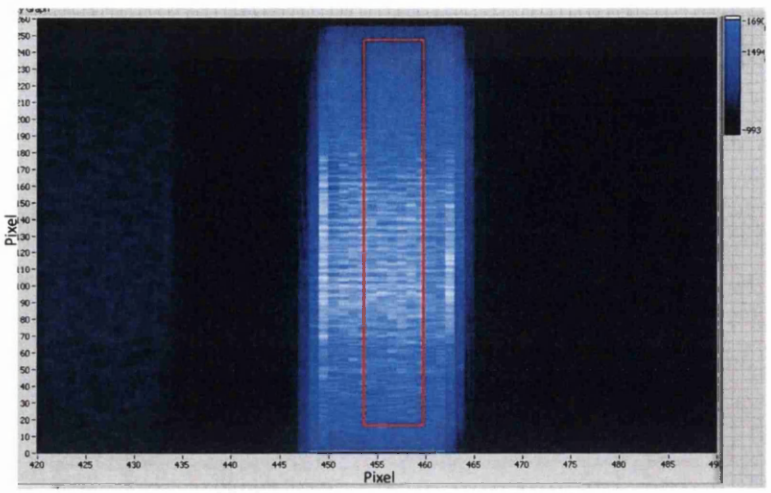

Figure 5.14: Image of the Cs line at 456 pixels ≈ 601.049 nm when L2 is not at its focal position. The rectangle represents the full width of the focussed line from figure 5.13. Slit width setting = 25 = 350 μm

line width as the focussed image, the slit width of the spectrometer would have to be reduced substantially. To get an idea of the effect this would have, a box of a similar width to the reduced line width is included in the figure. As can be seen, bringing the lens into its focal position reduces the line width and increases the maximum intensity. Note that intensity ripple is observed over the spectral line width for the non-focussed line. This fluctuation is partly due to the 1 MHz readout mode.

To look at the changes in more detail, for the focussed and non-focussed positions, the spectrometer slit width was varied in 50 μm steps and spectra were recorded (for on-chip binning and post-acquisition binning). The intensity differences were recorded.

A graph of the peak intensity (height) change is shown in figure 5.15 for three different imaging configurations. Trace I is an example of the focussed image onto the CCD detector plane, trace II corresponds to imaging onto the entrance slit plane and trace III is a misaligned image onto the entrance slit plane. Note, that the selected spectral line is different from the one shown in figures 5.13 and 5.14.

For the focussed case (trace I), opening the entrance slit of the spectrometer does not affect the observed spectral line width in first approximation, but only lets a larger fraction of the light cone enter the spectrometer, leading to an increase in the peak intensity. For the 456 pixels ≈ 601.049 nm line, the line width remains at approximately 4.6 ± 0.1 pixel throughout, in the focussed case. This corresponds to an image width of approximately 120 μm, and implies that the imaging is not optimal in this alignment. In the focussed case, for the spectral line visualised in figure 5.15 the line width remains at approximately 3.6 ± 0.1 pixel throughout. This corresponds to an image width of

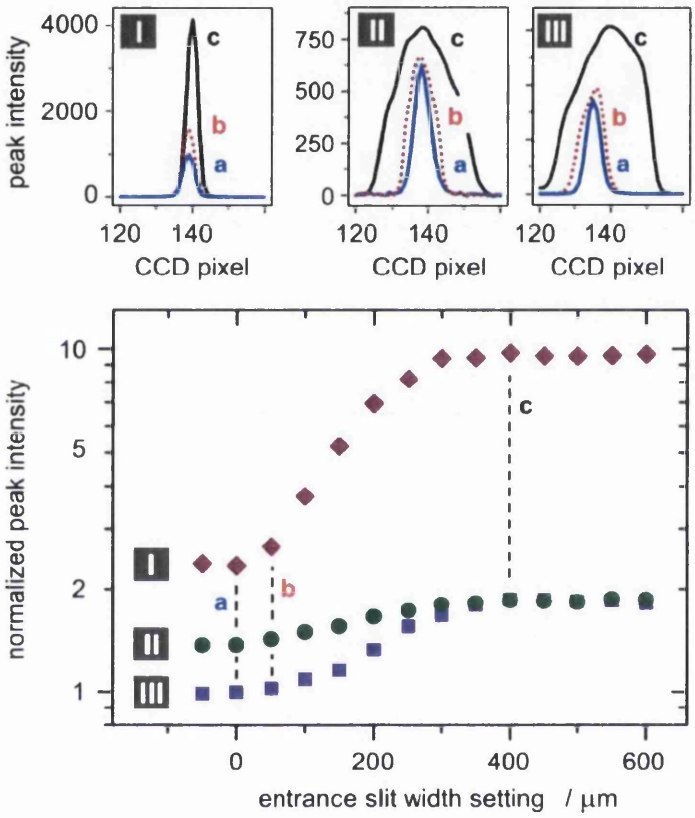

Figure 5.15: Intensity and width of a (Cs) calibration line imaged by a linear fibre bundle (48 fibres, individual core diameter 100 μm), as a function of entrance slit width of a SP500i spectrometer (minimum slit width 10 μm). Trace I imaging onto the CCD detector plane; trace II imaging onto the entrance slit plane; trace III misaligned image onto the entrance slit plane. For details see text.

approximately 95 μm in the detectors in this work. This is a slightly reduced diffraction-limited image of the fibre core. The intensity in the non-focussed and misaligned setups increases by a much smaller value and the image width increases from a minimum of $\approx$ 3.5 pixels at a 10 μm slit width to a maximum of $\approx$ 20 pixels, where the fibre core diameter has become dominant. This means that increasing the slit width increases the SNR of the focussed setup without increasing the line width. This could, therefore, be a useful way of obtaining a better signal, if required. Note that the intensities do not tend to zero when closing the slit, since the particular spectrometer used here incorporates a slit width limiter, set to a minimum of 10 μm. This is verified by viewing the data point when the slit adjustment micrometer has been turned beyond the zero-width position and the light throughput has not reduced further.

One other observation can be made from these measurements. When light is incident on a slit, Fresnel diffraction occurs and is observed in the spectrum in figure 5.13 as low intensity wings in the spectral profile. This is visible when lens L2 moves into its focal position, as the true edge of the light output is observed. The spectrometer slit can be used to cut off the diffraction pattern by setting its width such that it coincides with the first minimum of the diffraction pattern.

In the phenomenon described, the line-integrated amount of light collected by the detector is the same, in all cases. Due to the increased line width, when focussing onto the spectrometer slit, the peak intensity is reduced. Imaging onto the detector plane is a method of achieving a better SNR for the focussed case by approximately a factor of 5, whilst maintaining a narrow line width. The maximum increase occurs by setting the spectrometer slit width beyond the fibre core width, at best to coincide with the first minimum of the Fresnel diffraction pattern. For most measurements from here onwards the spectrometer slit width is set to approximately 350 μm.

5.6 Introduction of a linear (sheet) polariser

5.6.1 Single fibre polarisation dependence

As described in chapters 2 and 3, Raman scattered light is a mixture of two polarisations, $I_{\perp}$ and $I_{||}$. In the Raman measurements performed in this work, the intensity of this scattered light is measured with respect to wavelength, after the light has passed through several optical components that have polarisation dependent transmission. In the work of Lewis [Lew07] it was assumed that the fibre bundle scrambles the polarisation of the scattered light, so the polarisation dependence of any further components does not make any difference to the measured intensity. It was decided, for completeness, to measure the effect of the fibre bundle, used in this work, with respect to the polarisation of light.

First, the effect an individual fibre has on the polarisation of light was measured. The setup used to perform this measurement is shown in figure 5.16. A 50 mW Nd:YAG

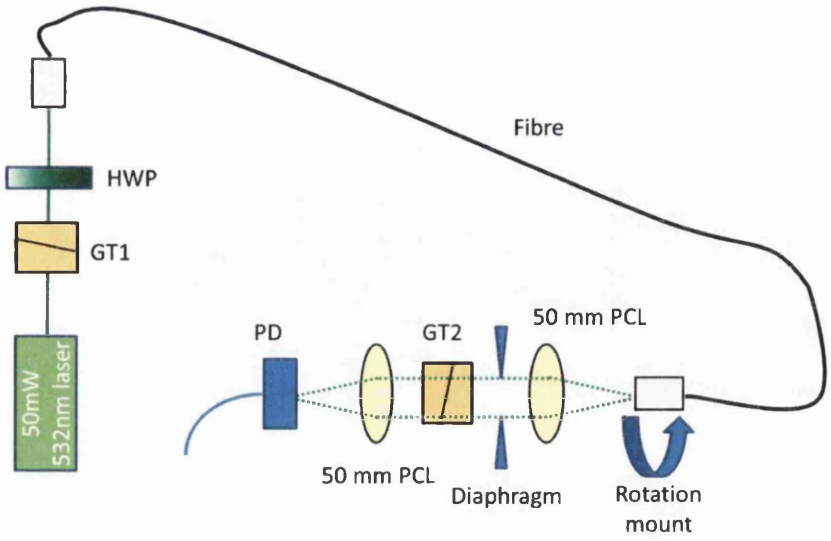

Figure 5.16: Experimental setup for single fibre tests. GT1 is a Glan-Taylor polariser used to clean up the polarisation of the laser beam, HWP is a half-wave plate used to rotate the polarisation of the incident beam, GT2 is a Glan-Taylor polariser that is set to fix the polarisation of the measured beam, PCL are plano-convex lenses and PD is a photodiode.

laser was used to illuminate the fibre, the Glan-Taylor polariser GT1 was adjusted to clean up the polarisation of the incident beam and GT2 was set at a fixed polarisation.

A few different test measurements were performed with this setup:

- The fibre was vibrated and the photodiode signal was recorded over time (figure 5.17).
- The fibre was rotated in increments of 10 degrees using a rotation mount at the exit and the photodiode signal was recorded (figure 5.18 A).
- The fibre entrance was angled and the half-wave plate rotation was repeated (figure 5.18 B).
- The half-wave plate was rotated in increments of 10 degrees, and the photodiode signal was recorded (figure 5.18 C).

When the polarisation of the light incident on the fibre is varied, the polarisation dependent output light varies by 44.6% maximum to minimum. When the fibre entrance is at an angle, the same variation is 51% maximum to minimum. The polarisation of the output light from the fibre is dependent on the rotation angle and the intensity of the output light shifts when the fibre is moved.

These measurements show some of the parameters that affect the polarisation of light passing through a fibre. This can then be applied to each individual fibre in a fibre bundle.

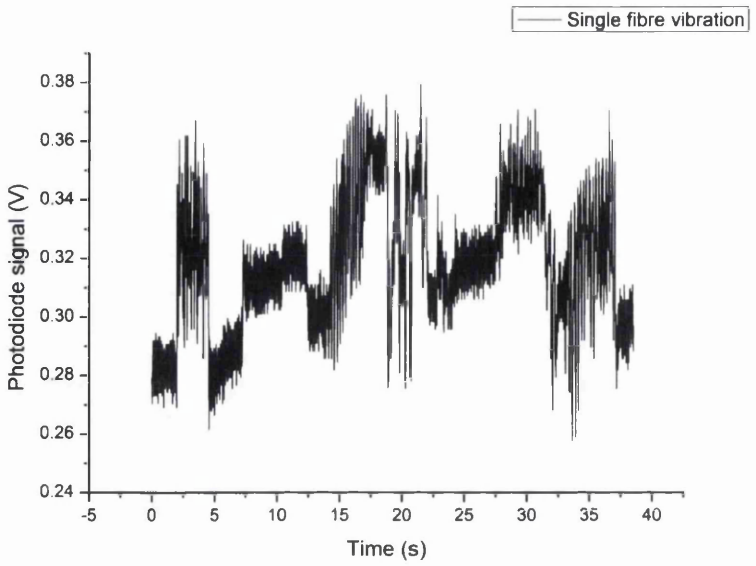

Figure 5.17: Graph of the single fibre vibration test. The photodiode signal is recorded vs. time whilst the fibre was moved and vibrated.

5.6.2 Fibre bundle polarisation dependence

When polarised light is passed through a fibre bundle, it is generally assumed that the emitted light's polarisation will be scrambled (unpolarised) as is stated above. This can be logically understood, as the number of fibres in a standard bundle are usually large and unfixed. This means that each individual fibre would undergo varying degrees of the effects demonstrated in the section above and the output polarisation would become scrambled i.e. unpolarised.

In the LARA setup for KATRIN, the fibre bundles contain 48 fibres in a slit-to-slit configuration, i.e. they are in a fixed position. Also, as the fibre input is a horizontal slit and the fibre output is a vertical slit, the fibres are all being rotated by at least 90 degrees within the bundle. This means that the polarisation of the light coming out of each fibre is expected to be rotated. From preliminary measurements, using a similar setup to the one used in the above section, the fibre output appeared to show an unexpectedly large polarisation dependence (approx 40% variation). This was not understood, as for the polarisation to be maintained, each fibre would have to be fixed in exactly the same way throughout the 2m length of the fibre bundle. It is unlikely that this is the case.

To test the fibre output more explicitly a configuration was setup, which enabled the output of each fibre to be observed individually. A suggestion by Magnus Schlösser was to use the CCD detector with a white light source, as each fibre could be separately identified on the output image.

One other outcome from the single fibre measurements is that, if the input light is

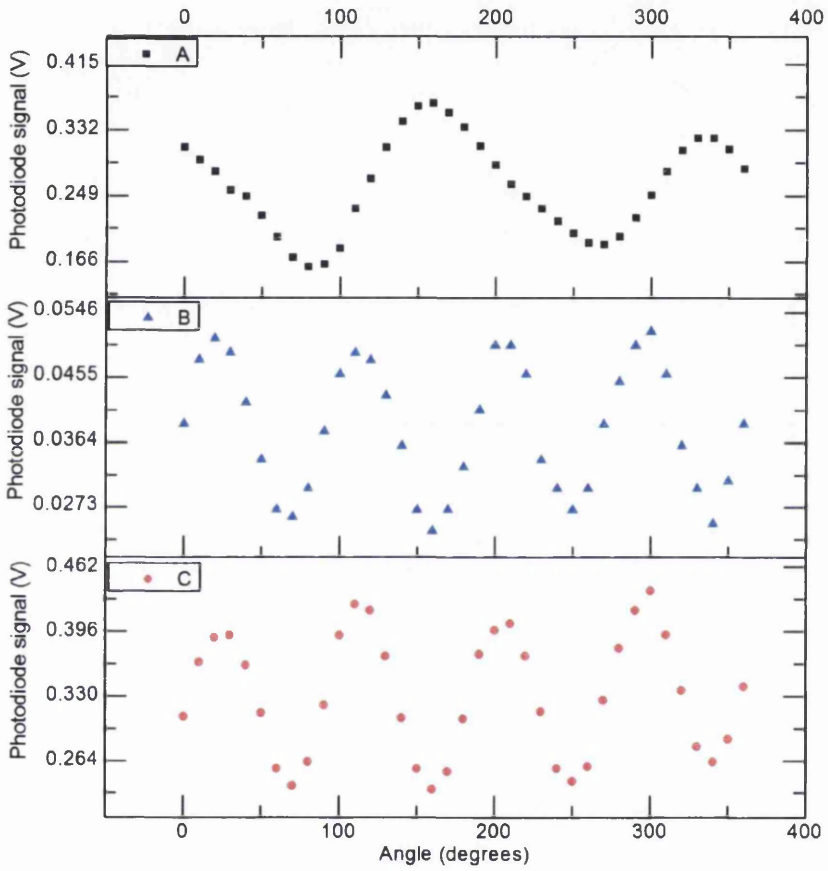

Figure 5.18: Graphs of single fibre polarisation tests. A) Single fibre rotated, B) Single fibre light incident at an angle with half-wave plate rotated and C) Single fibre incident light perpendicular. The expectation for 'scrambled' polarisation would be a constant intensity and for 'perfect' polarisation the minimum intensity = 0.

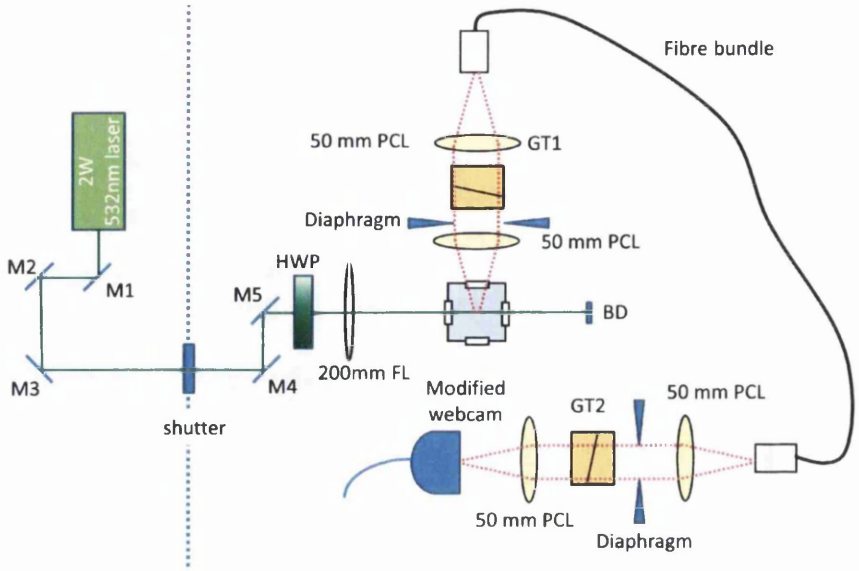

Figure 5.19: Experimental setup for fibre bundle test. M1 - M5 are broadband mirrors used to guide the laser beam to the cell, HWP is a half-wave plate, FL and PCL are plano-convex lenses, BD is a beam dump and GT1 and GT2 are Glan-Taylor polarisers. GT1 is set to ensure that the light incident on the fibre bundle is of one polarisation only and GT2 is rotated to measure the polarisation dependence of each fibre in the bundle.

entering the fibre at an angle, the polarisation preservation changes. This means that, in these test measurements, the light needs to be focussed onto the fibre in the same way as it will be during the Raman measurements. To obtain preliminary results more quickly, a simple ethanol Raman scattering experiment was set up to create the incident light. The setup configuration can be seen in figure 5.19.

GT1 is used to ensure the light incident on the fibre is linearly polarised and GT2 is rotated to check the polarisation dependence of the light for each fibre bundle. A modified webcam was used as it enabled a section of the light, and up to 12 fibres, to be observed individually. The routine to extract the data from the webcam is shown in appendix A.6. An example of the observed image is shown in figure 5.20. Rotating GT2 results in a small amount of beam walk, which makes it difficult to ensure the same fibre is always observed. So, the height of the webcam was adjusted such that the top fibres could be observed and GT2 was rotated in increments of 10 degrees, between 0° and 180°, recording an image with the webcam for each angle. The webcam height was readjusted to observe the bottom fibres and the experiment was repeated. The data was binned over each of the fibres and the intensity of each fibre output was determined (peak heights were used). An example of the variation curves for two of the fibres is shown in figure 5.21.

To give an indication of the variation of the peak intensity (height), the angle that

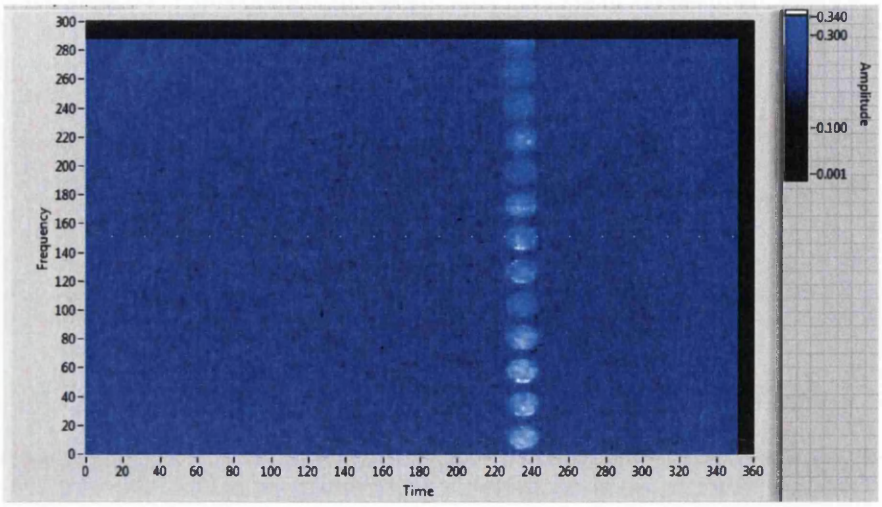

Figure 5.20: Screenshot of the observed image of the modified webcam

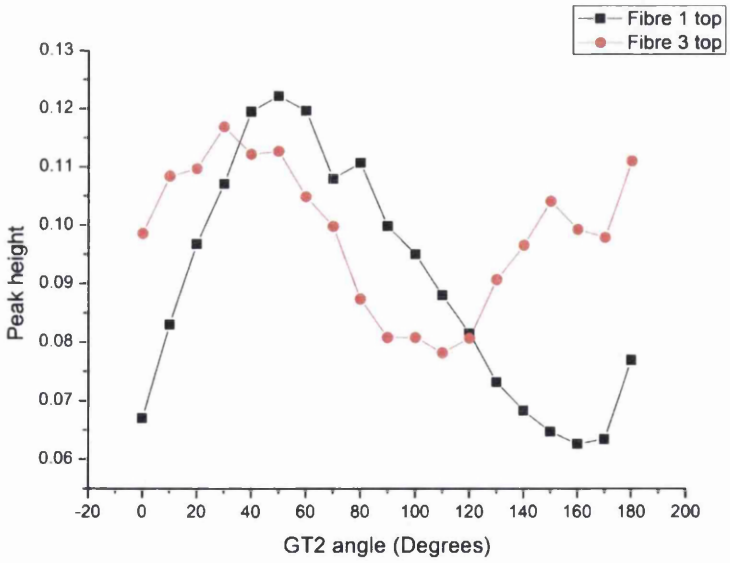

Figure 5.21: Peak height vs GT2 angle for two of the fibres near the top of the fibre bundle output slit.

the minimum intensity occurred at for each fibre was recorded. These are collated in table 5.8. As can be seen the maximum observed shift is 60°. This is not the only thing

Table 5.8: The GT2 angle of minimum intensity for each observed fibre.

Top fibre	GT2 Angle of minima (degrees)	Bottom fibre	GT2 Angle of minima (degrees)
1	160	2	160
2	110	3	130
3	100	4	120
4	120	5	100
		6	120
		7	140
		8	140

that will determine whether the polarisation is completely scrambled. Looking back at figure 5.21 shows that the polarisation preservation of each fibre also changes.

5.6.3 Conclusions

These measurements show that the polarisation preservation through each fibre in the fibre bundle is different. None of the observed fibres within the bundle completely scrambles the polarisation of the incident light. The results from section 5.6.1 show that, if the polarisation of the light incident on a fibre changes, the output polarisation changes. As the collected Raman light is a mixture of two polarisations, $I_{\perp}$ and $I_{||}$, it means that the polarisation preservation of each component is different for each fibre within the bundle. This makes it difficult to accurately measure how the intensity incident on the fibre changes when passing through the optical system.

As a result of the measurements, a linear (sheet) polariser was inserted into the standard 90° LARA collection system between the two collection lenses. The rotation angle of the polariser was set such that the transmitted light is vertically polarised. In the LARA setup in this work, this corresponds to the Raman component $I_{\perp}$. As a result of this, the polarisation beyond this point is fixed. A result of this is that changes to the polarisation caused by the optics in the collection path beyond this point will always be the same. However, this statement is only true if the fibre bundle is not moved. Therefore, the fibre bundle needs to be kept as static as possible during measurement runs. Any changes to the polarisation of the radiation incident on the sheet polariser will be observed in the detection system as a change in intensity only.

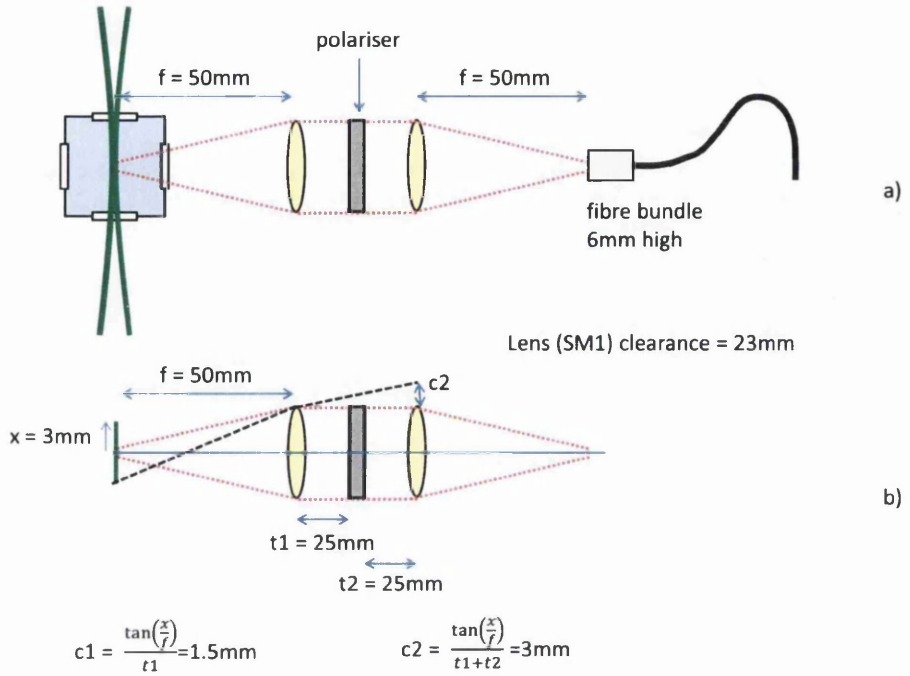

Figure 5.22: Sketch of the collection optics for Swansea's LARA system considering the solid angle for non point like sources. a) Collection optics, b)Aperture reduction for non point-like source

5.6.4 Effect of linear polariser on Raman collection angle

Inserting a sheet polariser into the collection path potentially influences the solid angle of the collection system. A sketch of the light collection optics for Swansea's LARA system is shown in figure 5.22 a).

For a point like source the collected light is completely collimated and collection angle is governed by that of the first lens. This collection path is shown in red in the figure. However, for sources of extended length the collected light has a small divergence angle, θ_d, given by [new]

$$\theta_d = \frac{x}{f} \tag{5.1}$$

where x is the height of the source from the lens centre and f is the focal length of the first lens. For a multi aperture system this results in light being lost as depicted in figure 5.22 b).

As the KATRIN LARA collection system has two additional apertures after the first collection lens, the lost light at the second aperture (c2) only needs to be calculated. As shown in the figure this is approximately equal to 3 mm. The reduced aperture size is

then $11.5 - 3 = 8.5\,\text{mm}$ which limits the angle of the collected light θ_{lim} to

$$\theta_{\text{lim}} = \tan^{-1}(\frac{8.5}{100}) \approx 4.9^{\circ} \tag{5.2}$$

This angle limit will be verified with solid angle tests relating to the depolarisation measurements in chapter 6.

Chapter 6

Depolarisation measurements of the hydrogen isotopologues

6.1 Chapter overview

In this chapter the depolarisation measurements of all six hydrogen isotopologues have been successfully completed. The corrected depolarisation ratios of the Q_1-branch agree with the theoretical values within a 1σ confidence level. This is the first time depolarisation measurements of the radioactive hydrogen isotopologues have been performed. The comparison of the depolarisation measurements of hydrogen with the literature show that the results here are more accurate than previously published data.

Depolarisation measurements of the pure rotational S_0 and vibration-rotation S_1 and O_1-branches of hydrogen have been completed and the depolarisation ratio of $\rho = 0.75$ has been successfully verified. The uncertainties in these measurements are higher, due to the signal-to-noise ratio of the measurements being much lower than for the Q_1-branches.

The work presented in this chapter, on the depolarisation measurements of the Q-branch of the hydrogen isotopologues, and the procedure to relate the measured depolarisation ratio to the theoretical values, has been published in two papers [Jam12a] and [Sch12a]. The routine developed for the correction procedure is available to download from the open source software distribution site Sourceforge [SJLb] and is fully documented [SJLa], so it can be applied when necessary.

Note than the successful method of the depolarisation measurements is not limited to the hydrogen isotopologues. It has been applied to some atmospheric gases, which will be discussed in more detail in chapter 7.

The line positions of the non-tritiated hydrogen isotopologues have been accurately measured and compared with the theoretically calculated energy levels of LeRoy and the experimental approximations of the line positions given in chapter 2. The measured

line positions of the Q-branch of D_2 are found to agree with both sets of values within the experimental uncertainty. The H_2 and HD lines have been found with an offset of $0.8\,cm^{-1}$ and $0.5\,cm^{-1}$, respectively, compared to the LeRoy values. The reason for this offset is suspected to be an inaccurate wavelength calibration. The experimental approximations of the line positions of HD given in chapter 2 are no longer valid for $J > 4$ as the offset between the values measured here increases beyond this point.

6.2 Introduction

In this chapter the aim is to experimentally verify the polarisability tensors of the hydrogen isotopologues that are calculated from *ab-initio* calculations in the literature [LRoy88]. The measurements used to do this are so called depolarisation measurements, where the depolarisation ratio, ρ, is measured. The theory behind these measurements and Raman intensities was discussed in chapter 3.

To experimentally determine this ratio, a stable excitation source, in power and wavelength, is needed, as drift would result in uncertainties in the measured values. The sources used in this work (in Swansea and TLK) are stabilised by water cooling the laser head, as described in chapter 4. The other main experimental variable is the change in the polarisation of the light beam. The accuracy and effect of this is included in the analysis and correction procedure.

In the KATRIN experiment, the intensity of the hydrogen isotopologues needs to be determined accurately, so the isotopologue composition calculated from these intensities is reliable. As described in chapter 3, the concentration is determined by fitting the measured intensities with a theoretical intensity curve. Embedded inside this theoretical curve are the polarisability tensors, which have been calculated using *ab-initio* calculations from the literature [LRoy88]. There is no indication of uncertainty in these measurements, and the theory only applies for pure single-point, zero solid angle (SP0SA) configurations. Therefore, a method to compare the measured values with the literature needed to be developed. The theory behind this extension is discussed in chapter 3. The experimental procedure and application of the correction model is discussed in this chapter.

The challenges and the measurements required to experimentally verify the depolarisation ratio are included in this chapter, along with a full discussion of the results and comparison to the values in the literature.

On top of the *ab-initio* calculations, experimental depolarisation measurements of hydrogen have been performed by Holzer *et al* [Hol73] and Yu *et al* [Yu07]. However, to the best of our knowledge no experimental verification of the tritiated values can be found in the open literature.

The early investigations into the depolarisation measurements of the non-tritiated hy-

drogen isotopologues in Swansea are included in Alshahrie [Als11]. The work described in this chapter is discussed and published in [Jam12a] and [Sch12a].

6.3 Depolarisation measurements

The concept of a depolarisation measurement was discussed in chapter 3. They are used as an experimental verification of the polarisability tensors derived in the literature, by comparing the measured depolarisation ratio, ρ_{obs}, with the one calculated using the polarisability tensors. The definition of the depolarisation ratio will be restated for clarity.

6.3.1 Depolarisation ratio

The phenomenon of depolarisation is associated with the change of the intensity of the perpendicular and parallel components of the Raman scattered irradiation by either changing the polarisation of the incident exciting radiation for a fixed intensity component, or by the change in intensity of the perpendicular and parallel components of the scattered radiation for a fixed incident exciting radiation polarisation. The ratio between the two components (in either case) is referred to as the depolarisation ratio, ρ.

In this work the depolarisation ratio is measured for a fixed scattered polarisation, $\perp^s$, and the depolarisation ratio is given as

$$\rho_{\text{obs}} = \frac{I_{\perp^s,\|^i}(\theta,\varphi)}{I_{\perp^s,\perp^i}(\theta,\varphi)} = \frac{\Phi_{\perp^s,\|^i}(\theta,\varphi)}{\Phi_{\perp^s,\perp^i}(\theta,\varphi)} \tag{6.1}$$

where I is measured Raman scattered light intensity, θ and φ are angles, which define the direction of the scattered light and Φ is the line strength function. The terms in the equation are discussed and considered in full in chapter 3.

This depolarisation ratio is the observed (measured) depolarisation ratio. This is obtained experimentally by acquiring Raman spectra when the incident laser polarisation is vertically polarised ($\perp^i$) and horizontally polarised ($\|^i$), calculating the intensity as the area underneath a Raman line and determining the ratio. The theoretical description of the intensities within this ratio is obtained using the extended source, non-zero solid angle (ESSA) approximation with the addition of optics effects (polarisation aberrations) as described in section 3.3.5.

The depolarisation ratio referred to in the literature is the same as the SP0SA approximation and this depolarisation ratio is given by

$$\rho_{\text{SP0SA}} = \frac{\Phi_{\perp^s,\|^i}(\theta=\pi/2,\varphi=0)}{\Phi_{\perp^s,\perp^i}(\theta=\pi/2,\varphi=0)} = \frac{3b^2_{Jf_0:Ji_0}|\langle v^f|\gamma|v^i\rangle|^2}{45|\langle v^f|a|v^i\rangle|^2 + 4b^2_{Jf_0:Ji_0}|\langle v^f|\gamma|v^i\rangle|^2} \tag{6.2}$$

This can be calculated from the literature values of LeRoy [LRoy88] and [Roy12].

Following the theory described in chapter 3, the full expression for the depolarisation ratio (ESSA plus optics effect) is

$$\rho_{\text{calc}} = \frac{\xi A + (1-\xi)B}{\xi B + (1-\xi)A} \tag{6.3}$$

where

$$A = \iiint_{\varphi,z,\theta} I_{\perp^s,\parallel^i}(\theta,\varphi)\sin\theta d\theta dz d\varphi \tag{6.4}$$

$$B = \iiint_{\varphi,z,\theta} I_{\perp^s,\perp^i}(\theta,\varphi)\sin\theta d\theta dz d\varphi \tag{6.5}$$

and the integrals are parameterised over the collection solid angle, as described in section 3.3.6. ρ_{calc} can be determined for any theoretically known ρ_{SP0SA} value, provided the solid angle is parameterised and the laser beam cleanness is known. The theory can also be extended to include corrections due to polarisation changes caused by optics in the collection path. For the final analysis these corrections are neglected. The measurements and discussions on why are included in section 6.4.

6.3.2 Theoretical depolarisation ratio

The theoretical (SP0SA) depolarisation ratio can be calculated using equation (6.2), as long as the polarisability tensors are known.

As stated above, calculations of the polarisability tensors have been performed in the literature using *ab-initio* calculations. In this work, we have obtained newly calculated polarisability tensors for 532 nm excitation radiation from LeRoy [Roy12]. The model he used is the updated version of the one described in Schwartz and LeRoy [LRoy88], where the calculations are done for 488 nm radiation. The polarisability tensors are included in appendix A.4.1. The depolarisation ratio is calculated using equation (6.2) and the resultant depolarisation ratios are included in table 6.7. These theoretical depolarisation ratios will be compared with the measured values in section 6.7.

6.4 Effects influencing polarisation

As discussed in chapter 3, the correction procedure depends on how clean the polarisation of the incident laser beam is. In terms of the laser beam, we have defined this parameter as the beam cleanness $\xi = \cos^2\alpha$ where α is the angular deviation from the vertical polarisation direction. This beam cleanness can have a significant influence on the measured depolarisation ratio. This was demonstrated in the early depolarisation measurements included in Alshahrie [Als11], where stress induced birefringence in one

of the cell windows leads to a large increase in the measured depolarisation ratio. These measurements will be briefly referred to again in section 6.6 for clarity.

To maximise the beam cleanness, investigations into the effect that optics in the beam path have on the polarisation of the light beam have been performed. The components' locations have been optimised to ensure that the beam cleanness is as high as possible.

An experimental procedure to determine the cleanness and polarisation effects of optics is required. The polarisation tests on the main components in the beam path will be discussed individually.

Note that the test measurements discussed were only performed using the LARA system in Swansea.

6.4.1 Experimental procedure

The experimental procedure to verify the effect of polarisation involves using a combination of a Glan-Taylor polariser and a photodiode to measure the polarisation of the incident light beam. The polariser is rotated and the power that is passed through it is recorded. If the light is polarised, this leads to a sinusoidal curve. The cleanness is then determined as the ratio of the maximum and minimum of this sinusoidal curve by either taking the nearest reading to the maximum and minimum or fitting the data with a $\sin^2$ curve of the form

$$y = y_0 + A(\sin^2(\pi(x - x_c)/w)) \tag{6.6}$$

where y_0, A, x_c and w are the fit parameters. The cleanness ξ is then

$$\xi = 1 - \frac{y_0}{y_0 + A} \tag{6.7}$$

For highly polarised light, the most accurate method of determining the cleanness was found by rotating the polariser in small steps around the maximum and minimum.

The experimental setup is shown in figure 6.1. The optics placed in front of the Glan-Taylor polariser can be altered so that the effect the optic has on the beam cleanness can be determined.

6.4.2 Glan-Taylor polariser

In the LARA setup, a Glan-Taylor polariser is used to ensure that the polarisation of the incident beam is as clean as possible as is shown in chapter 4. This is a starting point to measure the cleanness of the laser beam and this will be taken as the highest cleanness possible in the given system. The measurement setup was as shown in figure 6.1, with no optic present at the "analysis optic location" (AOL). The measurement procedure described above was followed and the maximum and minimum of the sinusoidal curve

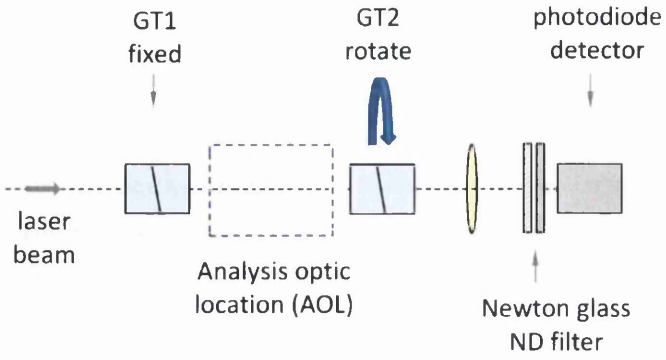

Figure 6.1: Experimental setup for polarisation tests. The optics that have been inserted at the analysis location are: none, half-wave plate, window, plano-convex lens or a combination of these. The number of neutral density filters in the stack is selected to prevent the photodiode from saturating.

were determined. This resulted in a beam cleanness of $\xi = 0.99995(3)$.

The test was repeated with GT1 moved to a position in front of the laser output. This meant that the polarised light was reflected off 5 mirrors before the polarisation was analysed. This resulted in a cleanness of $\xi = 0.99713(10)$. This is much worse than when the Glan-Taylor polariser is immediately in front of the analysis system and would noticeably affect the depolarisation measurements. This means that the Glan-Taylor polariser needs to be installed in front of the half-wave plate in the LARA setup to maximise the beam cleanness.

A beam cleanness of $\xi = 0.99995(3)$ proved to be the maximum cleanness measurable. The effect other optics between the Glan-Taylor polariser and the cell have on the beam cleanness will now be determined.

6.4.3 Half-wave plate

The first optical component in the setup after the Glan-Taylor polariser is the half-wave plate. As this optic is inserted into the path by hand there is a possibility that it could be tilted. Therefore, the polarisation cleanness determination described above was tested for multiple tilt positions of the wave plate at the AOL position in figure 6.1. This was repeated, where the wave plate rotation angle was set so that horizontally polarised light and vertically polarised light were generated, as would be the case in the depolarisation measurements. The tilt was adjusted about the perpendicular position in steps of 4°. Graphs of $1 - \xi$ vs the tilt angle were produced for both polarisations and are shown in figures 6.2 and 6.3.

The figures show that, as the wave plate is tilted, the beam cleanness becomes worse. For example, when the tilt is as high as 16° (away from the minimum) the cleanness has reduced to $\xi = 0.99041(13)$ for the vertically polarised case. The cleanness may

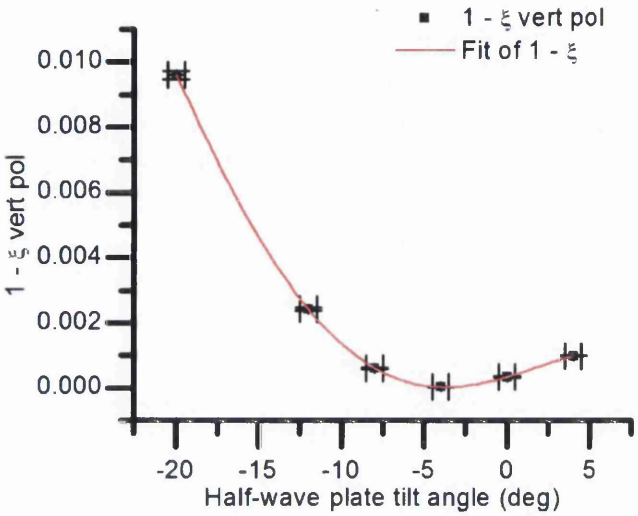

Figure 6.2: $(1 - \xi)$ vs half-wave plate tilt. The half-wave plate is rotated so that the emerging polarisation is vertically polarised.

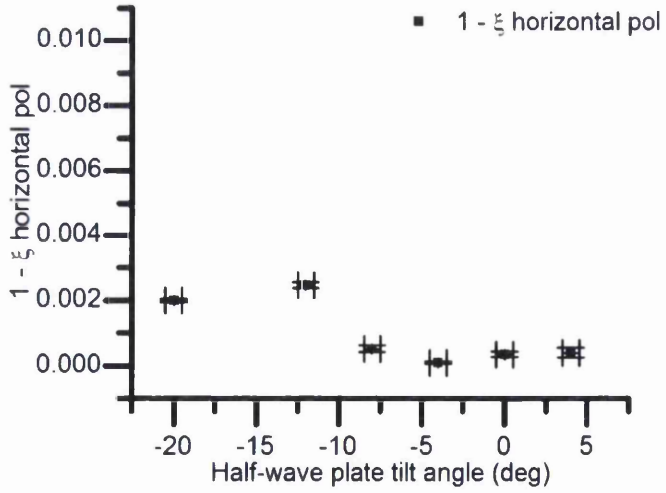

Figure 6.3: $(1 - \xi)$ vs half-wave plate tilt. The half-wave plate is rotated so that the emerging polarisation is horizontally polarised.

still appear to be very high, but even this small reduction, of approximately 1%, is sufficiently large that it would have an influence on the measured depolarisation ratio, as is demonstrated in section 6.6. The reduction in beam cleanness with tilt, when the emitted light is horizontally polarised, is less severe. However, an effect is still observed.

Overall, as long as the half-wave plate is aligned so that it is as close as possible to perpendicular to the laser beam direction, the cleanness remains high for both of the $\perp$ and $\parallel$ polarisations. The cleanness after passing through the half-wave plate, when it is optimally aligned, was found to be $\xi = 0.99996(1)$. This is approximately the same as the cleanness after only passing through the Glan-Taylor polariser.

6.4.4 Raman cell laser windows

As the hydrogen isotopologues are harmful (especially tritium), the leak tightness on the cells is important and the minimum leak rate requirements are stringent. This means that O-ring sealing is not used in the cell, as the leak tightness is not sufficiently high. Glass-metal components alongside metal compression seals are utilised. This type of sealing of the cell induces non-negligible stress in the windows. This induced stress can cause birefringence ([Shr02] and [Log94]), which has a potentially large effect on the polarisation of light passing through it.

The windows in the cell have different anti reflection coatings on them, depending on whether they are for the laser transmission or the scattered light transmission, as is shown in chapter 4. The coatings may have an influence on the polarisation. In this section, the laser window cleanness will be measured, as it only involves one beam passing through the optic in a small cross section. For the collection windows determining the effect is more complicated, as the entire window would have to be mapped at multiple angles to produce a 2-dimensional cleanness plot, with respect to the angle of incidence of the light beam.

To try and verify the amount of stress in the laser windows, the polarisation cleanness determination, described above, has been performed with a spare laser window at the AOL position. The actual cell windows in use could not be used individually as they are fixed in location on the cell. The cleanness can, however, be measured for both laser windows combined. This has been checked, along with separate measurements using the spare cell windows.

The Raman cell was placed at the AOL position and the polarisation determination measurement procedure was followed. In one of the test measurements the cleanness was found to be $\xi = 0.9424(5)$. This was drastically lower than expected. The reason behind this was determined by viewing one of the laser windows. The window surface had some dirt/small damage on it. This had a major effect on the polarisation of the beam. The other window appeared to be clean on visual inspection. It is assumed that the decrease in cleanness was caused by the second cell window. This will be verified in the

depolarisation measurements in section 6.6, by comparing the measured depolarisation ratio with 1 and 2 passes of the beam through the system.

The spare cell windows were placed in the beam path at the AOL position. To try and make the situation as similar to the real measurement as possible, the half-wave plate, at its optimum tilt, was placed in front of the windows. The measurement procedure, described above, was followed twice, once with the window and half-wave plate at the AOL position and once with the half-wave plate only at the AOL position, so the change in cleanness could be more easily determined. This measurement was repeated with the window repositioned. The cleanness, when the laser window was inserted into the beam path was found to be $\xi = 0.99481(1)$ and $\xi = 0.98986(1)$; when the laser window was removed, the cleanness was measured as $\xi = 0.99879(1)$ and $\xi = 0.99988(1)$.

This shows that the window does indeed reduce the cleanness. However, these numbers cannot be taken as the real values to be used for the depolarisation measurements as they are not the same windows as in the cell(s). When the windows are secured to the cell, there is a chance that the stress acting on the optic could change because of the tightening procedure. A method is required to determine the cleanness of the beam from within the cell. This method is proposed and implemented in the analysis of the depolarisation measurements in sections 6.5 and 6.7.

The laser windows potentially have the largest effect on the cleanness of the laser beams polarisation. However, if the windows are not damaged the cleanness can still be as high as $\xi = 0.99$. This method cannot be used to determine the cleanness of the individual laser windows when they are mounted on the cell. Another method to obtain these values is implemented in the analysis of the depolarisation measurements in section 6.7.

6.4.5 Raman collection windows

To determine the cleanness of the collection window is more complicated as the scattered light is divergent and passes through the window at multiple angles. The light then also strikes a collection lens at multiple angles before it is re-collimated and the polarisation is analysed by the sheet polariser. The same method as described above can be applied to determine the cleanness. However, multiple tilt angles of the window and collection lens need to be taken into account.

In this work, complete tilt measurements have not been performed. Proof of principle tests at a few tilt angles have been performed to give an indication of the potential reduction in cleanness caused by the collection window. A spare Raman collection window was placed in the beam path at the AOL position. The polarisation determination measurement procedure was followed at 3 different tilt angles (0°, −5° and +5°). The cleanness was also measured when the window was removed for comparison. The resultant cleanness values were $-5° : \xi = 0.99495(4)$, $0° : \xi = 0.99451(5)$, $+5° : \xi = 0.99406(1)$ and

no window $\xi = 0.99911(2)$. These measurements show that the collection window does have a major effect on the cleanness of the beam passing through it, and the measured value changes with angle of incidence.

A second method to verify the stress in the collection windows has been applied in KIT, using perpendicular polarisers and a microscope ([Sch13]). The Raman collection window was placed between two "crossed" polarisers, i.e. one rotated so it transmits vertically polarised light and one rotated so it transmits horizontally polarised light. If the window did nothing to the polarisation of the light the resultant image on the microscope would be one colour. An example of one of the measured images is shown in figure 6.4. The image shows that the polarisation of the light passing through the

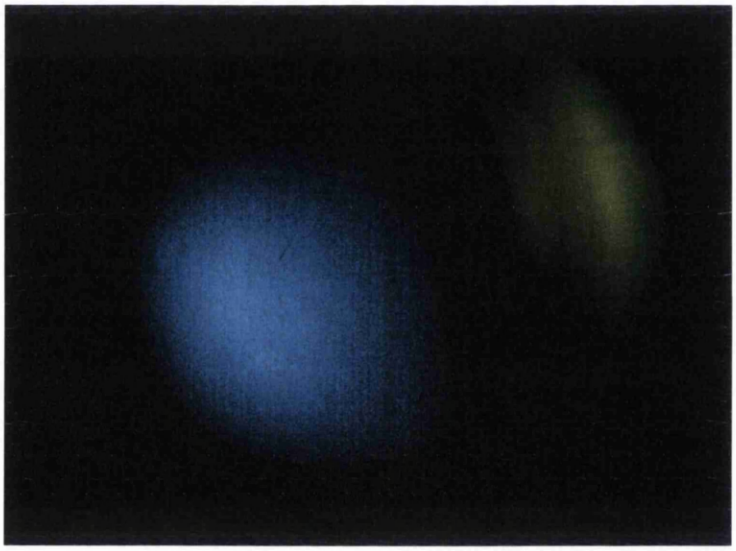

Figure 6.4: Microscope image of Raman collection window placed between two "crossed" polarisers. The false-colour change corresponds to intensity of the light. From Schlösser [Sch13]

window is no longer uniform. It gives an indication of the stress across the window. These measurements were performed several times for different cell windows in [Sch13] to demonstrate that the effect changes if the window changes.

Transmission of light through optical components can be considered theoretically using Jones or Müller calculus ([Kit09], [McG94], [Ini03] and [Col05]). This has been considered as a possible method to take into account the polarisation effects in the collection optics. This will be discussed in the next section

6.4.6 Jones and Müller calculus

Jones and Müller calculus can both be used to quantify the effect that optics have on the polarisation and intensity of light. The difference being that Jones calculus deals with light in terms of electric field vectors, whereas Müller calculus treats light in its intensity form. Both methods lead to the same results and will be summarised here.

Jones calculus

When considering the collection system of the LARA system in this work (see figure 6.6) the optics consist of a sample cell window, collection lens and a sheet polariser. Using Jones calculus 2×2 Jones matrices, $\mathcal{J}$, are used to obtain the relationship between the incident and transmitted light beams (for more details see Hecht [Hec02] or Kita [Kit09])

$$\vec{E}_{\text{out}}(\theta, \varphi) = \mathcal{J}_P \mathcal{J}_{A1} \mathcal{J}_{A2} \cdot \vec{E}_{\text{in}}(\theta, \varphi). \tag{6.8}$$

where $\mathcal{J}_P$ is the Jones matrix for the sheet polariser, $\mathcal{J}_{A1}$ is the Jones matrix for the collection lens (aperture 1) and $\mathcal{J}_{A2}$ is the Jones matrix for the cell window (aperture 2). The following assumptions need to apply for this equation to be valid, namely:

- the whole collection system can be described as exhibiting a (homogeneous) net effect on the polarisation (mainly linear di-attenuation and linear retardance);
- the polarisation aberrations have (nearly) no angular dependence; and
- circular di-attenuation and retardance are negligible, as indicated by Kita [Kit09].

Using the assumption that we are only concerned about an angular-independent net effect from the collection system, then equation (6.8) can be simplified by using a new Jones matrix, $\mathcal{J}_C$, which defines the net effect of the collection system

$$\vec{E}_{\text{out}}(\theta, \varphi) = \mathcal{J}_P \mathcal{J}_C \cdot \vec{E}_{\text{in}}(\theta, \varphi). \tag{6.9}$$

The vector $\vec{E}_{\text{in}}$ defines the effective polarisation state of integrated Raman light generated in the scattering region.

$$\vec{E}_{\text{in}} = \begin{pmatrix} E_{||^s,p^i} e^{i\phi_{||}} \\ E_{\perp^s,p^i} e^{i\phi_{\perp}} \end{pmatrix} \tag{6.10}$$

with $\phi_{||}$ and $\phi_{\perp}$ being the initial phase shifts of the perpendicular and parallel components of the scattered radiation. The Jones matrix of the polariser aligned to transmit

Table 6.1: Physical significance of Pauli coefficients $\mathbf{a_k}$. Table adapted from McGuire and Chipman [McG94].

Coeff.	Physical sign. of $\Re(a_k) = a_{Pk}$	Physical sign. of $\Im(a_k) = a_{Rk}$
a_0	Pol.-indep. amplitude	Pol.-indep. phase
a_1	Lin. diattenuation along coord. axes	Lin. retardance along coord. axes
a_2	Lin. diattenuation at 45° to the coord. axes	Lin. retardance 45° to the coord. axes
a_3	Circ. diattenuation	Circ. retardance

vertically polarised ($\perp^i$) light is given as [Hec02]

$$\mathcal{J}_P = \begin{pmatrix} 0 & 0 \\ 0 & 1 \end{pmatrix} \tag{6.11}$$

The only unknown part is the Jones matrix of the collection system. It is convenient to write the Jones matrix in the exponential form $\mathcal{J} = \exp \mathcal{V}$. $\mathcal{V}$ is a matrix exponential expression that characterises the Jones matrix [Kit09]. This matrix can be expressed by Pauli expansion (σ_i are the Pauli matrices) as

$$\mathcal{V} = \sum_{k=0}^{3} a_k \sigma_k \tag{6.12}$$

Thus the Jones matrix of the collection system can be written as

$$\mathcal{J}_C = \exp\left(a_0\sigma_0 + a_1\sigma_1 + a_2\sigma_2 + a_3\sigma_3\right) \tag{6.13}$$

where the Pauli coefficients, a_k, are given as $a_k = a_{Pk} + i a_{Rk}$ (see table 6.1). As mentioned above, the assumption is made that no circular polarisation effects occur and thus $a_3 \approx 0 + i0$.

Therefore, the matrix $\mathcal{J}_C$ becomes

$$\mathcal{J}_C = \exp\begin{pmatrix} (a_{P0} + a_{P1}) + i\,(a_{R0} + a_{R1}) & a_{P2} + i a_{R2} \\ a_{P2} + i a_{R2} & (a_{P0} - a_{P1}) + i\,(a_{R0} - a_{R1}) \end{pmatrix} \tag{6.14}$$

A homogeneous amplitude aberration $a_{P0} \neq 0$ would only alter the amplitude equally. In the depolarisation measurements, this would cancel out if the depolarisation ratio is calculated (as $\rho = I_{\parallel^i}/I_{\perp^i}$). Therefore, this constant can be set to $a_{P0} = 0$.

with this equation (6.9) becomes

$$\vec{E}_{\text{out}}(\theta,\phi) = \begin{pmatrix} 0 \\ E_{||^s,p^i} e^{a_{P2}} e^{i(a_{R2}+\phi_{||^s})} + E_{\perp^s,p^i} e^{-a_{P1}} e^{i(a_{R0}-a_{R2}+\phi_{\perp^s})} \end{pmatrix} \tag{6.15}$$

This last equation allows one to calculate the observed intensity $I = |\vec{E}_{\text{out}}|^2$. In the following, the parameters a_{R0}, a_{R1} and a_{R2} have been collated in a total parameter $a_{R,\text{tot}}$ and it is assumed there is no initial phase difference between both polarisations ($\phi_{||^s} - \phi_{\perp^i} = 0$) of the initial beam. Thus, the resulting term for the intensity with incident polarisation p^i is

$$\begin{aligned} I_{\perp^s,p^i} = & \underbrace{E^2_{\perp^s,p^i} \exp(-2a_{P1})}_{\text{transmitted } \perp^s\text{-component}} + \underbrace{E^2_{||^s,p^i} \exp(2a_{P2})}_{\text{leakage from } ||^s\text{-component}} \\ & + \underbrace{2E_{\perp^s,p^i} E_{||^s,p^i} \exp(a_{P2} - a_{P1}) \cos(a_{R,\text{tot}})}_{\text{contamination induced by retardance}} \end{aligned} \tag{6.16}$$

Thus, the intensity term has been reduced to a three parameter representation, which describe linear diattenuation (a_{P1}, a_{P2}) and the retardance from stress birefringence ($a_{R,\text{tot}}$).

Müller calculus

The same formula which has been derived using Jones calculus (equation (6.16)) can be obtained by using Müller calculus (see Toro Inesta [Ini03] or Collett [Col05]). Both derivations (Jones and Müller) are shown here to demonstrate that both theoretical methods can be used to determine the same result.

The optical system is the same as in equation (6.8). The relationship between the incident and transmitted beams passing through the LARA collection system is

$$\vec{S}_{\text{out}} = M_P M_C \vec{S}_{\text{in}} \tag{6.17}$$

where M_P is the Müller matrix for the polariser and M_C is the Müller matrix for the collection system.

The vector $\vec{S}$ defines the polarisation state in intensity form and is given as

$$S = \begin{pmatrix} I \\ Q \\ U \\ V \end{pmatrix} = \begin{pmatrix} E^2_{||^s,p^i} + E^2_{\perp^s,p^i} \\ E^2_{||^s,p^i} - E^2_{\perp^s,p^i} \\ 2E_{||^s,p^i} E_{\perp^s,p^i} \cos\Delta \\ 2E_{||^s,p^i} E_{\perp^s,p^i} \sin\Delta \end{pmatrix} \tag{6.18}$$

where I is the total intensity, $Q = I_0 - I_{90}$, $U = I_{+45} - I_{-45}$, $V = I_{Rcp} - I_{Lcp}$ (Rcp is

right circular polarised and Lcp is left circular polarised) and the electric field vector of a completely polarised system is defined as

$$\vec{E} = E_{||^s,p^i} \sin(\omega t + \phi_{||^s,p^i})\hat{i} + E_{\perp^s,p^i} \sin(\omega t + \phi_{\perp^s,p^i})\hat{j} \tag{6.19}$$

and $\Delta = \phi_{\perp^s,p^i} - \phi_{||^s,p^i}$.
The Müller matrix of the vertical polariser in the collection path is given by [Ini03]

$$M_P = \frac{1}{2}\begin{pmatrix} 1 & -1 & 0 & 0 \\ -1 & 1 & 0 & 0 \\ 0 & 0 & 0 & 0 \\ 0 & 0 & 0 & 0 \end{pmatrix} \tag{6.20}$$

After substituting this into equation (6.17), along with the standard 4×4 Müller matrix with notations w_{ij} for M_C, the intensity, $I_{\perp^s,p^i}$, can be extracted. This is the first entry of the resulting $\vec{S}_{\text{out}}$ vector.

$$\begin{aligned} I_{\perp^s,p^i} =& \frac{1}{2}\Big(w_1(E^2_{||^s,p^i} + E^2_{\perp^s,p^i}) + w_2(E^2_{||^s,p^i} - E^2_{\perp^s,p^i}) + \\ & w_3(2E_{||^s,p^i}E_{\perp^s,p^i}\cos\Delta) + w_4(2E_{||^s,p^i}E_{\perp^s,p^i}\sin\Delta)\Big) \end{aligned} \tag{6.21}$$

where $w_1 = w_{11} - w_{21}$, $w_2 = w_{12} - w_{22}$, $w_3 = w_{13} - w_{23}$ and $w_4 = w_{14} - w_{24}$. Equation (6.21) simplifies to

$$\begin{aligned} I_{\perp^s,p^i} =& \frac{1}{2}\Big((w_1 + w_2)E^2_{||^s,p^i} + (w_1 - w_2)E^2_{\perp^s,p^i} + \\ & 2w_3E_{||^s,p^i}E_{\perp^s,p^i}\cos\Delta + 2w_4E_{||^s,p^i}E_{\perp^s,p^i}\sin\Delta\Big) \end{aligned} \tag{6.22}$$

This can now be converted to the final formula of the Jones calculus (cf. equation (6.16))

$$\begin{aligned} I_{\perp^s,p^i} = & \underbrace{E^2_{\perp^s,p^i}\exp(-2a_{P1})}_{\text{transmitted } \perp^s\text{-component}} + \underbrace{E^2_{||^s,p^i}\exp(2a_{P2})}_{\text{leakage from } ||^s\text{-component}} \\ & + \underbrace{2E_{\perp^s,p^i}E_{||^s,p^i}\exp(a_{P2} - a_{P1})\cos(a_{R,\text{tot}})}_{\text{contamination induced by retardance}}, \end{aligned} \tag{6.23}$$

where the following parameters are defined as

$$e^{-2a_{P1}} = \frac{1}{2}(w_1 - w_2) \tag{6.24}$$

$$e^{2a_{P2}} = \frac{1}{2}(w_1 + w_2) \tag{6.25}$$

$$e^{a_{P2}-a_{P1}} = \frac{1}{2}\sqrt{w_3^2 + w_4^2} \tag{6.26}$$

$$a_R, tot = \Delta - \tan^{-1}(w_4/w_3) \tag{6.27}$$

This equation can be used to describe the scattered intensity. To enable it to be implemented in the discussion on the correction procedure of the depolarisation measurements in section 6.4.7 the depolarisation ratio can be calculated from this equation as

$$\rho = \frac{I_{\perp^s,\parallel^i}}{I_{\perp^s,\perp^i}} \tag{6.28}$$

$$= \frac{X^2_{\perp^s,\parallel^i} + Y^2_{\parallel^s,\parallel^i} + 2X_{\perp^s,\parallel^i}Y_{\parallel^s,\parallel^i}\cos(a_{R,\text{tot}})}{X^2_{\perp^s,\perp^i} + Y^2_{\parallel^s,\perp^i} + 2X_{\perp^s,\perp^i}Y_{\parallel^s,\perp^i}\cos(a_{R,\text{tot}})} \tag{6.29}$$

with

$$X_{\perp^s,p^i} = E_{\perp^s,p^i}e^{-a_{P1}}$$
$$Y_{\parallel^s,p^i} = E_{\parallel^s,p^i}e^{a_{P2}}$$
$$X_{\perp^s,p^i}Y_{\parallel^s,p^i} = E_{\perp^s,p^i}E_{\parallel^s,p^i}e^{a_{P2}-a_{P1}}$$

The other possibility would be a full characterisation of the optical system from which these coefficients can be determined. The method behind this would be similar to that described by Logan *et al* [Log94].

6.4.7 Correcting for polarisation aberration effects

As already demonstrated above, the optical components in the laser beam and scattered light path have an effect on the polarisation of the radiation. Using the described formulae, these effects can be taken into account using equation (6.16) and the solid angle integration described in chapter 3. The procedure that has been used for the calculations of geometrical influence is described in section 6.7.4, where ξ is input by the user, rather than determined from a measured depolarisation ratio. Using these two approaches, it is possible to estimate the influence polarisation aberrations have on the depolarisation ratio. Four different polarisation scenarios are considered

1. Only the geometrical influence is considered, i.e. no polarisation aberrations are included meaning the cleanness of the laser beam is set to $\xi = 1$.

2. The geometrical influence and the reduced polarisation cleanness of the laser beam are considered i.e. $\xi \neq 1$. However, aberrations in the collection optics are not included.

3. Observing equation (6.16) shows that the cleanness of the scattered light can be reduced by leakage of polarisation and/or retardance. Both effects can be investigated individually by splitting the light intensities into two mutually perpendicular components. Simplifying the equation reduces the complexity and allows one to

identify any dominating mechanism. Two scenarios are considered where each equation is a simplified form of equation (6.29).

(a) In the first scenario, the induced retardance is neglected so that any polarisation shifts are introduced by different attenuation losses in the polarisation components. This would be the case if the related reflection losses of the optic had a strong dependence on the angle on incidence. Equation (6.29) can then be rewritten as

$$\rho_A = \frac{c_{A,\perp^s} E^2_{\perp^s,\|^i} + c_{A,\|^s} E^2_{\|^s,\|^i}}{c_{A,\perp^s} E^2_{\perp^s,\perp^i} + c_{A,\|^s} E^2_{\|^s,\perp^i}} \tag{6.30}$$

(b) In the second scenario, the leakage term is neglected and only polarisation changes introduced by retardance in an optical material (i.e. stress induced birefringence) are considered. In this case equation (6.29) can then be rewritten as

$$\rho_B = \frac{c_{B,\perp^s} E^2_{\perp^s,\|^i} + c_{B,\|^s} E_{\|^s,\|^i} E_{\perp^s,\|^i}}{c_{B,\perp^s} E^2_{\perp^s,\perp^i} + c_{B,\|^s} E_{\|^s,\perp^i} E_{\perp^s,\perp^i}} \tag{6.31}$$

In both scenarios the polarisation cleanness of the incident beam is assumed to be perfect $\xi = 1$. The c-parameters for the two scenarios are defined as

$$\begin{aligned} c_{A,\perp^s} &= c_{B,\perp^s} = e^{-2a_{P1}} \\ c_{A,\|^s} &= e^{2a_{P1}} \\ c_{B,\|^s} &= 2e^{a_{P2}-a_{P1}} \cos(a_{R,\text{tot}}) \end{aligned}$$

with the restriction that $0 \leq c \leq 1$.

To study the influence of polarisation impurity in the four scenarios a single parameter in each has to be changed. In the second scenario, the cleanness ξ is changed and in the third and fourth scenarios the ratio between $c_\perp$ and $c_\|$ is changed. The dependence of the calculated depolarisation ratio with respect to the collection solid angle related to the four scenarios is shown in figure 6.5 for $\rho_{SP0SA} = 0$. For the second scenario only small impurities are considered ($\xi = 0.999$ and $\xi = 0.998$) while for the third and fourth scenarios the parameter ratio of $c_\perp$ and $c_\|$ is $0.9 : 1$ is quite extreme and can be considered as a "worst-case" scenario. The following observations can be made from the figure.

- A large contribution to the deviations between the theoretical and measured depolarisation ratios stems from polarisation impurities in the excitation laser beam. Even minute admixtures of the unwanted polarisation leads to offsets substantially larger than the experimental uncertainty (typically $\Delta\rho \approx \pm 5 \times 10^{-4}$).

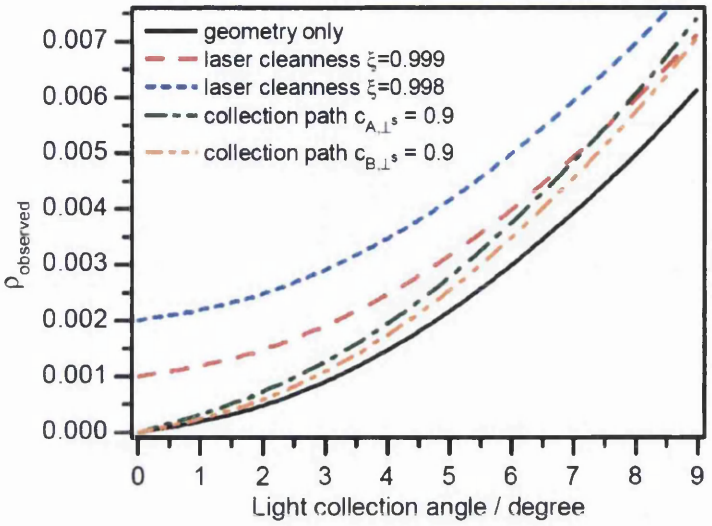

Figure 6.5: Influence of the polarisation aberrations in the laser excitation (polarisation cleanness ξ) and the light observation paths (admixtures $c_{A,\perp^s}$ and $c_{B,\perp^s}$) on the calculated depolarisation ratio. In this plot $\rho_{SP0SA} = 0$.

- With small collection angles that are smaller than is practicably achievable in many measurement setups, the deviation between theoretical and measured depolarisation ratios is noticeable and quickly surpasses the measurement uncertainty as the solid angle increases.

- For small collection angles of less than 5° the influence of the deterioration caused by the collection optics is small. Even in this case, where a "worst-case" scenario has been assumed, the unwanted contamination only reaches 10%. However, if the collection angle exceeds 10° the effect becomes non-negligible.

- The two scenarios that account for the polarisation aberrations in the collection path exhibit similar behaviour, so neither can be regarded as the dominant mechanism.

As a result of these discussions, the contributions that affect the depolarisation ratio originate from the geometry and polarisation impurities in the incident laser beam particularly for small collection angles, which is the case here, as will be shown in section 6.5.4. Therefore, polarisation aberrations caused by the optical components in the collection path will be neglected from the analysis of depolarisation measurements. The only cleanness parameter which will be included is ξ, the cleanness in the incident excitation radiation.

6.5 Experimental setup for depolarisation measurements

The measurement procedure to obtain the depolarisation ratio is important as it can have fairly large effects on the accuracy of the observed and corrected values. In this section the experimental configuration will be discussed, specifically highlighting the changes from the normal Raman setup, described in chapter 4 that are required and stating the selected measurement parameters.

6.5.1 Experimental configuration

The setups used for the depolarisation measurements of the hydrogen isotopologues are, by and large, identical to the setups used in the normal analytical Raman measurements at Swansea and the Tritium Laboratory Karlsruhe (TLK) at KIT, as described in chapter 4. Only a few minor modifications have been introduced to allow for (i) controlled changes in the polarisation orientation of the excitation laser and (ii) higher spectral resolution to resolve all Q_1(J)-branch lines. A schematic summary of the measurement setups is shown in figure 6.6.

6.5.2 Changes specific to depolarisation measurements

In the depolarisation measurements of the Q_1-branch of the hydrogen isotopologues the *Acton* SP500i spectrometer (see chapter 4) had its highest resolution grating selected (2400gr/mm), so the depolarisation ratio for the individual lines for each J value, within the Q_1-branch, could be determined.

The polarisation orientation of the Raman excitation laser could be set (arbitrarily) by using a combination of a Glan-Taylor polariser and a precision (multi-order) half-wave plate, which provides a combined, initial polarisation cleanness of the order 1.5×10^{-4} as is verified in section 6.4. The polarisation direction can be adjusted to any angular orientation, using a motorised rotational assembly (*Thorlabs* PRM1/MZ8 plus TDC001), with an overall precision and repeatability of better than 0.2°. The positioning of these polarising components is selected to (i) guarantee highest maintenance of the polarisation and at the same time to (ii) minimise any beam walk which may occur during polarisation rotation; thus the half-wave plate was placed after the Glan-Taylor polariser. The measurements showing how the polarisation maintenance changed and was optimised are in section 6.4. The laser radiation is focussed into the Raman cell by an AR-coated plano-convex lens with f = 250 mm. To obtain the accurate polarisation required to measure an accurate depolarisation ratio, the half-wave plate is calibrated to find the maximum (vertical) and minimum (horizontal) polarisation angles. The procedure and measurements behind this are described in section 6.7.1.

As mentioned in chapter 3, an additional aperture (diaphragm) is inserted between the Raman cell and the collection lens, L2. This was done to enable the solid angle to

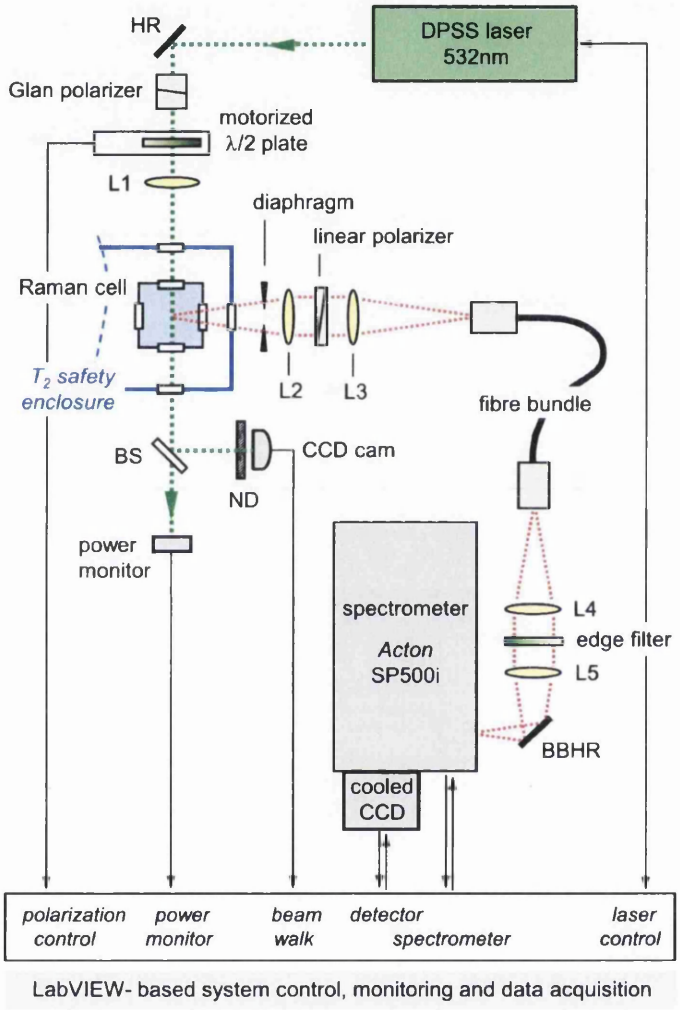

Figure 6.6: Conceptual setup for Raman depolarisation measurements of hydrogen isotopologues. HR = high reflector; L1 L5 = plano-convex lenses; BS = beam sampler; ND = neutral density filter; BBHR broad-band high reflector. For further details, see text.

be limited by the diaphragm and so it could be easily be calculated. The measurements to determine the required size of this aperture are included in section 6.5.4. The reasons behind introducing a sheet polariser into the setup have been explained in chapter 5. The polarisation setting of this optic was aligned so that vertically-linearly-polarised light passes through it. In the Raman notation this corresponds to a collected polarisation of $\perp^s$. This is why the depolarisation ratio equations stated in section 6.3.1 are limited to only include this scattered polarisation component.

It needs to be ensured that during a depolarisation measurement run the laser power and wavelength remain stable. The reason behind this is, that to obtain the required high signal-to-noise ratio, for the branches that depolarise, the measurement time is fairly large (up to 1000 s for the measurements in Swansea). With the stabilisation measurements shown in chapter 5, the laser power drift is minimised. However, over a working day it is still noticeable.

Since the precision of the Raman measurement data (which is directly proportional to the laser excitation power) of the order of a few 10^{-4} was desired, the laser power needed to be monitored with a similar precision. For this, a *Thorlabs* power meter (S302C/PM100A with 16-bit resolution) was used; as an alternative with faster response times a photodiode sensor with suitable attenuators was used.

Equally, any misalignment of the excitation volume with respect to the imaging optics impacts on the collected Raman light intensity; in our setup this meant that the pointing stability of the laser needed to be kept within the order of ± 2 mm. The actual laser beam position was monitored at regular intervals by a modified CCD webcam (lens removed, with suitable neutral-density filter attenuation); the positioning measurement precision was about 1 μm. The restrictions on laser wavelength and power apply if the analysis method involves averaging/comparing non-consecutive measurements. This is the case in the "partial-average" method. However, in the "pairs" analysis method the power stability needs to remain stable for at least 4× the exposure time. The "pairs" method involves averaging consecutive spectra only and the "partial-average" method involves averaging approximately 80% of all data multiple times. The "pairs" and "partial-average" analysis methods will be described in more detail in section 6.7.2.

6.5.3 Measurement parameters

The measurement parameters in both TLK and Swansea are collated in table 6.2. The main considerations when acquiring the spectra to calculate the depolarisation ratios are

- exposure times,
- binning,

Table 6.2: Settings and parameters for the depolarisation measurements of the hydrogen isotopologues. For more details see text.

Parameter	Units	at Swansea	at TLK
Laser (532 nm) power	W	2.1 (±0.15% drift over 8 h)	5.0 (±0.10% drift over 8 h)
Laser wavelength drift (over 8 h)	cm^{-1}	0.5 - 1.5	0.3 - 0.8
Laser focussing lens, $f =$	mm	250	250
Light collection lenses, $f =$	mm	50	75
Distance scattering volume to diaphragm	mm	38 (±1)	69(±1)
Diaphragm opening, $r =$	mm	3 (±0.25)	5 (±0.5)
Spectral Raman resolution with 2400 gr/mm grating (FWHM)	cm^{-1}	2.3 (±0.2)	1.8 (±0.2)
Binning areas on CCD chip		3	5
Acquisition order		repetitive 2×max / 2×min	repetitive 2×max / 2×min

- stepping of polarisation direction over 180° range to determine the minimum and maximum angles (only needs to be done once),
- and Min-Max measurements.

These will be considered individually.

Exposure time The detector exposure times were chosen for each measurement to maximise the intensity of the $\perp^i$-polarisation (maximum, vertical polarisation) Raman signal. This was achieved by viewing the most intense spectral region and adjusting the acquisition time until the maximum intensity was approximately 55000 counts. This is close to, but not exceeding, the 65535 count limit of 16 bit detectors.

Binning As in all measurements in this work, the binning method is on-chip binning as described in chapter 5. The detector chip was split into 3 or 5 areas and binned internally by the detector. These values were selected to maximise the signal-to-noise ratio whilst enabling astigmatism correction to be performed. For more information see [Jam13].

Determining $\perp^i$- and $\parallel^i$-polarisation To determine the depolarisation ratio, the input laser beam needs to be set to the $\perp^i$- and $\parallel^i$- laser polarisations and spectra need to be taken. These correspond to the maximum and minimum intensity of the Q-branch respectively. As has been mentioned above, a half-wave plate mounted in an

automated rotation stage is used to select the polarisation of the laser beam. In each setup, this mount was rotated between 0 and 180° in 2° steps, where two spectra were taken for each angle. Plotting the Raman signal vs. the rotation angle enables one to determine the angles required for the maximum and minimum intensity. To determine the minimum and maximum angles more accurately, the measurement is repeated where the angle is stepped over in steps of 0.1° around the minimum and maximum. These measurements only have to be performed once at each location, as these rotation angles of the half-wave plate can now be used directly once they are determined.

The diaphragm opening angles are set to ensure the exact solid angle is known i.e. the aperture is limiting the solid angle. To obtain the diaphragm opening angles stated in the table, test measurements need to be performed to verify how the intensity varies with diaphragm radius. This then needed to be related to a theoretical description to determine when the solid angle is limited and governed by this aperture radius. This will be at the point where the solid angle becomes smaller than the limiting aperture in the LARA setup. These measurements will now be discussed.

6.5.4 Diaphragm aperture determination

A method is required that enables the limiting solid angle of the collection side of the setup to be determined for Raman scattered light. The best way of doing this would be to compare how one would expect the intensity of scattered light to vary with solid angle. In a very rough approximation, the scattering centre of Raman light can be assumed to be an isotropic light source. In reality, the intensity distribution is more similar to a dipole antenna distribution. This means that the intensity would be proportional to $\cos^2(\theta)$. However, for small angles this is equal to one. This means that the intensity can be approximated as an isotropic light source and the intensity per second should scale with aperture radius as

$$\frac{dI}{dt} = cr^2 \tag{6.32}$$

which implies that

$$\frac{I}{t} = Cr^2 \tag{6.33}$$

Where c and C are proportionality constants, I is the measured intensity, t is the acquisition time and r is the aperture radius. The term $\frac{I}{t}$ is referred to as the normalised absolute intensity. Therefore, if the diaphragm radius is increased and is the only device limiting the collection angle, the normalised absolute intensity should be directly proportional to the radius squared. If the intensity starts to drop off sooner it means something else is limiting the collection angle, namely any other of the components in the light collection path. The KATRIN LARA collection setup is visualised in figure 6.7 top.

To obtain the data to determine the required aperture size, Raman spectra were taken

for a variety of different diaphragm radii. The normalised absolute Raman intensities were plotted against the collection angle. This measurement was performed at both TLK and Swansea. The resultant data are shown in figure 6.7 bottom. The figure shows that the diaphragm is the aperture that governs the solid angle for collection angles below $\approx 4.7°$, as shown by the green box in the figure. For the aperture locations included in table 6.2, this would correspond to an aperture radius of 3.12 mm in Swansea and 5.67 mm in TLK. This means that the selected radius at both locations was 3 mm in Swansea and 5 mm in TLK, as is shown in table 6.2. The observed Raman intensity appears to saturate for larger angles well below that related to the numerical aperture of the fibre bundle (NA = 0.22 corresponding to $\approx 12°$). The reason for this is discussed in detail in chapter 5, but simply put the reason is that the scattered light originates along an extended line and is imaged onto a "slit" (fibre bundle), while the collected light is limited by a round aperture. This means that the amount of scattered light collected does not start to reduce until relatively small diaphragm radius (small collection angles).

6.5.5 Pre-analysis

The measured Raman line intensity is the area under the observed Raman line. However, these Raman lines sit on a non-linear background, cosmic rays are also observed by the CCD detector and these individual Raman lines may convolute as the line spacing reduces below the resolution of the measurement.

The determination of depolarisation ratios from Raman spectra measured at $\perp^i$- and $\|^i$-polarisation requires a quantitative analysis procedure with an as high as possible accuracy. A procedure was found that:

- reduces cosmic ray events,
- removes background distortions to a negligible amount,
- and determined the Raman intensity by a peak fitting technique which enables the use of the best approximation possible for the peak shapes and can extract intensities from convoluted peaks.

This procedure has been tested thoroughly on various Raman spectra and is described in full in appendix A.6 and in [Jam13]. Briefly, it consists of the following steps

1. In the cosmic ray removal step, a temporal removal method (TCRR) is employed which requires two consecutive spectra with the same experimental parameters.
2. In the baseline flattening step, the Savitzky-Golay coupled advanced rolling circle filter (SCARF) is applied twice with optimised input parameters. Since the SCARF produces only positive values, the baseline needs to be pulled down to obtain a symmetric noise distribution around the zero line.

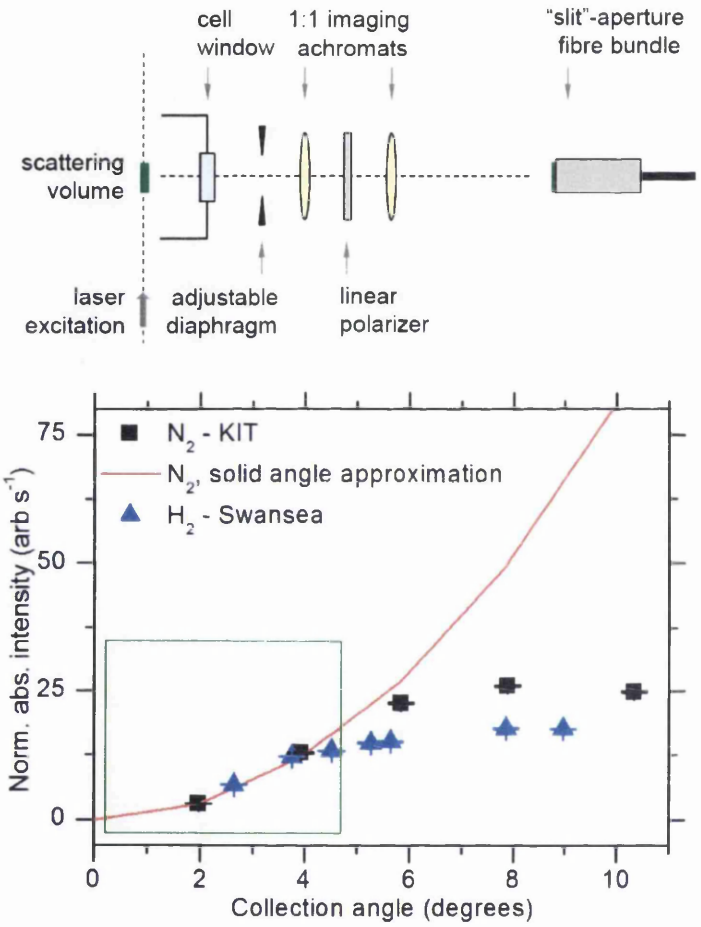

Figure 6.7: Top: Optical and geometrical mounting components in the light collection path affecting the collection solid angle. Bottom: Verification of numerical aperture size of the optical fibre from Raman measurement; exemplified for nitrogen (TLK) and hydrogen (Swansea). The green box indicates the region where the aperture is limiting the solid angle.

3. Intensity determination is performed by the peak fitting routine ShapeFit, which is applied on each of the peaks corresponding to the different rotational numbers.

These lead to an output line intensity for the different rotational numbers within the Q_1-branch for each pair of spectra.

6.6 First depolarisation measurements of the non-trititated hydrogen isotopologues

The early depolarisation measurements of the non-tritiated hydrogen isotopologues are included in Alshahrie [Als11]. These measurements will be summarised highlighting the problem of the lower cleanness of the two pass measurement using the Swansea LARA cell.

6.6.1 Measurement procedure

With the introduction of the gas mixing system in Swansea [Als11](and appendix A.2), mixtures of H_2, HD and D_2 could be made. It also enabled pure fillings of the cell with approximately 1 bar of either H_2 or D_2. Depolarisation measurements of the Q_1-branch of H_2, HD and D_2 were performed using the high resolution grating (2400gr/mm) of the SP500 spectrometer centred at the appropriate wavelength. In this experimental method, the half-wave plate was rotated in 4° steps over a 260° range to ensure that at least one maximum and one minimum intensity was recorded. Measurements were performed with 2 passes of the laser beam through the cell to increase the sensitivity by approximately a factor of 2 (as shown in chapter 5). The acquisition time was 6×150 s. The other experimental parameters were the same as for the Swansea setup described in section 6.5.3 above.

Before the measured intensity can be extracted cosmic rays and the spectral background need to be removed. The routines used to do this are described in appendix A.6. The intensity is taken from a multi curve Gaussian fit and is the area under each individual curve. The intensity is then plotted vs. the half-wave plate rotation angle to produce a full sinusoidal relationship.

As full sinusoidal curves are recorded, the depolarisation ratio ρ_{obs} is calculated by fitting a $\sin^2$-curve to the measured intensity vs. half-wave plate angle of the form

$$I = y_0 + A(\sin^2(\pi(h - x_c)/w)) \tag{6.34}$$

Where I is the peak intensity and h is the half-wave plate angle. The depolarisation ratio is then

$$\rho_{\text{obs}} = \frac{y_0}{y_0 + A} \tag{6.35}$$

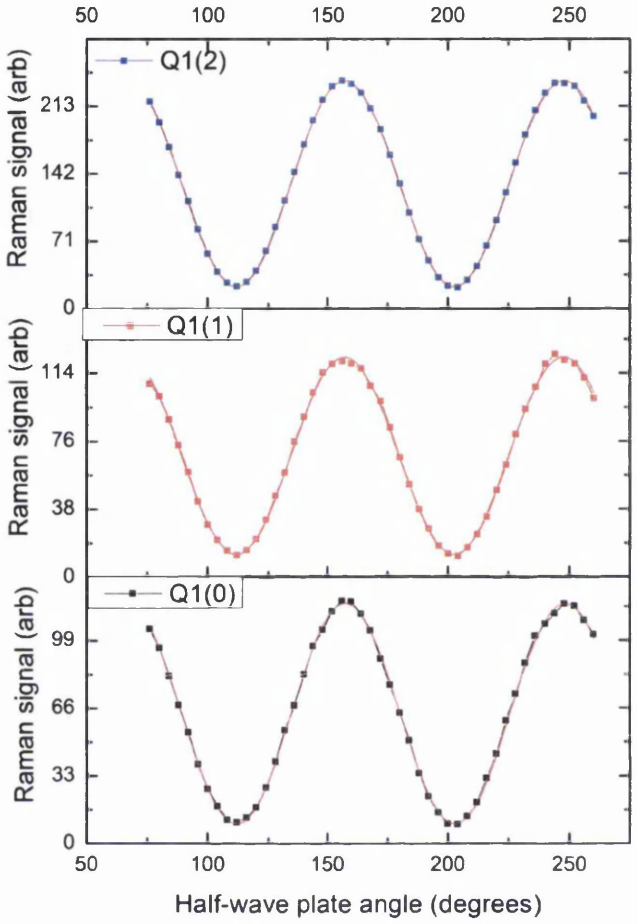

Figure 6.8: Raman signal (peak area) variation of selected Q_1-branch lines of D_2 with respect to the half-wave plate angle. The red curves are the sinusoidal fits used to determine ρ_{obs}

An example of the measured sinusoidal intensity curves for the Q_1-branch of hydrogen are shown in figure 6.8.

6.6.2 Results

The resultant measured depolarisation ratios of the Q_1-branch of H_2, HD and D_2 are shown in table 6.3 along with the corresponding $\rho_{\text{SP0SA-theory}}$, based on matrix elements calculated by LeRoy [Roy12].

The table shows that the measured values are substantially larger than the theory values. If a crude approximation is performed where the integral terms are removed from equation (6.3) for the $J = 0$ depolarisation ratio i.e. assume there is no solid angle and

Table 6.3: Measured depolarisation ratios of the Q_1 branches of H_2, HD and D_2

Isotopologue	**Branch**	ρ_{obs}	$\rho_{\text{SP0SA-theory}}$ [Roy12]
D_2	$Q_1(0)$	0.08433	0
D_2	$Q_1(1)$	0.1027	0.01764
D_2	$Q_1(2)$	0.09641	0.01272
D_2	$Q_1(3)$	0.09702	0.01194
H_2	$Q_1(0)$	0.08022	0
H_2	$Q_1(1)$	0.1057	0.01830
H_2	$Q_1(2)$	0.09782	0.01324
H_2	$Q_1(3)$	0.09837	0.01248
HD	$Q_1(0)$	0.0946	0
HD	$Q_1(1)$	0.1701	0.01800
HD	$Q_1(2)$	0.1461	0.01300
HD	$Q_1(3)$	0.1465	0.01223

the cleanness is set to $\xi = 1$. Then for $\rho_{\text{calc}} = 0$ this implies that $I_{\perp^s,\parallel^i} = 0$ substituting this back into equation (6.3) would lead too

$$\rho_{\text{calc}} = \frac{(1-\xi)B}{\xi B} = \frac{1-\xi}{\xi} \tag{6.36}$$

which implies that

$$\xi = \frac{1}{1+\rho_{\text{calc}}} \tag{6.37}$$

Substituting in one of the measured values from table 6.3 for ρ_{calc} e.g. $\rho_{J=0,D_2} = 0.08433$ leads to

$$\xi = \frac{1}{1+0.08433} = 0.9222 \tag{6.38}$$

This is considerably worse than expected for a clean beam entering the cell window.

On closer inspection of the cell windows, it was noticed that the cell window where the laser beam enters on the first pass had some dirt and a small amount of damage to the coating. This could cause the disturbance of polarisation to be higher than expected. To test this theory the cell was rotated by 180°, so the laser beam entered the other cell window first. A quick check of the depolarisation ratio was performed, with one and two passes of the laser beam through the cell for the ν_1-branch of methane (see chapter 7 for information on Raman spectroscopy of methane) by looking at the maximum and minimum spectra only. The spectra had the background and cosmic rays removed and are shown in figure 6.9. From these spectra the depolarisation ratio for each can be

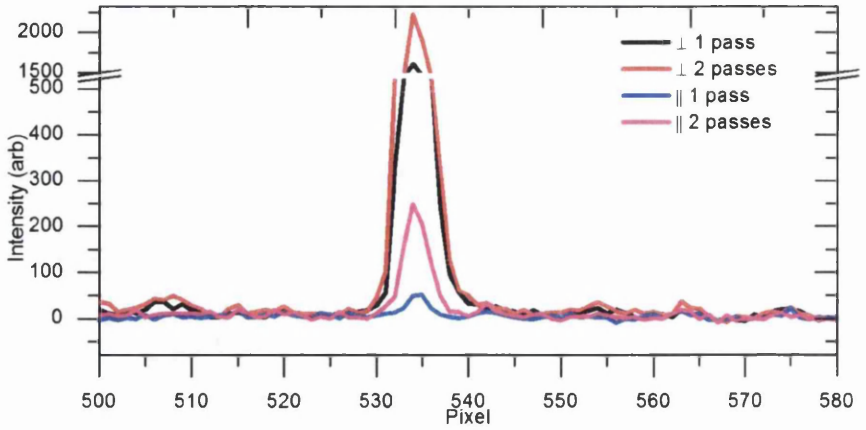

Figure 6.9: $I_{\perp^z}$ and $I_{\parallel^z}$ ν_1 Raman spectra of methane when the cell is flipped 180° with 1 and 2 passes of the laser beam through the cell.

calculated, which leads to

$$\rho_{\text{obs}-1\text{pass}} = 0.0329 \tag{6.39}$$

$$\rho_{\text{obs}-2\text{pass}} = 0.111 \tag{6.40}$$

The observed depolarisation ratio for the double-pass measurement is much larger than the single pass. This implies that the cleanness of the beam after it has passed through the second window is considerably lower due to the damage. Therefore, for all future depolarisation measurements using this cell in Swansea, the cell will remain in the "flipped" orientation and 1 pass of the laser beam will be used, as a high polarisation cleanness is needed for accurate measurements of the depolarisation ratio.

The potential effect reduced beam cleanness has on the measured depolarisation ratios has been observed. The laser beam now has a high beam cleanness so the complete depolarisation measurements of all six hydrogen isotopologues will be discussed in the next sections.

6.7 Depolarisation measurements of the Q-branch of the six hydrogen isotopologues

The complete depolarisation measurements of all six hydrogen isotopologues have been performed, including the tritiated species T_2, DT and HT. The analysis procedure using the model derived above, in section 6.3, enables a comparison with the literature values of LeRoy [Roy12] and previous measurements of the non-tritiated isotopologues. The overview raw spectrum in figure 6.10 (top) shows the Q_1-branches of all hydrogen isotopologues and additional O_1- and S_1-branches for both states of excitation polarisation.

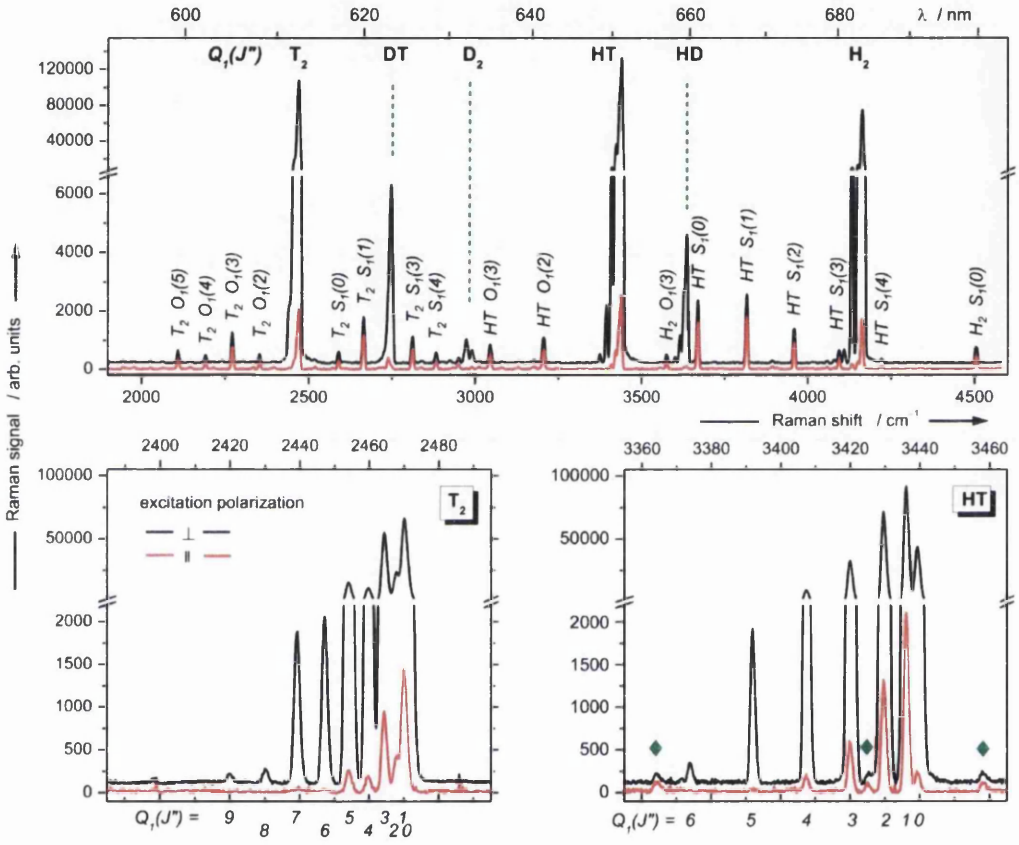

Figure 6.10: Raman spectra (for both $\perp^i$ and $\|^i$ excitation polarization) of an equilibrated mixture of T_2 and H_2, utilised in the depolarisation measurements; a small impurity of D_2 means that all six hydrogen isotopologues are observed in the mixture. Upper panel low resolution (600gr/mm) with relevant O_1-, Q_1- and S_1-branch lines annotated; lower panels high resolution (2400gr/mm) spectra for the J-resolved Q_1-branches of T_2 (left) and HT (right). The (green) diamond symbols indicate polarisation-independent lines from stray ambient light. For further details see text.

6.7.1 Max and min determination

As mentioned in section 6.5, a half-wave plate is used to select the polarisation of the incident laser beam. As only the $\perp^i$ and $\|^i$ states of polarisation are required to perform depolarisation measurements, the wave plate rotation angle that corresponds to these polarisation states needs to be determined only once, then the automated rotation mount can be rotated to these two locations for repeat measurements. The angles are determined by recording high resolution spectra for subsequent wave plate angles and fitting a $\sin^2$ function to the acquired Q_1-branch line intensities (see figure 6.11 for curve for HT). The angles are extracted from the maximum and minimum values of this fit. For a higher accuracy, the step size was reduced and the angle rotation steps were only performed around the maximum and minimum intensity.

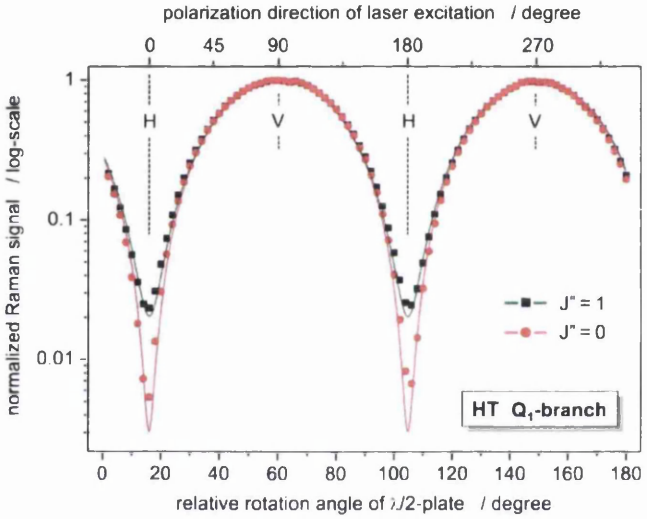

Figure 6.11: Dependence of the Raman signal of the $J = 0$ (black symbols) and $J = 1$ (red symbols) Q_1-branch lines of HT, as a function of excitation polarisation; $\perp^i$ = excitation laser polarisation vertical to the excitation-observation plane (maximum Raman signal); $\|^i$ = excitation laser polarisation horizontal to the excitation-observation plane (minimum Raman signal). For clarity of the minima, the (normalised) data are shown on a logarithmic intensity scale. The solid lines are $\sin^2$-function fits to the data points. For further details see text.

After the angles for the $\perp^i$ and $\|^i$ states were determined, between 29 and 600 sets of 2 $\perp^i$ and 2 $\|^i$ high-resolution spectra were acquired for each isotopologue. Depending on the gas pressure in the cell, the acquisition times were set between 300 s and 1000 s to maximise the line intensities without saturating the CCD detector in use. The different depolarisation ratios of the individual Q_1-branch lines already become evident in figure 6.11 as a change of the minimum intensity in the $\|^i$-polarisation state. However, as described above, further corrections have to be applied to the data to extract the

depolarisation ratios, as the $J = 0$ line does not decrease to zero for $\|^i$-polarisation, contrary to theoretical expectations.

6.7.2 Spectral analysis

The measured intensities are extracted using the method described in section 6.5.5. Large sets of repeat measurements for both polarisation states have been taken to improve statistics.

When using intensities extracted from spectra, minimising noise as efficiently as possible improves the accuracy of the extracted values. In the given case of the depolarisation ratio analysis at the minimum intensity, a low signal-to-noise ratio can result in a rather random intensity extraction which is influenced by the noise in the data. Therefore, it is useful to measure a full set of spectra and average all pixel wise in order reduce the random noise significantly. However, due to this process, some of the statistical information on the data is lost in the single averaged resulting spectrum. There are two proposed methods to circumvent this problem, the "pairs" method or the "partial averaging" method. The pairs method is a post intensity extraction averaging method, whereas the partial averaging method is a pre intensity extraction method. The procedures behind these methods are described below.

Pairs method

As pairs of spectra are required for the cosmic ray removal routine TCRR, the simplest analysis method is to calculate individual depolarisation ratios for each pair of maximum and minimum spectra. This is visualised in figure 6.12. The figure shows that, for each

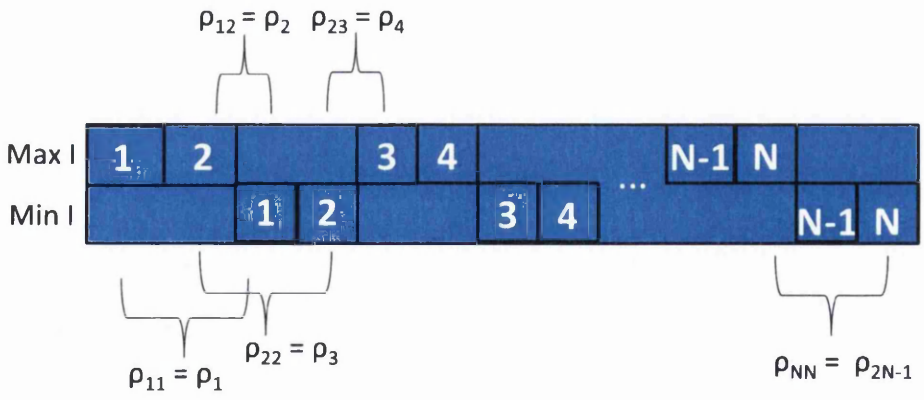

Figure 6.12: Diagram showing how the pairs analysis works. For details see text.

consecutive maximum and minimum pair, a depolarisation ratio is calculated as

$$\begin{aligned}
\rho_{11} &= \frac{I_{\mathrm{min1}}}{I_{\mathrm{max1}}} = \rho_1 \\
\rho_{12} &= \frac{I_{\mathrm{min1}}}{I_{\mathrm{max2}}} = \rho_2 \\
\rho_{22} &= \frac{I_{\mathrm{min2}}}{I_{\mathrm{max2}}} = \rho_3 \\
\rho_{23} &= \frac{I_{\mathrm{min2}}}{I_{\mathrm{max3}}} = \rho_4 \\
&\dots \\
\rho_{NN} &= \frac{I_{\mathrm{minN}}}{I_{\mathrm{maxN}}} = \rho_{2N-1}
\end{aligned} \tag{6.41}$$

Then the observed depolarisation ratio ρ_{obs} is

$$\rho_{\mathrm{obs}} = \frac{\rho_{11} + \rho_{12} + \rho_{22} + \rho_{23} + \ldots + \rho_{NN}}{2N - 1} \tag{6.42}$$

The uncertainty in the measured value is calculated from the standard deviation as

$$\mathrm{SD}_{\rho_{\mathrm{obs}}} = \sqrt{\sum_{i=1}^{2N-1} \frac{(\rho_i - \rho_{\mathrm{obs}})^2}{2N - 1}} \tag{6.43}$$

$$\Delta\rho_{\mathrm{obs}} = \frac{\mathrm{SD}_{\rho_{\mathrm{obs}}}}{\sqrt{2N - 1}} \tag{6.44}$$

This averages the depolarisation ratio over the large samples of data and is valid if the laser power is stable for at least 3× the individual accumulation time. If the sets of two $\perp^i$ and two $\|^i$ high-resolution spectra increase and the laser power is stable over a longer period of time (as is the case here) another analysis method, with a reduced noise, can be implemented, the partial averaging method.

Partial averaging method

The second analysis method involves "partial averaging" of the data. It combines the advantages of good statistics (which are offered by a set of many single measurements) and low spectral noise of an average spectrum (which is beneficial for the accuracy of intensity extraction). The concept of the partial averaging is visualised in figure 6.13. Generally, about 80% of the single spectra are randomly selected. Then, a pixel-wise average spectrum is generated from these selected spectra. This process is repeated until the number of generated average spectra is about 80% of the total number of single spectra. ShapeFit (see appendix A.6) is then used to extract the peak intensities from the partial averaged data set as described above. The same analysis as described in the pairs method is then performed on the data. However, the uncertainty in the

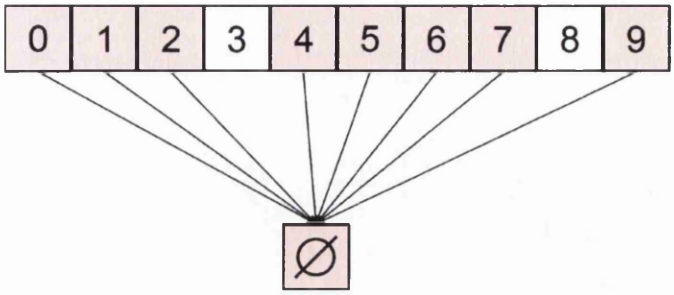

Figure 6.13: Diagram showing the concept of partial averaging analysis. For details see text.

depolarisation ratio ρ_{obs} is taken as the standard deviation of the intensities. The reason behind this is that the averaging over all the data has already been applied, so it would be unrealistic to reduce the uncertainty by a factor of the arbitrarily (user chosen) number of partial averaged data sets.

6.7.3 Observed depolarisation ratios

The analysis methods described in section 6.7.2 have been applied to sets of depolarisation measurements taken from four separate cells (3 in TLK and 1 in Swansea). The cell fillings were as follows

- TLK LARA cell 1, total pressure of 763.1 mbar consisting of H_2 : 25%, HT: 46%, T_2 : 26% and Rest (HD and D_2) :3%
- TLK LARA cell 2, total pressure of 400 mbar consisting of D_2 : 15%, DT: 47%, T_2 : 34% and Rest (HD and HT) :4%
- TLK LARA cell 3, total pressure of 1500 mbar consisting of H_2 : 26.3%, HD: 47.4%, D_2 : 26.3%
- Swansea LARA cell, filled twice; first filling 900 mbar H_2 : 100%; second filling 870 mbar D_2 : 100%

The values of ρ_{obs} obtained for the three cells are collated in table 6.4. The table shows that, for each cell, the measured values are quite different. This is due to the different stress induced birefringence in the cell windows, which leads to a different laser beam cleanness, ξ. One other point to note is that as the isotopic mass increases, the spacing between the individual lines in the Q_1-branch reduces. This means that for tritium the $J = 0$ line is very convoluted with the $J = 1$ line. This can be seen in the measured Raman spectrum of tritium in the bottom left of figure 6.10, above. This means that the accuracy of the measured $J = 0$ depolarisation ratio is lower.

Table 6.4: Observed depolarisation ratios of the Q_1-branches of H_2 , HT and T_2 using TLK LARA cell 1; D_2 and DT using TLK LARA cell 2; and H_2, HD and D_2 using the Swansea LARA cell and TLK LARA cell 3. Error in brackets in the last digit. * indicates underlying contaminant feature, discard from analysis.

	ρ_{obs} TLK LARA cell 1 **Isotopologue**			ρ_{obs} TLK LARA cell 2 **Isotopologue**	
J	H_2	HT	T_2	D_2	DT
0	0.00639(4)	0.00601(3)	0.00339(24)	0.02279(4)	0.02291(5)
1	0.02408(2)	0.02331(3)	0.02251(7)	0.04075(7)	0.03989(3)
2	0.01971(5)	0.01864(3)	0.01794(5)	0.03607(2)	0.03518(3)
3	0.01923(7)	0.01822(3)	0.01716(4)	0.12850(8)*	0.03564(4)
4		0.01854(9)	0.01642(7)	0.03367(9)	0.03442(7)
5		0.02101(37)	0.01733(10)	0.03658(55)	0.03592(17)
6			0.01756(31)	0.06829(110)	0.03554(44)
7			0.02163(42)		

	ρ_{obs} TLK LARA cell 3 **Isotopologue**			ρ_{obs} Swansea cell **Isotopologue**	
J	H_2	HD	D_2	H_2	D_2
0	0.01048(4)	0.01152(1)	0.01137(2)	0.00182(16)	0.00186(7)
1	0.02846(2)	0.02917(3)	0.02880(2)	0.02124(5))	0.02033(7)
2	0.02526(4)	0.02415(2)	0.02312(1)	0.01561(16)	0.01516(4)
3	0.02341(5)	0.02358(3)	0.02252(3)	0.01487 (22)	0.01463(10)
4			0.02236(4)		0.01383(16)

To enable a comparison between the observed depolarisation ratios ρ_{obs} and the literature values, the correction procedure discussed in section 6.3 needs to be implemented. The integration is performed in a C++ and ROOT libraries ([ROO]) routine called DepolTools [Sch12a]. The routine is described and implemented on the observed depolarisation ratios of the hydrogen isotopologues, in the next section.

6.7.4 Correction method

The procedure to correct the observed depolarisation ratios, so that they can be compared with the SP0SA depolarisation ratios in the literature, occurs in two stages.

Firstly, the cleanness, ξ, is determined using a theoretically known depolarisation ratio and the measured value for that line. The program does this for the specified solid angle by calculating what the observed depolarisation ratio would be (ρ_{calc}) for a range of cleanness values ξ. The output ρ_{calc} are fitted against the corresponding cleanness ξ (see top panel of figure 6.14). This fit is then used to determine what the cleanness of the cell is, using the observed value corresponding to the theoretically known depolarisation ratio.

Secondly, the determined cell cleanness is input into the program to convert the observed depolarisation ratios, ρ_{obs}, of the other lines to the corrected depolarisation ratios $\rho_{\text{SP0SA-cor}}$ (see bottom panel of figure 6.14).

In the case of the Q_1-branches of the hydrogen isotopologues the theoretically known depolarisation ratio is the $J = 0$ line, which has a SP0SA depolarisation ratio of $\rho_{\text{SP0SA}}(J = 0) = 0$ as can be seen in table 6.7. The reason this value is zero is the vanishing Placzek-Teller $b^{(2)}$ factor when $J = 0$.

The input parameters required to define the solid angle in the program are: the distance from the scattering volume to diaphragm x_f; diaphragm opening radius r_f; LARA cell window radius r_w and the distance from the scattering volume to the LARA cell window x_w. The design of all cells is the same as described in chapter 4 and have the following parameters: $r_w = 3.5\,\text{mm}$ and $x_w = 8.8\,\text{mm}$; in the setups in TLK and Swansea x_f and r_f are different. The values are included in table 6.2 above.

6.7.5 Consideration of uncertainty in correction method

To enable a comparison between the corrected depolarisation ratios $\rho_{\text{SP0SA-cor}}$ with the SP0SA ratios of LeRoy, the uncertainties of the measurement and correction need to be considered. The first source of error comes from the uncertainties in the observed depolarisation ratios. These values are used as inputs into the correction procedure in two locations. Firstly, the $\rho_{\text{obs}}(J = 0)$ values are used to determine the cleanness, ξ, in the cleanness fit. The uncertainty in these measured values needs to be propagated onto the cleanness to give a cleanness uncertainty, $\Delta\xi$. This is achieved by mapping an array

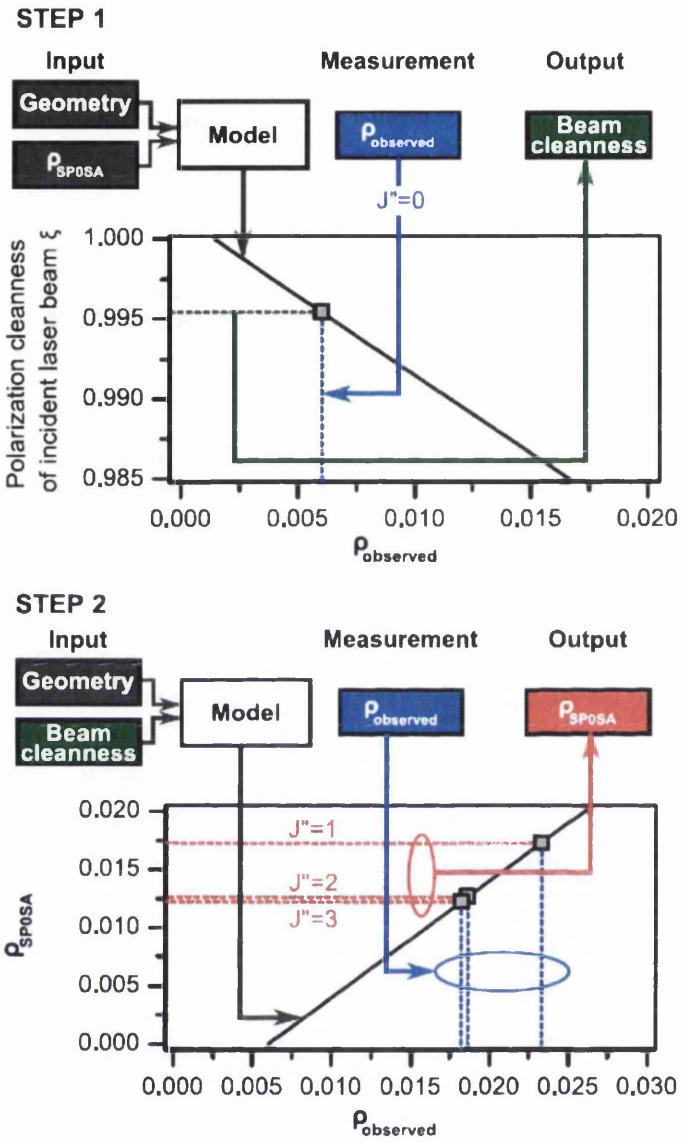

Figure 6.14: Two-step procedure to extract depolarisation values ρ_{SP0SA} from data sets with unclean beam polarisation. Step 1 - Determination of cleanness of the laser polarisation. The theoretical data (full line) are calculated for a known collection geometry and a known SP0SA depolarisation ratio $\rho_{\mathrm{SP0SA}}(J = 0) = 0$. From the observed depolarisation ratio of the $Q_1(J = 0)$ line one derives the related polarisation cleanness ξ. Step 2 - Correction of depolarisation ratios of all measured Q_1-branch lines, for a given polarisation cleanness. The polarisation cleanness derived in step 1 is used to correlate the ρ_{obs} to the ρ_{SP0SA} values of all Q_1-branch lines with $J > 0$.

of statistically weighted cleanness values across the cleanness fit. This is demonstrated in figure 6.15. The cleanness values, $\xi(x)$, are calculated from $\rho_{\text{obs}}(J=0)+x$ where x is

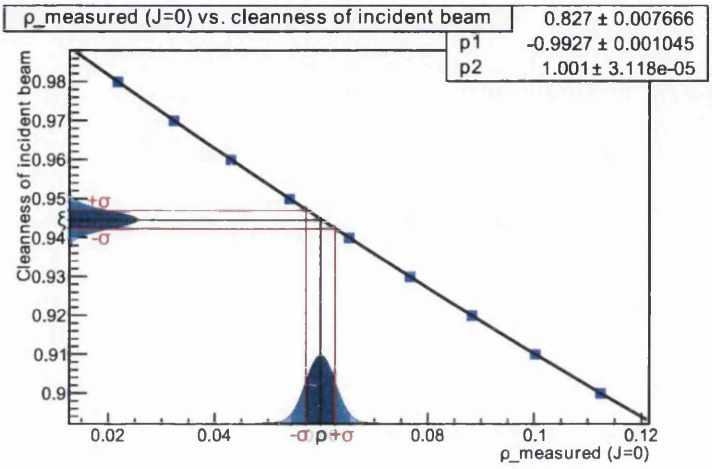

Figure 6.15: Calculation of cleanness array from $\rho_{\text{obs}}(J=0)$ and $\sigma(\rho_{\text{obs}}(J=0))$

varied from $-O\cdots\sigma(\rho_{\text{obs}}(J=0))$ to $+O\cdots\sigma(\rho_{\text{obs}}(J=0))$ in n steps. The parameters O and n are used to define a grid that the uncertainty is calculated over. O is defined by the number of standard deviations of the most outer points of the "cleanness plot" and n is defined by the number of points to be used in the calculation. For more details see Schlösser [Sch13]. The statistical weight $p_{\text{cleanness}}(x)$ is calculated from the Gaussian distribution

$$p_{\text{cleanness}}(x) = \frac{1}{\sigma(\rho_{\text{obs}}(J=0))\sqrt{2\pi}} e^{-\frac{1}{2}\left(\frac{x}{\sigma(\rho_{\text{obs}}(J=0))}\right)^2} \tag{6.45}$$

The next step is, instead of using an individual cell cleanness value, ξ, as the input to convert the observed $\rho_{\text{obs}}(J>0)$ to the corrected $\rho_{\text{SP0SA-cor}}(J>0)$, this conversion is performed for all the cleanness values in the cleanness array $\xi(x)$ and a "graph" is generated for each value. Each of these "graphs" is fitted with a second order polynomial to relate $\rho_{\text{obs}}(J>0)$ to $\rho_{\text{SP0SA-cor}}(J>0)$ for each $\xi(x)$.

To statistically weight the corrected depolarisation ratios, the statistical weight of the cleanness in equation (6.45) for all cleanness $\xi(x)$ needs to be combined with a similar statistical weight of the observed depolarisation ratios $\rho_{\text{obs}}(J>0)$ using the uncertainty $\sigma(\rho_{\text{obs}}(J>0))$. This is done by generating a statistical weight p_{obs}, which has the same form as equation (6.45), where all instances of $\rho_{\text{obs}}(J=0)$ are replaced with $\rho_{\text{obs}}(J>0)$. The statistical weights are then multiplied together to give a final statistical weight for the corrected depolarisation ratios. This is the general rule to combine independent probabilities of two events [Dro07].

The final step involves determining the values of $\rho_{\text{obs}}(J>0)$ that lie within a 1σ

confidence level. The method for doing this is described in Schlösser [Sch13] or James *et al* [Jam12a]. The maximum and minimum corrected values, $\rho_{\mathrm{SP0SA-cor}}(J > 0)$, within this confidence level plot are then used as the uncertainty $\Delta\rho_{\mathrm{analysis}}$ (i.e. uncertainty is $\frac{\mathrm{max}-\mathrm{min}}{2}$).

There are other sources of error in the correction procedure that need to be considered, namely: the accuracy of determining the dimensions of the geometry and accuracy of the correction in terms of polarisation aberrations (see section 6.4). These will now be discussed.

The uncertainties in the geometry stem from how accurately the parameters used to define the geometry (see section 6.7.4) have been measured. The LARA cell window radius and the distance from the scattering volume to the LARA cell window are obtained from the technical drawings (see chapter 4). The distance from the scattering volume to the diaphragm is measured using methods that have a fairly low accuracy (± 1 to 2 mm). The diaphragm radius is determined from either graduations on the diaphragm in the Swansea setup or a calliper rule in the TLK setups. The uncertainty of this measurement is approximately ± 0.5 mm.

As the aperture radius and diaphragm distance are independent of each other, these uncertainties are considered separately as $\Delta\rho_r$ and $\Delta\rho_x$ respectively. Several simulations have been performed using the correction routine, where the input parameters are varied. The diaphragm distance was varied by $\Delta x = 4$ mm, which resulted in a shift of $\Delta\rho_x = 0.0002$. The accuracy of the distance measurement should be better than this. Therefore, for all measurements, it is assumed that the maximum uncertainty of the depolarisation ratio caused by diaphragm distance is $\Delta\rho_x = 0.0001$.

The diaphragm radius was varied by $\Delta r = 1$ mm, which is the maximum assumed uncertainty in the diaphragm radius. This resulted in an uncertainty in the depolarisation ratio caused by the diaphragm radius of approximately $\Delta\rho_x = 0.0005$.

In the polarisation aberration discussion in section 6.4.7, it became clear that the effect on the beam cleanness caused by the laser window is 1 to 2 orders of magnitude higher than the collection window effect [for aperture radii of $r_f \approx 3$ mm for the Swansea aperture location ($x_f = 38$ mm)] assuming that the Jones/Müller formalism described in section 6.4 is correct. This means that the collection window effect may be neglected, leading to a small error in the depolarisation ratio, caused by the uncertainty in the collection window effect. Observing figure 6.5 at a light collection angle of 4°, the geometry only calculation gives a depolarisation ratio of 0.0015, whereas including the collection path in the calculation increases the value to approximately 0.002. The difference between these two values is 0.0005. This difference quantifies the potential underestimation of the correction, if the collection path aberrations are neglected and the cleanness reduction caused by the collection window is very high. Therefore, it is the uncertainty in this case. However, in real measurements the maximum observed

reduction in cleanness is approximately $\xi = 0.95$. This is halfway between the value used in figure 6.5 and a cleanness of 1. Therefore, one can assume that the depolarisation ratio increase caused by the collection window is approximately half of that shown above i.e. $0.0005/2 = 0.00025$. This uncertainty would still be an absolute upper limit of any aberration that has been observed in measurements. Therefore, the value can be reduced to 0.0002 giving a reasonable approximation of the theoretical uncertainty and bringing the cleanness value closer to that observed in measurements. Therefore, this is set to $\Delta\rho_{\text{theo}} \approx 0.0002$.

These uncertainties then need to be combined to give the total uncertainty in the corrected depolarisation ratios $\Delta\rho_{\text{SP0SA-cor}}(J)$. It is usually reasonable to add uncertainties in quadrature [Dro07], which gives

$$\Delta\rho_{\text{SP0SA-cor}}(J) = \sqrt{\Delta\rho_x^2 + \Delta\rho_r^2 + \Delta\rho_{\text{theo}}^2 + \Delta\rho_{\text{analysis}}^2} \tag{6.46}$$

This uncertainty is calculated for all the corrected depolarisation ratios and included in the results discussion below.

A point to note, from this uncertainty discussion, is that the resultant uncertainty in the corrected depolarisation ratio $\Delta\rho_{\text{SP0SA-cor}}(J)$ is dominated by inaccuracies in the geometrical measurements, rather than the spectral intensity data. This will lead to a higher uncertainty in the corrected values by approximately an order of magnitude over the measured uncertainties stated in table 6.4.

6.7.6 Results

Before the final results are discussed, the measured cleanness values were compared for the data sets from the four different LARA cells used for the depolarisation measurements. The measured cleanness values for all the cells in use from the first correction step are shown in figure 6.16. The different colours correspond to the four different cells, as described above, and these are the cleanness values calculated from the measured depolarisation ratios of the $Q_1(J = 0)$ lines in table 6.4; comparing the labelling in the figure with these tables shows which data corresponds to which cell. The figure shows that the values derived for the same cell are very close together. The variation within the same cell is of the order $\delta\xi < 0.001$, with relative uncertainties for individual measurements of less that 0.1%. The error bars in the figure, resulting from the uncertainty discussion above, are smaller than the symbol size.

The results clearly demonstrate that different cells lead to different beam cleanness, caused by the stress induced birefringence in the windows, which can be measured using this method. In the green data points (Swansea LARA cell) the cell was removed and replaced between fillings of the pure mixtures of D_2 and H_2. This shows that repositioning of the cell may introduce, in general, only minor deviations associated

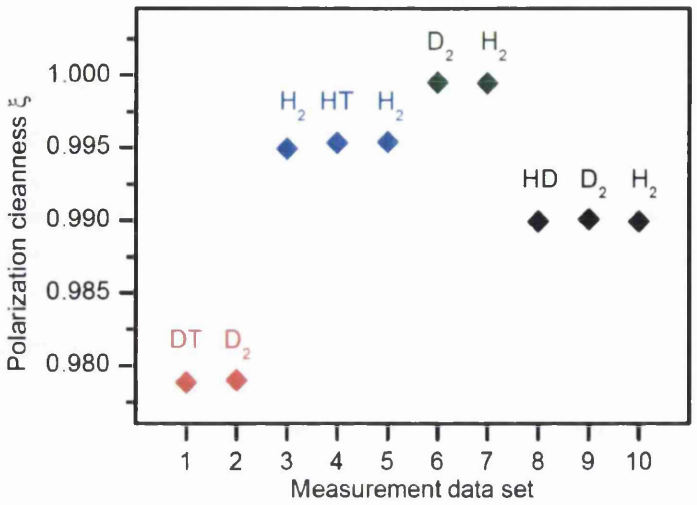

Figure 6.16: Polarisation cleanness of measurement cells, as determined in Step 1 of the evaluation procedure. The statistical measurement errors are within the symbol size. For further details see text.

with spatial inhomogeneity of the stress-induced birefringence. It also shows that the beam polarisation cleanness is largely independent of the gas filling.

With the cleanness values determined, these are used in the second step of the correction procedure as part of the cleanness array, $\xi(x)$, to determine $\rho_{\mathrm{SP0SA-cor}}$ from the observed values for $J'' > 0$ for all six hydrogen isotopologues, along with the resultant uncertainties.

For demonstration purposes, one corrected depolarisation data set, for each isotopologue, has been selected. The corrected depolarisation ratios of the six hydrogen isotopologues are collated in table 6.5. The analysis has been performed on all data sets, as they will be used in the comparison with literature and accuracy discussions in section 6.7.7. The corrected values of these are shown in appendix A.4.2. If the corrected $J = 0$ depolarisation ratios in the table are compared with the relevant observed values in table 6.4, even though the observed uncorrected depolarisation ratio for the $J = 0$ line vary by nearly an order of magnitude (between 0.00339 and 0.02291), the corrected values are all at the theoretically expected value of zero within the 1σ uncertainty. The uncertainty in the corrected $J = 0$ values is included as it gives an indication of the upper limit of deviation from the theoretically expected zero-value. As stated above in the uncertainty discussion the resultant uncertainty is dominated by inaccuracies in the geometry determination rather than the spectral intensity data with a deviation of the order of 5×10^{-4}. The exception is the T_2 value where the corrected value is not zero and the uncertainty on the value is quite large. This is a consequence of the fact that the $J = 0$ and $J = 1$ lines of its Q_1-branch cannot be fully decovoluted by the peak fitting routine. This greatly influences the measured intensity of the weak $\|^i$ compo-

Table 6.5: Experimentally derived (corrected) depolarisation ratios for $Q_1(J'' > 1)$ of all hydrogen isotopologues, for $\lambda = 532\,\text{nm}$ laser excitation. The errors in the last digit are given in brackets. [(a)] from different data set. * approaching noise level.

	$\rho_{\text{SpOSA-cor}}$ **Isotopologue**					
J	H_2	HD	HT	D_2	DT	T_2
0	0.0000(6)	0.0000(5)	0.0000(6)	0.0000(5)	0.0000(6)	−0.0030(100)
1	0.0177(6)	0.0177(6)	0.0173(6)	0.0174(6)	0.0170(6)	0.0165(6)
2	0.0133(6)	0.0126(6)	0.0126(6)	0.0118(6)	0.0123(6)	0.0119(6)
3	0.0128(6)	0.0121(6)	0.0122(6)	0.0112(4)	0.0127(6)	0.0112(6)
4			0.0125(6)	0.0113(7)[(a)]	0.0115(6)	0.0104(6)
5				0.0138(10)[(a)] *	0.0130(6) *	0.0113(6)
6					0.0126(9) *	0.0116(7)

nent. However, this uncertainty is larger than the difference from zero so the value is still consistent, i.e. within the experimental uncertainty.

Another comment that can be made about the data in table 6.5 is that the number of tabulated rotational levels varies for each isotopologue. Spectral lines measured for the $\perp^i$ polarisation can normally be measured to higher J-values than those tabulated. However, as the Q_1-branch depolarises the intensity of the $\parallel^i$ polarisation becomes too small to extract intensities, with a high enough signal-to-noise ratio, for those rotational levels with about $E_J \geq 0.25\,\text{eV}$. At room temperature, these levels carry less than 0.5% of the population compared to the most populated ones. The effect this has can be demonstrated by considering the Raman spectrum of T_2 in figure 6.10. Observing the $\perp^i$ polarisation, the $J = 9$ line can still be observed above the noise, whereas for the $\parallel^i$ polarisation, the $J = 6, 7$ lines are barely measurable above the noise. This leads to a break-off in the extent of the depolarisation ratio measurement, which differs for each isotopologue as the lines approach, or go below, the noise limit.

The depolarisation ratio of hydrogen has been measured previously in the literature by several different groups ([Hol73], [Yu07]). For comparison purposes in the next section table 6.8 collates the depolarisation ratio of hydrogen, described above, with other values in the literature ([Yu07], [Hol73] and [Roy12])

The reproducibility of the correction procedure to obtain $\rho_{\text{SP0SA-cor}}$ can also be determined by comparing repeat measurements of the Q_1-lines of H_2. The measurements were performed at different times, different cell pressures, with different filling compositions and with different cells. Using the different cells meant that the stress induced birefringence in the cell windows, and hence the laser beam cleanness for each measurement, was different. Two of the measurements were performed at TLK (blue and black data points) and one at Swansea (green data points). The limiting diaphragm (aperture) at the two

Table 6.6: Performance demonstration of the depolarisation ratio correction routine for different cells. The presented values (observed and corrected) are from measurements of the Q_1-branch lines of H_2 (in brackets: measurement uncertainty) where the utilised cell is indicated. The averaged SP0SA values (in brackets: standard deviation in the last digit) are compared to the theoretical values from LeRoy [Roy12].

H_2	ρ_{obs}			
J	TLK I	Swansea	TLK III	
1	.02408(2)	.02124(5)	.02846(4)	
2	.01971(5)	.01561(16)	.02526(4)	
3	.01923(7)	.01487(22)	.02341(5)	

H_2	$\rho_{Sp0SA-cor}$				ρ_{LeRoy}
J	TLK I	Swansea	TLK III	average	theory
1	.0177(6)	.0190(9)	.0180(6)	.0182(7)	.0183
2	.0133(6)	.0141(9)	.0148(6)	.0141(7)	.0132
3	.0128(6)	.0133(15)	.0129(6)	.0130(6)	.0125

sites was at a different location with a different diaphragm (aperture) radius. However, this is taken into account by the correct parameterisation and input of the geometry input parameters, as described above in section 6.7.4. The measured beam cleanness for the three measurements are shown in figure 6.16 (data points with the H_2 label). The extracted cleanness values for the hydrogen data from the figure are $\xi_{blue} = 0.9950$, $\xi_{green} = 0.9995$ and $\xi_{black} = 0.9899$, respectively. The resultant corrected depolarisation ratios for these measurements are collated in table 6.6. The averaged values of the corrected $\rho_{Sp0SA-cor}$ have a statistical variance of $\Delta\rho_{Sp0SA-cor} < 0.001$. Considering that the observed depolarisation ratios are spread over a much larger range, this shows that our correction routine is capable of compensating for the large variations in the beam cleanness, leading to large variations in the observed depolarisation ratios. The corrected values also virtually all agree, within the statistical reproducibility, with the theoretical values of LeRoy [Roy12]. This comparison will be discussed in more detail, for all the data sets of the depolarisation ratios of the hydrogen isotopologues, in the next section.

6.7.7 Comparison with literature

To verify the confidence we can place on the theoretical polarisability tensors of LeRoy [Roy12] the corrected experimental depolarisation ratios need to be compared with these theoretical values (collated in table 6.7). In the uncertainty discussion in section 6.7.5 all the uncertainties have been treated as 1σ values. This means that, from Gaussian distributed uncertainties, 68% of the measured data points should be in the range of the quoted error [Str01]. If this consideration follows for all the measured isotopologues

Table 6.7: Theoretical depolarisation ratios of the Q_1-branches of all six hydrogen isotopologues

	ρ_{LeRoy} Isotopologue					
J	H_2	HD	HT	D_2	DT	T_2
0	0	0	0	0	0	0
1	0.0183	0.0180	0.0179	0.0176	0.0175	0.0174
2	0.0132	0.0130	0.0129	0.0127	0.0126	0.0125
3	0.0125	0.0122	0.0121	0.0119	0.0118	0.0117
4	0.0123	0.0120	0.0119	0.0117	0.0116	0.0115
5	0.0123	0.0120	0.0119	0.0116	0.0115	0.0114
6	0.0124	0.0121	0.0119	0.0117	0.0115	0.0114
7	0.0126	0.0122	0.0120	0.0117	0.0116	0.0114
8	0.0129	0.0124	0.0122	0.0118	0.0116	0.0115
9	0.0131	0.0126	0.0124	0.0120	0.0117	0.0115

and we wish to state that the measured corrected depolarisation ratios agree with the theory, 68% of the corrected depolarisation ratios should be within the 1σ uncertainty of the depolarisation measurements. If this is the case, we can state that the measured values agree with the theory to a 1σ confidence level.

A method of verifying this is to calculate the depolarisation ratio difference (LeRoy - measured) normalised to the standard deviation, σ, for each measured depolarisation ratio. This is labelled as F_d, which is

$$F_d = \frac{\rho_{\text{LeRoy}} - \rho_{\text{SP0SA-cor}}}{\sigma(\rho_{\text{SP0SA-cor}})} \tag{6.47}$$

If a statistical histogram is created of these values and fitted with a Gaussian function, the resulting fit width gives an indication of the confidence level of the measured data i.e. a fit width of $\sigma = 1$ corresponds to a 1σ confidence level.

The statistical histogram of F_d, for all the measured corrected depolarisation ratios, is shown in figure 6.17. The histogram in the figure has been fitted with a Gaussian function, as described above, and the Gaussian function has a fit width of $\sigma = 1.19 \pm 0.08$. This is in reasonably good agreement with the expected value $\sigma = 1$; meaning that the corrected depolarisation ratios of the hydrogen isotopologues agree with the theoretical values of LeRoy to a 1σ confidence level. This means that, in future calibration measurements of the LARA system ([Rup12] and [Sch12b]), the theoretical values of LeRoy can be used as input parameters in the line strength function with the 1σ uncertainties of the depolarisation ratio measurements propagated through to the polarisability tensors. This will not be considered further here, but the discussion is included in Schlösser *et al* [Sch12b].

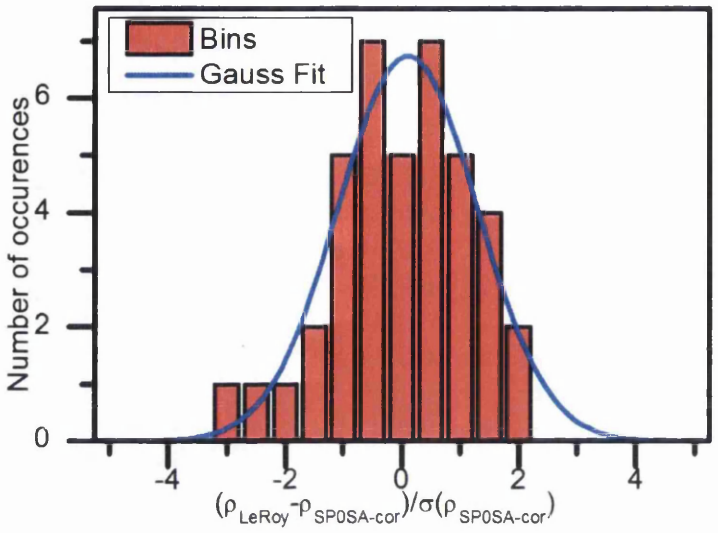

Figure 6.17: Statistical plot of $\frac{\rho_{\mathrm{LeRoy}}-\rho_{\mathrm{SP0SA-cor}}}{\sigma(\rho_{\mathrm{SP0SA-cor}})}$. The histogram has been fitted with a Gaussian function with a fit width $\sigma = 1.19 \pm 0.08$. This is in good agreement with the expected value of $\sigma = 1$. For further details see text.

Table 6.8: Comparison of experimental and theoretical depolarisation ratios for $Q_1(J)$ of hydrogen, H_2, for $\lambda = 532\,\mathrm{nm}$ laser excitation. The errors (where applicable) in the last digit are given in brackets.

J	$\rho_{\mathrm{Sp0SA-cor}}$	$\rho_{\mathrm{lit-Yu}}$	$\rho_{\mathrm{lit-Holzer}}$	ρ_{lit}	ρ_{lit}	$\rho_{\mathrm{lit-LeRoy-532\,nm}}$
0	0.0000(6)	0.002(2)	0.001(1)	0	0	0
1	0.0177(6)	0.021(2)	0.019(1)			0.0183
2	0.0133(6)	0.015(2)	0.014(1)			0.0132
3	0.0128(6)	0.014(2)	0.0135(10)			0.0124
4		0.013(5)				0.0123
5						0.0123
6						0.0124
7						0.0126
8						0.0129
9						0.0131

To further reinforce the improvement in the measurement technique, further comparisons with literature values can be considered. In the literature, several groups have measured the depolarisation ratio of hydrogen. These are collated in table 6.8, along with the values measured in this work. The values are compared with those of LeRoy. The table shows that the $\rho_{\mathrm{SP0SA-cor}}$ values agree with those of LeRoy within their experimental error, whereas the values of Yu *et al* [Yu07] and Holzer *et al* [Hol73] do not. Also, the uncertainty of the $\rho_{\mathrm{SP0SA-cor}}$ is lower than the previously measured values. This implies that the measurements performed here are the most accurate to date. Also, to the best of our knowledge, no depolarisation ratio measurements on the radioactive hydrogen isotopologues (HT, DT and T_2) are reported in the open literature. So the experimental measurement and verification of the depolarisation ratios of the radioactive hydrogen isotopologues has been completed successfully for the first time.

This work on the depolarisation measurements of the hydrogen isotopologues has just been published [Jam12a] and [Sch12a]. The first publication discusses the depolarisation measurement results, whereas the second is more focussed on the correction procedure.

It should be noted that other groups have performed types of depolarisation measurement of hydrogen ([Gol62], [Bri64], [Car72]). Even though these measurements are depolarisation measurements, the authors are looking at the entire Raman band rather than the individual lines within the band. In this work, we have restricted the measurements to only observe the $\perp^s$ scattered component. Golden and Crawford [Gol62] measure both scattered polarisations $\perp^s$ and $\|^s$ simultaneously for the entire band, so the measurement is not directly comparable. Carlson and Fenner [Car72] use the well-known Raman band of liquid benzene to calibrate their spectra and extract the information that they are after. Bridge and Buckingham [Bri64] do not have any wavelength selective optics, so they are looking at the depolarisation of all the scattered light (Rayleigh + Raman). This means that, even though their methods are very interesting, the measured values are not comparable with the measurements in this work

6.8 Depolarisation measurements: S- and O-branches of the hydrogen isotopologues

6.8.1 Changes to measurement/analysis procedure

The depolarisation measurement procedure can also be applied to the vibration-rotation S_1- and O_1-branches of the hydrogen isotopologues and the pure rotational S_0-branch.

The selection rules for these branches are $\Delta J = +2$ and $\Delta J = -2$. This simplifies

the SP0SA depolarisation ratio to

$$\rho_{\text{SP0SA}} = \frac{I_{\perp^s,\parallel^i}(\theta=\pi/2,\varphi=0)}{I_{\perp^s,\perp^i}(\theta=\pi/2,\varphi=0)} = \frac{\Phi_{\perp^s,\parallel^i}(\theta=\pi/2,\varphi=0)}{\Phi_{\perp^s,\perp^i}(\theta=\pi/2,\varphi=0)} \tag{6.48}$$

$$= \frac{b^2_{Jf0:Ji0}|\langle v^f|\gamma|v^i\rangle|^2}{15(\frac{4}{45}b^2_{Jf0:Ji0}|\langle v^f|\gamma|v^i\rangle|^2)} = \frac{3}{4} \tag{6.49}$$

The reason for this is described in chapter 3 and is linked to the Placzek invariants that are allowed for these branches.

The measurement procedure used for the Q_1-branch in section 6.7 is followed. The procedure was changed to use the lower resolution 600gr/mm grating of the SP500 spectrograph, as the vibration-rotation (and rotation) Raman lines within one branch are much further apart than for the lines within the pure vibrational Q_1-branch.

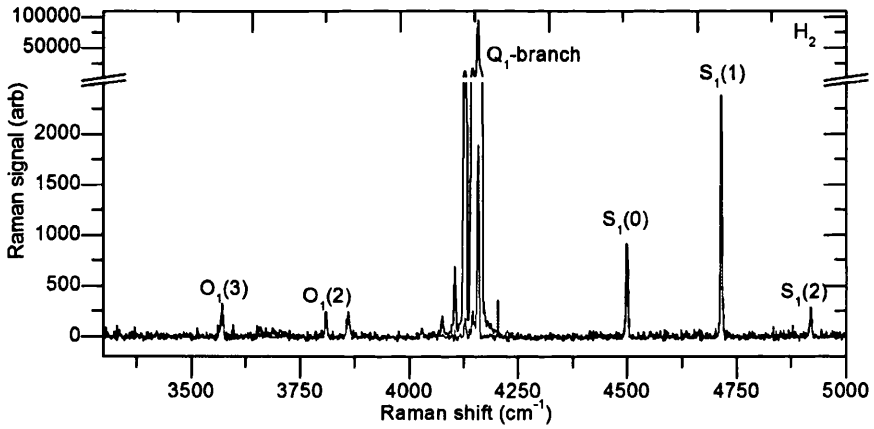

Figure 6.18: Raman spectra (for both $\perp$ (black) and $\parallel$ (red) excitation polarisation) of hydrogen.

6.8.2 Depolarisation measurements of the S_1- and O_1-branches of hydrogen

Measurements of the S_1- and O_1-branches of hydrogen around the Q-branch were performed. An example of the spectrum for the $\perp^i$ and $\parallel^i$ excitation polarisations is shown in figure 6.18. One point to note from this spectrum is that the S_1- and O_1-branches are approximately 50 times weaker than the Q_1-branch. This means that, even for relatively long acquisition times of 900 s (as is the case here) the signal is still relatively low. This means that the uncertainty in the measured intensities is higher, which results in a larger uncertainty in the depolarisation ratio.

For this data set, the depolarisation ratio was determined for the two vibration-rotation lines with the highest signal-to-noise ratio, $S_1(0)$ and $S_1(1)$. Due to the lower signal-to-noise ratio, and the separation of the lines, the intensities were extracted by

Table 6.9: Depolarisation ratio measurements of the S_1- and O_1-branch lines of H_2 (in brackets: measurement uncertainty). The observed depolarisation ratios are compared to the theoretical values from LeRoy [Roy12].

J H_2 Swansea	ρ_{obs} S_1	$\rho_{LeRoy-532\,nm}$ S_1	ρ_{obs} O_1	$\rho_{LeRoy-532\,nm}$ O_1
0	0.751(7)	0.75	–	–
1	0.753(4)	0.75	–	–
2			0.750(9)	0.75
3			0.767(11)	0.75

J HT TLK	ρ_{obs} S_1	$\rho_{LeRoy-532\,nm}$ S_1	ρ_{obs} O_1	$\rho_{LeRoy-532\,nm}$ O_1
0	0.745(5)	0.75	–	–
1	0.745(5)	0.75	–	–
2	0.747(7)	0.75	0.761(4)	0.75
3	0.763(17)	0.75	0.774(11)	0.75
4			0.742(17)	0.75

integrating the peaks i.e. summing the signal from all the pixels under the peak after background subtraction. The depolarisation ratios were then determined using the pairs method, as described above in section 6.7.2. Due to the lower signal-to-noise ratio of the $O_1(2)$ and $O_1(3)$ lines, the signal height is taken as the intensity. Some of the data points were excluded due to high noise levels.

The resultant depolarisation ratios are shown in table 6.9. The table shows that, even without correcting for the solid angle and laser beam cleanness, the measured depolarisation ratio of the S_1-branch agrees with the theoretical values. The reason for this is two-fold. Firstly, the experimental uncertainty is over an order of magnitude larger for these measurements than the corresponding Q_1-branch measurements, due to the lower signal-to-noise ratio. This uncertainty is now larger than the correction due to the solid angle as these measurements have been performed with a small collection angle ($r_f = 1.5\,mm$ with $x_f = 38\,mm$). Secondly, the effect of the laser beam cleanness is less strong when the depolarisation ratio is larger. This can be visualised by using the same considerations as in section 6.6.2 and removing the integral terms from equation (6.3). Now, if we calculate this simplified version of ρ_{calc} for a depolarisation ratio of $\rho_{SP0SA} = 0.75$ i.e. $A = 0.75$ and $B = 1$, for the cleanness of the Swansea Q_1-branch measurements (green data points from figure 6.16), which is $\xi = 0.9995$; the resultant crudely calculated depolarisation ratio is $\rho_{calc} = 0.75022$. The difference between this and the theoretical value is smaller than the experimental uncertainty.

This has shown that the measurement agrees with theory for the vibration rotation lines of the hydrogen isotopologues. The number of lines that have been measured could

Table 6.10: Depolarization ratio measurements of the S_0-branch lines of H_2 (in brackets: measurement uncertainty). The observed depolarisation ratios are compared to the theoretical values from LeRoy [Roy12].

J	ρ_{obs}	$\rho_{LeRoy-532\,nm}$
0	0.750(2)	0.75
1	0.753(1)	0.75
2	0.751(2)	0.75
3	0.750(3)	0.75

be increased by increasing the acquisition time. This would improve the statistics of the measurement.

Depolarisation measurements of the S_1- and O_1-branches of HT measured in TLK have also been included in table 6.9. The details of these measurements are included in Schlösser [Sch13]. These measurements have been included here to demonstrate that the agreement with the literature values of these branches is not limited to the branches of hydrogen. Note, the uncertainty of these measurements is higher and that almost all the measurements agree with the expected value of $\rho = 0.75$, within the experimental uncertainty.

6.8.3 Depolarisation measurements of the S_0-branch of hydrogen

The same measurement procedure as above was followed for the depolarisation measurements of the S_0-branch (pure rotation) of hydrogen. The cleaned measured Raman spectra of both the $\perp^i$ and $\|^i$ excitation polarisation can be seen in the top panel of figure 6.19. The Raman spectrum of SiO_2 in the cell windows is also in this region. However, the SCARF background removal routine is able to remove the Raman spectrum of SiO_2 as it is quite broad. This can be seen by comparing the spectra in the middle panel and bottom panel of the figure. Its presence increases the noise in the region of the $S_0(0)$ and $S_0(1)$ lines. The edge filter suppressed Rayleigh line is also just visible on the spectrum. The transition probability of the pure rotational lines is as high as that of the Q_1-branch. This, combined with the increased quantum efficiency of the CCD detector at this lower wavelength ([Syn09]) of approximately 550 nm, means that the required acquisition time for these spectra was 100 s.

Depolarisation measurements of the four visible S_0 lines of hydrogen were performed, where eight $\perp$- and eight $\|$-excitation polarisation spectra were taken for improved statistics. The depolarisation ratio was obtained using the pairs method and the resultant observed depolarisation ratios are shown in table 6.10. The table shows that the values virtually all agree with the theory without the need for correcting the depolarisation ratios, for similar reasons to the arguments given for the vibration-rotation lines. The

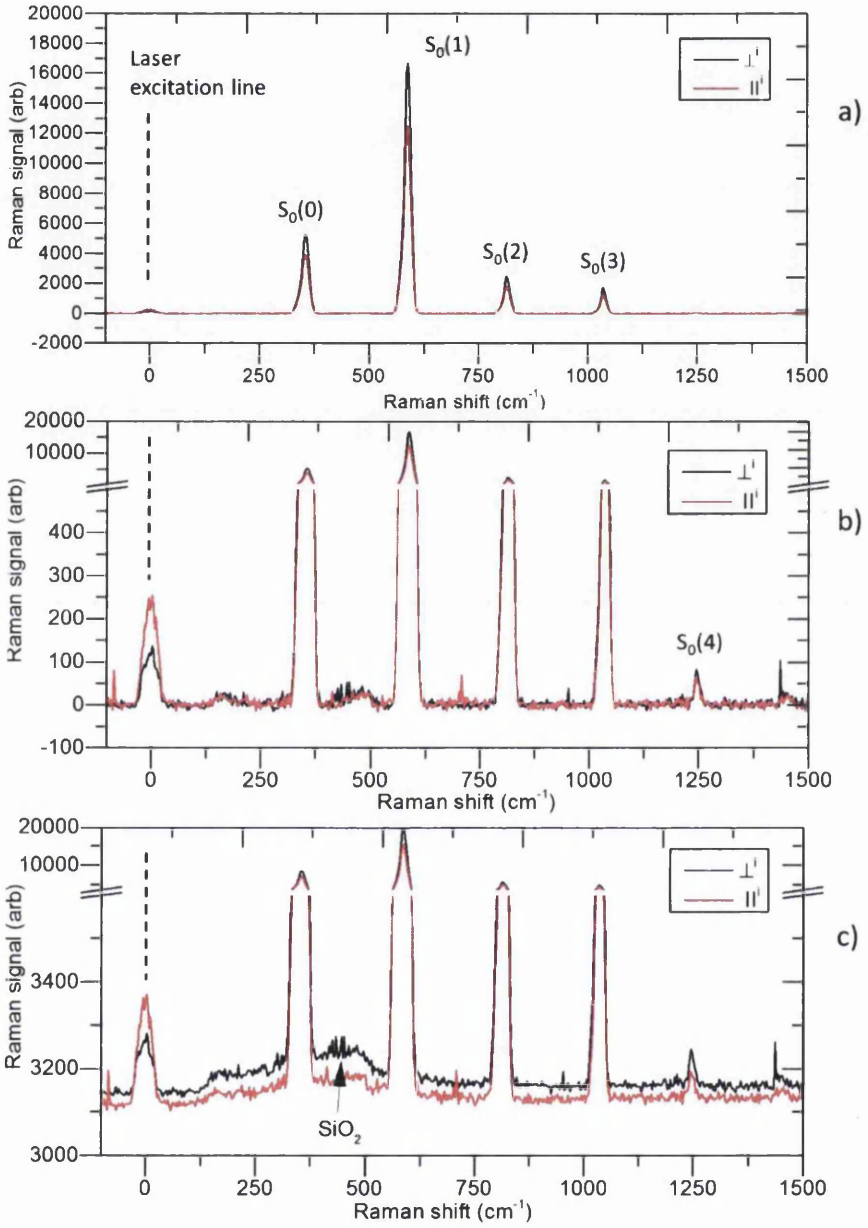

Figure 6.19: Raman spectra (for both $\perp^i$ and $\|^i$ excitation polarisation) of S_0-branch of hydrogen. (a) Top panel: spectra with background removed, (b) middle panel: spectra with background removed zoomed and (c) bottom panel: raw spectra zoomed showing the SiO_2 feature.

only line where correction would make sense is the $S_0(1)$ line, as this has the highest signal-to-noise ratio. It is also the only line measurement which does not agree with the theory without being corrected. The other reason this value could be slightly out is that it is overlaid by the strong SiO_2 Raman feature and additional error could be caused by extracting this feature.

6.9 Accurate Raman shift of non-tritiated hydrogen isotopologues

The line positions of the hydrogen isotopologues are determined for every spectrum that is taken. To accurately determine the Raman shift from these positions, high resolution Raman measurements need to be performed and the laser wavelength needs to be accurately known. To achieve this, the wavelength of the excitation laser needs to be measured accurately. Measurements in chapter 5 show that the laser wavelength of the *Laser Quantum* Excel laser drifts for the first 24 hours of operation. After this, the wavelength remains stable. There is no guarantee that the stabilised position will be the same every time the laser is switched on, due to different environment conditions. Therefore, to accurately determine the Raman shifts of the hydrogen isotopologues the laser wavelength and line positions need to be measured in the same laser switch-on period.

To avoid misaligning the system between measurements, the system was aligned when the Raman cell was filled with a mixture of H_2, HD and D_2, using the Swansea gas mixing system described in appendix A.2. Two 100 s spectra were taken, using the 600gr/mm grating of the SP500 spectrograph centred at 650 nm, to verify that the cell contained a sufficient amount of the three gases H_2, HD and D_2. The spectra had the cosmic rays and background removed using the routines described in appendix A.6. The resultant cleaned spectrum is shown in figure 6.20.

This filling will be used for all subsequent measurements. The wavelength centre and grating of the spectrometer will be changed to enable the Raman line positions to be measured with a sufficient accuracy.

6.9.1 Laser wavelength determination

As described in chapter 2, in a scattered spectrum, the Rayleigh line with the same wavelength as the excitation source is present. The wavelength of this Rayleigh line will be measured to determine the laser wavelength. This is achieved by using the standard Raman setup described above (see figure 6.6), with the 2400gr/mm grating of the SP500 spectrometer centred at 532 nm, with the edge filter removed from the system.

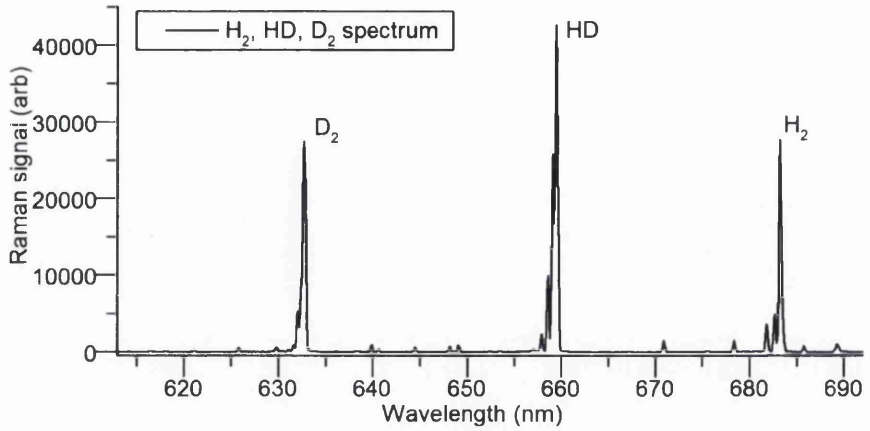

Figure 6.20: Raman spectrum of H_2, HD and D_2. This filling is used to measure the line positions of the Raman lines of the three gases.

Raman spectra of the Rayleigh line were acquired and its wavelength was measured after the laser had been running for a 24 hour period and was determined as $532.08(1)\,\text{nm} = 18794.1(5)\,\text{cm}^{-1}$

6.9.2 Raman measurements of non-tritiated hydrogen isotopologues

High resolution Raman measurements were taken (using the 2400gr/mm grating of the SP500 spectrometer centred at 633 nm, 658 nm, 683 nm) so that the Raman lines of the Q_1-branch of the non-tritiated hydrogen isotopologues could be measured. One lower resolution measurement was taken (using the 600gr/mm grating of the SP500 spectrometer centred at 650 nm) so that the Raman lines of the O_1- and S_1-branches could also be measured. Note that this results in a spectral region between 610 nm and 692 nm, which means that the S_1-branch lines of H_2 are not observable in this region. The acquisition time was set appropriately so that a high signal-to-noise ratio could be achieved without saturating the detector. The resultant measured wavelengths are collated in table 6.11.

The quoted uncertainties in the table are from the fit accuracy. Note that there will also be an uncertainty introduced from the accuracy of the wavelength calibration. As mentioned above, the H_2 Q_1-branch lines were measured using the 2400gr/mm grating of the SP500 spectrograph centred at 683 nm. This results in an observed spectral region between approximately 679 nm and 687 nm. The spectral regions wavelength is calibrated using spectral laps where the wavelength is well known. Of the lamps available, the only one with spectral lines in this region is xenon, and the visible lines only cover half of the spectral region. This will introduce further uncertainty to these values. To obtain a better wavelength calibration, more spectral lamps would need to be

Table 6.11: Measured wavelengths of the non-tritiated hydrogen isotopologues. * fitted using ShapeFit first, - refers to lines below the detection limit, $J = J''$ and uncertainty (in brackets) in the final digit. Note that the H_2 S_1-branch lines are outside of the measured spectral region, so they could not be measured.

	Wavelength $S_1(J)$ / nm			Wavelength $O_1(J)$ / nm		
J	H_2	HD	D_2	H_2	HD	D_2
0	n/a	670.863(1)	639.916(5)	–	–	–
1	n/a	678.349(1)	644.536(2)	–	–	–
2	n/a	685.683(1)	649.083(2)	667.250(4)	648.148(2)	625.828(4)
3	n/a	-	653.542(8)	-	-	621.139(4)

	Wavelength $Q_1(J)$ / nm 2400gr/mm			Wavelength $Q_1(J)$ / nm 600gr/mm		
J	H_2	HD	D_2	H_2	HD	D_2
0	683.424(1)	659.567(1)	632.902(7)*	683.418(2)*	659.564(3)*	632.915(3)*
1	683.149(1)	659.400(1)	632.817(8)*	683.125(2)*	659.405(3)*	632.827(3)*
2	682.603(1)	659.066(1)	632.649(1)	682.573(1)	659.063(3)*	632.672(3)*
3	681.790(1)	658.567(1)	632.396(1)	681.754(2)	658.558(3)*	632.430(3)*
4	680.718(1)	657.905(1)	632.060(1)	680.674(1)	657.898(3)	632.090(9)
5	-	657.087(1)	631.643(1)	679.324(14)	657.097(3)*	631.677(8)
6	-	656.114(3)	631.146(1)	-	-	631.168(7)
7	-	-	630.572(3)	-	-	630.63(4)*

Table 6.12: Measured Raman shift of the non-tritiated hydrogen isotopologues calculated from measured laser wavelength and Raman line positions. For details see text. * fitted using ShapeFit, - refers to lines below the detection limit and uncertainty (in brackets) in the final digit.

	Raman shift $S_1(J)$ / cm^{-1}			Raman shift $O_1(J)$ / cm^{-1}		
J''	H_2	HD	D_2	H_2	HD	D_2
0	n/a	3887.9(5)	3167.0(5)	–	–	–
1	n/a	4052.4(5)	3279.0(5)	–	–	–
2	n/a	4210.1(5)	3387.7(5)	3807.2(5)	3365.5(5)	2815.2(5)
3	n/a	-	3492.8(5)	-	-	2694.6(5)

	Raman shift $Q_1(J)$ / cm^{-1} 2400gr/mm			Raman shift $Q_1(J)$ / cm^{-1} 600gr/mm		
J''	H_2	HD	D_2	H_2	HD	D_2
0	4161.9(5)	3632.6(5)	2993.8(5)*	4161.7(5)*	3632.6(5)*	2994.2(5)*
1	4156.0(5)	3628.8(5)	2991.7(5)*	4155.5(5)*	3628.9(5)*	2992.0(5)*
2	4144.3(5)	3621.1(5)	2987.5(5)	4143.6(5)	3621.0(5)*	2988.1(5)*
3	4126.8(5)	3609.6(5)	2981.2(5)	4126.0(4)	3609.4(5)*	2982.1(5)*
4	4103.7(5)	3594.3(5)	2972.8(5)	4102.8(5)	3594.2(5)	2973.5(5)
5	-	3575.4(5)	2962.4(5)	4073.6(6)	3575.6(5)*	2963.2(5)
6	-	3552.8(5)	2949.9(5)	-	-	2950.4(5)
7	-	-	2935.5(5)	-	-	2937.0(11)*

available that cover the spectral region completely. The additional uncertainty caused by this is visualised in the 600gr/mm Q_1-branch spectral lines, collated in the table, as the difference between the measured wavelengths of the same line using the different gratings.

6.9.3 Raman shift determination

From the measured wavelength positions of the non-tritiated hydrogen isotopologues and the wavelength of the excitation source the Raman shift can be determined for each line by converting the measured wavelength (λ_s) to wavenumber ($\tilde{\nu}_s = 1/\lambda_s$) and then the Raman shift, $\tilde{\nu}_J$, is

$$\tilde{\nu}_J = \tilde{\nu}_0 - \tilde{\nu}_s \tag{6.50}$$

where $\tilde{\nu}_0 = 1/\lambda_0$ and λ_0 is the measured wavelength of the excitation radiation.

The Raman shift can be calculated for all the measured Raman lines of the Q_1-, O_1- and S_1-branches of the non-tritiated hydrogen isotopologues using equation (6.50). The resultant values are collated in table 6.12. The uncertainty in these values is dominated by the laser wavelength uncertainty in all cases except the D_2 $Q_1(J = 7)$ line, measured

Table 6.13: Theoretical Raman (wavenumber) shifts for the first ten lines of the Stokes S_1-, Q_1- and O_1-branches for the non-tritiated hydrogen isotopologues. Shifts of Lewis [Lew07] based on spectroscopic constants B_0, D_0, H_0, $\tilde{\nu}_{vib}$, B_1 and D_1 obtained from Edwards *et al* [Edw78].

	Raman Shift $O_1(J)$ / cm^{-1}					
	from [Lew07]			calculated from [LRoy88]		
J''	H_2	HD	D_2	H_2	HD	D_2
2	3803.669	3363.102	2813.709	3806.774	3365.074	2814.539
3	3556.093	3177.863	2690.820	3568.202	3185.206	2693.963

	Raman Shift $Q_1(J)$ / cm^{-1}					
	from [Lew07]			calculated from [LRoy88]		
J''	H_2	HD	D_2	H_2	HD	D_2
0	4161.140	3632.050	2993.560	4161.147	3632.143	2993.606
1	4155.194	3628.194	2991.439	4155.234	3628.287	2991.497
2	4143.374	3620.478	2987.205	4143.447	3620.593	2987.283
3	4125.824	3608.900	2980.871	4125.855	3609.096	2980.979
4	4102.760	3593.450	2972.460	4102.565	3593.850	2972.604
5	4074.470	3574.120	2962.000	4073.717	3574.922	2962.184
6	4041.314	3550.898	2949.527	4039.478	3552.398	2949.750
7	4003.724	3523.768	2935.085	4000.044	3526.376	2935.338

	Raman Shift $S_1(J)$ / cm^{-1}					
	from [Lew07]			calculated from [LRoy88]		
J''	H_2	HD	D_2	H_2	HD	D_2
0	4497.752	3887.554	3166.264	4497.820	3887.662	3166.350
1	4712.774	4051.954	3278.399	4712.887	4052.177	3278.513
2	4916.762	4209.374	3387.101	4916.990	4209.942	3387.252
3	5107.796	4358.564	3491.855	5108.388	4359.923	3492.084

using the 600gr/mm grating. This has a signal which is approaching the noise level therefore, the fitted uncertainty is higher.

6.9.4 Comparison with theoretical values

These experimentally determined Raman shifts (of the non-tritiated hydrogen isotopologues), can be compared with both the theoretical values determined from the energy levels calculated by LeRoy and the experimental approximated values discussed in chapter 2. The values that can be compared with the measured values above are collated in table 6.13. To enable a more visual comparison, the difference between the theoretical and measured values has been calculated. The difference is plotted vs. the rotational quantum number J for the Q-branch H_2, HD and D_2 in figure 6.21.

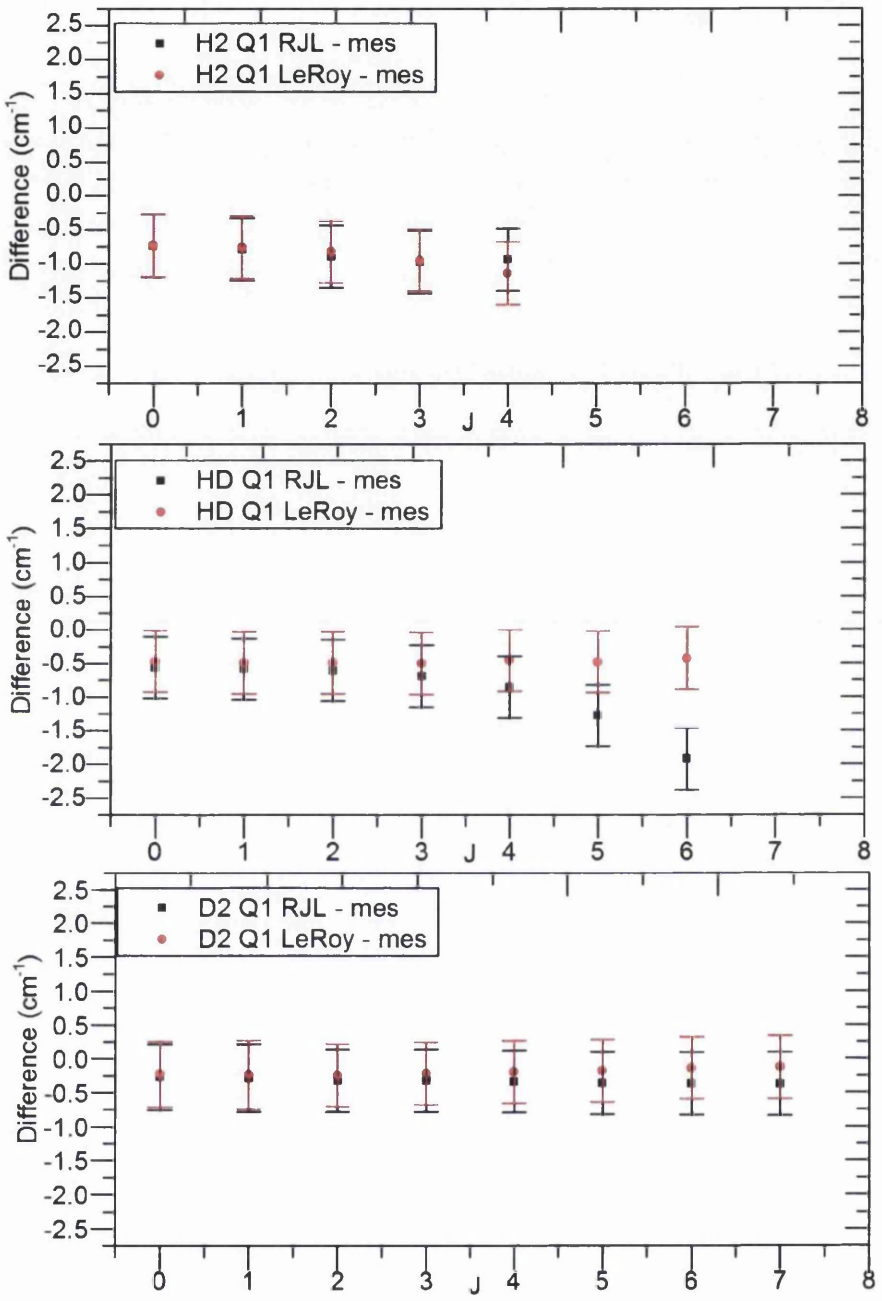

Figure 6.21: Difference between theoretical Raman shift and measured Raman shift for the non-tritiated hydrogen isotopologues. The theory values used are calculated/taken from Schwartz and LeRoy [LRoy88] and Lewis [Lew07]

The figure shows that:

- The measured line positions values of D_2 and the values calculated using the LeRoy data agree within experimental error.
- The line positions of HD and H_2 are offset from the values of LeRoy by $0.5\,\mathrm{cm}^{-1}$ and $\approx 0.8\,\mathrm{cm}^{-1}$ respectively. As these offsets are roughly constant, this could imply that the observed difference is associated with inaccurate wavelength calibration. These shifts correspond to a shift in laser wavelength of 0.013 nm for HD and 0.025 nm for H_2, or a shift of Raman peak position of 0.010 nm for HD and 0.020 nm for H_2.
- The H_2 and D_2 difference values of RJL and LeRoy agree within the experimental uncertainties.
- The HD difference values of RJL increase as J increases. This increase exceeds the experimental uncertainty when $J > 4$. This implies that the HD line position values of RJL are no longer valid for $J > 4$. This is most likely due to the fact that spectroscopic constants from the literature are used, which are incorrect or HD was 'scaled' by reduced mass for H_2 and/or D_2.

A point to note is that the resolution of the 600 gr/mm measurements is too low to produce accurate enough values for a comparison, which affects the accuracy of the measured line position. This means that difference values will not be calculated for the 600 gr/mm grating measurements, as the decrease in resolution makes it more difficult to determine the centre position of the peak; therefore the uncertainty in the Raman shift position is potentially higher than the values quoted in the tables. To accurately measure the positions of the S_1- and O_1-branches, more high resolution spectra would need to be taken.

The conclusions that can be drawn from this line position measurement are:

- The accuracy of Raman shifts determined from measured values is strongly dependent on the accuracy of the wavelength calibration and the laser wavelength. In this case the wavelength calibration for the high resolution measurements of H_2 and HD is less accurate due to an insufficient number of available spectral lines in this region for calibration.
- The measured line positions of the Q-branch of D_2 agree with the line positions of RJL and those calculated from the energy levels of LeRoy within the experimental uncertainty.
- To verify whether the H_2 and HD lines also agree, repeat measurements would have to be performed with a more accurate wavelength calibration, as an offset

in wavenumber shift is observed of approximately $0.8\,\mathrm{cm}^{-1}$ and $0.5\,\mathrm{cm}^{-1}$, respectively.

The same measurement principle can be applied to Raman spectra where all six hydrogen isotopologues are present, to obtain accurate Raman line positions of all six hydrogen isotopologues. This measurement is planned in the near future at TLK and will enable a full comparison with the theoretical and literature values.

Chapter 7

Spectroscopy and depolarisation measurements of atmospheric gases

7.1 Chapter overview

Spectroscopy and depolarisation measurements on the atmospheric gases methane, carbon dioxide, nitrogen and oxygen have been performed. The depolarisation ratios of the various ro-vibrational branches have been successfully determined and compared with the values that are available from the literature. The observed values could be made more accurate by applying the procedure to correct for the solid angle and polarisation aberrations discussed in chapter 6. This hasn't been applied, in this case, as there is not a measurable line corresponding to a theoretically known value. Further, for lines with a depolarisation ratio of $\rho_{\mathrm{SP0SA}} = 0.75$, the experimental uncertainty is too large for a reasonable correction to be applied. A method of accurately determining this correction could be to perform the measurements when the cell also contains hydrogen. The measured depolarisation ratio of the $J = 0$ line of the Q-branch could be used as the reference value to correct the observed values.

There is a lack of reliable literature values of the polarisability matrix elements for nitrogen and oxygen. This means that a similar verification of the depolarisation ratio, as obtained for the hydrogen isotopologues, was not possible.

The isotopic abundances of the different isotopologues in nitrogen, oxygen and carbon dioxide have been verified from Raman intensity ratios. The measured values match the literature values within the experimental uncertainty. A similar verification of the isotopic abundance of the minor isotopologue of methane could not be performed; this feature convolutes with the equivalent branch of the main isotopologue.

Table 7.1: Minor gases in the atmosphere of the earth [Pid06]. * means the abundance is variable.

Gas	Abundance	Raman active?	Important for LIDAR
Argon	9.3×10^{-3}	No	-
CO_2*	3.6×10^{-4}	Yes	Yes
Neon	1.8×10^{-5}	No	-
Helium	5.0×10^{-6}	No	-
CH_4*	1.7×10^{-6}	Yes	Yes
H_2	5.0×10^{-7}	Yes	Yes
Nitrous oxide*	3.0×10^{-7}	Yes	Yes
Ozone*	4.0×10^{-8}	Yes	Yes

7.2 Introduction

In this chapter, the aim is to apply the depolarisation measurement method described in chapter 6 to some of the atmospheric gases. The experimental methodology is summarised below for clarity.

Depolarisation measurements are an useful tool to verify the polarisability tensors, which are needed to obtain the composition of the gas directly from the measured Raman intensities. This is required to quantitatively interpret and evaluate the Raman signals. Quantitative interpretation of Raman signals is required in Raman LIDAR systems [Pou77]. In this case, alternative calibration methods (calibrated samples e.g. HYDE [Sch12c]) are not available (for an open air calibration) therefore, utilising polarisability tensors is the only method of quantifying the measured intensity.

The main molecules present in the atmosphere are nitrogen and oxygen, with abundances of 78.08% and 20.95% respectively. The next main constituent is water vapour, which has an abundance between 0% and 4%. This is the maximum value, as the saturation limit of water vapour is 4%. Some of the remaining minor constituent gases are collated in table 7.1. The table shows that the Raman active gases are CO_2, CH_4, H_2, nitrous oxide and ozone. As hydrogen is studied extensively in this work, extra research is not needed. The natural abundance of CO_2 and CH_4 is on the ppm level. Therefore, Raman measurements of the gases in the atmosphere will be difficult, with very long acquisition times, as high intensities are required to perform depolarisation measurements. However, high gas pressures enable the measurements to be performed accurately. The natural abundance of nitrous oxide and ozone is even lower, but high pressure mixtures would introduce additional complications. When high concentration mixtures of nitrous oxide are produced, clusters start to form and the nitrous oxide is lost. Therefore, the required high concentration (high pressure) mixtures are not possible. Ozone does not occur naturally, so it would need to be produced. This would require additional effort

beyond the scope of this work to produce the required high pressure mixture. As a result of this discussion, the gases that will be measured are nitrogen, oxygen, carbon dioxide and methane.

Alongside the depolarisation measurements of the gases mentioned above, the measured Raman intensities are used to obtain relative isotopologue and hot-band contributions from the measured high resolution spectra.

Some additional theory is required for the non-diatomic molecules of methane and carbon dioxide, to enable a full interpretation and evaluation of the spectra. Each of the monitored atmospheric gases will be discussed separately, with the extra information required to enhance the understanding included.

7.2.1 Methodology

Raman spectra of the chosen atmospheric gases are acquired using the standard 90° Raman setup in this work, described in detail in chapters 4 and 6. For clarity, the method of obtaining depolarisation ratios is summarised here.

Traditionally, the depolarisation ratio is measured as the ratio of scattered light intensities $I_\perp$ and $I_\parallel$, i.e. $\rho = I_\parallel / I_\perp$, where $I_\parallel$ and $I_\perp$ are the intensities of the scattered light with polarisations parallel and perpendicular to the polarisation plane of the incident laser beam, respectively.

For comparison with theory, the theoretical ratio is only valid for a pure 90° collection geometry. In reality, Raman signals are collected over an extended solid angle to maximise the collected light intensity. This leads to rays with different angular dependent polarisation being collected. This is taken into account by integrating the intensity over the known measured solid angle and fitting the measured depolarisation data to the solutions. This is discussed in more detail in chapter 6. The described procedure allows experimental and theoretical depolarisation ratios to be compared.

As the ratio of perpendicular polarisations is measured, the cleanness, ξ, of the laser beam's polarisation influences the measured depolarisation ratio. The cleanness can be expressed mathematically as $\xi = \cos^2 \alpha$, where α is the angular deviation from the vertical ($\perp$) polarisation direction.

In the method described in chapter 6, this cleanness is taken into account. In the measurements here, the polarisation cleanness was kept high to minimise this effect.

To calculate a statistical uncertainty of the depolarisation ratio, repeat measurements of $I_\perp$ and $I_\parallel$ are required. This enables a spectrum with less noise to be produced, when discussing the content of the chosen scattering substance (atmospheric gas). Before any intensity was extracted, the background and cosmic rays were removed from the spectra, using the routines described in appendix A.6. The intensity is then extracted from the spectra by either integrating the Raman peak or taking the peak height. The method used is indicated along with the results.

Table 7.2: Isotopes in stable isotopologues of CH_4 (from [Ber11] and NIST).

Isotope	Mass number / amu	Nuclear spin	Abundance	Raman detectability in natural mixture
^{1}H	1.00782503207(10)	+1/2	0.999885(70)	Yes
^{2}H	2.0141077778(4)	+1	0.000115(70)	too low
^{12}C	12	+0	0.9893(8)	Yes
^{13}C	13.0033548378(10)	-1/2	0.0107(8)	maybe

7.3 Raman depolarisation spectroscopy of methane

Methane has been a subject of many spectroscopic studies, as it is one of the greenhouse gases and is used in a wide range of technical applications. In most of these studies the spectroscopy method of choice is absorption spectroscopy, such as the highly-sensitive method of tuneable diode laser absorption spectroscopy TDLAS [Nag96]. However, some of the vibrational energy levels and modes are not infra-red (IR)-active. Therefore, they are not accessible to absorption techniques. Raman spectroscopy has the advantage that, in principle, all of the energy levels and modes are accessible. However, some of the bands may have a really low excitation probability, so they are not particularly useful in analytical applications.

7.3.1 Isotopic composition of methane

The main parent molecule of methane is $^{12}CH_4$. Beyond this molecule there are a number of isotopologues where the carbon or hydrogen atom are substituted by one of the (stable) isotopes. It should also be noted that the unstable (radioactive) isotopes ^{14}C and ^{3}H (or T) form isotopologues, even though they only exist naturally in trace amounts. Therefore, they also need to be considered. This was observed in the long-term studies of the KATRIN loop system LOOPINO (conducted by other members of the KATRIN LARA group see Fischer *et al* [Fis11]), with tritium flowing through the system significant measurable amounts of $CT_{4-x}D_x$ isotopologues were observed.

If one limits the task to detecting methane in the atmosphere, the isotopolgues with natural abundances within the detectability of the LARA system in Swansea need to be considered. The only detectable isotopolgue is $^{13}CH_4$ with abundance of approximately 1% of naturally occurring methane. The isotopes in the stable isotopologues of methane are collated in table 7.2 for clarity.

7.3.2 Ro-vibrational energy levels and transitions

To determine the structure of the Raman spectra that will be observed, the ro-vibrational energy levels need to be calculated. To do this, the symmetry of the molecule in question

needs to be considered. Methane is the simplest totally symmetric polyatomic molecule. It belongs to the tetrahedral symmetry group T_d. Therefore, it is a test case in many experimental and theoretical studies and has been studied extensively in the literature. For a full detailed description see Herzberg [Her89].

The molecule may appear to be simple. However, the observed spectra are quite complicated due to Coriolis splitting and interactions between ro-vibrational levels, which lead to perturbation of the rotational bands. Coriolis splitting is caused by the Coriolis force, which only occurs for moving particles. For more information see Johnston and Dennison [Joh35].

The tetrahedral symmetry group has two non-degenerate (A_1 and A_2), one doubly degenerate (E) and two triply degenerate (F_1 and F_2) symmetry types . The number reduces to only four vibrational bands occurring, one degenerate vibration $\nu_1(A_1)$, one doubly degenerate vibration $\nu_2(E)$ and two triply degenerate vibrations $\nu_3(F_2)$ and $\nu_4(F_2)$ (for more details see Herzberg [Her89]). There is also a pure rotational mode which has the symmetry A_1. These modes are only 'infra-red active' if the vibration is connected with a change in dipole moment. In symmetric molecules vibrations occur where the change in dipole moment is exactly zero, therefore, these modes would be 'infra-red inactive'. In methane this is the case for the ν_1 and ν_2 modes. Raman spectroscopy has the advantage that this limitation doesn't apply and all of the modes are Raman active to a certain degree.

The first mode to consider is the non-degenerate mode ν_1. The rotational levels of non-degenerate states are similar to that of the diatomic molecule (see chapter 2) and is expressed as F_ν

$$F_\nu = B_\nu J(J+1) - D_\nu J^2(J+1)^2 \tag{7.1}$$

Often the correction term, D_ν, is omitted, as it is small for small rotational quantum numbers.

The Raman modes with a degeneracy have the extra complication that the Coriolis forces that occur in the rotating molecule, may lead to an interaction between mutually degenerate vibrations. This interaction then could lead to a splitting of the degeneracy. As described above, the degenerate modes of methane are the ν_2, ν_3 and ν_4. The vibrational mode, ν_2, is of the doubly degenerate group E. If one component of the doubly degenerate vibration is excited the Coriolis force does not excite the other component. This means that no Coriolis splitting occurs for the doubly degenerate vibrational states and the rotational energy levels are the same as for the non-degenerate vibrational states as given by equation (7.1) (for more details see Herzberg [Her89]). The triply degenerate modes (ν_3 and ν_4) get influenced by the Coriolis force and Coriolis splitting occurs. Splitting occurs into three components, one having the original frequency while the other two are linear combinations of the vibrations that interact with each other. The

rotational levels of the splitting of these three modes are given as ([Her89] and [Den40])

$$F_\nu^{(+)} = B_\nu J(J+1) + 2B_\nu\zeta_i(J+1) \tag{7.2}$$

$$F_\nu^{(0)} = B_\nu J(J+1) \tag{7.3}$$

$$F_\nu^{(-)} = B_\nu J(J+1) - 2B_\nu\zeta_i(J+1) \tag{7.4}$$

where ζ_i is the magnitude of angular momentum associated with the superposition of the Coriolis-induced circular motion coupling, in units of $\hbar$.

The spectroscopic constants that are required to calculate the line positions of $^{12}CH_4$ and $^{13}CH_4$ are collated in table 7.3. Please note that many compilations of the line positions do not use these values, but list the line positions themselves taking perturbations into account. This is the case in Pine [Pin76] or the HITRAN 2004 molecular spectroscopic database [Hit04].

7.3.3 Selection rules for Methane

Analogous to the selection rules for Raman scattering of diatomic molecules discussed in chapter 2, selection rules verifying the allowed transitions of the more complicated molecules will need to be discussed. The selection rules for tetrahedral (symmetric) molecules are less restrictive than those for diatomic molecules (see chapter 2). Energy levels are found with the following selection rule for the angular momentum, J

$$\Delta J = 0, \pm 1, \pm 2 \tag{7.5}$$

when $J' + J'' \geq 2$. When the Raman mode is totally symmetric, this rule is reduced to $\Delta J = 0$ as, during the whole vibrational motion, the polarisability ellipsoid remains spherical. For the degenerate modes, only rotational levels of the same species can combine with one another. As a result of these selection rules, the totally symmetric ν_1 band's only observable feature is one strong "narrow" feature, which is the superposition of all the Q_1-lines. To give an example of the expected number of lines for a degenerate level, the ν_3-band will be considered. For the transition from the A_1 ground state to each of the $F_2^{(+)}$, $F_2^{(0)}$ and $F_2^{(-)}$ 15 branches occur (5 for each sub-band).

The notation of the branches that is linked to the selection rules is given in table 7.4.

7.3.4 Measured spectra

Raman spectra of methane were taken in the 90° Raman configuration used for the depolarisation measurements of the hydrogen isotopologues described in chapter 6. The LARA cell was filled with approximately 1000 mbar of methane. Nine repeat Raman spectra were taken for the $\perp^i$ and $\|^i$ incident laser polarisation, using the high resolution

Table 7.3: Vibrational and rotational term constants and Raman features for methane (in units of cm^{-1}). From [Bou06] and [Sto51]. const* are obtained experimentally.

Level / Band	**Vib const**	**Vib const***	**B** [Bou06]/[Sto51]	ζ [Bou06]/[Sto51]	**D** [Sto51]
$^{12}CH_4$					
Ground state					
A_1	0.000		5.240/5.253		1.9×10^{-4}
Dyad system					
F_2 ν_4	1310.762				
E ν_2	1533.336	1533.6	5.313/5.379		
Pentad system					
A_1 $2\nu_4$	2587.040				
F_2 $2\nu_4$	2614.262				
E $2\nu_4$	2624.618				
F_2 $\nu_2 + \nu_4$	2830.312				
F_1 $\nu_2 + \nu_4$	2846.078				
A_1 ν_1	2916.482	2916.7			
F_2 ν_3	3019.493	3018.9	5.178/5.204 5.195/5.217 5.212/5.235	0.054/0.056	1.4×10^{-4} 1.8×10^{-4} 3.8×10^{-4}
A_1 $2\nu_2$	3063.643				
E $2\nu_2$	3065.142				
$^{13}CH_4$					
Ground state					
A_1	0.000				
Dyad system					
F_2 ν_4	1302.781				
E ν_2	1533.493				
Pentad system					
A_1 $2\nu_4$	2572.099				
F_2 $2\nu_4$	2598.640				
E $2\nu_4$	2608.739				
F_2 $\nu_2 + \nu_4$	2822.451				
F_1 $\nu_2 + \nu_4$	2838.203				
A_1 ν_1	2915.442				
F_2 ν_3	3009.545				
A_1 $2\nu_2$	3063.962				
E $2\nu_2$	3065.461				

Table 7.4: Branch notation for Raman spectra of methane

Branch	ΔJ
O(J)	-2
P(J)	-1
Q(J)	0
R(J)	+1
S(J)	+2

(2400gr/mm) grating of the SP500i spectrograph, centred so that the fundamental ν_1 mode and the ν_3 and $2\nu_2$ modes could be measured. The method described in section 7.2.1 was used to obtain the depolarisation ratios from the measured spectra.

As is shown in chapter 5 and in Alshahrie [Als11], even when the Excel 2W laser is stabilised, using water cooling, the centre wavelength drifts as the laser is heating up for a period of approximately 24 hours. This drift has to be taken into account when calculating the depolarisation ratio and averaging multiple spectra.

The analysis method to determine the depolarisation ratios for methane is slightly different to the one used in chapter 6. The theoretical depolarisation ratios of the ν_1 and ν_3 modes of methane are $\rho_{\mathrm{SP0SA}} = 0$ and $\rho_{\mathrm{SP0SA}} = 0.75$ respectively [Yu07]. Due to the complexity of the Raman spectra, it proves useful to separate the branches that fully depolarise from the branches that do not. This enables one to identify the branches that depolarise more easily. The subtraction is achieved by multiplying the measured $\|^i$ spectrum by 4/3 to obtain $4/3I_{\|^i}$. This is subtracted from the measured $\perp^i$ spectrum. This means that any branch with a depolarisation ratio of 0.75 is subtracted from the $\perp^i$ spectrum to leave the branches that fully depolarise on their own. Note any laser wavelength shift needs to be corrected for to utilise this subtraction method.

To correct for the wavelength drift during the repeated measurements, the peak position of the main ν_1 peak is recorded for each measurement and the spectra are shifted to bring all the repeats into alignment; an average can be performed to reduce the noise of the spectrum increasing the accuracy of any extracted data. The resultant averaged spectra for the $\perp^i$ and $\|^i$ polarisations and the difference spectrum removing the branches with a depolarisation ratio of 0.75, is shown in figure 7.1. The figure identifies the observed Q-branches for the vibrational modes (ν_1, ν_3 and $2\nu_2$). The P(J"), R(J"), O(J") and S(J") branches are those of the ν_3 mode. The lines are annotated using the assignment of Herranz and Stoicheff [Her63].

As the figure contains a vast amount of spectral information the modes will be considered separately. The ν_1 mode and its Q-branch will be considered first.

The spectra in figure 7.1 clearly show that the Q-branch of the ν_1 mode "vanishes" when switching from $\perp^i$ to $\|^i$ polarisation of the incident laser beam, as is expected

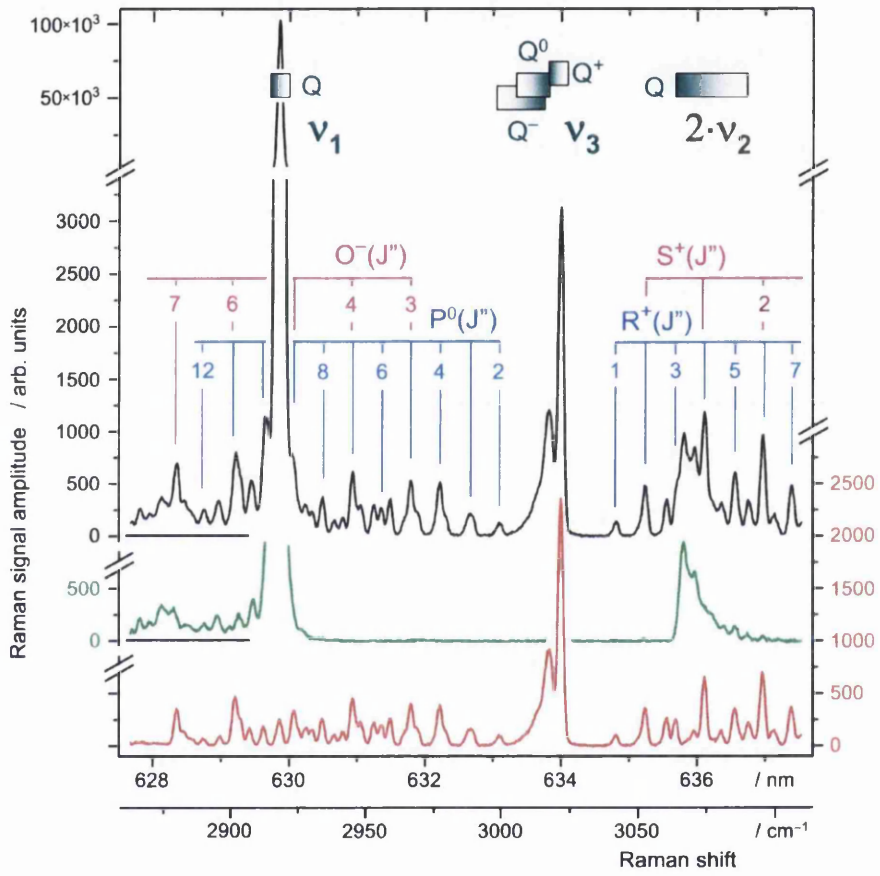

Figure 7.1: Raman depolarisation spectra of CH_4. Black (top) / red (bottom) traces: signals due to $\perp^i$-pol and $\|^i$-pol laser excitation. Green (middle) trace: $\rho = 0.75$ signal component extracted, isolating overtone band.

from the theory. However, at the peak location of the branch ($\approx 2017\,\mathrm{cm}^{-1}$) a small signal is still visible. The depolarisation investigations of the hydrogen isotopologues in chapter 6, showed that the line should not completely disappear, due to the solid angle contributions and imperfect cleanness of the laser beam induced by the cell windows. This residual signal appears to be larger than would be expected in this case. This can be explained as follows

- When assigning the line positions it becomes apparent that the line position of the Q-branch of $CH_4(\nu_1)$ almost exactly overlaps with the $P^-(J'' = 9)$ line of $CH_4(\nu_3)$.

- By measuring the intensity pattern of the neighbouring P^- lines ($J'' = 11$, 8, 7 and 6) the expected intensity should be lower than the measured peak at $\approx 2017\,\mathrm{cm}^{-1}$

- The theoretical/experimental ultra-high resolution spectra of the Q-branch of $CH_4(\nu_1)$, by Jourdanneau *et al* [Jou05], reveal that the bulk of the expected intensity is within $\approx 1\,\mathrm{cm}^{-1}$, centred at $2916.7\,\mathrm{cm}^{-1}$. This width is the same order as the spectral resolution of the measurements here.

As a result, one can state that the observed peak in the $\|^i$ spectrum is a superposition of contributions from the $P^-(J'' = 9)$ line of $CH_4(\nu_3)$

Looking at the spectra in figure 7.1 in more detail, a few observations about the Raman spectrum of methane can be made. Firstly, the spectrum is dominated in the intensity domain, by the $CH_4(\nu_1)$ Q-branch by about a factor of 30 with respect to the $CH_4(\nu_3)$ Q-branches. Whereas, in the spectral domain the $CH_4(\nu_3)$ rotational branches dominate.

Secondly, one would expect to observe the isotopologue $^{13}CH_4(\nu_1)$, from the intensity point of view, as this should be $\approx 1\%$ of the $^{12}CH_4(\nu_1)$ signal. However, the wavenumber shift of this isotopologue is only $\approx 1\,\mathrm{cm}^{-1}$ from the $^{12}CH_4(\nu_1)$. This shift is not large enough to resolve the line at the measured resolution. The ν_3 band of the isotopologue $^{13}CH_4$ should be visible from a spectral shift point of view, as it is expected to be shifted by about $10\,\mathrm{cm}^{-1}$ closer to the laser wavelength than the corresponding $^{12}CH_4$. Based on the expected isoptopologue amount of 1% of $^{12}CH_4$, the Q^+-branch signal amplitude would only be expected to have an intensity of approximately 30. This is visible as a tail of the $^{12}CH_4$ $Q^0 + Q^-$ branches, and can be observed by expanding the scale in the relevant region in figure 7.1 as the background/shot noise in this area is only approximately 10 counts.

Thirdly, a small contribution from the $CH_4(2\nu_2)$ overtone band is visible in the spectrum, with a signal amplitude of about half that of the $CH_4(\nu_3)$ Q^+-branch.

Table 7.5: Intensities of Raman features of CH_4 (in arb. units). For details on the acquisition parameters see text. The depolarisation ratios of the ν_1 and ν_3 modes are calculated from the integrated intensities over the line profile(s) (ρ_{int}) and from the central peak amplitude(s) (ρ_{Amp}); the depolarisation ratio of the Q_1-branch of the $2\nu_2$ mode is derived from the total amplitude only. n/a means not available and n = noise.

Vib mode	**Band**	$\perp^i$-pol	$\parallel^i$-pol	ρ_{Amp}	ρ_{int}
detec limit		$P_{max}(\nu_1)$: ≈ 100000	P_{min} $(2\sigma_n)$:≈ 10	< 0.0001	n/a
ν_1 ($2917\,cm^{-1}$)	all Q	P:102230(108)	P:247(8)	$< 0.00242(8)$	–
		$\int$:930236	$\int$:2445	–	< 0.003
ν_3 ($3019\,cm^{-1}$)	Q^+	P:3125(20)	P:2344(18)	0.750(8)	–
	$Q^+ + Q^0 + Q^-$	$\int$:62458	$\int$:47166	–	0.7552
	$S^+(0)$ & $R^+(2)$	P:478(8)	P:359(7)	0.751(19)	–
		$\int$: 5567	$\int$:4205	–	0.7553
	$P^0(4)$	P:513(8)	P:388(7)	0.756(18)	–
	All P(4)	$\int$:7333	$\int$:5539	–	0.7554
	full ν_3	$\int$:109539	$\int$:82547	–	0.7550
$2\nu_2$ ($3066\,cm^{-1}$)	all Q	P: 949(30)	n:$\approx \pm 5$	$< 0.0053(30)$	n/a
ν_2 ($1533\,cm^{-1}$)	all Q				
Lit [Yu07]	ν_1(Q)			0.002(2)	
	ν_3(Q)			0.752(3)	
	ν_3(O,P,R,S)			0.752(5)	J = 6,7,8
Theory	ν_1(Q)			0	
	ν_3(Q)			0.75	
	ν_3(O,P,R,S)			0.75	

7.3.5 Analysis of the depolarisation measurements of methane

The depolarisation ratios of methane can be obtained from the analysis of the spectra displayed in figure 7.1. As stated above, the resultant spectra consist of an average (over nine individual spectral acquisitions each of 150 s) for each polarisation, where the spectral background and cosmic rays have been removed. The peak amplitude and area have been extracted from the three modes of the pentad system, namely the ν_1, ν_3 and $2\nu_2$ modes. The resultant amplitudes and depolarisation ratios for both are collated in table 7.5.

From the table, the following conclusions can be drawn

1. For the ν_1-mode (symmetric stretch) and the ν_3-mode (asymmetric stretch) the depolarisation ratios are as expected, approaching zero and 0.75, respectively.

2. The observed depolarisation ratio of the ν_1-mode gives an upper limit, since its Q-branch overlaps completely with the $P^-(J'' = 9)$ line of $CH_4(\nu_3)$. Analysing the amplitudes of the neighbouring resolved $P^-(J'')$ ($J'' = 4, 5, 6, 7, 8$ and 11) lines suggests that the contribution from the $P^-(J'' = 9)$ line is above $30 - 40\%$ of the signal at the relevant spectral location.

3. The depolarisation ratio of the overtone band $2\nu_2$ seems to be close to zero.

The values in the table could be brought closer to the theoretical values by applying the solid angle correction used in the depolarisation measurements of the hydrogen isotopologues. The laser beam cleanness would have to be calculated using one of the ν_3 modes, as the ν_1 mode is not sufficiently resolved. However, as the uncertainty of the ν_3 branch ratios is higher, very little can be gained by using the correction procedure here.

7.4 Raman spectroscopy of carbon dioxide

The spectroscopy of carbon dioxide has been extensively covered in the literature (e.g. Langseth and Nielsen [Lan34], Garrabos *et al* [Gar80]). In atmospheric measurements it is the main greenhouse gas. To enable quantifiable measurements of the composition, the transition function of the molecule would need to be known accurately, as is the case for the hydrogen isotopologues (see chapter 6). Raman spectroscopy is an useful technique to use with carbon dioxide as the Raman bands are infra-red inactive and the infra-red active bands are Raman inactive, as is explained below.

7.4.1 Isotopic composition of carbon dioxide

The main parent molecule of carbon dioxide is $^{12}C^{16}O_2$. Analogous to methane, there are also a number of isotopologues where the carbon or oxygen atom is replaced by one of the other isotopes of carbon or oxygen. If this discussion is limited to the isotopologues that could be observed in the atmosphere the isotopic ratios used for methane can be used. The abundances of the oxygen isotopes and the possible carbon dioxide isotopologues are shown in table 7.6.

The isotopic composition can be verified using Raman spectroscopy, by measuring the intensities of the observed isotopologues. The comparison is limited to like-for-like branches i.e. a ratio of the ν_1 branch of $^{13}C^{16}O_2$ and the ν_1 branch of $^{12}C^{16}O_2$. The reason for doing it this way can be explained by looking at the Raman intensity equation.

$$I(\theta; p^s, p^i) = K\tilde{\nu_0}(\tilde{\nu_0} - \tilde{\nu}_{v,J})^3 g_i N_i \Phi(a^2, \gamma^2, \theta)\mathcal{I} \tag{7.6}$$

As the measurements of the isotopologues are performed in the same sample, the laser

Table 7.6: Isotopes in stable isotopologues of CO_2 and resultant CO_2 isotopologues Berglund and Wieser [Ber11] and HITRAN 2004 molecular spectroscopic database [Hit04]

Isotope	Mass number / amu	Nuclear spin	Abundance
^{16}O	15.995	0+	0.99757
^{17}O	16.999	5/2+ (Fermion)	3.80×10^{-4}
^{18}O	17.999	0+	2.05×10^{-3}
$^{12}C^{16}O_2$			0.98420
$^{12}C^{16}O^{18}O$			0.003947
$^{12}C^{16}O^{17}O$			0.000734
$^{13}C^{16}O_2$			0.01106
$^{13}C^{16}O^{18}O$			0.000044
$^{13}C^{16}O^{17}O$			0.000008

irradiance $\mathcal{I}$ is the same. The Raman lines are reasonably close together, so the assumption can be made that the constant, K, is the same for both lines, as the spectral efficiency will not change much over this region and the Raman shift is approximately the same. As the isotopologues are similar, one can assume that the line strength functions will be approximately the same for both isotopologues. This means that, if a ratio of two of the isotopologues within the same spectrum is taken giving:

$$\frac{I_1(\theta; p^s, p^i)}{I_2(\theta; p^s, p^i)} \approx \frac{g_{i1} N_{i1}}{g_{i2} N_{i2}} \tag{7.7}$$

where the subscripts 1 and 2 denote separate isotopologues within the same spectrum. This gives sufficient information to compare the isotopic composition with the expected theoretical value.

7.4.2 Ro-vibrational energy levels and transitions

Analogous to methane, the symmetry of carbon dioxide needs to be discussed to determine the expected Raman spectrum of carbon dioxide. Carbon dioxide is a triatomic molecule that is linear and symmetrical. It is in point group $D_{\infty h}$ and has a centre of symmetry. This means, from the rule of mutual exclusion, that transitions allowed in the infra-red are forbidden in the Raman spectrum and visa-versa. This, however, does not mean that, if a transition is forbidden in the Raman effect, it has to occur in the infra-red; transitions can be forbidden in both.

Molecules of point group $D_{\infty h}$ have three fundamental vibrations, ν_1, ν_2 and ν_3, which correspond to the symmetry types Σ_g^+, Σ_u^+ and Π_u. The ν_2 bending mode consists of two modes of the same frequency, which forms a degenerate pair. The theory of Herzberg [Her89] shows that the vibrational level of ν_1 is very close to the overtone of

the vibrational level ν_2 i.e. $2\nu_2$. This leads to an accidental degeneracy between the two vibrational levels, known as a Fermi resonance [Den40]. This leads to a shift in the observed vibrational level of ν_1 and $2\nu_2$ (one is shifted up, the other is shifted down) and two equally intense Raman lines are expected to be observed. The shift (perturbation) of the lines is caused by anharmonic vibrational coupling terms in the potential energy of the molecule [Ama65]. These lines can no longer be assigned directly to ν_1 and $2\nu_2$, but are both mixtures of the two vibrational levels. The two levels are referred to as the Fermi diad [Ros95]. The true mixing occurs between the totally symmetric ν_1 (Σ_g^+) and the symmetric part of the overtone $2\nu_2$. In full derivations of molecules of point group $D_{\infty h}$, there is also a contribution to point group $2\nu_2$ from the species Δ_g. However, this is much weaker than the resonance described above, so is not usually observed in the Raman spectrum of carbon dioxide.

Hot bands

Measured spectra of CO_2, in the literature, show the Fermi diad has two bands that flank it. These bands are referred to as hot bands. The hot bands arise from transitions that start from excited vibrational energy states. Their population is induced by thermal energy in the molecules. Therefore, the intensity of hot bands is a function of the sample temperature and the energy difference from the ground state. The hot bands also undergo Fermi resonance, which results in a shift from the expected locations.

Many studies have been performed that show the Fermi diad spacing is gas-density dependent (e.g. Howard-Lock and Stoicheff [HLo71], Wang *et al* [Wan11]). For a full discussion on the spectrum of carbon dioxide the reader is referred to Herzberg [Her89]. The expected locations of the Fermi resonance of the two Raman bands, ν_1 and $2\nu_2$, along with the hot bands, are shown in table 7.7.

7.4.3 Measured spectra

Raman spectra of carbon dioxide were recorded using the 90° Raman configuration, as used for the depolarisation measurements of the hydrogen isotopologues described in chapter 6. The LARA cell was filled with approximately 1000 mbar of carbon dioxide. Twenty repeat Raman spectra each with a 1400 s exposure time, were taken for the $\perp^i$ and $\|^i$ incident laser polarisation, using the high resolution (2400grpmm) grating of the SP500i spectrograph. The chosen acquisition time was selected to maximise the signal-to-noise ratio. The grating of the spectrometer was centred, so that the fundamental Fermi diad of the ν_1 and $2\nu_2$ modes and the hot bands, as identified in table 7.7, can be observed. The background and cosmic rays were removed from the spectra, using the routines described in appendix A.6. An averaged spectrum of three of the 20 repeats of the $\perp^i$ polarisation is shown in figure 7.2. In the figure, the modes of the Fermi

Table 7.7: Expected Raman shifts in the region of the Fermi diad of carbon dioxide and its isotopologues from the literature and the measured values from this work. * means convoluted with another line

Level / Band	**Raman shift** cm^{-1}	**Raman shift** cm^{-1}	**Raman shift** cm^{-1}
	lit [Ros95]	lit [Dic29]	obs
$^{12}C^{16}O_2$			
ν_1	1388.2	1387.7	1387.72(15)
$\nu_1, 1-2$	1409.0	1408.4	1408.78(15)
$\nu_1, 2-3$			1424.48(15)
$2\nu_2$	1285.4	1285.1	1284.58(15)
$2\nu_2, 1-2$	1264.8	1264.5	1264.12(15)*
$2\nu_2, 2-3$			1248.32(15)
$^{13}C^{16}O_2$			
ν_1	1370.0		1369.00(15)
$2\nu_2$			1264.12(15)*
$^{12}C^{16}O^{18}O$			
ν_1			1366.52(15)
$2\nu_2$			1257.52(15)

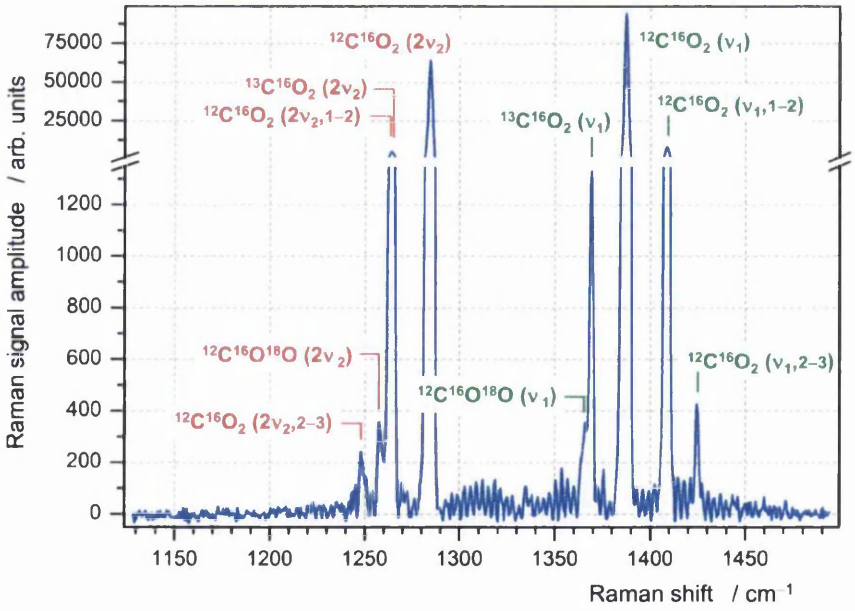

Figure 7.2: Raman depolarisation spectrum of CO_2; only the $\perp^i$-polarised signal component is shown, revealing isotopologues and vibrational hot bands.

Table 7.8: Measured isototopologue abundances of the low abundance isotopologues of carbon dioxide compared with the expected theoretical value. The experimental uncertainty is in the last digit.

	abundance	
	measured	**theoretical**
$^{13}C^{16}O_2$ / $^{12}C^{16}O_2$	0.01085(34)	0.01082
$^{12}C^{16}O^{18}O$ / $^{12}C^{16}O_2$	0.00355(47)	0.00401

diad, the corresponding hot bands and the Fermi diad of the isotopologues $^{13}C^{16}O_2$ and $^{12}C^{16}O^{18}O$ are observed. These are identified using the expected Raman shifts from the literature included in table 7.7. For comparison purposes, the measured Raman shifts from this spectrum are also included in the table. This shows that these peaks do correspond to the values in the literature. A point to note is that an exact match is not necessarily expected, as the Fermi diad spacing is affected by the density of the gas in question.

The intensities of this measured spectrum are extracted and the isotopologue abundance can be calculated for the low abundance isotopologues, $^{13}C^{16}O_2$ and $^{12}C^{16}O^{18}O$. The measured isotopologue abundances are collated in table 7.8 and compared with the theoretical values. The comparison shows that the isotopologue abundances are in good agreement with the expected theoretical value. Both of the measured values agree with the theoretical values, within the experimental uncertainty.

The Fermi diad bands in the Raman spectrum of CO_2 are dependent on the particle density of the sample. The Raman shift decreases with increasing density and the $2\nu_2$ band location is more dependent on the gas density than the ν_1 band. The intensity ratio $I_{\nu_1} : I_{2\nu_2}$ increases with density, i.e. the intensity of the ν_1 band increases and the intensity of the $2\nu_2$ band decreases [Gar80]. In most cases, this shift could be directly related to the environment of the gas mixture. However, in the case of CO_2, the shifts are more complicated due to the Fermi resonance of the two bands and the observed lines are both mixtures of the states ν_1 and $2\nu_2$. Rosso and Bodnar [Ros95] state that, for the pressure range in use (which is the same as here), the known nature of the coupling phenomenon can be used to describe the changes to the individual $2\nu_2$ and ν_1 excited states; this is beyond the scope of this work and will not be discussed further here.

By extracting the intensity from the hot bands and calculating the intensity ratio between the hot bands and the normal ground state excitation, the temperature of the sample can be extracted. This is because the population of the vibrational states in the sample is governed by the Boltzmann distribution, which depends on the temperature of the sample. Following the theory of Rosso and Bodnar, the intensity ratio of the hot

bands is

$$\frac{I_{\nu_1,1-2}+I_{2\nu_2,1-2}}{I_{\nu_1}+I_{2\nu_2}}=\frac{(\nu_0-\nu_{\nu_1,1-2})^4+(\nu_0-\nu_{2\nu_2,1-2})^4}{(\nu_0-\nu_{\nu_1})^4+(\nu_0-\nu_{2\nu_2})^4}\omega_{\nu_2}e^{-hc\nu_2/kT} \tag{7.8}$$

The intensities are taken as the areas under the band peaks, h is planks constant, c is the speed of light (cm/s), ν_2 is the frequency of the Raman shift of the ν_2 mode, $\omega_{\nu_2}=2$ is the degeneracy of the ν_2 mode of CO_2 and the ν terms are the observed frequencies of the lines in units of cm^{-1}. Rearranging the equation leads to the temperature of the sample. The temperature has been calculated for three situations

- The situation as highlighted in equation (7.8),
- The ratio of the ν_1 hot band only,
- The ratio of the $2\nu_2$ hot band only.

This leads to temperatures of $T=31.75\,°C$, $T=35.56\,°C$ and $T=26.05\,°C$, respectively. The accuracy of the measurement of the temperature is reduced, due to the increased complexity of the Raman band structure, caused by the Fermi diad coupling. Even though the accuracy of this measurement appears to be quite low, the average of the calculated temperatures are a few degrees above room temperature. This may reflect the elevated temperature in the Raman enclosure. This was not monitored during the measurement, so it cannot be verified.

7.4.4 Analysis of the depolarisation ratios of carbon dioxide

The depolarisation ratios of carbon dioxide can be calculated from the measured data described above. The peak amplitude and peak area for the labelled peaks were extracted after the background and cosmic rays were removed from the spectra for the main isotopologue of carbon dioxide. The observed depolarisation ratio was then calculated from the intensities of the $\perp^i$ and $\|^i$ measurements. The measured intensities and depolarisation ratios are collated in table 7.9. The quoted depolarisation ratios are the observed values. Note that these have not been corrected for laser beam cleanness or the geometry, as described in chapters 3 and 6. To obtain the observed depolarisation ratio of the $O_1/P_1(\nu_1)$ lines, multiple lines have been averaged. This is not trivial, due to the overlap of the counter-running branches from the ν_1 and $2\nu_2$ modes, which results in a lower accuracy in the measurement of the depolarisation ratio.

The observed depolarisation ratios can be compared with those repeated in the literature. As the peaks in the Fermi diad region are the result of the interaction between two vibrational states, the peaks cannot be said to be purely ν_1 or purely $2\nu_2$. This potentially complicates the expected depolarisation ratio. When comparing with the literature, a point to note is that most literature depolarisation measurements of CO_2 are

Table 7.9: Measured intensities and depolarisation ratios of the main carbon dioxide isotopologue.

Level / Band	cm^{-1}	$I_{\perp^i}$	$I_{\parallel^i}$	ρ_{obs}	ρ_{lit}
$^{12}C^{16}O_2$					[Dan81]
ν_1	1387.72(15)	94457(308)	3240(61)	0.0343(7)	0.027
$\nu_1, 1-2$	1408.78(15)	8433(95)	292(28)	0.03463(33)	0.081
$2\nu_2$	1284.58(15)	64241(254)	2893(57)	0.0450(9)	0.044
$2\nu_2, 1-2$	1264.12(15)*	5195(76)	237(25)	0.0456(49)	0.127
$O_1/P_1(\nu_1)$	var	var	var	$\approx 0.759(14)$	0.750

looking at a slightly different depolarisation ratio i.e. $\rho = \frac{I_{\parallel^s,\perp^i}}{I_{\perp^s,\perp^i}}$ rather than $\rho = \frac{I_{\perp^s,\parallel^i}}{I_{\perp^s,\perp^i}}$. For diatomic molecules in the SP0SA approximation this ratio is the same (see chapter 6). However, in the ESSA approximation the ratios are different due to the introduction of the φ dependence. So it can be assumed that this will also be the case for molecules that are not diatomic. The literature values of the depolarisation ratio of the Fermi diad of carbon dioxide are collated in table 7.9. The values show that the observed O_1/P_1 depolarisation ratio agrees with the literature value, within the experimental uncertainty. The literature values for the ν_1 and $2\nu_2$ branches are relatively close together. However, they do not agree within the experimental uncertainty. It appears that the depolarisation ratio of carbon dioxide has been studied less in the literature. The depolarisation measurements of the observed hot bands disagree with the literature value. It can be assumed that the measured values in this work are slightly higher than the true values. The correction routine, described in chapters 3 and 6, would have to be applied to correct for polarisation aberrations and the collection solid angle to produce values that can be compared with any future theoretical calculations in the literature.

7.5 Raman spectroscopy of nitrogen

Nitrogen is the main constituent of air and this may be used as a reference marker when measuring atmospheric gas mixtures. It is a diatomic molecule, so the theory of Raman spectroscopy is the same as that used for the diatomic hydrogen isotopologues.

7.5.1 Isotopic composition of nitrogen

The two naturally occurring stable isotopes of nitrogen are ^{14}N and ^{15}N. In a similar way to the hydrogen isotopologues these combine to form three isotopologues, $^{14}N^{14}N$, $^{14}N^{15}N$ and $^{15}N^{15}N$. The physical properties of the isotopes and isotopologues are collated in table 7.10. The table shows that the expected abundance of the isotopologue $^{15}N^{15}N$ will be below the detection limit of the LARA system. However, the abundance

Table 7.10: Physical properties of nitrogen atoms and molecules. μ_l corresponds to the reduced mass of the isotopologue and μ_1 is the reduced mass of $^{14}N^{14}N$.

Isotope Isotopologue	**Abundance**	**Mass number M**	**Reduced mass μ $\times 1.6610^{-27}$ kg**	$\rho = \sqrt{(\mu_l/\mu_1)}$
^{14}N	0.99636	14.003		
^{15}N	0.00364	15.000		
#1 $^{14}N^{14}N$	0.99272		0.14283	
#2 $^{14}N^{15}N$	0.00726		0.13808	0.98323
#3 $^{15}N^{15}N$	$\approx$ 0.00002		0.13333	0.96617

of the $^{14}N^{15}N$ isotopologue should be detectable using Raman spectroscopy. To do this the Raman line position locations need to be known.

7.5.2 Ro-vibrational energy levels and transitions

As stated above, nitrogen is a diatomic molecule, which means that the same theory used to find the Raman lines of the hydrogen isotopologues can be applied. The Raman band positions can be calculated using the formulae summarised in chapter 2. For hot bands to be considered, the anharmonicity needs to be introduced to the system. This changes the vibrational term of the diatomic molecule to

$$\tilde{G}(v) = (v + 1/2)\tilde{\nu_e} - (v + 1/2)^2\tilde{\nu_e}x_e \tag{7.9}$$

where $\tilde{\nu_e}$ is the harmonic vibration wavenumber and $\tilde{\nu_e}x_e$ is the 1st anharmonicity correction. If the selection rule for the diatomic molecules used here of $\Delta v = +1$ is considered, the pure vibrational Raman shift $\tilde{\nu}_{\text{vib}} = (\tilde{G}' - \tilde{G}'')$ is

$$\tilde{\nu_{\text{vib}}} = \tilde{\nu_e} - 2(v + 1)\tilde{\nu_e}x_e \tag{7.10}$$

where v is the vibrational quantum number of the initial state. For the normal Q_1-branch transition $v = 0$ and for the hot band $v = 1$.

The spectroscopic constants that are required to calculate the line positions of nitrogen are collated in table 7.11. The spectroscopic constants can be substituted into the equations for the Raman line positions of diatomic molecules in chapter 2, taking into account the definition of the vibrational constant in equation (7.10). The B_ν and D_ν terms are defined in terms of B_e and α_e as

$$B_\nu = B_e - \alpha_e(v + \frac{1}{2}) \tag{7.11}$$

Table 7.11: Spectroscopic constants for the nitrogen and oxygen isotopologues (in units of cm^{-1}). $^{14}N^{14}N$ values from Herzberg [Her50], $^{16}O^{16}O$ from Laher and Gilmore [Lah91]. The heavier isotopologue values are rescaled using reduced mass ratio ρ from table 7.10 and 7.14.

Isotopologue	$\tilde{\nu}_e$	$\tilde{\nu}_e x_e$	$\tilde{\nu}_e y_e$	B_e	α_e
$^{14}N^{14}N$	2359.61	14.456	7.51×10^{-2}	2.010	1.87×10^{-2}
$^{14}N^{15}N$	2320.04	13.975	7.14×10^{-3}	1.943	1.78×10^{-2}
$^{16}O^{16}O$	1580.390	12.112	0.0754	1.44510	0.01523
$^{16}O^{17}O$	1556.889	11.754	0.0721	1.40244	0.01456
$^{16}O^{18}O$	1535.776	11.438	0.0692	1.36466	0.1398

and

$$D_\nu = \frac{4B_\nu{}^3}{\omega_\nu^2} \tag{7.12}$$

where [Hos75]

$$\omega_\nu = (\tilde{\nu}_e - \tilde{\nu}_e x_e) - 2\nu\tilde{\nu}_e x_e \tag{7.13}$$

This then leads to the line positions of the Q_1-, S_1- and O_1-branches of the nitrogen isotopologues, which are collated in table 7.12. The calculation for the $^{14}N^{15}N$ isotopologue has only been performed for the Q-branch, as the intensity of the S- and O-branches is approximately a factor of 50 lower than the Q-branch, so they will not be detectable in the LARA system in Swansea.

The same calculation can be applied for the hot bands of the Q-branches of the isotopologues. The hot band of the Q-branch of the $^{14}N^{14}N$ has been calculated for J=0, where the initial state is $v = 1$ and is calculated to start at $2301.786\,cm^{-1}$.

7.5.3 Measured spectra

Raman spectra of nitrogen have been taken in the 90° Raman configuration. The measurement setup was the same as that used for the depolarisation measurements of the hydrogen isotopologues, described in chapter 6. The LARA cell was filled with air, i.e. the valves of the cell were opened. Three repeat Raman spectra with a 900 s acquisition time were taken for the $\perp^i$ and $\|^i$ incident laser polarisation, using the high resolution (2400 gr/mm) grating of the SP500i spectrograph, centred at 607 nm, which is the approximate location of the Q_1-peak of nitrogen when using 532 nm exciting radiation ($532\,nm = 18796.99\,cm^{-1}$, $\Delta\tilde{\nu} = 18796.99 - 2330.7 = 16466.29\,cm^{-1} = 607.301\,nm$). The background and cosmic rays were removed from the spectra, using the routines described in appendix A.6. Averaged spectra of the $\perp^i$ and $\|^i$ polarisation excitation are shown in figure 7.3.

In the figure, the Q-branch of the main isotopologue of nitrogen is the dominant

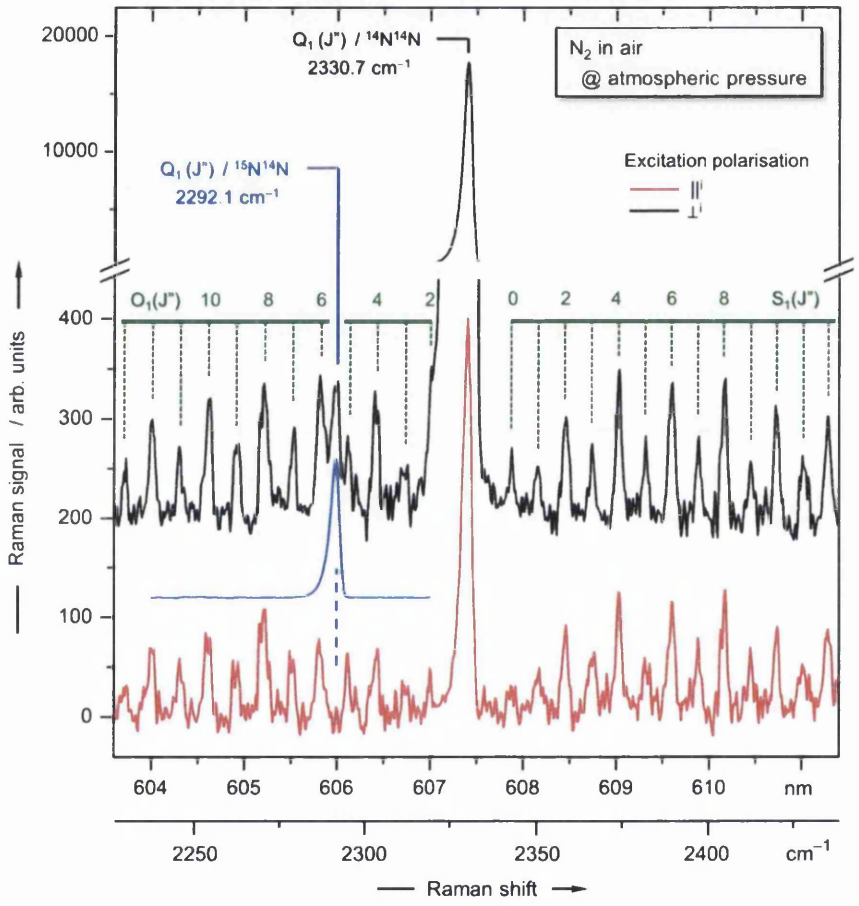

Figure 7.3: Raman spectra for N_2 in air (at atmospheric pressure), for $\|^i$- and $\perp^i$-polarisation excitation with 532 nm laser (P_{laser} = 2 W). The isotopologue $^{14}N^{15}N$ Q_1-peak (blue trace) has been scaled and position-fitted using the $^{14}N^{14}N$ Q_1-peak.

Table 7.12: Raman shift of the nitrogen isotopologues(in units of cm^{-1})

	$^{14}N^{14}N$			$^{14}N^{15}N$
J	Q_1	S_1	O_1	Q_1
0	2330.698	2342.589	–	2292.090
1	2330.661	2354.481	–	2292.054
2	2330.586	2366.334	2318.694	2291.983
3	2330.474	2378.148	2310.655	2291.876
4	2330.324	2389.924	2302.579	2291.734
5	2330.137	2401.661	2294.466	2291.556
6	2329.913	2413.359	2286.318	2291.342
7	2329.651	2425.017	2278.133	2291.093
8	2329.352	2436.636	2269.913	2290.808
9	2329.015	2448.215	2261.658	2290.488
10	2328.641	2459.753	2253.367	2290.132
11	2328.230	2471.251	2245.042	2289.741
12	2327.781	2482.708	2236.683	2289.314
13	2327.295	2494.123	2228.289	2288.851

Table 7.13: Intensities of Raman features for N_2 (in arb. units). Depolarisation ratios for the O_1/S_1-branches are averages over 17 individual lines, that for the Q_1-branch is derived from three averaged spectra. The depolarisation ratios are calculated from peak amplitudes. The isotopologue-peak ratio reflects the relative abundance within the error bars. Error values relate to last significant digit.

Isotopologue	Q_1-peak $\perp^i$-pol	$^{14}N^{15}N/^{14}N^{14}N$ peak ratio	Q_1-peak $\|^i$-pol	ρ_{obs} Q_1	ρ_{obs} O_1/S_1
$^{14}N^{14}N$	17510(130)		400(12)	0.02284(72)	0.757(12)
$^{14}N^{15}N$	133(10)	0.00760(57)			

feature; the S_1- and O_1-branch lines up to $J'' > 10$ can be easily followed. The Q-branch of the low abundance isotopologue, $^{14}N^{15}N$, is also visible in the spectrum. The identification is helped by observing that the feature at 2291.1 cm^{-1} depolarises (disappears) when the polarisation is switched to $\|^i$ polarisation. This identification can be made even clearer by taking advantage of the fact that the depolarisation ratio of the S_1- and O_1-branches is 0.75 and removing them from the $\perp^i$ polarisation spectrum by subtracting $\frac{4}{3}I_{\|^i}$ from the spectrum. This removes all lines which have a depolarisation ratio of 0.75, leaving the Q-branches isolated.

The intensities of the measured Q-branches are extracted from the uncorrected spectrum, so the abundance of the $^{14}N^{15}N$ can be calculated. The extracted intensities and isotopologue abundance are collated in table 7.13. The table shows the measured rela-

tive abundance of the $^{14}N^{15}N$ isotopologue. This can be compared with the theoretical relative abundance in table 7.10 by converting the true abundance to a relative theoretical abundance, which gives 0.00726/0.99272 = 0.00731. This value agrees with the measured value in table 7.13, within the experimental uncertainty.

7.5.4 Analysis of the depolarisation ratios of nitrogen

The depolarisation ratios of nitrogen can be calculated from the measured data described above. Due to the convolution of the Q-branch with the $O_1(J = 2)$ line, the peak signal amplitude has only been extracted. To calculate the depolarisation ratio of the low intensity S_1- and O_1-branches, 17 of the individual lines have been averaged. The calculated values are collated in table 7.13.

The measured depolarisation ratio of the O_1- and S_1-branches agrees with the theoretical value of 0.75, within the experimental uncertainty. The measured value of the Q-branch is in the same range as the other measured values in the literature (0.02 to 0.028 [Dan81]). Another example of the depolarisation ratio contained in the literature is that stated by Mayer *et al* [May03], which equals 0.022. This value is in good agreement with the one obtained here in this work.

A point to note is that the quoted depolarisation ratios are the observed values. They have not been corrected for the laser beam cleanness, and the collection geometry; thus, these depolarisation ratios have to be seen as an upper limit of the true value. The uncertainty in the measured depolarisation ratio of the O_1- and S_1-branches is too large to use this as a "true" value (i.e. 0.75) to apply the correction method.

Calculations of the average polarisability and anisotropy have been performed in the literature for nitrogen and oxygen [Bul03]; equations are given which enable one to calculate the matrix elements and theoretical depolarisation ratio, along with uncertainties. The equations to perform the calculation are included in appendix A.5. The result gives a theoretical depolarisation ratio for nitrogen of $\rho_{\text{theo}} = 0.0241(101)$. The uncertainty of this value is large (42% of the measured value). It does mean that the measured value obtained here, of $\rho_{\text{obs}} = 0.02284(72)$, agrees with the theoretical value, within its uncertainty. However, the uncertainties in the theory are too large to be useful for quantitative applications. For a proper comparison, a more accurate *ab-initio* calculation would need to be performed, along the lines of that of LeRoy for the hydrogen isotopologues [LRoy88].

7.6 Raman spectroscopy of oxygen

Oxygen is the second most abundant constituent of air. Its use in combustion experiments means it also requires monitoring in many applications (see for e.g. Wehremeyer *et al* [Weh92] or Fernàndez *et al* [Fer06]). It is a diatomic molecule so the theory of

Table 7.14: Physical properties of oxygen molecules. Isotopologue abundance according to [Hit04].

Isotopologue	**Abundance**	**Nuclear spin** $J_{odd} : J_{even}$	**Reduced mass** μ (amu)	$\rho = \sqrt{(\mu_l/\mu_1)}$
#1 $^{16}O^{16}O$	0.995262	$I_{even-J''} = 0$	7.9975	
#2 $^{16}O^{17}O$	0.000742		8.2408	0.98513
#3 $^{16}O^{18}O$	0.003991	$I_{even-J''} = 0$	8.4689	0.97177

Raman spectroscopy is the same as that used for the diatomic hydrogen isotopologues and the extension applied to nitrogen required to derive the hot band location.

7.6.1 Isotopic composition of oxygen

The three naturally occurring stable isotopes are ^{16}O, ^{17}O and ^{18}O. In a similar way to nitrogen and the hydrogen isotopologues, these isotopes combine to form multiple isotopologues. The three with a sufficiently high abundance to be detected by the KATRIN LARA system are $^{16}O^{16}O$, $^{16}O^{17}O$ and $^{16}O^{18}O$. The physical properties of the isotopes are collated in table 7.6, in the section when carbon dioxide was discussed above. The physical properties of the isotopologues are collated in table 7.14. The table shows that the abundances of the two minor isotopologues are large enough that they should be detectable in the LARA setup, as long as the signal of the main Raman peak of oxygen is maximised. This means that the isotopic composition of the $^{16}O^{17}O$ and $^{16}O^{18}O$ should be able to be verified using Raman spectroscopy. To do this, the location of the Raman lines needs to be calculated, to determine that they are resolvable from the Q_1-branch of the main $^{16}O^{16}O$ isotopologue.

7.6.2 Ro-vibrational energy levels and transitions

As stated above, oxygen is a diatomic molecule, which means the same theory that has been used to describe the hydrogen isotopologues and nitrogen can be applied. The Raman band positions can be calculated using the formulae summarised in chapter 2, with the changes required to calculate the hot band positions, which were discussed for nitrogen in section 7.5.2 above. The spectroscopic constants that are required to calculate the line positions of the oxygen isotopologues are collated in table 7.11. The same method, as used in section 7.5.2, can be used to determine the line positions of the Q_1-, S_1- and O_1-branches of the oxygen isotopologues. The calculation for the minor isotopologues has only been performed for the Q_1-branch, as the intensity of the S_1- and O_1-branches will be too low to be detected in the LARA system. The line positions are collated in table 7.15.

Table 7.15: Raman shift of the oxygen isotopologues(in units of cm^{-1}). Note that due to the spin of the $^{16}O^{16}O$ and $^{16}O^{18}O$ the even J-numbered transition lines disappear.

	$^{16}O^{16}O$			$^{16}O^{17}O$	$^{16}O^{18}O$
J	Q_1	S_1	O_1	Q_1	Q_1
0					
1	1556.136	1573.232	–	1533.352	1512.872
2				1533.294	
3	1555.983	1590.205	1541.761	1533.206	1512.732
4				1533.090	
5	1555.709	1607.052	1530.112	1532.944	1512.481
6				1532.769	
7	1555.313	1623.771	1518.345	1532.566	1512.117
8				1532.333	
9	1554.795	1640.360	1506.463	1532.071	1511.642
10				1531.779	
11	1554.156	1656.817	1494.466	1531.459	1511.055
12				1531.110	
13	1553.394	1673.142	1482.357	1530.731	1510.356
14				1530.324	
15	1552.511	1689.330	1470.138	1529.887	1509.545
16				1529.421	
17	1551.506	1705.382	1457.811	1528.926	1508.622
18				1528.402	
19	1550.379	1721.295	1445.377	1527.849	1507.588
20				1527.266	
21	1549.131	1737.067	1432.839	1526.655	1506.442
22				1526.015	
23	1547.760	1752.697	1420.198	1525.345	1505.184
24				1524.646	
25	1546.268	1768.182	1407.456	1523.919	1503.814
26				1523.162	
27	1544.654	1783.521	1394.615	1522.376	1502.333
28				1521.561	
29	1542.919	1798.712	1381.677	1520.717	1500.74

Table 7.16: Intensities of Raman features of O_2 (in arb. units). Depolarisation ratios for the O_1/S_1-branches are averages over 21 individual lines. The Q_1-branch value is derived from three averaged spectra. The isotopologue-peak ratio reflects the relative abundance within the error bars. Error values relate to last significant digit.

Isotopologue	Q_1-peak $\perp^i$-pol	Q_1-peak $\parallel^i$-pol	$^{16}O^XO$ / $^{16}O^{16}O$ peak ratio	ρ_{obs} Q_1 (int)	ρ_{obs} O_1/S_1 (int)
$^{16}O^{16}O$	9300(14)	477(4)		0.05129(35)	0.762(9)
$^{16}O^{17}O$	13(1)		0.00143(11)		
$^{16}O^{18}O$	37(1)		0.00402(10)		

The same calculation can be applied to calculate the hot bands of the Q-branches of the isotopologues. The starting position of the hot band for the Q_1 branch of the $^{16}O^{16}O$ isotopologue has been calculated by setting J=0 where the initial state is the $v = 1$ state. The expected line position is found to be at 1531.942 cm^{-1}. Note that this line shouldn't be populated, due to the degeneracy of oxygen related to its nuclear spin, but it gives an indication of the hot band's location.

7.6.3 Measured spectra

Raman spectra of oxygen have been taken in the 90° Raman configuration. The measurement setup was the same as that used for the depolarisation measurements of the hydrogen isotopologues, in chapter 6. The LARA cell was filled with $\approx$ 1080 mbar of oxygen gas. Seven repeat Raman spectra each with a 900 s acquisition time, were taken for the $\perp^i$ and $\parallel^i$ incident laser polarisation, using the high resolution (2400 gr/mm) grating of the SP500i spectrograph, centred at 580 nm. This is the approximate location of the Q_1 peak of oxygen when using 532 nm exciting radiation. The background and cosmic rays were removed from the spectra using the routines described in appendix A.6.

Averaged spectra of the $\perp^i$ and $\parallel^i$ polarisation excitation are shown in figure 7.4. In the figure, the Q-branch of the main isotopologue of oxygen $^{16}O^{16}O$ is easy to identify, along with the S_1- and O_1 branches up to $J'' = 27$; the Q-branches of the low abundance isotopologues $^{16}O^{17}O$ and $^{16}O^{18}O$ are also visible. The identification becomes clearer in the bottom panel of the figure where the branches with a depolarisation ratio of 0.75 have been removed using the method described in section 7.5.3, leaving the depolarising branches isolated. The $^{16}O^{17}O$ peak overlaps, within $< 1\,cm^{-1}$, with the hot-band $v'' = 1$ to $v' = 2$ of the $^{16}O^{16}O$ isotopologue.

The intensities of the Q-branches have been extracted from the uncorrected spectrum so that the abundance of the isotopologues can be calculated. The extracted intensities and isotopic abundances are collated in table 7.16. The table contains the

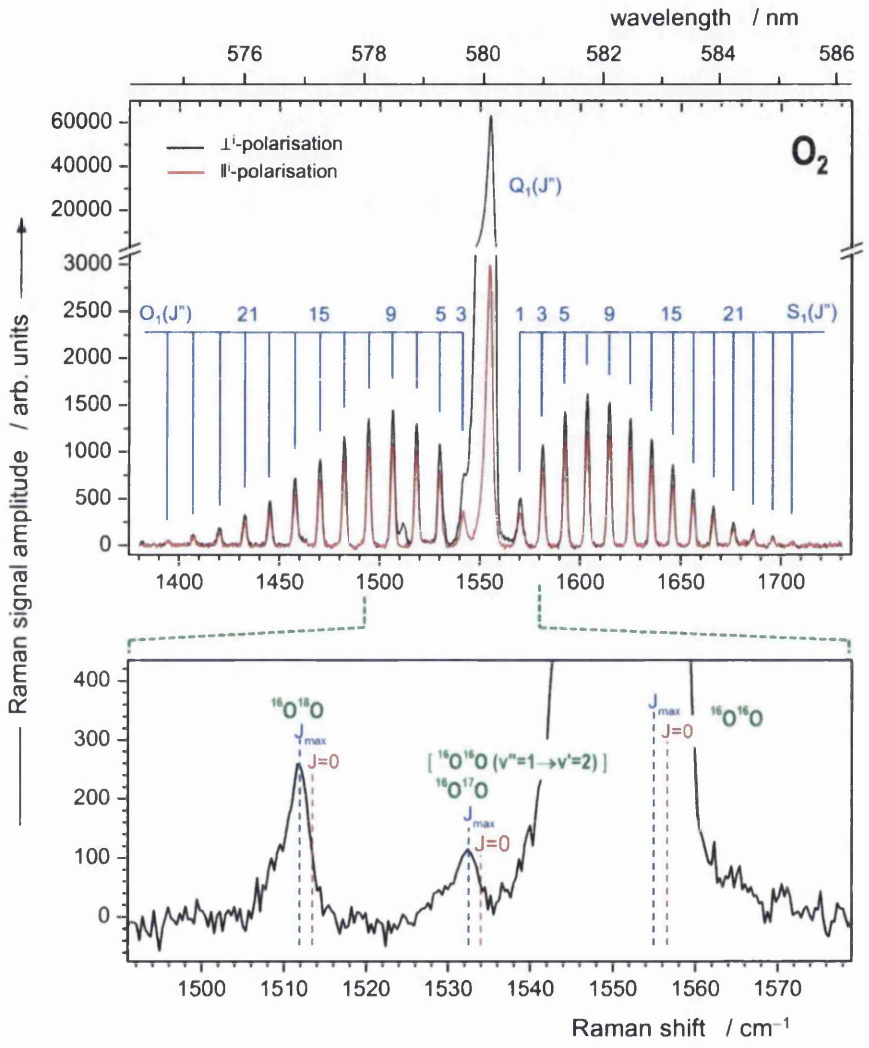

Figure 7.4: Raman spectra of O_2, measured for $\|^i$- and $\perp^i$-polarisation excitation with 532 nm laser (2W). Note that the isotopologue $^{16}O^{18}O$ signal reflects, within the measurement accuracy, its natural abundance relative to the $^{16}O^{16}O$ signal. The $^{16}O^{17}O$ peak overlaps, within $< 1\,cm^{-1}$, with the hot-band $\nu'' = 1$ to $\nu' = 2$ of $^{16}O^{16}O$; within the measurement accuracy the signal amplitude reflects the expected theoretical summary abundance. Note that, because the spin $I = 0$ for ^{16}O. all even numbered transition lines in the S_1- and O_1- branches of $^{16}O^{16}O$ are missing.

measured relative abundances of the $^{16}O^{17}O$ and $^{16}O^{18}O$ isotopologues. These can be compared with the theoretical values in table 7.14, by converting the true abundance to the relative theoretical abundance. This gives 0.003991/0.995262 = 0.00401 and 0.000742/0.995262 = 0.000746 for $^{16}O^{18}O$ and $^{16}O^{17}O$ respectively. The $^{16}O^{18}O$ value agrees with the measured value, within the experimental uncertainty. However, the $^{16}O^{17}O$ measured value is slightly larger than the expected value. This is caused by the overlap with the hot-band of the $^{16}O^{16}O$ isotopologue as stated above.

7.6.4 Analysis of the depolarisation ratios of oxygen

The depolarisation ratios can be calculated from the measured data, described above. The depolarisation ratios have only been calculated for the $^{16}O^{16}O$ isotopologue, as the $\|^i$ data of the other isotopologues is lost in the noise. To calculate the depolarisation ratio of the low intensity S_1- and O_1-branches, 21 of the individual lines have been averaged. The calculated values are collated in table 7.16.

The measured depolarisation ratio of the S_1- and O_1-branches is slightly out from the expected theoretical value of 0.75, if the quoted experimental uncertainty is considered. The reason for this is that the solid angle causes a slight increase to the observed depolarisation ratio, as described for the hydrogen isotopologues in chapter 6. The measured value of the Q-branch is in the same range as the values in the literature (0.043 to 0.061 [Dan81]).

A point to note is that the quoted depolarisation ratios are observed values. These values have not been corrected for the laser beam cleanness and the collection geometry observed in the depolarisation measurements of the hydrogen isotopologues in chapter 6. The observed depolarisation ratio can be seen as an upper limit on the true value. The uncertainty in the known depolarisation ratio of the O_1- and S_1-branches, in this measurement, is quite large. If this was used as the "true" value in the correction method, this uncertainty would propagate through and lead to a larger uncertainty in the corrected values.

As described in the nitrogen analysis section, calculations of the average polarisability and anisotropy have been performed for oxygen [Bul03], along with uncertainties. The equations to perform the calculation are included in appendix A.5. The result gives a theoretical depolarisation ratio for oxygen of $\rho_{\text{theo}} = 0.0548(285)$. The uncertainty in this value is large, as is the case in the nitrogen calculation. However, the large uncertainty does mean that the theoretical value certainly agrees with the observed value $\rho_{\text{obs}} = 0.05129(35)$, within the calculated uncertainty. As is the case for the nitrogen calculation, these uncertainties are too large for the calculated polarisability matrix elements to be useful for quantitative applications. For a proper comparison, a more accurate *ab-initio* calculation would need to be performed for oxygen, along the lines of that of LeRoy for the hydrogen isotopologues [LRoy88].

Chapter 8

Raman beyond KATRIN

8.1 Chapter overview

In this chapter various test setups have been investigated to improve sensitivity of Raman spectroscopy, beyond the scope of the KATRIN experiment. The main techniques that are discussed are: 0° (forward scattering), 180° (backward scattering) and capillary Raman spectroscopy.

The various test measurements are discussed in detail, starting with the initial investigation showing that 0° Raman has the potential of increasing the spectral sensitivity, culminating in an optimised capillary Raman setup that increases the Raman signal by two orders of magnitude.

As the observation of Raman light is in the same direction as the laser excitation, Raman and fluorescence light originating from optical components in the laser beam always contribute to the observed scattering light intensity. Therefore, fluorescence test measurements have been performed that demonstrate that the fluorescence from a BK7 optic is higher than an equivalent calcium fluoride optic. The thickness appears to be the dominant factor, therefore a thin calcium fluoride window was used in the capillary cell and the thinner BK7 lens was used to focus the laser light into the cell. It was shown that the intensity of the fluorescence from a quartz window is approximately the same as that from a calcium fluoride window. The observed fluorescence intensity from the capillary Raman setup has been shown to vary linearly with laser power.

Test measurements have shown that focussing the light onto the capillary cell correctly has a strong effect on the intensity of the observed Raman scattered light. For a 25.4 mm diameter lens, the maximum Raman intensity was obtained when a $f = 100\,\text{mm}$ length lens was used. The beam size incident on the lens also influences the intensity of the Raman light collected. The maximum Raman intensity was found when the laser beam was not expanded.

Furthermore, it has been shown that the Raman signal from the capillary setup

increased by a factor of two when the collection "slit-to-slit" fibre bundle was replaced with a new *CeramOptec* "dot-to-slit" fibre bundle.

The sensitivity increase has been demonstrated with the "final" optimal capillary Raman setup; carbon dioxide can be detected in air with short light collection times. Capillary Raman spectra of pure deuterium have also been measured successfully, with short acquisition times of less than 3 s reaching detection limits of $\approx 0.21\%$, demonstrating the feasibility of using the setup with the hydrogen isotopologues.

Capillary Raman spectroscopy has been found to produce Raman signals that are a factor of 170 higher than single-pass 90° Raman, when comparing the Raman Q_1-branch of nitrogen in air. The increase in the signal-to-noise ratio (SNR) is between a factor of 9 (five averaged 2 s acquisitions) and 24 (five averaged 0.2 s acquisitions). There is potential to reduce the noise further without attenuating the signal, improving the SNR.

8.2 Introduction

In this chapter, the measurements beyond the scope of laser Raman spectroscopy for the KATRIN experiment will be discussed.

The main aim of the investigation was to find whether it is feasible to improve the sensitivity of the Raman system beyond that of the one used for the KATRIN experiment. Various non-linear Raman enhancement techniques have been reported in the literature, such as: coherent anti Stokes Raman scattering (CARS); stimulated Raman scattering (SRS); and photoacoustic Raman scattering (PARS) ([Bar79], [Witt00], [Owy78]). These techniques have reported detection limits on the ppm level [Oki99], but they make use of pulsed laser sources, which are relatively expensive. Also, with techniques such as PARS, a medium is required for the sound wave to propagate through, meaning that the sensitivity may be affected in low pressure gas measurements, as is the case in KATRIN-like measurements.

Other enhancement techniques are reported in the literature that extend the scattering region of forward Raman scattering configurations. This has the potential to improve the signal compared to the 90° Raman measurements, described in chapters 5, 6 and 7 of this work; by collecting the scattered light from forward (and backward) Raman over an extended length of the laser beam, compared to the 6 mm length collected in the LARA setup for KATRIN. This increases the number of excited particles, N_i, in the Raman intensity equation (equation (8.1)) and thus increases the measured intensity. The scattering length can either be enhanced using a true multi-pass cell or an innovative capillary configuration. Based on the work of the groups of Okita *et al* [Okit10] and Buric *et al* [Bur09], [Bur10] the possible enhancement from using a capillary as a Raman cell is a factor of 20 [Pea08] (over their standard fibre optic probe) and can be used with a variety of gases. This, along with the cost of the additional parts being

fairly low, makes it a good method to test.

The following enhancement methods and measurements will be discussed in this chapter:

1. Forward and backward Raman scattering,
2. Capillary Raman spectroscopy

8.3 Forward and backward Raman scattering

All enhancement test measurements in this work are performed using diatomic gases. Therefore, the principal theory of Raman scattering of diatomic molecules, described in chapters 2 and 3 applies. The minor differences between the theory for the different configurations will now be considered.

8.3.1 Theory differences

The intensity of Raman scattered light from a diatomic molecule is given by

$$I(\theta; p^s, p^i) = k_{\tilde{\nu}} \tilde{\nu_0} (\tilde{\nu_0} - \tilde{\nu}_{v,J})^3 g_i N_i \Phi(a^2, \gamma^2, \theta) \mathcal{I} \tag{8.1}$$

This is the same as the equation used for 90° Raman scattering, the difference being that for forward Raman $\theta = 0°$ and for backward Raman $\theta = 180°$.

The change in the angle only affects the line strength function. As the line strength function has been derived in full in chapter 3, this variation can be quantified. However, the line strength functions are defined in terms of the polarisation direction of the incident and scattered beams relative to the scattering plane. In the forward and backward Raman configurations, rotating the polarisation of the incident beam does not change the polarisation direction relative to the scattering plane (it is either forwards or backwards), due to the rotational symmetry of forward and backward scattering. This means that the intensity of the scattered light will not be as strongly dependent on the laser beam polarisation, as is shown in chapter 6 for the 90° configuration. However, this aspect will not be considered any further here.

The term that influences the sensitivity change between 90° Raman scattering and forward/backward Raman scattering is N, which is directly proportional to the number of particles illuminated by the laser beam, over which the scattered light is collected. In the 90° configuration the imaging only occurs over a 6 mm long region. In a forward or backward configuration the scattered light is collected along the direction of the laser beam. Thus scattering occurs over the entire length of the laser beam. The amount of light collected is governed by the solid angle of the collection lens. This will potentially collect more scattered light than the 90° configuration.

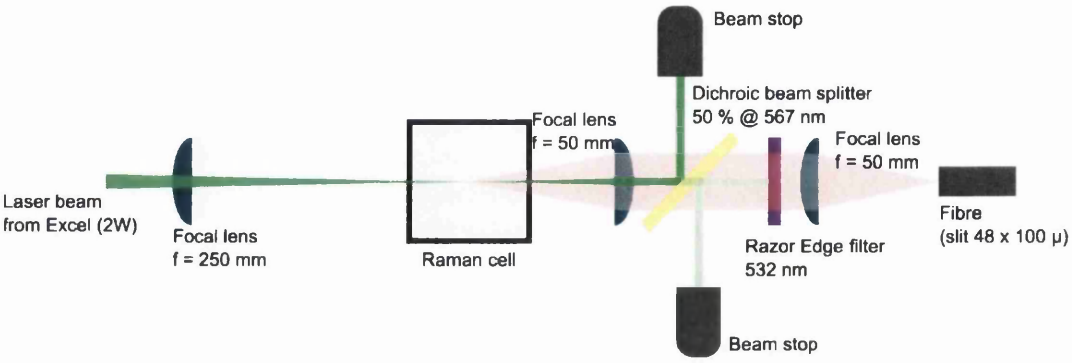

Figure 8.1: Sketch of initial forward Raman test setup. The fibre bundle was mounted in a x-y-z mount and its position was optimised

The fluorescence induced by the high powered laser beam passing through optics will need to be considered. As the collection of the scattered light is in the same direction as the laser beam propagation, this fluorescence will also be collected. This will influence the measured spectrum as a non-linear spectral background and increase the noise.

The best way to verify the changes between the standard 90° Raman and forward (or backward) Raman is to optimise a setup for forward Raman scattering. This will then give a baseline to compare the later improvement from capillary Raman. The measurement setup for the forward Raman measurements is discussed in the next section.

8.3.2 Measurement setup

The Raman setup for forward Raman measurements has been gradually optimised as a result of the various test measurements. For the first proof-of-principle test of Forward Raman, the LARA 3 setup in KIT was modified. To minimise disruption to the setup, most of the optical components in the beam path before the LARA cell were kept in place. An additional Razor Edge filter was placed in front of the fibre bundle, to prevent interactions of the laser light in the fused silica of the fibre. The resultant setup is found in figure 8.1.

A similar optimised setup was built in Swansea; this is shown in figure 8.2. To change from this setup to the one for backward Raman, the laser line filter is removed and all optics before this are swapped with the HR 350-700nm mirror. The housing for the 45° edge filter is described in chapter 4.

The measurements are described in the next sections. Please note that all raw spectra have had any cosmic rays removed using the TCRR, routine described in appendix A.6, and the multiple spectral regions have been combined (summed) to produce one resultant spectrum. When a spectral background is removed, the SCARF routine has been implemented (included in appendix A.6).

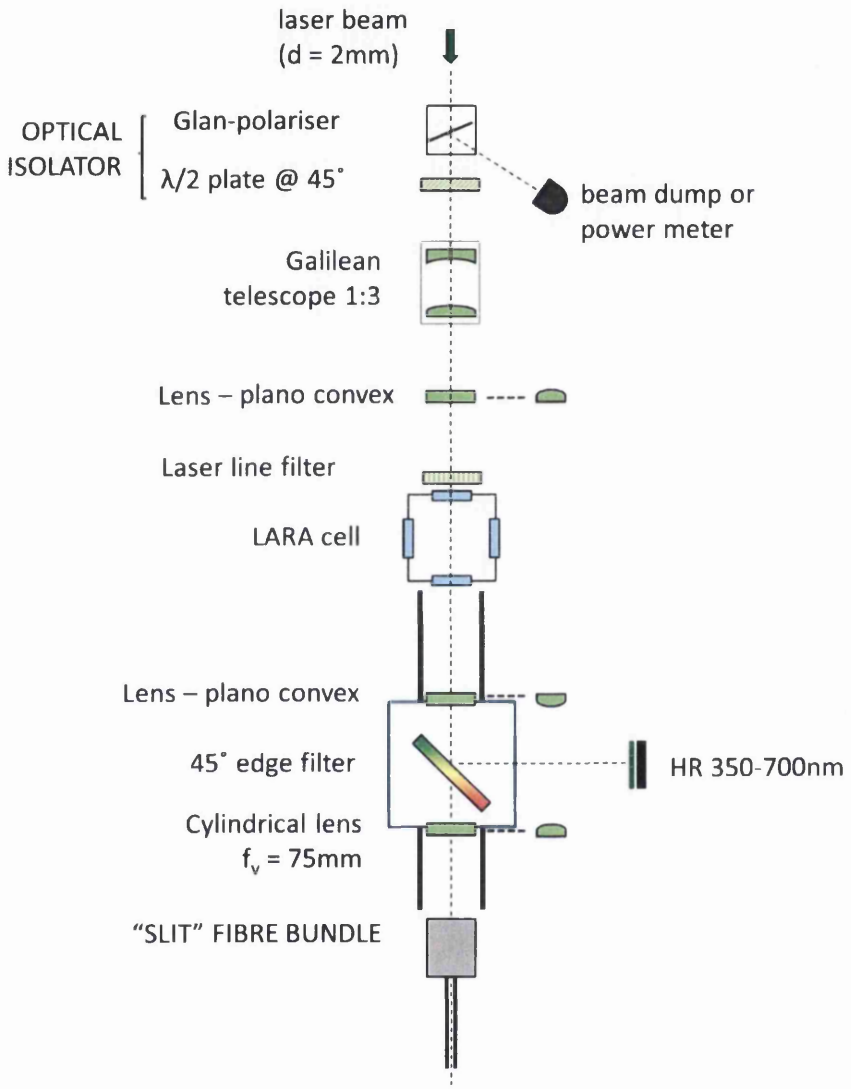

Figure 8.2: Sketch of optimised setup for forward Raman measurements. Note: the Galilean telescope is optional.

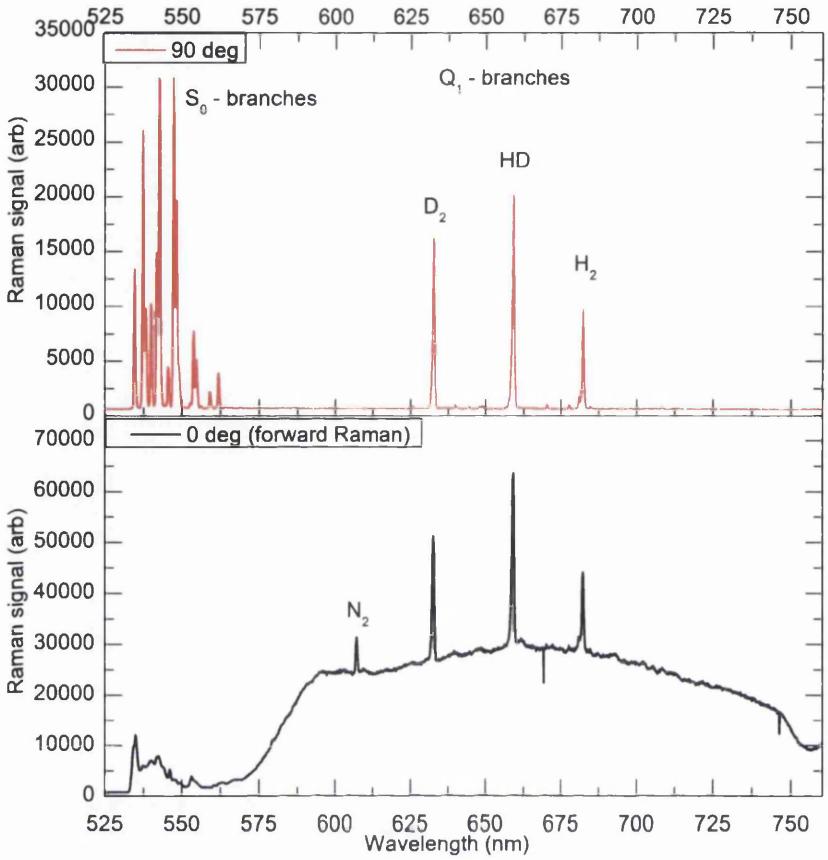

Figure 8.3: Raw spectra of 90° and 0° Raman setups. Note that the features $< 567\,\text{nm}$ in the 0° Raman spectrum are suppressed by the dichroic beam splitter.

8.3.3 Initial measurements in KIT

The first measurements of forward Raman scattering, using the setup in figure 8.1, were performed with a H_2, HD, D_2 mixture in the LARA cell. The measured forward Raman spectra were compared with 90° Raman spectra, recorded using the same cell filling. Both measurements have been performed using the PIXIS detector with the same settings; 3 s acquisition time, gain 3, 100 kHz readout rate, and the same laser power of approximately 2 W. For both setups the fibre mount was optimised (in $x - y - z$ and θ) to obtain the highest intensity.

An example of the raw spectra can be found in figure 8.3. It can be seen that the forward Raman spectrum has a very distinct fluorescence background that is nearly of the same order of intensity as the Raman lines themselves. However, the intensity of the Raman light collected in the forward geometry is about 1.7 times higher in comparison with the ordinary (90°) geometry. Note, that the forward Raman spectral features $< 567\,\text{nm}$ are suppressed by the dichroic beam splitter.

The fluorescence background can be completely removed using the SCARF back-

ground removal routine, described in appendix A.6. However, the background noise level is higher, due to the increased fluorescence signal shot noise.

This fluorescence background is caused by the various optics in the beam path (two lenses, dichroic beam splitter and cell windows). Methods of minimising this fluorescence are discussed in the next section.

In addition, Raman signals for N_2 can be identified, stemming from the scattering in air along the excitation path outside the cell.

8.3.4 Improvements

Figure 8.2 depicts the optimised forward Raman setup in Swansea, for which a variety of improvements, over the initial configuration, have been implemented. To verify the effect these improvements have on the fluorescence background in the Raman spectrum, measurements of the Raman spectrum of air (cell removed) were taken using the Swansea setup with the Excel laser, SP500 spectrometer and Synapse detector.

The implemented improvements are

- The setup is installed in a cage system to increase the reproducibility and ensure a robust alignment procedure. It also minimises the collection of stray light.

- The dichroic beam splitter has been replaced by a beam splitter with a higher transmission and suppression in the appropriate regions.

- The lens focussing the light onto the fibre bundle has been replaced by a $f = 75\,mm$ cylindrical lens, to ensure all fibres within the bundle are illuminated. The focal length is selected based on the numerical aperture of the fibre bundle.

- A laser line filter has been placed after the first focal lens (before the cell). This removes scattering effects from before this point. The effect that the introduction of this filter has on the raw forward Raman spectrum of air is shown in figure 8.4. Clearly, the introduction of the laser line filter reduces the fluorescence background of the forward Raman spectrum. However, it has not removed it completely. Further improvements will be needed to try and minimise the observed fluorescence; these are discussed in section 8.3.5.

- The beam-stop blocking the light reflected off of the dichroic beam splitter has been replaced by mirrors. This enables the light to be reflected back down the beam path for two passes of the beam through the scattering medium. This leads to an increase in the signal by up to a factor of two. A Faraday rotator has been installed in the beam to stop the reflection going all the way back into the laser cavity. This can be implemented in a forward Raman setup as, due to the geometrical symmetry, the intensity of the scattered light is not as strongly

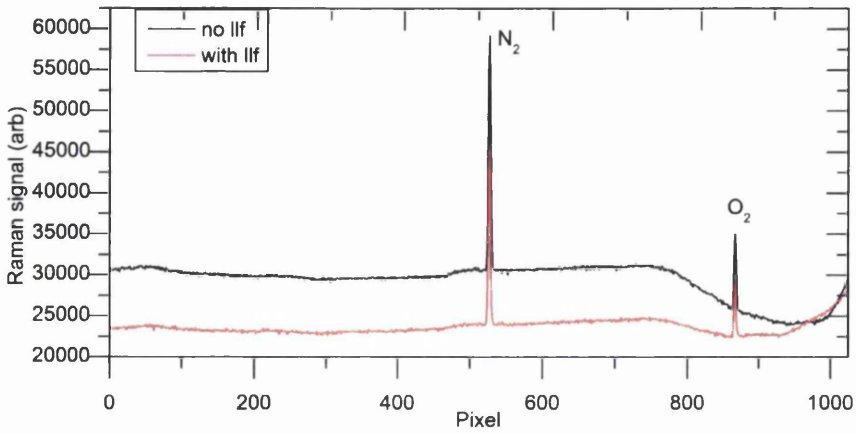

Figure 8.4: Comparison of raw forward Raman spectra of air with and without a laser line filter placed in front of the scattering region. Note that the Raman shift/wavelength increases to the left.

dependent on the polarisation of the incident beam. A comparison of the forward Raman spectrum with one and two passes of the laser beam is shown in figure 8.5. The figure shows that passing the laser beam through the system a second time

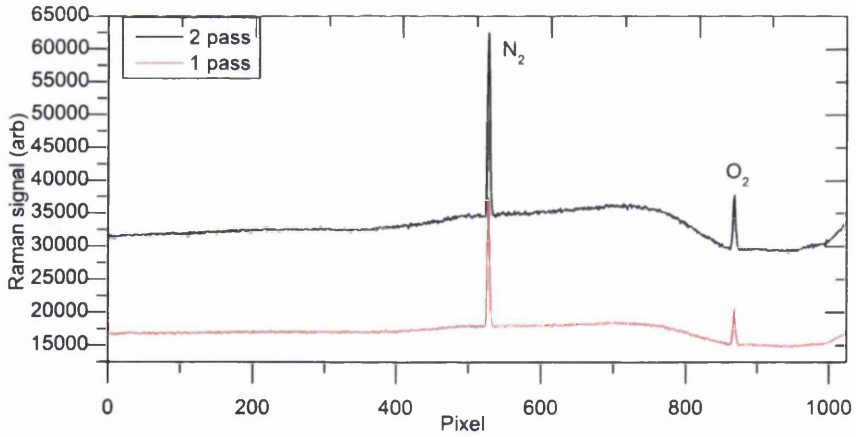

Figure 8.5: Comparison of raw forward Raman spectra of air with 1 pass and 2 passes of the laser beam through the Raman cell. Note that the Raman shift/wavelength increases to the left.

increases the signal by approximately a factor of 1.4. The reason for the incomplete doubling is the imperfect matching of the focal lengths of the collection lenses of the first and second pass. Also, the Raman intensity of forward and backward Raman is not completely identical, which may cause a slight difference in the intensities of the two spectra. What is also observed, is that the fluorescence of

the signal increases by approximately the same factor as the Raman signal when introducing the second pass. This is expected as the laser beam is passing through the windows twice.

The next step, to ascertain whether it is possible to reduce the fluorescence even further, requires a closer look at the effect of the materials in the optics.

8.3.5 Fluorescence test measurements

The normal material used for the optical components, where the light transmission is in the visible spectrum, is N-BK7. As was shown in the previous section, these components introduce a substantial amount of fluorescence in the measured Raman spectrum for forward/backward configurations. BK7 is not the only possible component to use for lenses and windows in the beam path. Another possibility that is used in some Raman microscope configurations is calcium fluoride, CaF_2.

It is important to verify what material leads to the lowest possible fluorescence, as in the capillary Raman measurements, discussed in section 8.4, a window is needed to seal the cell. Having a window with the lowest fluorescence will increase the sensitivity of the setup. In the literature, fluorescence induced by optical components has been investigated (see e.g [Wei98], [Nea09], [Zha11]). However, most of these measurements are related to laser-induced fluorescence and data applicable to this work cannot easily be generalised.

To verify the difference between the fluorescence caused by BK7 and CaF_2 optics, forward Raman measurements were performed with a BK7 or CaF_2 window inserted into the beam path. The windows both had a thickness of approximately 1 mm. This is important as the observed fluorescence will be dependent on the thickness of the sample that the beam passes through. The resultant observed Raman spectra are shown in figure 8.6. The figure shows that the BK7 window causes the most fluorescence with a height of 41249 at pixel number 747. The fluorescence level of the CaF_2 window and when no window was inserted were 36431 and 34095, respectively. This implies that a 1 mm CaF_2 window has a smaller effect on the fluorescence background than a BK7 window of the same thickness.

Another point to note is that a large amount of fluorescence is caused by the other optics in the beam path. The lenses in use are made of BK7. This measurement implies that using a CaF_2 lens could lead to a reduction in the observed fluorescence in the Raman spectra. To test this, two custom made CaF_2 plano-convex lenses, coated with a broadband anti-reflection coating, were ordered from *INGCRYS* with focal lengths of 200 mm. A broadband anti reflection coated CaF_2 window was also ordered, which could be used with the capillary Raman cell.

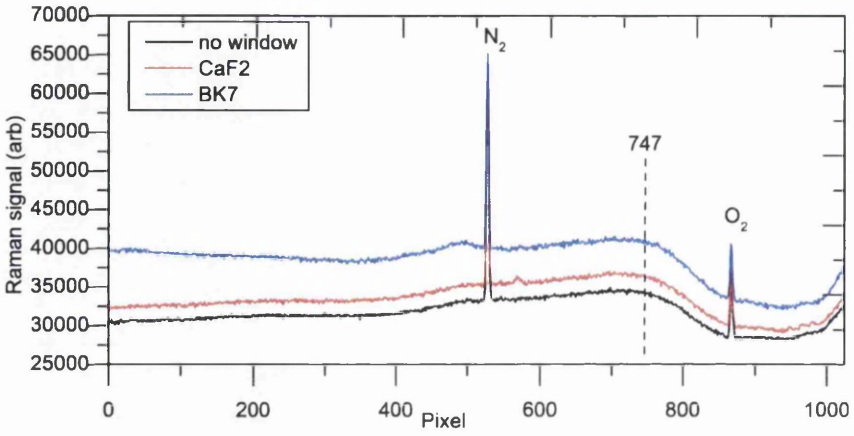

Figure 8.6: Comparison of raw forward Raman spectra of air with a CaF_2, BK7 and no window inserted into the beam path. The window thickness is ≈ 1 mm. The acquisition time for all measurements was 45 s. Note that the Raman shift/wavelength increases to the left and pixel 747 is used as the fluorescence height reference point.

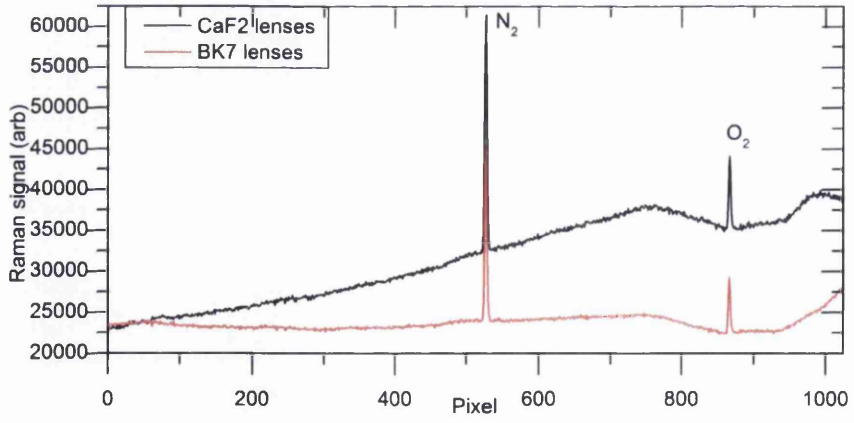

Figure 8.7: Comparison of raw forward Raman spectra of air where the scattered light is collected using BK7 or CaF_2 lenses. Note that the Raman shift/wavelength increases to the left.

Fluorescence for lenses in the beam path

Forward Raman measurements of air were taken using CaF_2 lenses, to focus the laser beam and collect the scattered light. These were compared with equivalent measurements taken using BK7 lenses. The resultant raw spectra are collated in figure 8.7 for a 100 s acquisition time. The figure shows that, when the CaF_2 lenses are used, the fluorescence in the Raman spectrum is higher. The height of the florescence at the high wavelength (low pixel) end is approximately the same (23776 and 23803 at pixel number 42). However, at the low wavelength (high pixel) end, the fluorescence from the CaF_2 lenses is considerably higher (38144 compared to 24645 at pixel number 762).

Based on the concept tests performed above, the fluorescence being larger for CaF_2 lenses is not what was expected. The reason for the unexpected outcome can be determined by comparing the dimensions of the lenses used. Both lenses have diameters of 25.4 mm and focal lengths of 200 mm. However, the CaF_2 lens has a centre thickness of 4 mm whereas the BK7 lens has a centre thickness of 2.8 mm. The edge thicknesses are 3 mm and 2 mm respectively. The increase in thickness of the CaF_2 lens, compared to the BK7 lens, means that the fluorescence increases.

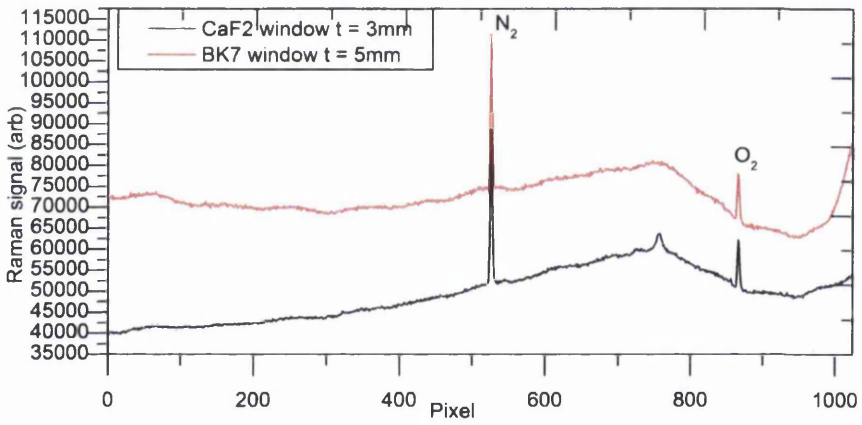

Figure 8.8: Comparison of raw backward Raman spectra of air where a window is placed in the beam path between the scattering centre and the collection optics. The compared windows are a *INGCRYS* CaF_2 window with a thickness of 3 mm and a *ThorLabs* BK7 WG11050 window with a thickness of 5 mm. The acquisition time was 100 s. Note that the Raman shift/wavelength increases to the left.

Fluorescence from window in the beam path

The setup orientation for the capillary Raman measurements will be equivalent to backward Raman with a second pass. This means that the window fluorescence comparison tests were performed for a backward Raman setup. The windows that were compared are the *INGCRYS* CaF_2 window with a thickness of 3 mm and a *ThorLabs* BK7 WG11050

window with a thickness of 5 mm. Both windows have a diameter of 25.4 mm. The resultant backward Raman spectra of air are collated in figure 8.8. The figure shows that the shape of the fluorescence from both windows is fairly similar, with the exception of an additional feature in the CaF_2 window spectrum at pixel number 757. This is not the Raman feature of CaF_2, as this should be at a Raman shift of $322\,cm^{-1}$. On consulting the literature, it has not been possible to identify exactly what this feature is, but it is caused by the CaF_2 window or its coating. The feature can be removed using background removal routines so it will not be discussed any further. The main difference is that the fluorescence of the BK7 window measurement is considerably higher than the CaF_2 window measurement (79034 vs. 57210 at pixel number 674). One further point to note is that the BK7 window that was available is thicker than the CaF_2 window.

8.3.6 Summary

Forward/backward Raman is more sensitive than normal 90° Raman measurements. However, as a penalty, fluorescence in the windows is collected in the measurements. The forward Raman setup has been optimised and fluorescence test measurements have been performed, showing that the fluorescence from an optic appears to be dominated by the optic thickness rather than the material. Based on the available optics the lowest fluorescence is obtained by using the thinner BK7 lenses. In measurements of gases, other than the open air a cell is required to hold the sample. In these cases (capillary Raman) a window is needed so that the excitation and scattered radiation can pass through the system. It has been found that the thinner CaF_2 window lead to a lower fluorescence observed in the Raman spectrum. Therefore, in both cases the thinnest optic available at the time of these tests was used.

8.4 Capillary Raman spectroscopy

A method of enhancing the Raman signal from gas measurements in the forward (or backward) configuration was proposed by Pearman *et al* [Pea08], using a hollow silver coated glass-fibre as the Raman cell. The method has been developed further by other groups [Bur09], [Bur10], [Okit10]. The concept of using a metal coated hollow fibre is discussed below, together with the specific construction and testing of the capillary cell in Swansea using N_2, O_2 and D_2.

8.4.1 Metal-coated hollow fibre enhancement

If light is focussed into a hollow glass-fibre coated with silver (or any other suitable metal coating), such that the light strikes the silver at a high enough grazing angle that the reflectivity at the silver surface approaches 100%. This means that the light

will propagate along the fibre length. For the grazing angle matching condition to be maintained along the fibre length, the fibre needs to be kept reasonably straight. The internal diameter of this fibre can be as large as 1 mm. This means that gases can flow through the fibre without significant pumping restriction, i.e. the gas flow is relatively fast.

As described in chapter 2, light propagating through a medium will lead to Raman scattered light being produced. The propagation of the laser light along the silver-coated hollow glass-fibre's length leads to Raman scattering from the gas sample, inside the fibre, along its entire length. The light scattered in the forward/backward direction will also satisfy the grazing angle matching condition i.e. it will have near-perfect reflectivity. This means that scattered light from the entire length of the fibre will be propagated to the end and can be collected. Therefore, the Raman signal has been collected from the entire cell length, which increases N_i and hence the Raman intensity.

In the ideal case, the scattering length would be equal to the length of the cell. In reality, there will be some losses from attenuation of the laser and scattered radiation in the fibre. This means that the scattering length will be equal to an effective cell length x_e which is equal to [Alt01]

$$x_e = l\Big(\frac{1 - e^{-2(a_1+a_2)l}}{2(a_1 + a_2)}\Big) \tag{8.2}$$

where l is the physical cell length and a_1 and a_2 are the attenuation coefficients for the excitation and Raman scattered light, respectively. This implies that a long cell with low attenuation losses would lead to the longest effective cell length and hence a higher intensity. If a mirror is added at the output of the hollow fibre, to reflect the output light back down the length of the fibre, equation (8.2) is modified to

$$x_e = l\Big(\frac{1 - e^{-2(a_1+a_2)l}}{2(a_1 + a_2)} + \frac{R(e^{-4a_1l} - e^{-4a_2l})}{2(a_1 - a_2)} + \frac{R^2(e^{-2(a_1+a_2)l} - e^{-4(a_1+a_2)l}}{2(a_1 + a_2)}\Big) \tag{8.3}$$

where R is the mirror's reflectivity, assuming this is the same for both the excitation and scattered radiation. Okita *et al* [Okit10] showed experimentally and theoretically, using the equations above, that a straight hollow fibre in a two pass configuration, with an inner diameter of 700 μm, has a maximum Raman intensity for a fibre length of 0.8 m. The group have since commercialised their metal-coated, hollow fibre manufacturing process and sell the devices through a company called *Doko Engineering*, Japan.

A more rigorous theoretical treatment has been developed by Buric *et al* [Bur10], who calculate the Stokes power collected from a silver coated, hollow fibre, by integrating the Stokes power generated in a length, dz, and in a solid angle, $d\Omega$, over the fibre length and light collection solid angle. The conclusion from these model calculations was that increasing the collection angle increases the amount of Raman light collected.

The second variable to enhance the Raman signal is the coupling angle of the pump beam into the hollow fibre. The theoretical treatment of Buric *et al* [Bur10] showed that the losses within the fibre are strongly dependent on the entrance angle. This implies that more light will propagate through a hollow fibre if the entrance angle is small. This is achieved by either using long focal length lenses or a small laser beam diameter. The change in the collected Raman signal from the silver lined, hollow fibre, when the laser beam diameter is reduced, is discussed further below in section 8.5.3.

The final variable to be considered when using a metal-coated, hollow fibre as a Raman cell is the fibre inner diameter. This affects the fibre loss coefficient as shown by Buric *et al* [Bur10] using mode propagation theory. They show that the loss coefficient is lower for hollow fibres with a larger diameter. This means that fewer modes will propagate through a narrower fibre and the light output angle will be smaller. Therefore, the fibre diameter needs to be large enough to ensure the collected light can be imaged properly by the collection optics, but not so large that it cannot be imaged at all i.e. the numerical apertures of the two systems need to approximately match. As mentioned previously, the fibre diameter will affect the gas flow through the tube. The selected tube diameter needs to be large enough to allow sufficient gas flow through the system.

To give an indication of the possible enhancement from using a hollow fibre as a Raman cell, Pearman *et al* [Pea08] observed an increase in sensitivity of approximately a factor of 20 over their standard fibre optic probe. These measurements were performed with a 2 mm × 4 mm × 496 mm multi-pass capillary cell This is a good indication that the method could improve the sensitivity of the Raman system.

8.4.2 Capillary cell construction

From here onwards, the silver-coated, hollow glass fibre will be referred to as the "capillary". To enable different gas mixtures to be circulated through the capillary, a cell housing needed to be designed. The design and construction of the capillary cell, used in this work, is contained in chapter 4. As described above, the optimal length of the capillary is about 0.8 m. However, the length was limited to 0.65 m, in this work, due to space limitations within the Raman enclosure. The inner diameter of the capillary was 1 mm. This is large enough that gas flow would not be too limited and the scattered light should be able to be collected fairly easily.

To seal the chosen gas within the cell, a window is required. As described in section 8.3.5, a 3 mm thick, calcium fluoride window was chosen as this minimised the observed fluorescence.

8.4.3 Experimental setup for capillary Raman

The experimental setup required for capillary Raman spectroscopy is similar to that of the optimised setup for forward Raman spectroscopy in section 8.3.2. It is shown in figure 8.9. Some of the test measurements, discussed below, involve optimising the focal length of the radiation into/collected from the capillary. For these measurements, a variety of focal length lenses were used in place of the lens with $f = 100\,\text{mm}$.

To optimise the capillary Raman setup, a variety of test measurements have been performed, using the 532 nm 2W *Laser Quantum* Excel laser system. The tests included:

1. Initial capillary Raman tests with air
2. Capillary Raman with various focal length lenses in place of the lens with $f = 100\,\text{mm}$
3. Capillary Raman spectroscopy of D_2
4. Capillary Raman spectroscopy of D_2 at varied pressures
5. Tests of image size of collected Raman signal on the fibre bundle
6. Capillary Raman spectroscopy vs. 90° Raman of D_2.
7. Optimised fibre bundle collection
8. Optimised capillary Raman spectroscopy vs. 90° Raman of D_2

All spectra were analysed using our Spectrum Processing Suite (SpecTools), described in appendix A.6 (and [SJLc], [SJLd]).

8.4.4 Initial capillary Raman tests with air

To check that the silver-coated capillary was mounted correctly inside the cell, initial measurements were performed with the back end of the cell open, i.e. only one pass of the laser beam went through the capillary. This enabled the transmission through the capillary to be checked whilst aligning the system for the first time. It also meant that there was definitely air from the room contained within the capillary. The initial measurements were performed with a $f = 75\,\text{mm}$ cylindrical lens placed in front of the fibre bundle. This was chosen as this is the required focal length for normal forward and backward Raman spectroscopy.

The initial tests were performed using lenses with focal lengths $f = 100, 150$ and $200\,\text{mm}$; the raw spectra are shown in figure 8.10. The figure shows that the signal is higher when the focal length becomes shorter. This makes sense based on the results reported by other groups in the literature, who used shorter focal length lenses to match the numerical aperture of the capillary [Okit10], [Bur09]. Light over a larger solid angle

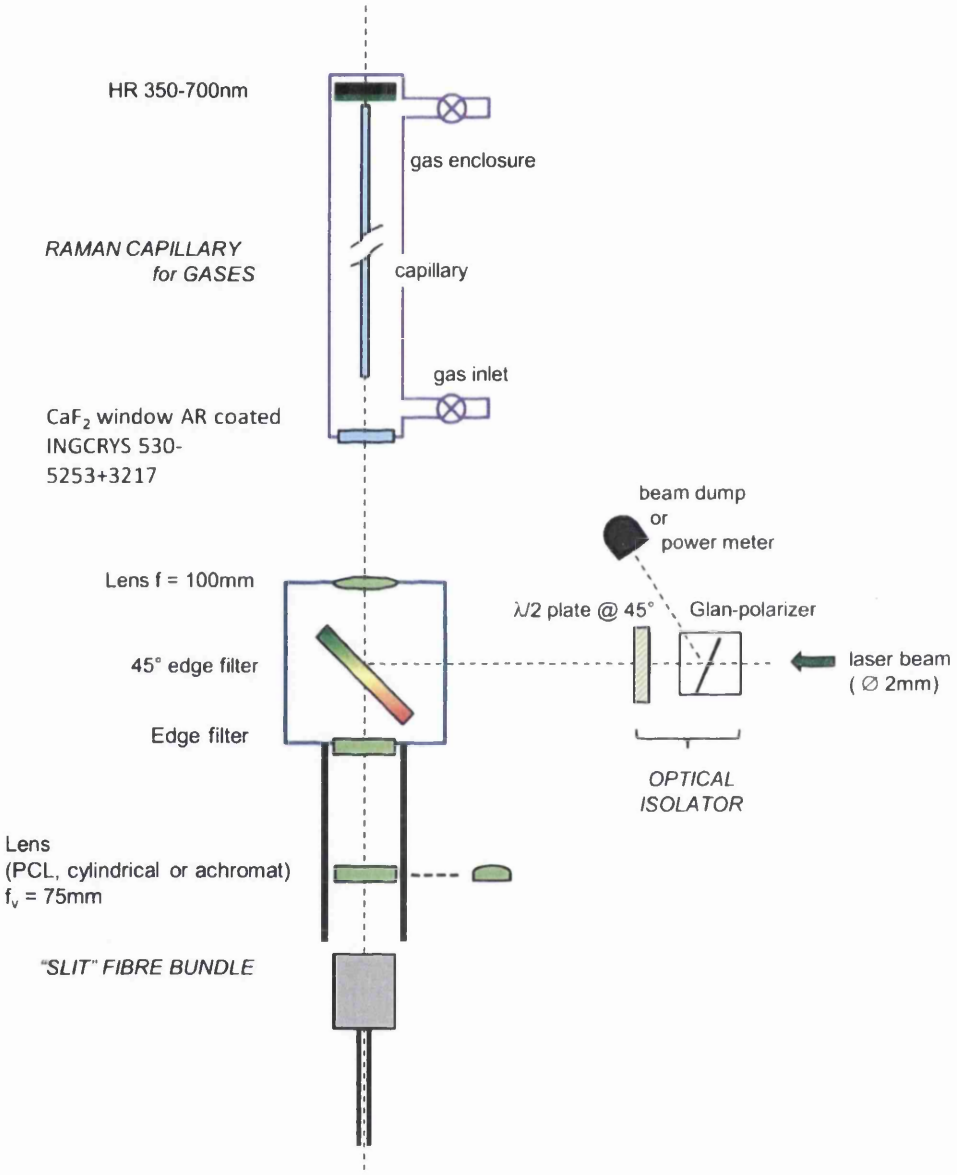

Figure 8.9: Sketch of experimental setup for capillary Raman spectroscopy.

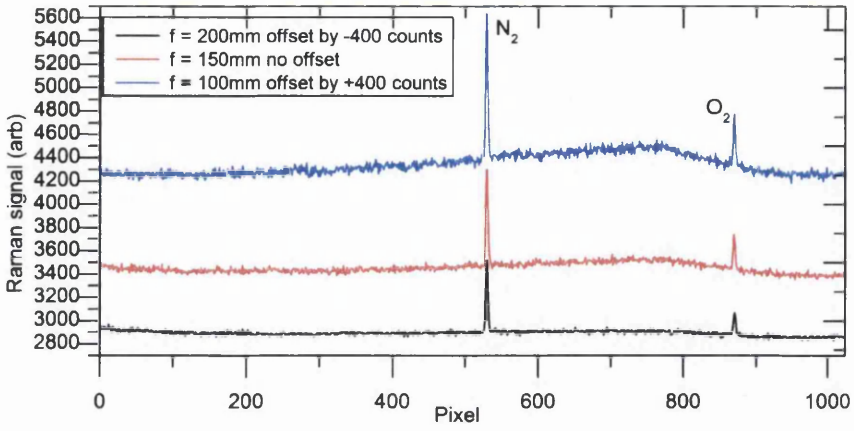

Figure 8.10: Raw 1 pass capillary Raman spectra of air with focal lens lengths of $f = 100, 150$ and 200 mm. Note that the Raman shift/wavelength increases to the left and the spectra have been offset to display the peak intensities more clearly.

will also be collected if the same sized lens (25.4 mm) is closer to the object that is being imaged. For all measurements, discussed below, a $f = 100$ mm focal length lens was used. Note that the spectra in the figure have only been binned (background has not been subtracted), so the fluorescence height is real; the spectra are offset in the figure for clarity. This means that, for shorter focal length lenses, the fluorescence increases slightly. This will not be considered here, as the fluorescence varies when the imaging alignment is changed/optimised.

With the lens of $f = 100$ mm, the capillary Raman signal was compared with normal backward (180°) Raman of air (i.e. when the capillary cell was removed). Raman spectra were taken for acquisition times of $0.5, 1, 5, 10, 20$ and 30 s. For each acquisition time, 2 spectra were recorded back-to-back, to remove cosmic rays using TCRR, and the background was removed using the SCARF routine. An example of the post-TCRR spectra (to compare the fluorescence) for the 1 s acquisition time is shown in figure 8.11. This shows that the fluorescence of the capillary Raman signal is higher than normal backward Raman. However, the signal is noticeably more intensive.

To obtain a better Raman signal comparison, the fluorescence background from each spectrum was removed and the nitrogen Q_1-branch (607 nm) peak height for each acquisition time was compared, as an indication of the gain when using the capillary. This was found to be approximately a factor of 4.

Further tests were performed by fixing the capillary cell in place and adjusting the position of the $f = 100$ mm lens along its cage system until the signal was optimised. The system alignment was carefully checked to ensure the laser beam was parallel to the cage system and the beam passed through the centre of the lens. After the alignment was optimised, a pair of 20 s spectra were recorded. The spectra were cleaned and the background was removed. The cleaned spectrum was compared with a 20 s capillary

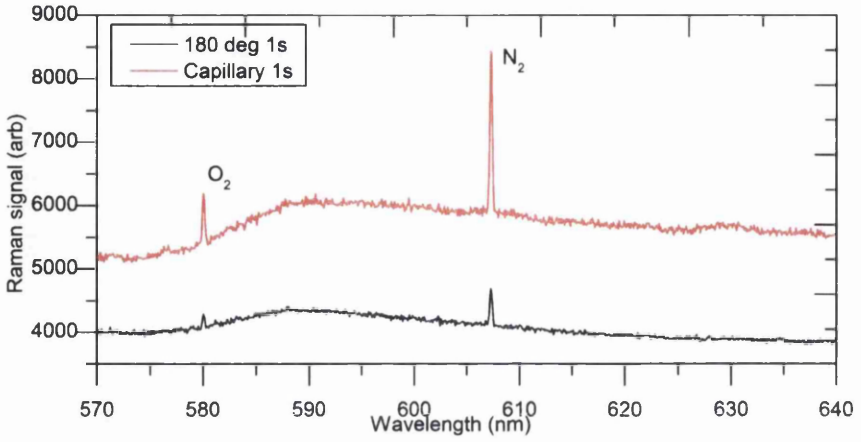

Figure 8.11: Post-TCRR single pass capillary Raman spectra of air compared with 180° Raman spectra. Both spectra were acquired with a 1 s acquisition time.

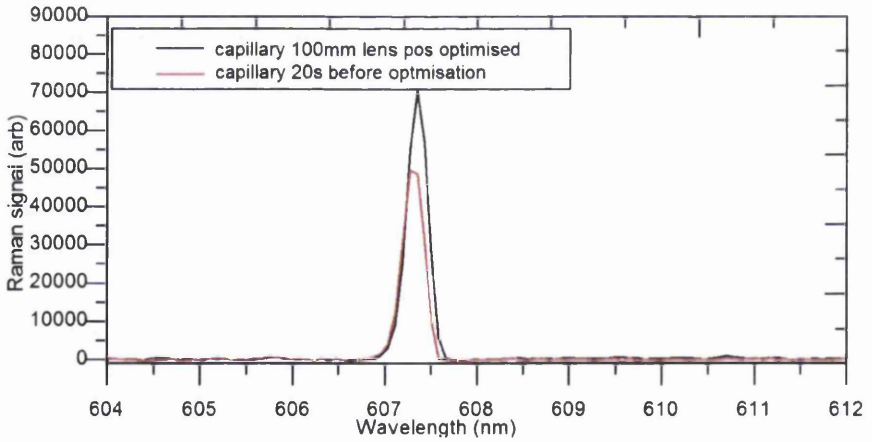

Figure 8.12: Comparison of post-SCARF capillary Raman spectra taken before and after the position of the focussing lens has been optimised. Both spectra were taken with a 20 s acquisition time.

measurement before the lens position was optimised. The resultant comparison is shown in figure 8.12. The figure shows that, in the optimised position, the signal has increased further, by about a factor of 1.4. This shows that ensuring the system is aligned properly and that the position of the lens that is focussing light into and collecting light from the capillary is in its optimal location, is important to achieve the highest signal from the capillary.

8.4.5 Capillary Raman spectroscopy with D_2

The mirror for the second pass of the signal was installed, both ends of the cell were sealed using the custom made flanges and the valves were installed on top of the cell. The system was leak tested and the sealing of the gas inlet threaded connectors was improved by inserting Viton O-rings inside the threaded hole. PTFE tape was used on all the threaded connections. After this was completed a leak check was performed with helium gas and the leak rate was approximately $5 \times 10^{-7}\,\mathrm{mbar\,l^{-1}s^{-1}}$. This was considered to be low enough to connect the capillary cell to the mixing system, evacuate it and fill it with $\approx 1030\,\mathrm{mbar}$ deuterium gas. The capillary cell remained in the optimum location, found in the previous subsection, and was connected to the gas mixing system using flexible hoses, to avoid disturbing the good system alignment.

Spectra were taken using the SP500i spectrograph and Synapse detector. The SP500's 600 gr/mm grating was selected and centred at 633 nm, so that the Q_1-branch of deuterium could be observed. To determine the shortest possible acquisition time, such that the signal of the Q_1-branch was visible above the noise level, a series of measurements were taken starting at 0.5 s. The Q_1-branch was still visible with an acquisition time of 0.005 s. A comparison between the 0.5 s and 0.005 s measurements is shown in figure 8.13. The figure shows that the signal is still observable above the noise level, even at 5 ms light collection time. Note that the detectors quoted minimum acquisition time is 0.001 s.

For a better indication of the sensitivity and dynamic range of the current setup, the S_1- and O_1-branches were also investigated, as they are 50 times weaker than the Q_1-branch for the same isotopologue. Therefore, for the same gas mixture, a variety of longer acquisition times were taken, so these lines could be observed. Multiple repeats, of up to twenty back-to-back acquisitions, were recorded so that the effect averaging multiple spectra have on the noise can be obtained. Since the important quantity, when discussing system sensitivity, is the SNR, knowledge about the system noise behaviour is important.

Twenty repeats of spectra, with acquisition times of 0.5 s, 1 s, 5 s and 7 s were recorded. These spectra were analysed using our Spectrum Processing Suite and were averaged in sets so that the averaging sets were 1 (2 back-to-back), 3, 5, 10 and 20.

The 5× averaged, post-SCARF spectra are collated in figure 8.14. The figure shows

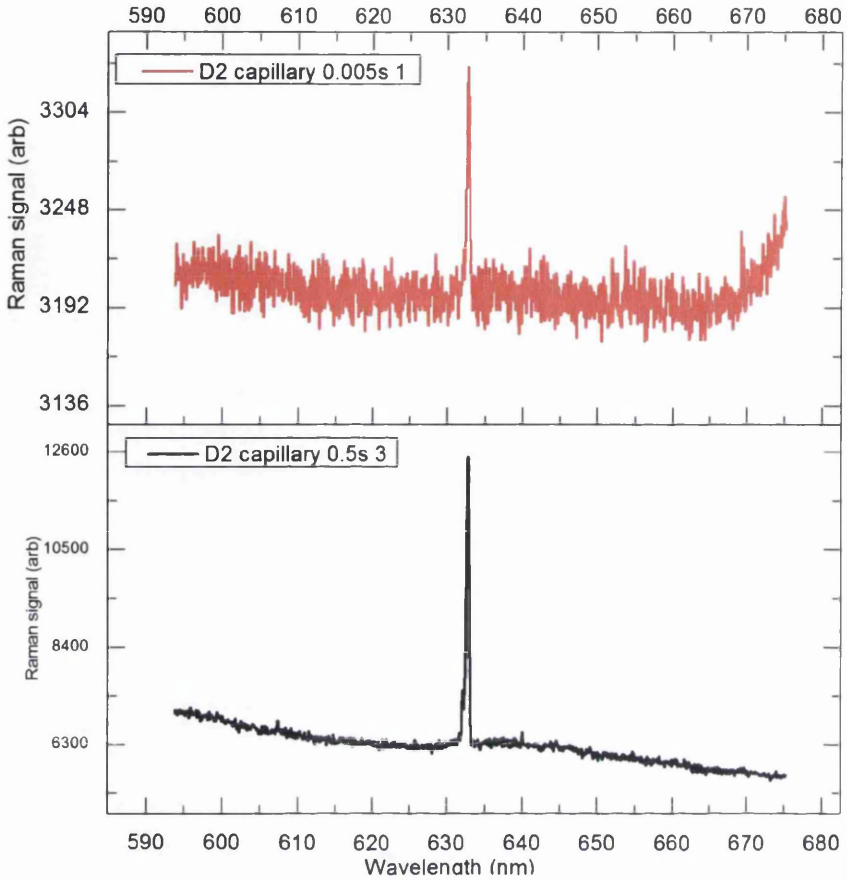

Figure 8.13: Comparison of D_2 capillary Raman spectra. Acquisition times 0.005 s and 0.5 s, 1030 mbar gas pressure, 600gr/mm grating centred at 633 nm

a few things, namely:

- The S_1-branches are visible up to $J = 5$ for the 5 and 7 s acquisition times.
- The Q-branch of HD is visible in the spectrum, which matches with the small quantity expected in a deuterium gas bottle.
- The nitrogen Q-branch is visible at 607 nm. This is caused by the Raman signal that is picked up from air outside the cell.
- The background has a ripple that is present in the longer acquisition times. This is caused by the dichroic beam splitter and edge filter that are required to remove the laser beam from the collected signal. This ripple can be removed by reapplying and retuning the SCARF background removal routine.

One last discussion that can be made on this data is an indication of the sensitivity. The low intensity $S_1(J = 4)$ line is visible for the 5×1 s acquisition. The SNR of this line was calculated to be ≈ 1.7. This is a good approximation of the detection limit

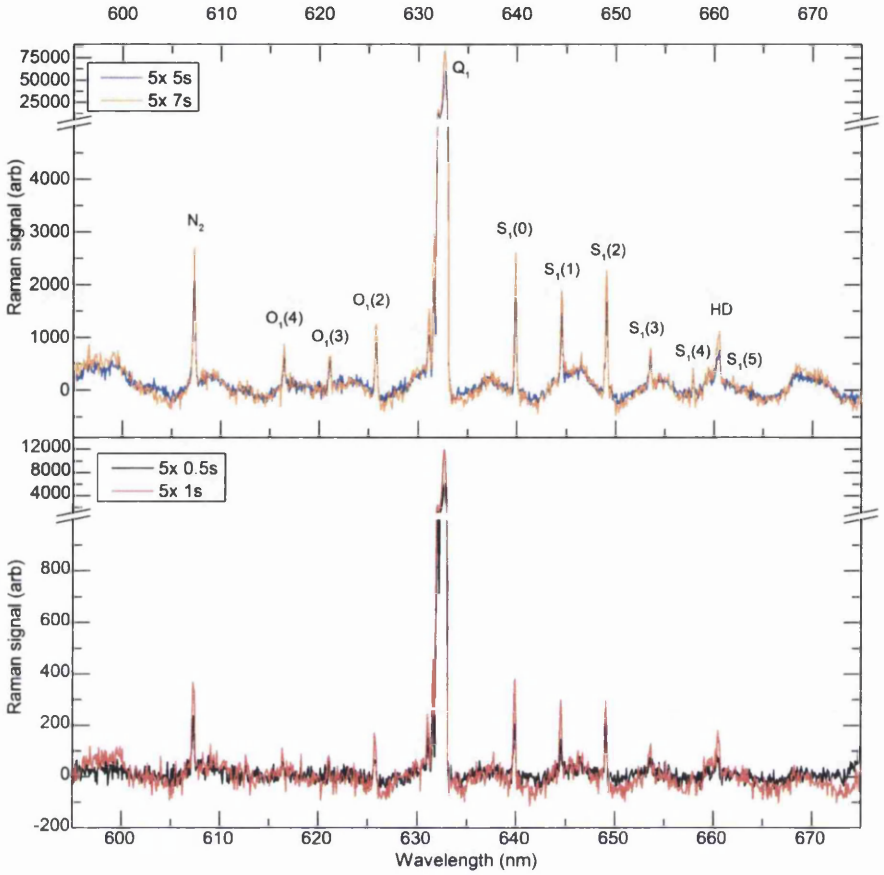

Figure 8.14: Comparison of D_2 capillary Raman spectra each averaged over 5 repeat acquisitions.

SNR of the system. Comparing this with the SNR of the high intensity Q-branch (419) shows that the $S_1(J = 4)$ is ≈ 243 times smaller than the Q-branch of deuterium. If the assumption is made that the Raman signal is directly proportional to the gas pressure (which is valid based on equation (8.1)) the Q-branch would be at the detection limit SNR at a pressure of $1000/243 \approx 4$ mbar. This means that, using the setup in the stated configuration, 4 mbar of deuterium could be detected with a SNR of approximately 1.7. This is a reasonably good indication of the detection limit of this setup in the current configuration for a 5×1 s acquisition.

To verify whether these numbers, for the limit of detection, were correct, the gas pressure inside the capillary was reduced, by reconnecting the cell to the gas mixing system. Gas pressures of 1030 mbar of deuterium were compared with a gas pressure of ≈ 20 mbar. The spectra were recorded 5 times, at an acquisition time 0.5 s and averaged. A comparison plot of the spectra of the two pressures is shown in figure 8.15. The

figure shows that at a pressure of approximately 20 mbar the Q-branch of deuterium

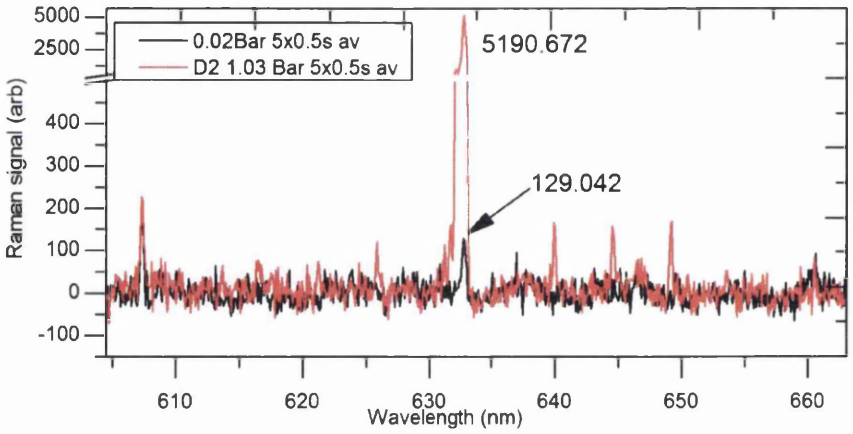

Figure 8.15: Comparison between the Raman spectrum of D_2 at 1030 mbar and 20 mbar. The height of the Q-branch is labelled in the figure.

is still clearly visible above the noise. It also shows that the nitrogen peak at 607 nm is still roughly the same height. This backs up the comment made above that this is the Raman signal of nitrogen in the air outside the cell. The noise of these spectra is approximately 23. This means that with a gas pressure of approximately 20 mbar the Raman peak height (129) is approximately 5 times the noise. Therefore, the signal would be double the noise (at the detection limit), if the pressure was reduced by a factor of 2.5 which would be a pressure of 8 mbar. This is the indication of the detection limit of deuterium for five back to back averaged 0.5 s acquisitions.

A point to keep in mind is that the quoted pressure is a fairly crude approximation. This is because it is measured in the gas mixing system, which is spatially separated from the capillary cell by a long plastic tube (length $\approx$ 3.7 m) and the measurement is performed by a differential pressure gauge with an accuracy of $\pm$0.5 mBar and a minimum detectable pressure of 1 mbar (i.e. atmospheric pressure - 999 mBar). This means that the pressure values exhibit an estimated uncertainty of about $\pm$2 mbar. This is verified by taking a ratio of the heights of the deuterium Q-branch, at both pressures, gives 5191/129 $\approx$ 40. If we then assume that the higher pressure is 1000 mbar and divide it by this number, it gives a pressure of approximately 25 mbar. If 25 mbar is used to calculate the limit of detection for deuterium, for five back to back averaged 0.5 s acquisitions, the limit of detection would be 10 mbar.

This gives more of an indication of the sensitivity of capillary Raman using the current collection method and setup. A further point to note is that the detection limit depends on the collection system. Other systems used by the KATRIN LARA group have a much higher sensitivity, due to a more sensitive detector and a spectrometer with higher light collection power.

8.4.6 Capillary image size

The next test measurements are to verify how much of scattered light from the capillary, imaged by the collection system, is collected by the fibre bundle and transported to the spectrometer system. The easiest way of doing this is to try and determine the size of the image at the fibre location. This can either be done by using an image detector (like a webcam) or by the method which was used here.

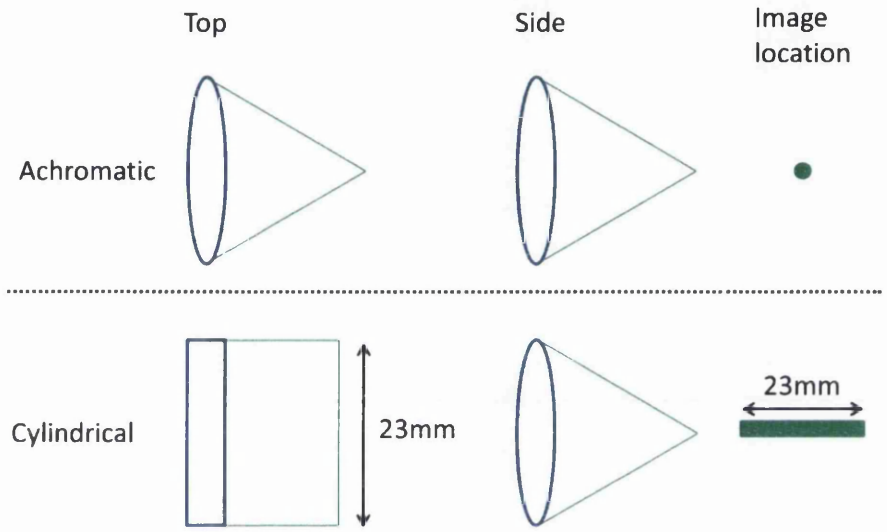

Figure 8.16: Sketch showing imaging when using an achromatic lens and a cylindrical lens. The figure shows the top view, side view and resultant image shape.

The fibre bundle in use is a slit-to-slit mounted configuration of 48 single, adjoining step-index multi-mode fibres with a 100 μm/125 μm core/cladding diameter ratio, as described in chapter 4. The slit dimensions, at each end of the fibre bundle, are approximately 6 × 0.1 mm. The imaging for the measurements above is such that the collected light is focussed in one dimension using a cylindrical lens onto the slit entrance of the fibre bundle. The imaging of light using a cylindrical lens is visualised in figure 8.16 (bottom). The figure shows that a cylindrical lens only focusses the light in one dimension, so at the image location the light is in the form of a slit. This means that the imaged light overlaps the slit entrance of the fibre bundle (figure 8.17 a). However, if the slit entrance of the fibre bundle is rotated by 90° and the transmitted Raman signal is viewed by the detector in 2-dimensional readout mode, the width of the image will equal the image height at the fibre location (figure 8.17 b). This width can be measured by changing the height of the fibre, using the translation stage and calculating how far the fibre has to move, for the image on the detector to move a distance equal to its height.

The method of determining the width is as follows:

- The height of the fibre was adjusted in 10 μm steps and a 5 s 2D Raman spectrum was recorded at the detector (with the fibre bundle rotated by 90°) for each fibre height location, i.
- The centre of the fibre image, x_{ci}, was determined using a custom Gaussian fitting routine; this was taken as the fixed location for each height.
- The fibre height location, i, was fitted, using a linear fit, against the calculated x_{ci} values obtaining the relation $i = Ax_{ci} + B$.
- The fibre image width was determined by inputting the width of the image in pixels, w_f, into this fit to convert the measured width to a real length, Δi.

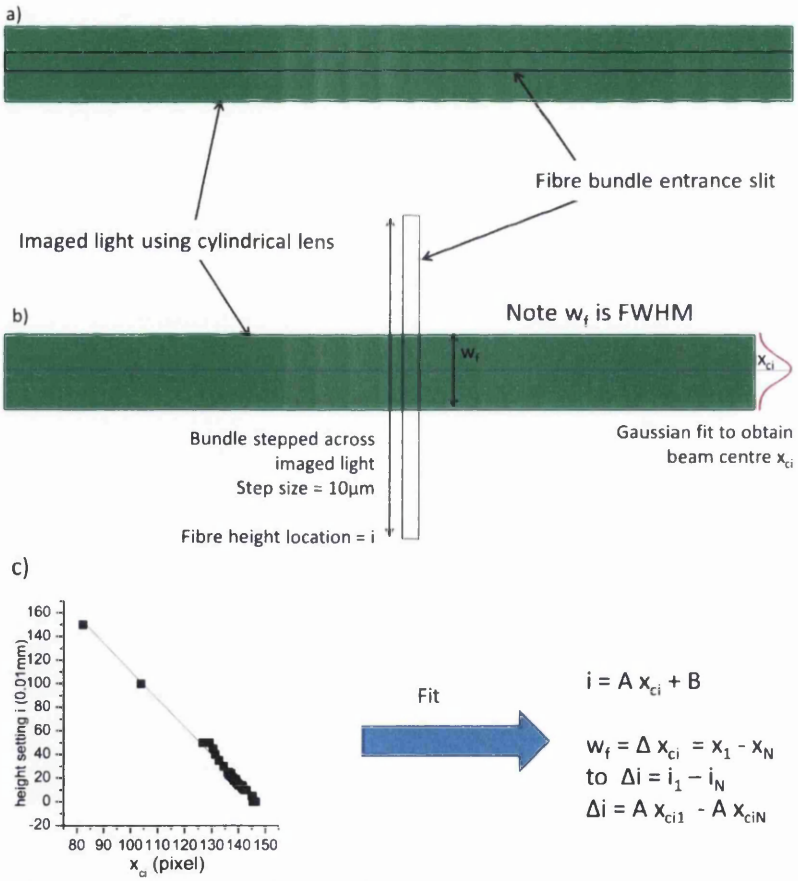

Figure 8.17: Concept for measuring the image of the scattered light from the capillary at the fibre bundle location. a) Imaging onto the slit entrance of the fibre bundle, b) fibre bundle rotated by 90° and moved across image light and c) fit to produce image width in units of length.

The procedure to convert the values mathematically is visualised in figure 8.17 c. However, for clarity the steps are as follows

$$w_f = \Delta x_{ci} = x_1 - x_N \tag{8.4}$$

The required width in units of length is

$$\Delta i = i_1 - i_N \tag{8.5}$$

using the fit relation between i and x_{ci} above leads to

$$\Delta i = A x_{ci1} - A x_{ciN} \tag{8.6}$$

Using the measured values and these equations gives the image width as $\Delta i = 1.183\,\text{mm}$. In the normal imaging location the fibre bundle has a width of $100\,\mu\text{m}$, which means only a small proportion of the light is collected if the entire image size from the capillary is approximately 1 mm.

At this point, the 75 mm cylindrical lens, that is used to focus the light onto the fibre bundle, has been changed to a 75 mm achromatic lens. This means that the image of the capillary is now a "spot" rather than a "slit" 23 mm in length, as shown in figure 8.16 (top); meaning that most of the light, which is collected by the first lens, is imaged onto the fibre bundle, which may increase the signal slightly.

To give an indication of how much light is lost, a second measurement has been proposed. The concept of these next measurements is visualised in figure 8.18. This method assumes that, if the fibre bundle height is adjusted by $100\,\mu\text{m}$, none of the collected light at the new location was collected at the previous height. The fibre height is adjusted in $100\,\mu\text{m}$ steps, over the entire image of the scattered light from the capillary. At each height location the Raman signal is measured (twice), with an acquisition time of 0.5 s. The spectra were all analysed so that cosmic rays and the background were removed. To verify the potential amount of light lost, the spectra of all heights were added together. This is then plotted, along with the most intense height location's spectrum, in figure 8.19.

The figure shows that the summation of the heights leads to an increase in intensity of a factor of 4.73. This means that the signal could increase by another factor of approximately 5, if all the light is collected in an appropriate fibre bundle configuration. The idea for the new fibre bundle is discussed in section 8.5.

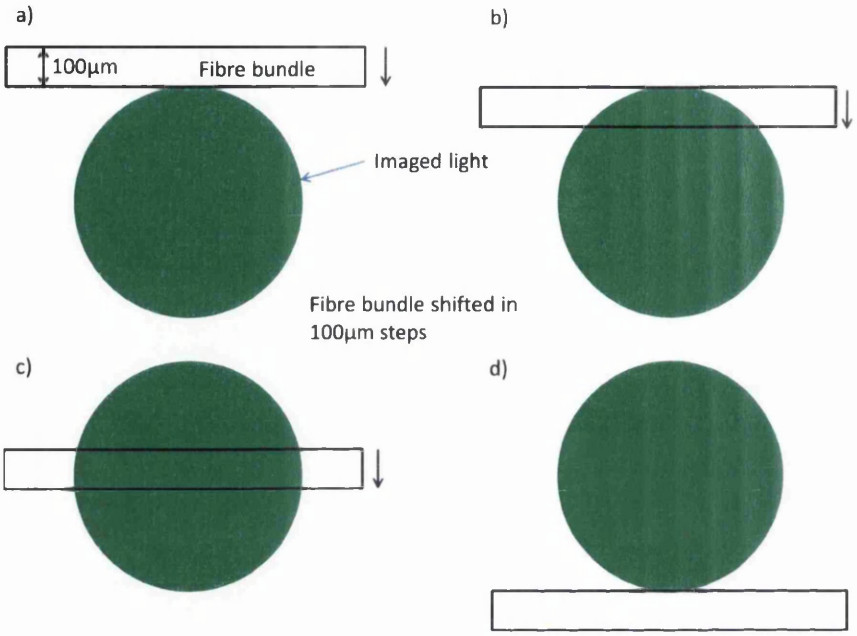

Figure 8.18: Concept for determining the amount of scattered light that is lost by not collecting all of the imaged light at the fibre bundle location. a) Fibre bundle start location, b) fibre bundle moved 100 μm down over capillary image, c) fibre bundle moved in 100 μm steps over the capillary image and d) measurement complete when the full image size has been covered.

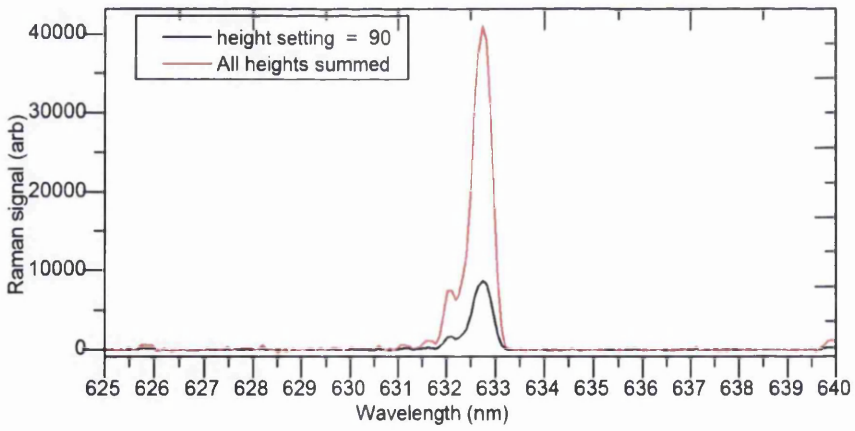

Figure 8.19: Comparison between the Raman spectra of deuterium at the most intense individual fibre bundle height and for the summation of all sequential fibre heights. For measurement description see text.

8.4.7 Capillary Raman spectroscopy vs. 90 degree Raman spectroscopy of deuterium

To give an indication of the gains from using capillary Raman spectroscopy over the normal 90° Raman configuration used in the LARA setups for KATRIN, the system in Swansea was aligned so that the two setups could be measured with the minimum change of optical components. This is implemented as shown in figure 8.20. To switch between

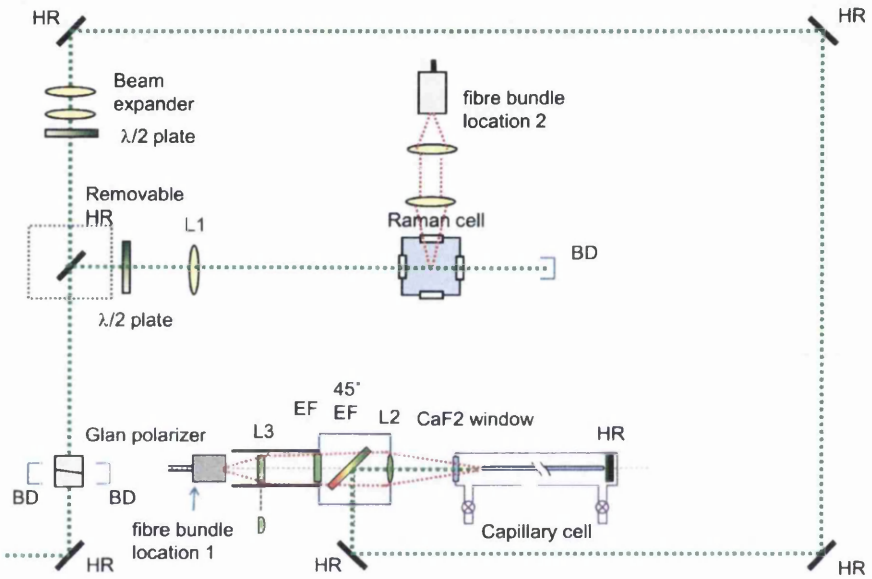

Figure 8.20: Sketch of setup for capillary vs 90° Raman comparison. To switch between the two setups, the mirror, "removable HR" is inserted/removed and the fibre bundle is switched between location 1 and 2. Note that the beam expander is optional.

the two measurement configurations a removable HR mirror is inserted or removed, and the fibre bundle is switched from fibre bundle location-1 to fibre bundle location-2 or vice versa. For the comparison measurements, the lenses in the diagram are L1 = 250 mm plano-convex lens, L2 = 100 mm plano-convex lens and L3 = 75 mm achromatic lens. BD stands for beam dump; the beam expander is a Galilean telescope, to expand the beam (if required) to optimise coupling of the laser beam to the capillary; HR are broadband high reflection mirrors (*Thorlabs* BB1-E02); and EF stands for edge filter.

Both cells were simultaneously connected to the gas mixing system. The Raman cell was removed from its location and connected directly to the gas mixing system and the capillary cell was connected via plastic tubing so that it remained in its optimal location. The cells were filled with approximately 1000 mbar of deuterium gas. The Raman cell was replaced in the LARA setup and the alignment for the 90° setup was optimised.

Once this is aligned, the removable HR can be extracted and replaced without affecting the alignment.

Comparative measurements of sensitivity were taken for acquisition times of $0.5, 1, 2$ and $3\,\mathrm{s}$. This was the maximum achievable acquisition time for the capillary measurements before the detector saturated. The 600gr/mm SP500 grating was selected and centred at $633\,\mathrm{nm}$, so that the Q-branch of deuterium could be analysed. All spectra were taken twice so that cosmic rays could be removed and the background was subtracted, using our Spectrum Processing Suite. The peak height was taken as the most intense peak in the Q-branch and this is used as the indication of peak signal. The noise was calculated as the standard deviation of a flat region of the cleaned background.

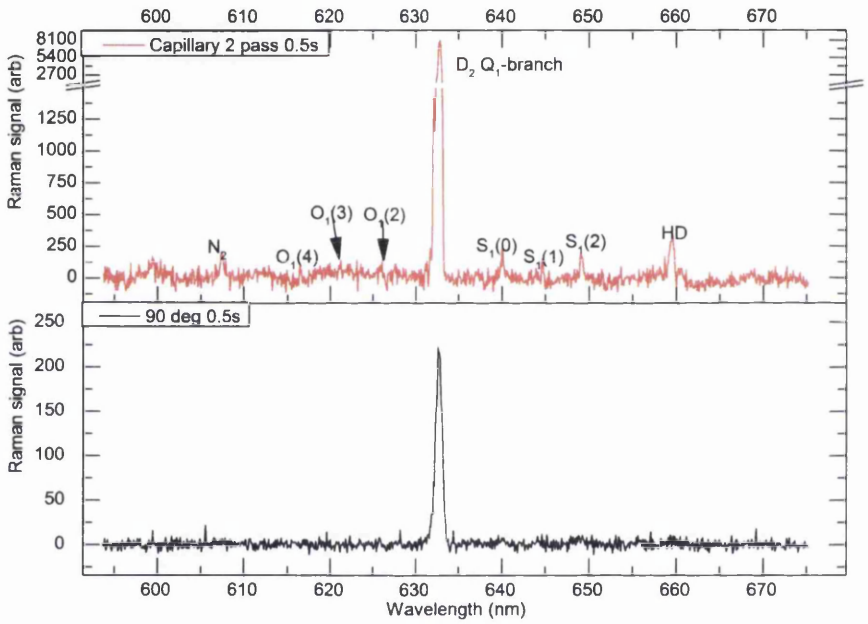

Figure 8.21: Comparison between the Raman spectra of deuterium taken using capillary Raman and 90° Raman with an acquisition time of 0.5 s.

An example comparing the spectra for $0.5\,\mathrm{s}$ acquisition time is shown in figure 8.21. The figure shows that the intensity of the capillary Raman measurement is considerably higher (approximately a factor of 36). However, the noise is also significantly larger.

The SNR was calculated for all acquisitions and the values are collated in table 8.1. The data in the table shows that the Q-branch signal of deuterium has increased by a factor of ≈ 40 for all of the acquisition times. However, the SNR increase is much smaller (between a factor of 1.69 for the $3\,\mathrm{s}$ acquisition time and 4.19 for the $0.5\,\mathrm{s}$ acquisition time). A point to note is that this data was taken using the $100\,\mu\mathrm{m}/125\,\mu\mathrm{m}$ slit-to-slit fibre bundle, described above. This means that the same signal losses, of a factor of (as much as) 4.7 apply. One further point to note is that the observed gain will reduce to

Table 8.1: Signal-to-noise ratio comparison of 90° Raman and capillary Raman.

	90° Raman			capillary Raman		
Ac time (s)	Signal	Noise	SNR	Signal	Noise	SNR
0.5	222.852	3.515	63.408	8100.566	30.571	264.976
1	442.001	3.675	120.280	16167.403	59.152	273.320
2	868.778	3.578	242.785	32689.423	61.897	528.130
3	1299.082	4.108	316.175	48716.997	91.207	534.139

approximately a factor of 20 if two passes of the laser beam were used in the 90° setup.

A method of collecting a higher proportion of the scattered light is proposed in section 8.5, which could lead to two improvements. Firstly, the gain in signal of up to a factor of 4.7 and secondly, the noise will reduce from adding together signal contributions from multiple binning segments of the CCD detector.

Overall, this first implementation of capillary Raman leads to substantially higher signals of approximately a factor of 20 over normal 90° Raman (2 pass capillary vs 2 pass 90°). However, the gain in SNR is less, with a maximum observed enhancement of a factor of 4.19, due to the increased noise, caused by the fluorescence in the capillary and optics in the light beam path. These numbers are the level of improvement where only 100 μm of the scattered light at the fibre location is collected. Measurements have shown that the scattered light image has a diameter of approximately 1 mm and up to a factor of 4.7 of the collected intensity is lost.

8.5 Capillary Raman spectroscopy with new fibre bundle

To optimise light collection for capillary Raman spectroscopy and maximise the signal of the light collected, the fibre bundle needs to be changed. The key of this design is to maintain the same resolution and collection improvements described in chapter 5. This means the dimensions of the individual fibres want to be kept as 48 single, adjoining step index multi-mode fibres with a 100 μm/125 μm core/cladding diameter ratio with a slit configuration that is 6 mm long at the spectrometer end.

8.5.1 CeramOptec fibre bundle

An appropriate fibre bundle design was provided by *CeramOptec*, which consists of 48 100 /125 μm fibres mounted in a dot-to-slit configuration, as shown in figure 8.22. The fibre is constructed such that the dot-end has a radius of < 1 mm. The individual fibres are fused together at the dot-end so that the distance between the individual fibres is as small as possible. The advantage of doing this is that less light will be lost in the gaps between the individual fibres. This results in a total bundle diameter of approximately

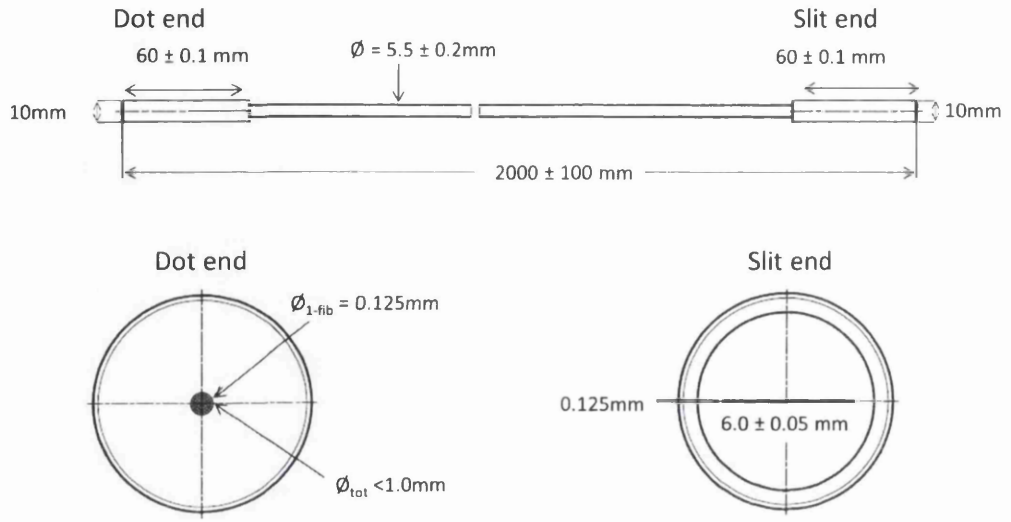

Figure 8.22: Design of dot-to-slit fibre bundle. Adapted from *CeramOptec* design document.

0.75 mm. Even though this is smaller than the spot size measured in section 8.4.6 the close packing of the fibres in the dot-end will result in a higher proportion of light being collected whilst maintaining the advantages of the improved imaging technique at the slit-end (the technique is discussed in chapter 5).

8.5.2 New bundle installation

The new dot-to-slit fibre bundle had its dot-end placed at fibre bundle location 1 in figure 8.20. The old slit-to-slit fibre bundle is then permanently mounted at fibre bundle location 2. The method described to switch between the 90° and capillary Raman measurement configurations, described in section 8.4.7, changes so that the fibre bundles remain permanently fixed at their respective locations. To switch between the two, the bundle connected to the spectrometer cage system is swapped and realigned.

Capillary Raman test measurements with the new fibre bundle are described in the next section.

8.5.3 Optimised deuterium capillary Raman

With the new fibre bundle installed, the capillary Raman measurements of deuterium, described in section 8.4.5, were repeated with the new bundle configuration. This means that the cell contained $\approx$ 1030 mbar of deuterium and spectra were taken using the SP500 spectrograph's 600 gr/mm grating, centred at 633 nm, so that the Q_1-branch of deuterium could be observed. The new fibre bundle was optimised using the custom made translation stage and spectra were taken with a variety of acquisition times. A

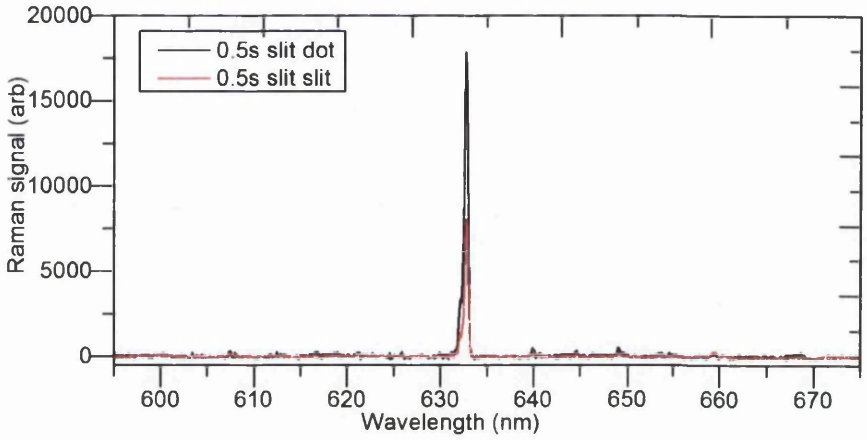

Figure 8.23: Comparison between 0.5 s capillary Raman spectra of deuterium using the original slit to slit fibre bundle and the new dot to slit bundle configuration.

comparison of two of the resultant spectra are collated in figure 8.23. The figure shows that, with the introduction of the new bundle, the observed signal has increased by a factor of approximately two. However, the noise has increased ever so slightly, due to the higher fluorescence level across the entire chip.

A point to note is that, if an acquisition reaches saturation for the on-chip binning area setting, this would usually be the limiting acquisition time. However, the acquisition time can be increased further by increasing the number of on-chip binning segments. As shown in chapter 5, increasing the number of on-chip binning segments usually reduces the SNR. In these situations the noise is predominantly caused by readout noise, so this would be expected (more readouts = more noise). However, for capillary measurements, fluorescence from the capillary and optics is observed. This means that the observed spectral noise is now predominantly caused by the shot noise of the fluorescence. The shot noise for any on-chip binning acquisition is the same, as it is only dependent on the signal height ($= \sqrt{N}$). This is observed by comparing a 50 area and a 3 area on-chip binning 2×2 s capillary Raman acquisition of deuterium in figure 8.24. In the figure, the signal has been normalised to the maximum intensity of the Q_1-branch of deuterium. This means that the noise levels can be compared directly. Observing the noise in the figure shows that, for both acquisitions, the noise is essentially the same. This verifies that these spectra are shot noise dominated and the improvements, observed in chapter 5, that on-chip binning increases the SNR no longer applies, as the on-chip binning enhancement is reducing the readout noise. Therefore, the number of on-chip binning segments should be minimised to keep the readout time as short as possible, but can be increased to enable longer acquisition times.

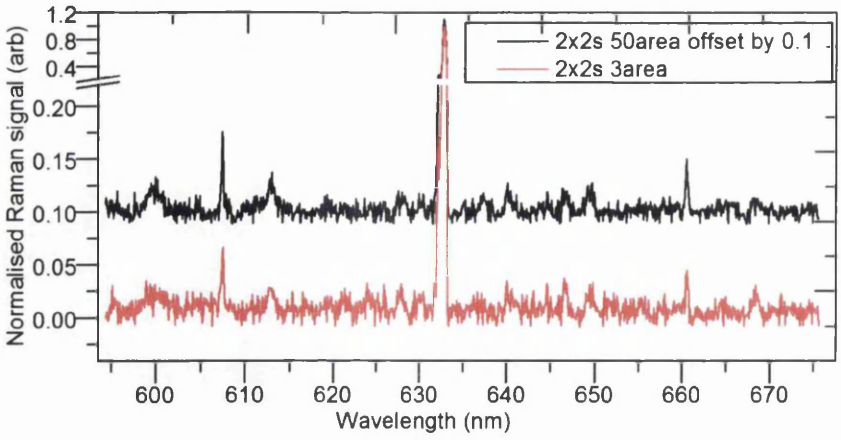

Figure 8.24: Comparison between 50 area and 3 area on-chip binning $2 \times 2\,\mathrm{s}$ acquisition of capillary Raman spectrum of deuterium.

Influence of laser beam size on capillary Raman spectroscopy

The size of the incident laser beam needs to be considered, as it will change the capillary entrance angle, θ, for the same lens focal length, f. This can be calculated using the "geometrical optics" limit for a laser beam, $\theta = R/f$, where R is the beam radius. Reducing the capillary entrance angle will mean that more light should propagate through the capillary, as was shown by Buric *et al* [Bur10].

To test the influence of the laser beam size, measurements were performed with and without a Galilean telescope inserted into the setup and the system alignment was optimised in both situations. Raman spectra of deuterium were taken at various acquisition times, so that the signal and fluorescence, of measurements with and without the telescope, could be compared. A comparison of the raw spectra for an acquisition time of 2 s is shown in figure 8.25. The figure shows that, when the telescope is removed, the fluorescence reduces by approximately a factor of two, which leads to a reduction in the spectral noise. This can be observed in the figure, as the S/O branches of D_2 can be determined more easily. The signal has also increased by approximately 19%. The signal is extracted from the spectrum by removing the fluorescence background, using the routines described in appendix A.6, and taking the maximum peak height of the observed Q_1-branch of D_2. The noise is measured as the standard deviation of a flat region of the spectrum, after the fluorescence background has been removed. The resultant signal, noise and SNR for the no-telescope measurements are collated in table 8.2. If these SNRs are compared with the 90° Raman measurements in table 8.1, in section 8.4.7, it shows that, for all acquisitions, the signal is approximately a factor of 100 larger; as with the previous capillary Raman measurements, the noise is also larger. This means that the SNR increase is between a factor of 3.6 (2 s ac time) and 5.3 (0.5 s

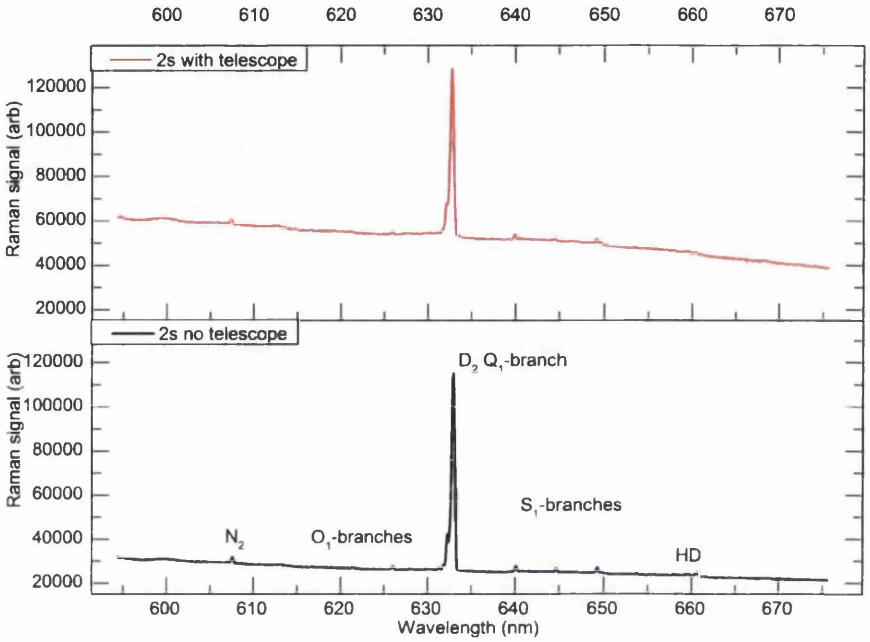

Figure 8.25: Comparison between raw capillary Raman spectra of deuterium when a telescope is used and when it is removed.

Table 8.2: SNR comparison of capillary Raman of the Q_1-branch of deuterium when the incident beam has not been expanded. Uncertainties in brackets are in the final digit.

Ac time (s)	Signal	Noise	SNR
0.1	4724(69)	21(3)	223(35)
0.2	9141(96)	33(5)	279(44)
0.5	22476(150)	66(11)	338(53)
1	44900(212)	80(13)	561(89)
2	89223(299)	101(16)	880(139)
2.5	112287(335)	118(19)	948(150)

ac time). The SNR can be increased by averaging multiple spectra to reduce the noise level.

Fluorescence dependence on laser beam power

To test the dependence of the observed fluorescence on the laser power, a half-wave plate was inserted into the setup in front of the Glan polariser in figure 8.20. Rotating the half-wave plate enables the power of the laser beam to be varied, without affecting the alignment of the system. Capillary Raman spectra of air were taken, with an acquisition time of 3 s, for half-wave plate angles between 0° and 120° in 10° steps, to enable a sufficient number of spectra at various laser powers to be measured. The height of the Q-branch of nitrogen above the fluorescence background was used as an indication of the laser beam power. Note that the Synapse detector in use has a dark background level of approximately 3000 counts in this instance; this has not been subtracted from the fluorescence measurements. As the fluorescence varies with respect to wavelength, the small feature at 660 nm (pixel number 191) was used as a marker of the fluorescence magnitude. The resultant graph of fluorescence height vs. Raman signal is shown in figure 8.26.

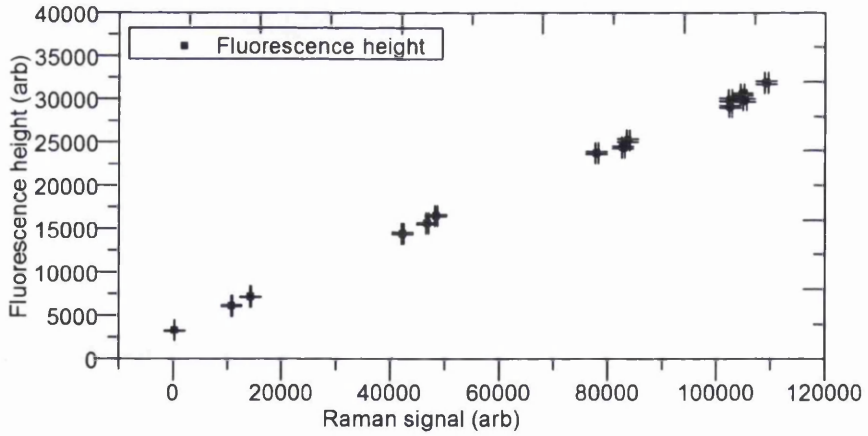

Figure 8.26: Graph of fluorescence height vs. Raman signal. All acquisitions were 3 s capillary Raman measurements of air. For details see text.

The figure shows that the relationship between Raman signal and fluorescence height is linear. If the data is extrapolated back to zero Raman signal the fluorescence height appears to be non-zero. This offset corresponds to the dark background offset of the detector, when zero intensity is observed, of approximately 3000 counts. Please note these measurements were performed with the calcium fluoride window and NBK7 plano-convex lens installed in the system.

Quartz window test

Due to the success of the test measurements discussed above, in future measurements the capillary setup will be tested with the tritiated hydrogen isotopologues at TLK. The current window in use, a 2 mm thick CaF_2 window, is not tritium compatible, so it will need to be changed. Therefore, test measurements have been performed where the calcium fluoride window has been replaced by a 2 mm thick quartz window, which is compatible with tritium. Capillary Raman spectra were taken, with a 2 s acquisition time with no window, a CaF_2 window and a quartz window installed in the cell. Cosmic rays were removed using the routines described in appendix A.6. The fluorescence in the spectra is compared in figure 8.27. The figure shows that the fluorescence of the

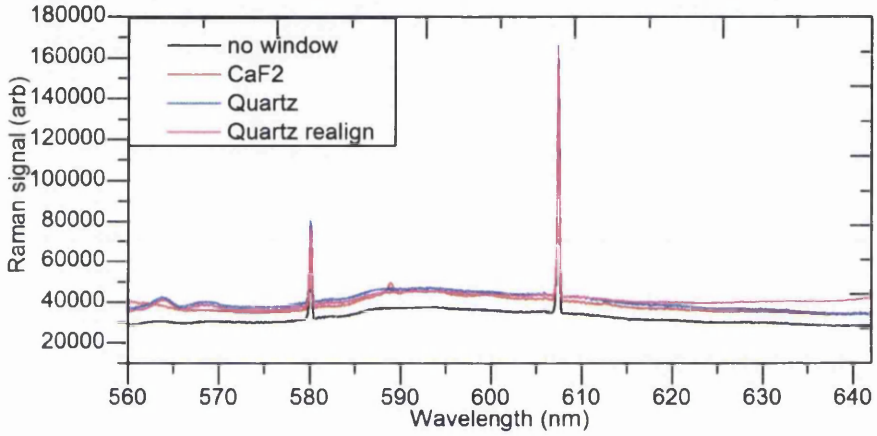

Figure 8.27: Graph of fluorescence height vs. Raman signal. All acquisitions were 3 s capillary Raman measurements of air. For details see text.

calcium fluoride window and the Quartz window are similar. The structure present in the spectra at 565 nm and 589 nm are the Raman features of quartz and calcium fluoride respectively.

The figure also shows that, even when no window is in place, there is still a noticeable fluorescence background. This will be caused by a combination of the focussing optics (focussing lens and dichroic beam splitter) and the capillary itself. The fluorescence of the lens can be reduced by replacing the *ThorLabs* LA1509-A N-BK7 100 mm lens with a thinner optic with the same focal length. Changing the material of the optic to quartz may also be beneficial in reducing the fluorescence.

One other observation that can be made from this data can be obtained by removing the fluorescence background using the SCARF routine, described in appendix A.6 and measuring the peak height of the Q-branch of nitrogen at 607.38 nm. The resultant intensities are collated in table 8.3. The data shows that, when the calcium fluoride window is in place, the signal is noticeably lower than when a quartz window, or no window, is used (17.6% lower than no window measurement). This implies that the

Table 8.3: Measured signal of the Raman Q-branches of nitrogen and oxygen when different windows are installed in the system. Note the uncertainty (in brackets) is in the last digit.

Window	N_2 Signal	O_2 Signal
no window	120315(347)	37383(193)
CaF_2	99149(315)	30842(176)
Quartz	123196(351)	40458(201)
Quartz realign	120897(348)	39094(198)

quartz window leads to an improvement in the Raman signal even if the fluorescence is still approximately the same as when calcium fluoride is used. The reason for this is linked to the coating used on the respective optics.

To try and determine the sensitivity of the current measurements, one hundred 2 s capillary Raman spectra of air were taken. The spectra were analysed and averaged to reduce the noise. The resultant comparison between 2×2 s and 100×2 s Raman spectra is shown in figure 8.28. The figure shows that multiple repeats reduces the noise level and hence increases the SNR. This means that the low intensity peaks that are just visible at 571.1 nm and 574.5 nm in the 2×2 s are clearly visible in the 100×2 s spectrum. These features have been identified as the Fermi doublet of carbon dioxide, using the measurements and discussion included in chapter 7.

As the Raman feature of carbon dioxide has been identified in the capillary Raman spectrum of air, some quantitative information can be extracted from the spectrum and compared with the expected literature values. To do this, the data was re-analysed by averaging the spectra before the background was removed using SCARF. This is to ensure that the background has been removed more accurately. The resultant labelled spectrum is included in figure 8.29. The figure shows that the Raman lines of nitrogen, oxygen and carbon dioxide are observed along with the minor isotopologue of nitrogen $^{15}N^{14}N$. The broad features between 560 nm and 570 nm are the Raman lines of the quartz window installed in the cell.

From this spectrum, the Raman signal of the observed lines has been extracted and are collated in table 8.4. From the measured Raman signal, the ratio with respect to the N_2 Q_1-branch has been calculated and is also included in the table. To compare these ratios with the expected values from the literature, the Raman cross section and spectral response need to be taken into account. Several groups have measured the relative Raman cross section of various gases with respect to the cross section of nitrogen. Some of these results are summarised by Fenner *et al* [Fen73] and Danichkin *et al* [Dan81].

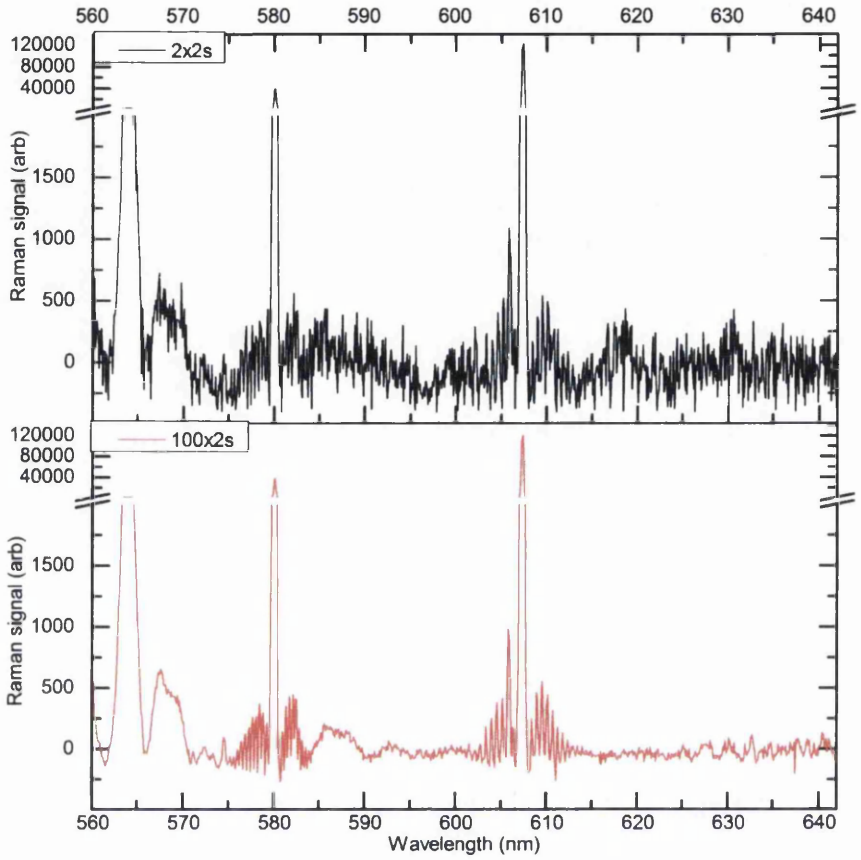

Figure 8.28: Comparison between $2 \times 2\,\mathrm{s}$ and $100 \times 2\,\mathrm{s}$ capillary Raman spectra. Both have been averaged so the Raman signal height is the same.

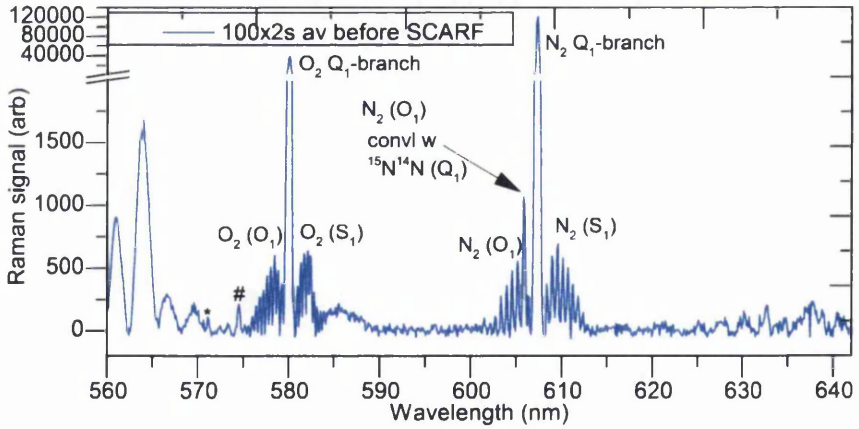

Figure 8.29: Labelled capillary Raman spectrum of air. Average of $100 \times 2\,\mathrm{s}$ spectra. * and # correspond to the ν_1 and $2\nu_2$ Fermi doublet of CO_2.

Table 8.4: Measured signal and composition (relative to the N_2 Q-branch) of the observed Raman branches in the averaged 100 × 2 s capillary Raman spectra of air.

Peak	Signal	Ratio to N_2 Q_1	Rel Raman cross sec σ_i/σ_{N_2} [Dan81]	Comp N_i/N_{N_2}
N_2 Q_1-branch	122322(350)	1.0000(41)	1.00(0)	1.0000(41)
O_2 Q_1-branch	39034(198)	0.3191(19)	1.23(6)	0.2594(128)
CO_2 ν_1 Fermi doublet	217(23)	0.00178(19)	1.51(9)	0.00118(14)
CO_2 $2\nu_2$ Fermi doublet	115(23)	0.00094(19)	1.00(10)	0.00094(21)
$^{15}N^{14}N$ + N_2 O_1	1075(33)	0.00879(27)	1.00(0)	0.00879(27)
noise	23(5)	0.00019(4)	NA	NA

The Raman intensities dependence on the spectral response is

$$I = \sigma N V D \tag{8.7}$$

where N is the number of molecules, V is the scattering volume, σ is the cross section and D is the collated constants that are independent of the scattering substance. For two gases in the same Raman measurement V and D are the same. Therefore, if a ratio of the two Raman line intensities is taken, this gives

$$\frac{I_1}{I_2} = \frac{\sigma_1 N_1}{\sigma_2 N_2} \tag{8.8}$$

This can be used to obtain the required composition ratio to compare with the theory. The resultant relative compositions are collated in table 8.4.

The expected atmospheric compositions of nitrogen, oxygen and carbon dioxide are 0.78082(12), 0.20945(12) and 0.00039(1) [NPL12]. These can be used to obtain compositions relative to that of nitrogen and give 1.00000(22), 0.26824(16) and 0.00050(1) respectively. The relative composition of oxygen agrees within the experimental uncertainty. However, the measured value for carbon dioxide is out by approximately a factor of two. The reason for the inaccuracy can be linked to the spectral response of the collection system not being taken into account. To obtain accurate measurements of the composition, the system would have to be calibrated. Even though these measurements do not fully agree with the literature values, they give an indication of the sensitivity of the system, as carbon dioxide can be detected in the ambient air.

8.5.4 Comparison of capillary, backward and 90° Raman of air

As a final indication of the improvement from capillary Raman spectroscopy, the spectra of air were taken using the optimised capillary Raman, backward Raman and 90° Raman,

at the same focal location. Note that only one pass of the laser beam is used for 90° Raman and 180° Raman. Spectra with a variety of acquisition times were taken. For each acquisition time setting, 5 back-to-back measurements were taken, to enable the spectra to be averaged to reduce the noise level.

The backward and 90° Raman spectra were taken of open air i.e. no cell was used. An example of the raw spectra for an acquisition time of $2 \times 1\,\mathrm{s}$ and an example of the cleaned spectra for the $5 \times 2\,\mathrm{s}$, acquired using each method, are shown in figure 8.30.

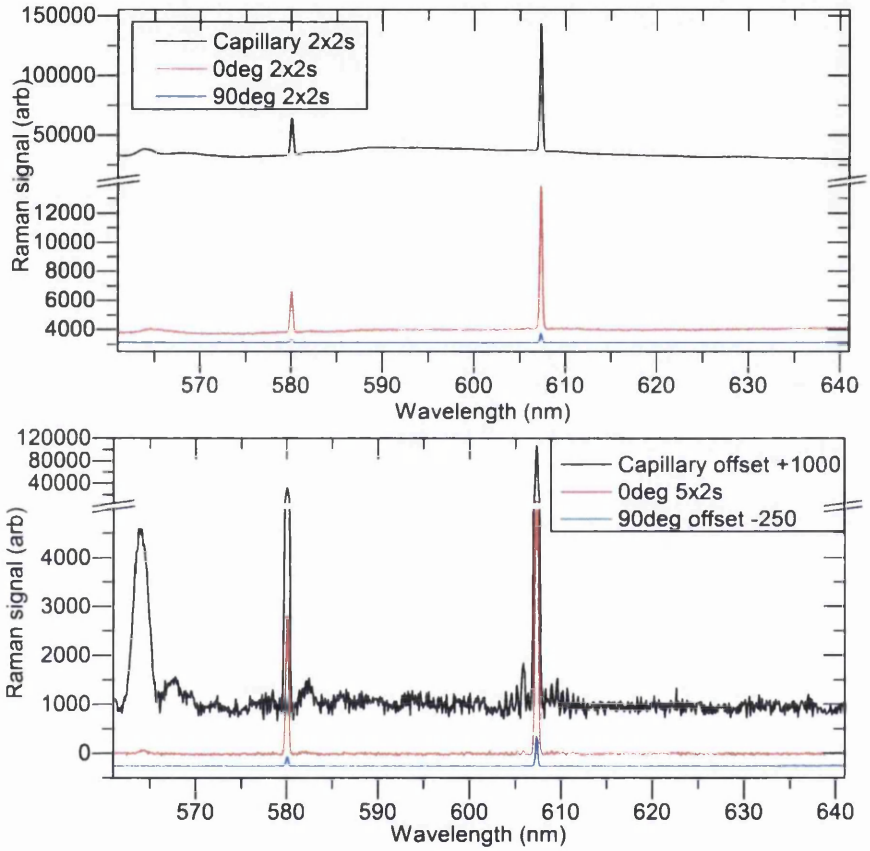

Figure 8.30: Raman spectra of air taken using capillary Raman spectroscopy, 180° Raman and 90° Raman. Top panel: Raw Raman spectra, where the fluorescence height is real (acquisition time $2 \times 2\,\mathrm{s}$); Bottom panel: Cleaned Raman spectra (acquisition time $5 \times 2\,\mathrm{s}$), where the Raman signal is offset for clarity. The capillary Raman spectrum is offset by $+1000$, the 0° Raman spectrum is not offset and the 90° Raman spectrum is offset by -250.

The figure shows that the Raman signal from capillary Raman is two orders of magnitude (a factor of ≈ 100) higher than that for 1 pass 90°. This gain would reduce to a factor of approximately 50, if two passes of the laser beam are used with the 90° setup. The figure also shows that the signal from capillary Raman is one order of magnitude higher than that for 1 pass backward Raman. Another observation that can be made

from the figure, is that the noise of capillary Raman and 180° Raman is higher than that of 90° Raman. This was already observed in section 8.4.7 above.

A further observation that can be made, is that the background level of capillary Raman is significantly higher than that of 0° and 90° Raman. As the 0° and capillary spectra are acquired with exactly the same beam alignment, this shows that most of the observed fluorescence background in the capillary Raman spectrum is caused by the capillary Raman cell ($38291 - 4042.5 = 34176.5$). 180° Raman has a much smaller fluorescence background, caused by the collection lens ($4042.5 - 3142.5 = 900$). This will also be present in the capillary Raman spectrum and could be reduced by changing the collection lens. However, as the contribution to the capillary Raman fluorescence is small ($900/34176.5 = 0.0263 \approx 2.6\%$) the gain from reducing its magnitude is minimal. Therefore, possible improvements by changing the collection lens material were not investigated further.

To enable a quantitative comparison, the Raman signal was extracted from the spectra as the peak height of the nitrogen Q_1-branch and the noise as the standard deviation of a flat region of the background spectrum. These values were used to calculate the SNR. The signal, noise and SNR are collated in table 8.5.

The table shows that the Raman signal for the comparable acquisition times increases by a factor of 170 between 1 pass 90° Raman and capillary Raman. As the noise in the capillary Raman measurement increases with acquisition time from 4.5 ($5 \times 0.002\,\mathrm{s}$) to 54 ($5 \times 2\,\mathrm{s}$) the SNR increase is smaller and reduces as the acquisition time increases. The gain in SNR between 1 pass 90° Raman and capillary Raman varies between a factor of 9 ($5 \times 2\,\mathrm{s}$) and a factor of 24 ($5 \times 0.2\,\mathrm{s}$). The Raman signal gain between 1 pass 90° Raman and 1 pass 180° Raman is approximately a factor of 15. The gain in SNR is also smaller, due to the increase in noise with acquisition time and varies between a factor of 1.39 ($5 \times 20\,\mathrm{s}$) and a factor of 9.73 ($5 \times 0.2\,\mathrm{s}$). For clarity the signal and SNR gain between 90° and capillary Raman is also included in table 8.5.

8.6 Outlook

The measurements included in this chapter show that capillary Raman spectroscopy (in the optimised configuration) results in a signal gain of two orders of magnitude over the standard 90° Raman setup. The gain in SNR is less than the signal gain factor, due to the increase in the background noise caused by fluorescence in the capillary and cell entrance window.

To push this gain further, the collection setup could be optimised by:

- Increasing the size of the fibre bundle entrance so that it is larger than the capillary image size. This would need to be done whilst keeping the individual fibres as close together as possible. To do this the fibre layout at the spectrometer end would

Table 8.5: Measured Raman signal, noise and SNR of the nitrogen Q_1-branch obtained using capillary, 180° and 90° Raman spectroscopy. The noise is taken as the standard deviation of a flat region of the spectrum. All acquisitions are averages of 5 repeat spectra at the specified acquisition time.

Ac	Capillary			180°		
time(s)	Signal	Noise	SNR	Signal	Noise	SNR
0.002	463(12)	4.5(9)	104(21)	44(3)	2.5(3)	18(2)
0.005	463(11)	4.9(7)	94(13)	40(3)	2.5(3)	16(2)
0.01	748(14)	6.3(9)	120(17)	69(4)	2.6(3)	26(3)
0.05	2862(27)	9.5(17)	301(54)	259(8)	2.8(3)	92(10)
0.1	5507(37)	17.6(25)	314(45)	497(11)	3.4(4)	146(18)
0.2	10918(52)	19.8(37)	550(103)	994(15)	3.8(6)	264(42)
0.5	26550(82)	30.5(46)	872(132)	2497(25)	6.8(7)	365(37)
1	53397(116)	39.0(83)	1371(292)	4863(35)	10.8(11)	450(46)
2	106607(163)	54.0(96)	1973(351)	9757(49)	12.0(13)	810(87)
5	-	-	-	24359(78)	22.0(25)	1108(126)
10	-	-	-	48757(110)	30.0(40)	1625(217)
20	-	-	-	97583(156)	42.3(42)	2307(229)
25	-	-	-	121876(175)	47.2(52)	2580(284)

Ac	90°			Gain		
time(s)	Signal	Noise	SNR	S (Cap/90°)	SNR (Cap/90°)	
0.1	32(3)	2.2(2)	15(2)	172(16)	21(4)	
0.2	64(4)	2.8(4)	23(4)	170(11)	24(6)	
0.5	156(6)	2.6(2)	61(5)	170(7)	14(3)	
1	324(9)	2.5(2)	128(11)	165(5)	11(2)	
2	616(12)	2.7(3)	225(25)	173(3)	9(2)	
5	1567(20)	2.8(3)	605(71)			
10	3179(28)	3.6(4)	879(98)			
20	6287(40)	3.8(5)	1658(219)			
50	15806(63)	4.1(5)	3837(466)			

need to be modified to ensure that the maximum amount of light is transmitted to the spectrometer.

- Imaging the scattered Raman light from the capillary onto the dot-to-slit fibre bundle is very sensitive to movements in the x and y directions. The current translation stage only allows precise adjustment in the x- and z-directions. Replacing this mount by an x-y translation stage (*ThorLabs* ST1XY-S) would enable accurate alignment more easily.

- The intensity of the scattered Raman light from the capillary is also very sensitive to the alignment of the laser beam into the capillary. The alignment process could be improved by mounting the entire cage system (fibre bundle not connected) to a x-y translation stage. This would enable a more accurate adjustment of the laser beam position to optimise the alignment.

As the measurements in this chapter have shown the potential increase in sensitivity of capillary Raman spectroscopy, the setup will be converted so that it is tritium-compatible. This will involve modifying the gas connectors within the cell, so the cell leak tightness is higher. To do this, the setup will be shipped to TLK. It will also enable the setup to be tested with the more sensitive spectrometer systems available and obtain real capillary Raman limits of detection. The increase in sensitivity reported here could lead to further applications of Raman spectroscopy type systems within the tritium analysis and monitoring systems at TLK.

Chapter 9

Summary and outlook

9.1 Summary

Each chapter in this work contains a chapter overview summarising the findings for that chapter. Rather than repeating the same statements, a general overview of the findings will be given here, followed by an outlook of the laser Raman research of gases. Overall, the achievements of this work can be split into the following categories:

1. KATRIN LARA system improvements
2. Depolarisation measurements
3. Raman beyond KATRIN

9.1.1 KATRIN LARA system improvements

The signal-to-noise ratio (SNR) of Swansea's LARA system has been improved, bringing it closer to that of the systems in Tritium Laboratory Karlsruhe (TLK) at Karlsruhe Institute of Technology (KIT). Some of the improvements have also been implemented in all the KATRIN LARA systems; namely:

1. adding a second pass of the laser beam through the LARA cell, as it approximately doubles the laser excitation intensity,
2. on-chip binning readout of the CCD detector, with three or five areas to maximise the SNR whilst enabling astigmatism correction to be implemented,
3. improved spectrometer imaging of the fibre bundle onto the CCD plane and
4. introducing a linear (sheet) polariser between the two collection lenses, which enables the polarisation effects in the system beyond this point to be neglected.

When the improvements were implemented in the Raman systems at TLK, the acquisition time required to achieve the KATRIN requirements of precision has been reduced from 250 s used in Fischer *et al* [Fis11] to 60 s. This has been calculated from measurements of tritium, at lower pressures, performed in the set-up of the third LARA system at TLK (LARA3).

9.1.2 Depolarisation measurements

A technique of accurately measuring the depolarisation ratio in the 90° Raman configuration has been developed, along with a method of correcting for solid angle and polarisation aberration effects in the optics. This technique has been applied to measure the depolarisation ratio of the hydrogen isotopologues and some of the atmospheric gases.

Depolarisation measurements of the hydrogen isotopoloogues

Depolarisation measurements of all six hydrogen isotopologues have been successfully completed and the corrected depolarisation ratios of the Q_1-branch agree with the theoretical values, calculated by LeRoy, with a 1σ confidence level. Comparing the values of hydrogen with others in the literature, shows that the results obtained in this work are more accurate than previously published data. The results of these measurements have been accepted for publication in James *et al* [Jam12a] and the depolarisation correction method has been described in a separate publication, Schlösser *et al* [Sch12a].

The line positions of the non-tritiated hydrogen isotopologues have been accurately measured and compared with the theoretically calculated energy levels of LeRoy, as well as the experimental approximations of the line positions given in chapter 2. The measured line positions of D_2 agree with the theoretical values, within the experimental uncertainty. The H_2 and HD lines have been found with an offset of $0.8\,\mathrm{cm}^{-1}$ and $0.5\,\mathrm{cm}^{-1}$ respectively, compared to the LeRoy values. This offset is probably caused by an inaccurate wavelength calibration. The measurements show that the approximations of the line positions of HD, based on literature spectroscopic constants given in chapter 2, are no longer valid for $J > 4$, as the offset between the values measured here increases beyond this point.

Depolarisation measurements of atmospheric gases

Spectroscopy and depolarisation measurements on the atmospheric gases methane, carbon dioxide, nitrogen and oxygen have been performed. The depolarisation ratios of the various branches have been successfully determined and compared with the values that are available from the literature. Reliable calculations of the polarisability matrix

elements would need to be performed, to enable a similar rigorous comparison with the theory, as was made for the hydrogen isotopologues.

The isotopic abundances of the different isotopologues in nitrogen, oxygen and carbon dioxide have been verified from Raman intensity ratios. The measured values match the literature values, within the experimental uncertainty. A similar verification of the isotopic abundance of the minor isotopologue of methane could not be performed; this feature convolutes with the equivalent branch of the main isotopologue.

Overall, this indicates that the KATRIN LARA setup can measure compositions to a reasonably high accuracy, as long as the spectral lines are sufficiently resolved.

9.1.3 Raman beyond KATRIN

Various test setups to improve the sensitivity of Raman spectroscopy beyond the scope of the KATRIN experiment have been investigated. The main techniques that have been discussed are: 0° (forward scattering), 180° (backward scattering), and capillary Raman spectroscopy. The sensitivity increase has been demonstrated with the "final" optimal capillary Raman setup, using air as the scattering medium. In these measurements it was possible to detect carbon dioxide, at the ppm level, for short light collection times. Capillary Raman spectra of pure deuterium have also been measured successfully, with short acquisition times of less than 3 s reaching detection limits of $\approx 0.21\%$, demonstrating the feasibility of using the setup with the hydrogen isotopologues.

Capillary Raman spectroscopy has been found to produce Raman signals that are a factor of 170 higher than single-pass 90° Raman, when comparing the Raman Q_1-branch of nitrogen in air. The increase in the SNR varies, as the acquisition time changes, between a factor of 9 for five averaged 2 s acquisitions, and 24 for five averaged 0.2 s acquisitions. This variation is associated with the noise increasing with acquisition time for capillary Raman spectroscopy, whereas it remains approximately constant for 90° Raman spectroscopy. Consequently, there is a potential to reduce the noise further without attenuating the signal, and thus improving the SNR.

9.2 Outlook

As the research discussed in this thesis is part of an on-going collaboration between Swansea University and the Tritium Laboratory Karlsruhe (TLK) at the Karlsruhe Institute of Technology (KIT), further improvements can be made, and the research can be taken forward.

As a result of the successful verification of the theoretical polarisability matrix elements of LeRoy [LRoy88] [Roy12], with a 1σ confidence level, these will be used to produce an accurate calibration of the KATRIN LARA system for all six hydrogen isotopologues. This is achieved by using the polarisability matrix elements to form

a theoretical Raman intensity, and combining this with the spectral sensitivity of the LARA system. Before this work had been completed, a method of accurately measuring the spectral sensitivity of the KATRIN LARA system had been developed at TLK by other members of the LARA group [Rup12]. This calibration method, using theoretical intensities and spectral sensitivity, could be compared with the HYDE calibration of accurate gas samples ([Her11], [Rup12]), for the non-tritiated hydrogen isotopologues H_2, HD and D_2. This comparison is discussed in Schlösser *et al* [Sch12b] and demonstrated that the resultant relative response functions agreed within 2%. This comparison will be extended to include the tritiated hydrogen isotopologues, by extending the HYDE calibration method; this will be investigated at TLK in the near future.

To complete the full comparison of the measured and theoretical Raman spectra, the preliminary accurate measurements of the line positions of the non-tritiated hydrogen isotopologues will be repeated and extended at TLK to include all six hydrogen isotpologues. To enable an accurate comparison, a sufficient number of calibration lamps will be used to calibrate all of the relevant spectral regions accurately.

As the KATRIN LARA system in TLK can now be fully calibrated and the system exhibits higher sensitivity, a repeat of the long-term LOOPINO test run will be performed. To make this situation as similar to the real KATRIN run, the system would have to output compositions in real time, throughout the measurement run of approximately one month. This is shorter than an individual KATRIN run of 60 days, but it will enable a thorough test of the LARA system in KATRIN-like conditions. To do this, the analysis software routines, discussed in the appendix of this work, will be combined with the acquisition routine, as one integrated software package in *National Instruments* LabVIEW. Methodologies will also have to be devised and the appropriate equipment identified to provide operator-feedback on LARA-fail situations. The system will be calibrated before the start of the measurement run, to determine the spectral sensitivity. This will be combined with the experimentally verified polarisability tensors of LeRoy to enable the measured Raman signals to be converted to a composition. This composition will be output in real time and the precision of these values will also be monitored. The aim is to perform this KATRIN-like LARA test run before the end of June 2013.

As a result of the successful tests of capillary Raman spectroscopy increasing the measurement sensitivity, the system has been sent to TLK to be converted, so that it is tritium compatible. This will involve fully testing the system with various non-tritiated gas mixtures, to identify the modifications that would be required to make the capillary setup tritium compatible. After the conversion is complete, the system will be retested with the tritiated hydrogen isotopologues and the more sensitive detection systems available in TLK. This will enable the sensitivity of the setup to be quantified and to either demonstrate, or reject, the use of capillary-enhancement for tritium monitoring

and accounting at TLK.

Close to the submission point of this thesis, whilst the capillary Raman system was still in Swansea, additional gas circulation measurements were performed. This involved connecting the capillary cell in-line to Swansea's gas mixing system and circulating gas mixtures through the cell. This enabled the formation of HD from a H_2 and D_2 gas mixture to be monitored and observed in real time. The results of these measurements along with the sensitivity improvement comparisons included in this work will be submitted in a forthcoming publication, as they demonstrate the possible capabilities of the system.

To try and improve the sensitivity of Raman spectroscopy of gases, further tests will be performed, where the excitation source wavelength is changed from 532 nm to 405 nm. The excitation source that will be tested is a temperature and current stabilised laser diode, where the wavelength is narrowed and locked, using a holographic grating. As the Raman intensity is proportional to $\tilde{\nu}_0(\tilde{\nu}_0 - \tilde{\nu}_{v,J})^3$, it is therefore inversely proportional to about the 4th power of the laser wavelength. Changing the laser wavelength from 532 nm to 405 nm should lead to an increase in the Raman intensity of between a factor of 2.98 ($\tilde{\nu}_{v,J} = 0\,\mathrm{cm}^{-1}$) and a factor of 3.70 ($\tilde{\nu}_{v,J} = 4500\,\mathrm{cm}^{-1}$). If this potential increase in intensity, from the change in excitation wavelength, is combined with the capillary Raman setup, the increase in the system sensitivity over the KATRIN LARA system would approach two orders of magnitude. This would mean the system is capable of monitoring gas composition in real time, as the acquisition plus analysis time would be on the 1 s time scale. The acquisition plus analysis time scale will be quantified for both the KATRIN LARA system (90°) and capillary Raman setups as this number is important to know the feedback time of a monitoring system.

The KATRIN LARA group in Swansea and TLK intend to investigate these improvements in the coming months as part of the on-going collaboration between the two institutes.

Appendix A

Appendices

These appendices contain extra information that should enhance the understanding of the main content of this thesis. The sections included are

- A.1 Raman intensity theory
- A.2 Swansea's gas mixing system
- A.3 Synapse CCD detector characterisation
- A.4 Depolarisation measurement data of the hydrogen isotopologues
- A.5 Derivation of the polarisbility matrix elements for nitrogen and oxygen
- A.6 Software and analysis routines

A.1 Raman intensity theory

This section contains the step-by-step derivations of different parts of the Raman intensity theory discussed in chapter 3.

A.1.1 Single point, zero solid angle (SP0SA) approximation

This section contains the full derivation of the intensity components for the single point, zero solid angle (SP0SA) approximation. The definitions are repeated for clarity.

We firstly define the line strength function with the scattering geometry such that $\varphi = 0$ i.e. the SP0SA approximation. There are four intensity configurations to be considered for linearly polarised incident radiation these being: $I(\theta; \perp^s, \perp^i)$, $I(\theta; \perp^s, \|^i)$, $I(\theta; \|^s, \|^i)$ and $I(\theta; \|^s, \perp^i)$.
For $I(\theta; \|^s, \perp^i)$ the polarisation of the scattered ray is

$$(p_{\|0}) \equiv (p_{c0}) \tag{A.1}$$

Then using equation (3.19) leads to

$$(p_{c0}) = -(p_{x0})\cos\theta + (p_{z0})\sin\theta \tag{A.2}$$

From the definition of the incident polarisation we know that $E_{\perp^i} = E_{y0}$, so that $E_{x0} = E_{z0} = 0$ and substituting in the definitions of (p_{x0}) and (p_{z0}) from equations (3.23) and (3.25) leads to

$$(p_{\|0}) = (p_{c0}) = -(\alpha_{xy})E_{y0}\cos\theta + (\alpha_{zy})E_{y0}\sin\theta \tag{A.3}$$

Then squaring and introducing isotropic averages leads to

$$(p_{\|0})^2 = (p_{c0})^2 = (\langle(\alpha_{xy})^2\rangle\cos^2\theta + \langle(\alpha_{zy})^2\rangle\sin^2\theta)E_{y0}^2 \tag{A.4}$$

Using $\langle(\alpha_{xy})^2\rangle = \langle(\alpha_{zy})^2\rangle$ (Long (2002) [Lon02]) and $\cos^2\theta + \sin^2\theta = 1$ leads to

$$(p_{\|0})^2 = \langle(\alpha_{xy})^2\rangle E_{y0}^2 \tag{A.5}$$

This can be substituted into equation (2.4) (with the correct wavelength dependence) and the irradiance $\mathcal{I}$ is introduced as $\mathcal{I} = \frac{1}{2}c\epsilon_0 E_{y0}^2$ for $\perp^i$ and $\mathcal{I} = \frac{1}{2}c\epsilon_0 E_{x0}^2$ for $\|^i$, where c is the speed of light in the vacuum and ϵ_0 is the permittivity of free space to give

$$I(\theta; \|^s, \perp^i) = k_{\tilde{\nu}}\tilde{\nu_0}(\tilde{\nu_0} - \tilde{\nu}_{v,J})^3 g_i N_i \langle(\alpha_{xy})^2\rangle\mathcal{I} \tag{A.6}$$

Following similar derivations for $I(\theta; \perp^s, \perp^i)$, $I(\theta; \perp^s, \|^i)$ and $I(\theta; \|^s, \|^i)$ gives:

for $I(\theta; \perp^s, \perp^i)$

$$(p_{\perp 0}) = (p_{b0}) = (\alpha_{yy})E_{y0} \tag{A.7}$$

$$(p_{\perp 0})^2 = (p_{b0})^2 = \langle(\alpha_{yy})^2\rangle E_{y0} \tag{A.8}$$

using the definitions of irradiance from above

$$I(\theta; \perp^s, \perp^i) = k_{\tilde{\nu}}(\tilde{\nu_0}(\tilde{\nu_0} - \tilde{\nu}_{v,J})^3 g_i N_i \langle(\alpha_{yy})^2\rangle \mathcal{I} \tag{A.9}$$

for $I(\theta; \perp^s, \|^i)$ $E_{\|^i} = E_{x0}$ so

$$(p_{\perp 0}) = (p_{b0}) = (\alpha_{yx})E_{x0} \tag{A.10}$$

$$(p_{\perp 0})^2 = (p_{b0})^2 = \langle(\alpha_{yx})^2\rangle E_{x0}^2 \tag{A.11}$$

using the definitions of the irradiance from above

$$I(\theta; \perp^s, \|^i) = k_{\tilde{\nu}}\tilde{\nu_0}(\tilde{\nu_0} - \tilde{\nu}_{v,J})^3 g_i N_i \langle(\alpha_{yx})^2\rangle \mathcal{I} \tag{A.12}$$

and for $I(\theta; \|^s, \|^i)$ $E_{\|^i} = E_{x0}$

$$(p_{\|0}) = (p_{c0}) = -(\alpha_{xx})E_{x0}\cos\theta + (\alpha_{zx})E_{x0}\sin\theta \tag{A.13}$$

$$(p_{\|0})^2 = (p_{c0})^2 = (\langle(\alpha_{xx})^2\rangle \cos^2\theta + \langle(\alpha_{zx})^2\rangle \sin^2\theta)E_{x0}^2 \tag{A.14}$$

using the definitions of irradiance from above

$$I(\theta; \|^s, \|^i) = k_{\tilde{\nu}}\tilde{\nu_0}(\tilde{\nu_0} - \tilde{\nu}_{v,J})^3 g_i N_i \left(\langle(\alpha_{xx})^2\rangle \cos^2\theta + \langle(\alpha_{zx})^2\rangle \sin^2\theta\right)\mathcal{I} \tag{A.15}$$

A.1.2 Extended source, non-zero solid angle (ESSA) approximation

This section contains the full derivation of the intensity components for the extended source, non-zero solid angle (ESSA) approximation. The definitions are repeated for clarity. To bring the theory into line with a real measurement setup the line strength function will now be defined, where φ and θ are both allowed to vary i.e. the ESSA approximation. The four intensity configurations for linearly polarised incident radiation are the same as for the SP0SA approximation. The notation is changed to also include the dependence on φ. For $I(\theta, \varphi; \|^s, \perp^i)$ the polarisation of the scattered ray is

$$(p_{\|0}) \equiv (p_{\underline{c}0}) \tag{A.16}$$

Then using equation (3.22) this becomes

$$(p_{\underline{c}0}) = -(p_{x0})\cos\varphi\cos\theta - (p_{y0})\sin\varphi\cos\theta + (p_{z0})\sin\theta \tag{A.17}$$

From the definition of the incident polarisation we know that $E_{\perp^i} = E_{y0}$, so that $E_{x0} = E_{z0} = 0$ and substituting in the definitions of (p_{x0}), (p_{y0}) and (p_{z0}) from equations (3.23), (3.24) and (3.25) leads to

$$(p_{\|0}) = (p_{\underline{c}0}) = -(\alpha_{xy})E_{y0}\cos\varphi\cos\theta - (\alpha_{yy})E_{y0}\sin\varphi\cos\theta + (\alpha_{zy})E_{y0}\sin\theta \quad \text{(A.18)}$$

Then squaring and introducing isotropic averages leads to

$$\begin{aligned}(p_{\|0})^2 = ((p_{\underline{c}0}))^2 = (&\langle(\alpha_{xy})^2\rangle\cos^2\varphi\cos^2\theta \\ &+ \langle(\alpha_{yy})^2\rangle\sin^2\varphi\cos^2\theta + \langle(\alpha_{zy})^2\rangle\sin^2\theta)E_{y0}^2\end{aligned} \quad \text{(A.19)}$$

using the definitions of irradiance from above leads to

$$\begin{aligned}I(\theta,\varphi;\|^s,\perp^i) = k_{\tilde{\nu}}\tilde{\nu_0}(\tilde{\nu_0} - \tilde{\nu}_{v,J})^3 g_i N_i(&\langle(\alpha_{xy})^2\rangle\cos^2\varphi\cos^2\theta \\ &+ \langle(\alpha_{yy})^2\rangle\sin^2\varphi\cos^2\theta + \langle(\alpha_{zy})^2\rangle\sin^2\theta)\mathcal{I}\end{aligned} \quad \text{(A.20)}$$

Following similar derivations for $I(\theta,\varphi;\perp^s,\perp^i)$, $I(\theta,\varphi;\perp^s,\|^i)$ and $I(\theta,\varphi;\|^s,\|^i)$ gives for $I(\theta,\varphi;\perp^s,\perp^i)$

$$(p_{\perp 0}) = (p_{\underline{b}0}) = -(p_{x0})\sin\varphi + (p_{y0})\cos\varphi \quad \text{(A.21)}$$

From the definition of the incident polarisation we know that $E_{\perp^i} = E_{y0}$ so that $E_{x0} = E_{z0} = 0$ and substituting in the definitions of (p_{x0}) and (p_{y0}) from equations (3.23) and (3.24) leads to

$$(p_{\perp 0}) = (p_{\underline{b}0}) = -(\alpha_{xy})E_{y0}\sin\varphi + (\alpha_{yy})E_{y0}\cos\varphi \quad \text{(A.22)}$$

Then squaring and introducing isotropic averages leads to

$$(p_{\perp 0})^2 = ((p_{\underline{b}0}))^2 = (\langle(\alpha_{xy})^2\rangle\sin^2\varphi + \langle(\alpha_{yy})^2\rangle\cos^2\varphi)E_{y0}^2 \quad \text{(A.23)}$$

$$= (\langle(\alpha_{yy})^2\rangle - (\langle(\alpha_{yy})^2\rangle - \langle(\alpha_{xy})^2\rangle)\sin^2\varphi)E_{y0}^2 \quad \text{(A.24)}$$

using the definitions of irradiance from above leads to

$$I(\theta,\varphi;\perp^s,\perp^i) = k_{\tilde{\nu}}\tilde{\nu_0}(\tilde{\nu_0} - \tilde{\nu}_{v,J})^3 g_i N_i(\langle(\alpha_{yy})^2\rangle - (\langle(\alpha_{yy})^2\rangle - \langle(\alpha_{xy})^2\rangle)\sin^2\varphi)\mathcal{I} \quad \text{(A.25)}$$

For $I(\theta,\varphi;\perp^s,\|^i)$ the polarisation of the scattered ray is

$$(p_{\perp 0}) = (p_{\underline{b}0}) = -(p_{x0})\sin\varphi + (p_{y0})\cos\varphi \quad \text{(A.26)}$$

From the definition of the incident polarisation we know that $E_{\|^i} = E_{x0}$ so that $E_{y0} = E_{z0} = 0$ and substituting in the definitions of (p_{x0}) and (p_{y0}) from equations (3.23) and (3.24) leads to

$$(p_{\perp 0}) = (p_{\underline{b}0}) = -(\alpha_{xx})E_{x0}\sin\varphi + (\alpha_{yx})E_{x0}\cos\varphi \quad \text{(A.27)}$$

Then squaring and introducing isotropic averages leads to

$$(p_{\perp 0})^2 = ((p_{\underline{b}0}))^2 = (\langle(\alpha_{xx})^2\rangle \sin^2\varphi + \langle(\alpha_{yx})^2\rangle \cos^2\varphi)E_{x0}^2 \tag{A.28}$$

using the definitions of irradiance from above leads to

$$I(\theta,\varphi;\perp^s,\|^i) = k_{\tilde{\nu}}\tilde{\nu}_0(\tilde{\nu}_0 - \tilde{\nu}_{v,J})^3 g_i N_i(\langle(\alpha_{xx})^2\rangle \sin^2\varphi + \langle(\alpha_{yx})^2\rangle \cos^2\varphi)\mathcal{I} \tag{A.29}$$

For $I(\theta,\varphi;\|^s,\|^i)$ the polarisation of the scattered ray is

$$(p_{\|0}) = (p_{\underline{c}0}) = -(p_{x0})\cos\varphi\cos\theta - (p_{y0})\sin\varphi\cos\theta + (p_{z0})\sin\theta \tag{A.30}$$

From the definition of the incident polarisation we know that $E_{\|^i} = E_{x0}$ so that $E_{y0} = E_{z0} = 0$ and substituting in the definitions of (p_{x0}), (p_{y0}) and (p_{z0}) from equations (3.23), (3.24) and (3.25) leads to

$$(p_{\|0}) = (p_{\underline{c}0}) = -(\alpha_{xx})E_{x0}\cos\varphi\cos\theta - (\alpha_{yx})E_{x0}\sin\varphi\cos\theta + (\alpha_{zx})E_{x0}\sin\theta \tag{A.31}$$

Then squaring and introducing isotropic averages leads to

$$\begin{aligned}(p_{\|0})^2 = ((p_{\underline{c}0}))^2 = (&\langle(\alpha_{xx})^2\rangle \cos^2\varphi\cos^2\theta \\ &+ \langle(\alpha_{yx})^2\rangle \sin^2\varphi\cos^2\theta + \langle(\alpha_{zx})^2\rangle \sin^2\theta)E_{x0}^2\end{aligned} \tag{A.32}$$

using the definitions of irradiance from above leads to

$$\begin{aligned}I(\theta,\varphi;\|^s,\|^i) = k_{\tilde{\nu}}\tilde{\nu}_0(\tilde{\nu}_0 - \tilde{\nu}_{v,J})^3 g_i N_i(&\langle(\alpha_{xx})^2\rangle \cos^2\varphi\cos^2\theta \\ &+ \langle(\alpha_{yx})^2\rangle \sin^2\varphi\cos^2\theta + \langle(\alpha_{zx})^2\rangle \sin^2\theta)\mathcal{I}\end{aligned} \tag{A.33}$$

A.1.3 Complete line strength function - ESSA

This section contains the additional lines of calculation that enable the derivation of the line strength function equations for the ESSA approximation for diatomic molecules to be followed more easily. For clarity the four polarisation configurations are:
$I(\theta,\varphi;\|^s,\perp^i)$, $I(\theta,\varphi;\perp^s,\perp^i)$, $I(\theta,\varphi;\|^s,\|^i)$ and $I(\theta,\varphi;\|^s,\|^i)$.

Firstly for $I(\theta,\varphi;\|^s,\perp^i)$ if we substitute equations (3.42) and (3.43) into equation (A.20) gives

$$\begin{aligned}I(\theta,\varphi;\|^s,\perp^i) = k_{\tilde{\nu}}\tilde{\nu}_0(\tilde{\nu}_0 - \tilde{\nu}_{v,J})^3 g_i N_i\Big(&\frac{1}{15}b^2_{Jf0:Ji0}|\langle v^f|\gamma|v^i\rangle|^2\cos^2\varphi\cos^2\theta \\ &+ (|\langle v^f|a|v^i\rangle|^2 + \frac{4}{45}b^2_{Jf0:Ji0}|\langle v^f|\gamma|v^i\rangle|^2)\sin^2\varphi\cos^2\theta \\ &+ \frac{1}{15}b^2_{Jf0:Ji0}|\langle v^f|\gamma|v^i\rangle|^2\sin^2\theta\Big)\mathcal{I}\end{aligned} \tag{A.34}$$

Rearranging leads to

$$
\begin{aligned}
I(\theta,\varphi;\|^s,\perp^i) &= k_{\tilde{\nu}}\tilde{\nu_0}(\tilde{\nu_0}-\tilde{\nu}_{v,J})^3 g_i N_i\Big(|\langle v^f|a|v^i\rangle|^2\sin^2\varphi\cos^2\theta \\
&+ \frac{1}{45}b^2_{Jf0:Ji0}|\langle v^f|\gamma|v^i\rangle|^2(3+\sin^2\varphi)\cos^2\theta \\
&+ \frac{3}{45}b^2_{Jf0:Ji0}|\langle v^f|\gamma|v^i\rangle|^2\sin^2\theta\Big)\mathcal{I} \qquad \text{(A.35)} \\
&= k_{\tilde{\nu}}\tilde{\nu_0}(\tilde{\nu_0}-\tilde{\nu}_{v,J})^3 g_i N_i\Big(|\langle v^f|a|v^i\rangle|^2\sin^2\varphi\cos^2\theta \\
&+ \frac{1}{45}b^2_{Jf0:Ji0}|\langle v^f|\gamma|v^i\rangle|^2(3(\cos^2\theta+\sin^2\theta)+\sin^2\varphi\cos^2\theta)\Big)\mathcal{I} \qquad \text{(A.36)} \\
&= k_{\tilde{\nu}}\tilde{\nu_0}(\tilde{\nu_0}-\tilde{\nu}_{v,J})^3 g_i N_i\Big(|\langle v^f|a|v^i\rangle|^2\sin^2\varphi\cos^2\theta \\
&+ b^2_{Jf0:Ji0}\frac{|\langle v^f|\gamma|v^i\rangle|^2}{45}(3+\sin^2\varphi\cos^2\theta)\Big)\mathcal{I} \qquad \text{(A.37)}
\end{aligned}
$$

Then for $I(\theta,\varphi;\perp^s,\perp^i)$ if we substitute equations (3.42) and (3.43) into equation (A.25) gives

$$
\begin{aligned}
I(\theta,\varphi;\perp^s,\perp^i) &= k_{\tilde{\nu}}\tilde{\nu_0}(\tilde{\nu_0}-\tilde{\nu}_{v,J})^3 g_i N_i\Big(|\langle v^f|a|v^i\rangle|^2+\frac{4}{45}b^2_{Jf0:Ji0}|\langle v^f|\gamma|v^i\rangle|^2 \\
&- (|\langle v^f|a|v^i\rangle|^2+\frac{4}{45}b^2_{Jf0:Ji0}|\langle v^f|\gamma|v^i\rangle|^2 \\
&- \frac{1}{15}b^2_{Jf0:Ji0}|\langle v^f|\gamma|v^i\rangle|^2)\sin^2\varphi\Big)\mathcal{I} \qquad \text{(A.38)}
\end{aligned}
$$

Rearranging leads to

$$
\begin{aligned}
I(\theta,\varphi;\perp^s,\perp^i) &= k_{\tilde{\nu}}\tilde{\nu_0}(\tilde{\nu_0}-\tilde{\nu}_{v,J})^3 g_i N_i\Big(|\langle v^f|a|v^i\rangle|^2+\frac{4}{45}b^2_{Jf0:Ji0}|\langle v^f|\gamma|v^i\rangle|^2 \\
&- |\langle v^f|a|v^i\rangle|^2\sin^2\varphi-\frac{4}{45}b^2_{Jf0:Ji0}|\langle v^f|\gamma|v^i\rangle|^2\sin^2\varphi \\
&+ \frac{3}{45}b^2_{Jf0:Ji0}|\langle v^f|\gamma|v^i\rangle|^2)\sin^2\varphi\Big)\mathcal{I} \qquad \text{(A.39)} \\
&= k_{\tilde{\nu}}\tilde{\nu_0}(\tilde{\nu_0}-\tilde{\nu}_{v,J})^3 g_i N_i\Big(|\langle v^f|a|v^i\rangle|^2(1-\sin^2\varphi) \\
&+ \frac{1}{45}b^2_{Jf0:Ji0}|\langle v^f|\gamma|v^i\rangle|^2(4-\sin^2\varphi)\Big)\mathcal{I} \qquad \text{(A.40)} \\
&= k_{\tilde{\nu}}\tilde{\nu_0}(\tilde{\nu_0}-\tilde{\nu}_{v,J})^3 g_i N_i\Big(|\langle v^f|a|v^i\rangle|^2\cos^2\varphi \\
&+ \frac{1}{45}b^2_{Jf0:Ji0}|\langle v^f|\gamma|v^i\rangle|^2(4-\sin^2\varphi)\Big)\mathcal{I} \qquad \text{(A.41)}
\end{aligned}
$$

Then for $I(\theta,\varphi;\perp^s,\|^i)$ if we substitute equations (3.42) and (3.43) into equation (A.29)

gives

$$I(\theta,\varphi;\perp^s,\|^i) = k_{\tilde{\nu}}\tilde{\nu}_0(\tilde{\nu}_0-\tilde{\nu}_{v,J})^3 g_i N_i\Big(\big(|\langle v^f|a|v^i\rangle|^2 + \frac{4}{45}b^2_{Jf0:Ji0}|\langle v^f|\gamma|v^i\rangle|^2\big)\sin^2\varphi + \frac{1}{15}b^2_{Jf0:Ji0}|\langle v^f|\gamma|v^i\rangle|^2\cos^2\varphi\Big)\mathcal{I} \tag{A.42}$$

Rearranging leads to

$$I(\theta,\varphi;\perp^s,\|^i) = k_{\tilde{\nu}}\tilde{\nu}_0(\tilde{\nu}_0-\tilde{\nu}_{v,J})^3 g_i N_i\Big(|\langle v^f|a|v^i\rangle|^2\sin^2\varphi + \frac{1}{45}b^2_{Jf0:Ji0}|\langle v^f|\gamma|v^i\rangle|^2(4\sin^2\varphi+3\cos^2\varphi)\Big)\mathcal{I} \tag{A.43}$$

$$= k_{\tilde{\nu}}\tilde{\nu}_0(\tilde{\nu}_0-\tilde{\nu}_{v,J})^3 g_i N_i\Big(|\langle v^f|a|v^i\rangle|^2\sin^2\varphi + \frac{1}{45}b^2_{Jf0:Ji0}|\langle v^f|\gamma|v^i\rangle|^2(3(\sin^2\varphi+\cos^2\varphi)+\sin^2\varphi)\Big)\mathcal{I} \tag{A.44}$$

$$= k_{\tilde{\nu}}\tilde{\nu}_0(\tilde{\nu}_0-\tilde{\nu}_{v,J})^3 g_i N_i\Big(|\langle v^f|a|v^i\rangle|^2\sin^2\varphi + \frac{|\langle v^f|\gamma|v^i\rangle|^2}{45}b^2_{Jf0:Ji0}(3+\sin^2\varphi)\Big)\mathcal{I} \tag{A.45}$$

And finally for $I(\theta,\varphi;\|^s,\|^i)$ if we substitute equations (3.42) and (3.43) into equation (A.33) gives

$$I(\theta,\varphi;\|^s,\|^i) = k_{\tilde{\nu}}\tilde{\nu}_0(\tilde{\nu}_0-\tilde{\nu}_{v,J})^3 g_i N_i\Big(\Big(|\langle v^f|a|v^i\rangle|^2 + \frac{4}{45}b^2_{Jf0:Ji0}|\langle v^f|\gamma|v^i\rangle|^2\Big)\cos^2\varphi\cos^2\theta + \frac{1}{15}b^2_{Jf0:Ji0}|\langle v^f|\gamma|v^i\rangle|^2\sin^2\varphi\cos^2\theta + \frac{1}{15}b^2_{Jf0:Ji0}|\langle v^f|\gamma|v^i\rangle|^2\sin^2\theta\Big)\mathcal{I} \tag{A.46}$$

Rearranging leads to

$$I(\theta,\varphi;\|^s,\|^i) = k_{\tilde{\nu}}\tilde{\nu}_0(\tilde{\nu}_0-\tilde{\nu}_{v,J})^3 g_i N_i\Big(|\langle v^f|a|v^i\rangle|^2\cos^2\varphi\cos^2\theta + \frac{1}{45}b^2_{Jf0:Ji0}|\langle v^f|\gamma|v^i\rangle|^2((4\cos^2\varphi+3\sin^2\varphi)\cos^2\theta) + \frac{3}{45}b^2_{Jf0:Ji0}|\langle v^f|\gamma|v^i\rangle|^2\sin^2\theta\Big)\mathcal{I} \tag{A.47}$$

$$= k_{\tilde{\nu}}\tilde{\nu}_0(\tilde{\nu}_0-\tilde{\nu}_{v,J})^3 g_i N_i\Big(|\langle v^f|a|v^i\rangle|^2\cos^2\varphi\cos^2\theta + \frac{1}{45}b^2_{Jf0:Ji0}|\langle v^f|\gamma|v^i\rangle|^2((3+\cos^2\varphi)\cos^2\theta) + \frac{3}{45}b^2_{Jf0:Ji0}|\langle v^f|\gamma|v^i\rangle|^2\sin^2\theta\Big)\mathcal{I} \tag{A.48}$$

$$I(\theta,\varphi;\|^s,\|^i) = k_{\tilde{\nu}}\tilde{\nu}_0(\tilde{\nu}_0-\tilde{\nu}_{v,J})^3 g_i N_i(|\langle v^f|a|v^i\rangle|^2\cos^2\varphi\cos^2\theta$$
$$+\frac{1}{45}b^2_{Jf0:Ji0}|\langle v^f|\gamma|v^i\rangle|^2(\cos^2\varphi\cos^2\theta+3\cos^2\theta+3\sin^2\theta))\mathcal{I} \quad (A.49)$$
$$= k_{\tilde{\nu}}\tilde{\nu}_0(\tilde{\nu}_0-\tilde{\nu}_{v,J})^3 g_i N_i(|\langle v^f|a|v^i\rangle|^2\cos^2\varphi\cos^2\theta$$
$$+\frac{|\langle v^f|\gamma|v^i\rangle|^2}{45}b^2_{Jf0:Ji0}(3+\cos^2\varphi\cos^2\theta))\mathcal{I} \quad (A.50)$$

The line strength functions for the ESSA approximation can be extracted from the final equations for each polarisation regime.

A.1.4 Solid angle parameterisation

The solid angle influences the integration by defining the limits to integrate φ, θ and z over. The simplest collection solid angle that could be considered is that where Raman light is imaged by a single lens. However in all measurements in this work an additional aperture is in place, this being the Raman cell window, as can be seen in figure A.1. If the scattered ray comes from a single point, the smaller aperture would govern the

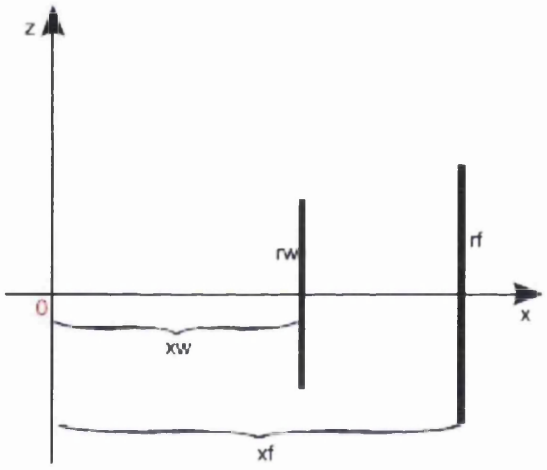

Figure A.1: Sketch of the apertures making up the collection geometry. rw is the window radius, rf is the radius of the "lens aperture", xw is the distance from the scattering centre to the window and xf is the distance from the scattering centre to the "lens aperture".

collection angle. However, as has been discussed in chapter 3, the real collection is extended, 6 mm in length, along the length of the laser beam (z-axis). This means that the aperture overlap becomes more complicated.

The solid angle is parameterised in 3 steps. Firstly the z parameterisation is considered, followed by the θ parametrisation then the φ parameterisation. The solid angle parameterisation that is considered here is the same as that used in the depolarisa-

tion ratio correction software procedure discussed in Schlösser *et al* [Sch12a] and in the documentation for the Depol Tools analysis software ([SJLb] and [SJLa]). The z parameterisation is fairly straightforward, so it will be considered first.

z-parameterisation Figure A.1 can be modified to visually shown the integration limits of z, this is shown in figure A.2. The maximum z position is the furthest position

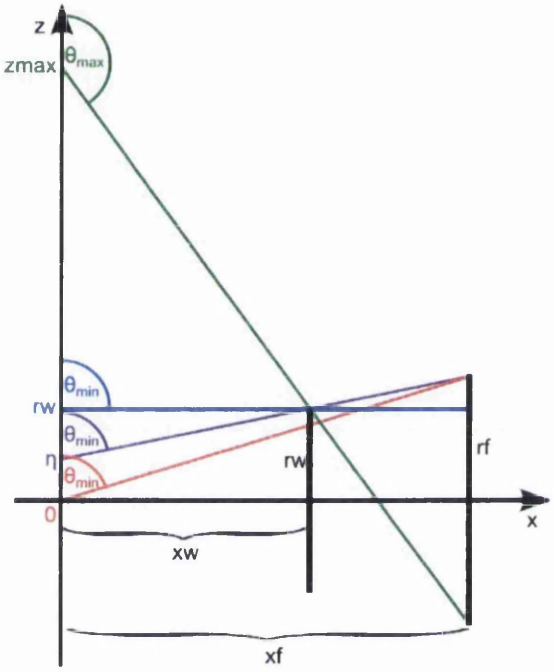

Figure A.2: Sketch of the apertures making up the collection geometry with the limits for z-parameterisation. For details see text.

along the z-axis where light emitted from this location passes through both apertures (z_{max}). It can be calculated using Thale's theorem

$$z_{max}(r_w, x_w, r_f, x_f) = r_w + \frac{x_w}{x_f - r_w}(r_f + r_w) \tag{A.51}$$

As can be seen visually in the figure, the limiting aperture changes as z increases. The positions on the z axis, where the limiting aperture changes, need to be defined when parameterising θ and φ. The first of these is equal to the window radius r_w. The second distance we will define as η as shown in the figure, which is

$$\eta = r_w - x_w \frac{r_f - r_w}{x_f - x_w} \tag{A.52}$$

These definitions are valid when $r_f > r_w$ as is shown in figure A.2. However, in some measurements in this work $r_w > r_f$, which changes figure A.2 to figure A.3. z_{max} is the

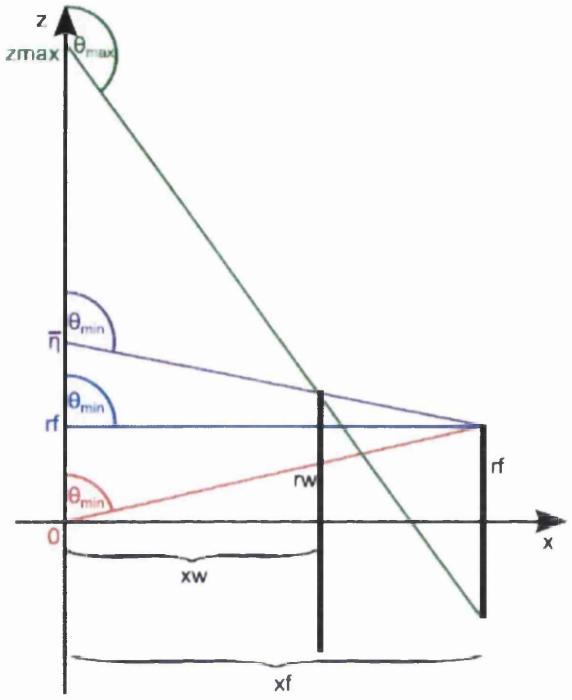

Figure A.3: Sketch of the apertures making up the collection geometry with the limits for z-parameterisation when $r_w > r_f$. For details see text.

same as in the $r_f > r_w$ case and r_f is the second required distance parameter. A new definition of the intermediate distance $\bar{\eta}$ is required

$$\bar{\eta} = r_f + x_f \frac{r_w - r_f}{x_f - x_w} \tag{A.53}$$

This parameterisation splits the light collection limitation up into three regions namely: $0 \leq z \leq \eta$, $\eta < z \leq r_w$ and $r_w < z \leq z_{\max}$ when $r_f > r_w$
and
$0 \leq z \leq r_f$, $r_f < z \leq \bar{\eta}$ and $\bar{\eta} < z \leq z_{\max}$ when $r_w > r_f$. This means that the z-integration is split into three separate terms.

θ-parameterisation Using the distances defined along the z-axis the maximum and minimum values of θ can be defined for both $r_f > r_w$ and $r_w > r_f$. For $r_f > r_w$

$$\theta_{\min}(r_w, x_w, r_f, x_f, z) = \begin{cases} \sin^{-1}\left(\frac{x_f}{(x_f^2+(r_f-z)^2)^{0.5}}\right) & 0 \leq z \leq \eta \\ \sin^{-1}\left(\frac{x_w}{(x_w^2+(r_w-z)^2)^{0.5}}\right) & \eta < z \leq r_w \\ \pi - \sin^{-1}\left(\frac{x_w}{(x_w^2+(r_w-z)^2)^{0.5}}\right) & r_w < z \leq z_{\max} \end{cases} \tag{A.54}$$

and the maximum value of θ in the range $0 \leq z \leq z_{\max}$ is

$$\theta_{\max}(r_w, x_w, r_f, x_f, z) = \frac{\pi}{2} + \tan^{-1}\left(\frac{r_f + z}{x_f}\right) \tag{A.55}$$

For $r_w > r_f$

$$\theta_{\min}(r_w, x_w, r_f, x_f, z) = \begin{cases} \sin^{-1}\left(\frac{x_f}{(x_f^2+(r_f-z)^2)^{0.5}}\right) & 0 \leq z \leq r_f \\ \pi - \sin^{-1}\left(\frac{x_f}{(x_f^2+(r_f-z)^2)^{0.5}}\right) & r_f < z \leq \bar{\eta} \\ \pi - \sin^{-1}\left(\frac{x_w}{(x_w^2+(r_w-z)^2)^{0.5}}\right) & \bar{\eta} < z \leq z_{\max} \end{cases} \tag{A.56}$$

and the maximum value of θ in the range $0 \leq z \leq z_{\max}$ is the same as for $r_f > r_w$

These are the solid angle definitions for $\varphi = 0$. To parameterise φ an additional dependence on φ will need to be included in some of the definitions of the distances and radii.

φ-parameterisation Figure A.4 helps to visualise the φ dependence. The figure shows that the distances x_w and x_f will stretch to new distances x'_w and x'_f. The aperture radii r_w and r_f also get changed to $r_{z,w}$ and $r_{z,f}$, which are the effective radius of the limiting aperture along the φ plane. The effective radii are given by (using Pythagoras)

$$r_{z,w}(\varphi) = (r_w^2 - \tan^2(\varphi)x_w^2)^{0.5} \tag{A.57}$$

$$r_{z,f}(\varphi) = (r_z^2 - \tan^2(\varphi)x_f^2)^{0.5} \tag{A.58}$$

The stretched aperture distances are then given by

$$x'_w(\varphi) = \frac{x_w}{\cos\varphi} \tag{A.59}$$

$$x'_f(\varphi) = \frac{x_f}{\cos\varphi} \tag{A.60}$$

These expressions then can be substituted into the z and θ parameterisation equations ($z_{\max}$, η, $\theta_{\min}$ and $\theta_{\max}$) to obtain for $r_f > r_w$.

$$\begin{aligned} z_{\max}(A, \varphi) = (r_w^2 - \tan^2(\varphi)x_w^2)^{0.5} + \frac{x_w}{x_f - x_w}\Big((r_z^2 - \tan^2(\varphi)x_f^2)^{0.5} \\ + (r_w^2 - \tan^2(\varphi)x_w^2)^{0.5}\Big) \end{aligned} \tag{A.61}$$

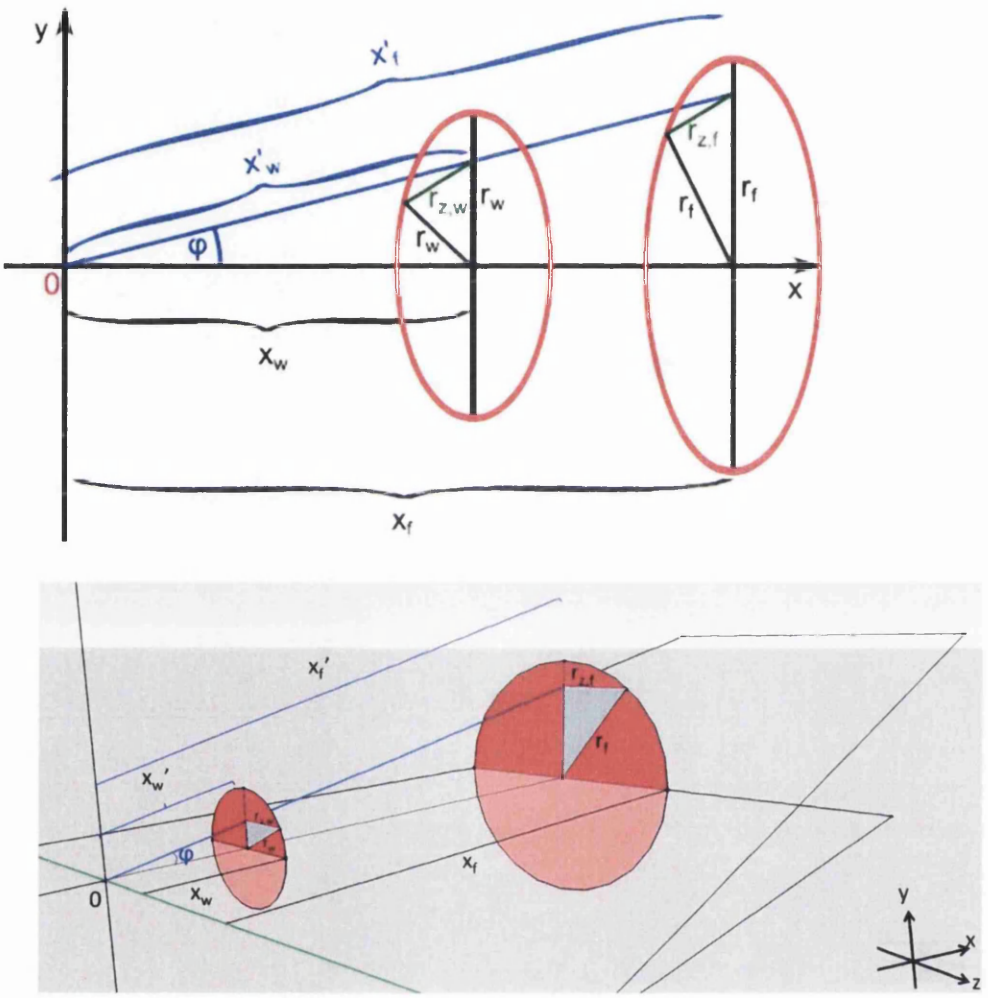

Figure A.4: Sketch of the apertures making up the collection geometry to help visualise the φ-parameterisation. Note the red circles are the apertures and are perpendicular to the y-axis and $r_{z,w}$ is along the φ-plane. For details see text.

$$\eta(A,\varphi) = (r_w^2 - \tan^2(\varphi)x_w^2)^{0.5} - \frac{x_w}{x_f - x_w}\Big((r_w^2 - \tan^2(\varphi)x_w^2)^{0.5} - (r_z^2 - \tan^2(\varphi)x_f^2)^{0.5}\Big) \tag{A.62}$$

$$\theta_{\min}(A,z) = \begin{cases} \sin^{-1}\left(\dfrac{x_f/\cos\varphi}{\left((x_f/\cos\varphi)^2 + \left((r_z^2 - \tan^2(\varphi)x_f^2)^{0.5} - z\right)^2\right)^{0.5}}\right) & 0 \le z \le \eta \\ \sin^{-1}\left(\dfrac{x_w/\cos\varphi}{\left((x_w/\cos\varphi)^2 + \left((r_w^2 - \tan^2(\varphi)x_w^2)^{0.5} - z\right)^2\right)^{0.5}}\right) & \eta < z \le r_w \\ \pi - \sin^{-1}\left(\dfrac{x_w/\cos\varphi}{\left((x_w/\cos\varphi)^2 + \left((r_w^2 - \tan^2(\varphi)x_w^2)^{0.5} - z\right)^2\right)^{0.5}}\right) & r_w < z \le z_{\max} \end{cases} \tag{A.63}$$

and

$$\theta_{\max}(A,z,\varphi) = \frac{\pi}{2} + \tan^{-1}\left(\frac{(r_z^2 - \tan^2(\varphi)x_f^2)^{0.5} + z}{x_f/\cos\varphi}\right) \tag{A.64}$$

Note that for the as a function of $A = r_w, x_w, r_f, x_f$ for display purposes.

For $r_w > r_f$, $z_{\max}$ and $\theta_{\max}$ are the same as for $r_f > r_w$ the other two parameters are

$$\bar{\eta}(A,\varphi) = \left(r_z^2 - \tan^2(\varphi)x_f^2\right)^{0.5} + \frac{x_f}{x_f - x_w}\Big((r_w^2 - \tan^2(\varphi)x_w^2)^{0.5} - (r_z^2 - \tan^2(\varphi)x_f^2)^{0.5}\Big) \tag{A.65}$$

and

$$\theta_{\min}(A,z) = \begin{cases} \sin^{-1}\left(\dfrac{x_f/\cos\varphi}{\left((x_f/\cos\varphi)^2 + \left((r_z^2 - \tan^2(\varphi)x_f^2)^{0.5} - z\right)^2\right)^{0.5}}\right) & 0 \le z \le r_f \\ \pi - \sin^{-1}\left(\dfrac{x_f/\cos\varphi}{\left((x_f\cos\varphi)^2 + \left((r_z^2 - \tan^2(\varphi)x_f^2)^{0.5} - z\right)^2\right)^{0.5}}\right) & r_f < z \le \bar{\eta} \\ \pi - \sin^{-1}\left(\dfrac{x_w/\cos\varphi}{\left((x_w/\cos\varphi)^2 + \left((r_w^2 - \tan^2(\varphi)x_w^2)^{0.5} - z\right)^2\right)^{0.5}}\right) & \bar{\eta} < z \le z_{\max} \end{cases} \tag{A.66}$$

The final parameter than needs defining is $\varphi_{\max}$ which is simply

$$\varphi_{\max} = \tan^{-1}\left(\frac{r_f}{x_f}\right) \tag{A.67}$$

and is valid in all situations.

All the parameterisations are now dependent on φ. This means that the parameterisations can now be set as the integration limits for the intensity integral.

A.2 Swansea's gas mixing system

A.2.1 Introduction

The discussion here is a reproduction of the manual on how to use the gas mixing system in Swansea safely and correctly. The gas mixing system is mounted to the trolley containing the Swansea laser Raman (LARA) enclosure and is spread over two plates as can be seen in figures A.5 and A.6. A circuit diagram of the gas mixing system is contained in figure A.7.

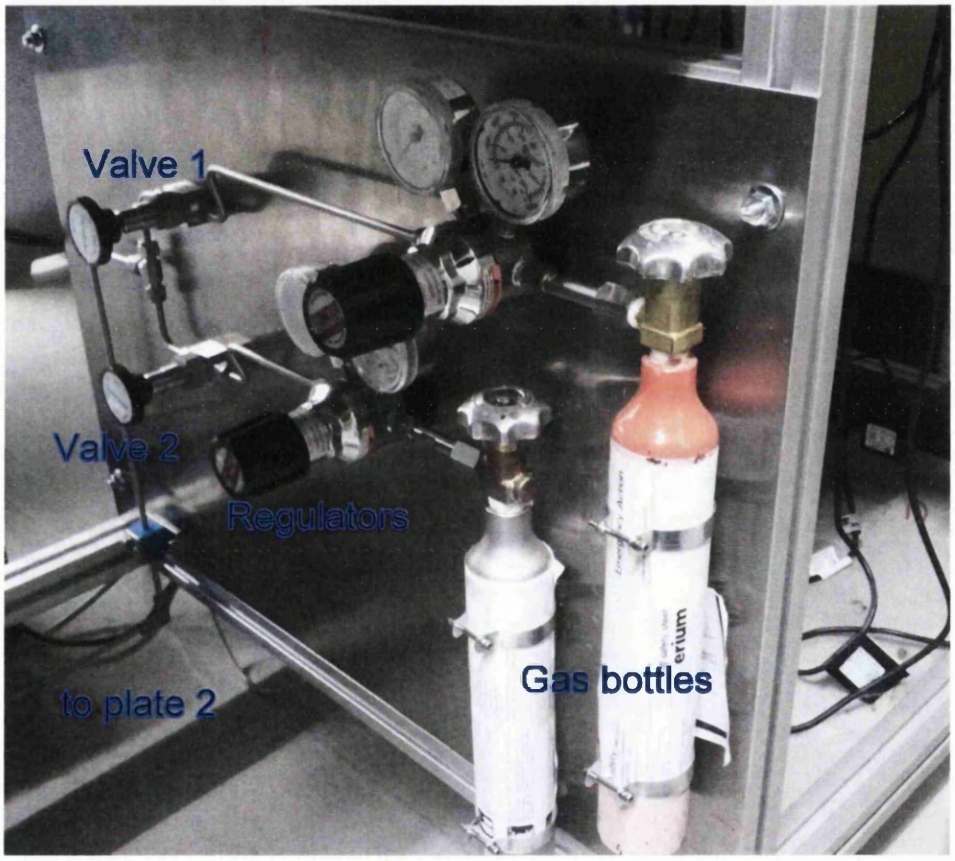

Figure A.5: Plate 1 of the gas mixing system. This contains the gas bottles, regulators and valves 1 and 2

The tubing is 6 mm *Swagelok* stainless steel tubing. The pressure gauges (*SUNX* DP-100 series) P1 and P2 need to be powered by an external power supply. The manual states that the supply voltage is DC 12 to 24 V. The voltage and current threshold is around about 8 V with a current of 60 mA for a bright display using a variable voltage power supply. The valves are *Swagelok* SS-6BK-MM bellows sealed valves, the catalyst tube is custom made in the Tritium Laboratory Karlsruhe (TLK) at the Karlsruhe

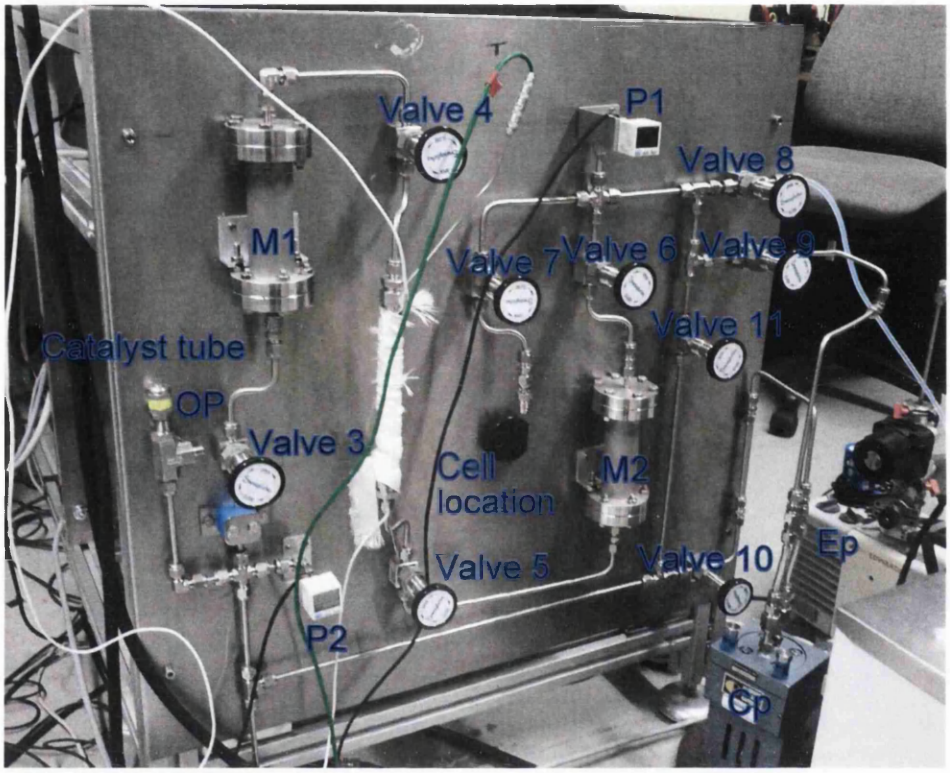

Figure A.6: Plate 2 of the gas mixing system. This contains the over pressure valve (OP), the two buffer vessels (M1 and M2), catalyst tube, pressure centres (P1 and P2), evacuation pump (Ep), circulation pump (Cp) and valves 3 to 11.

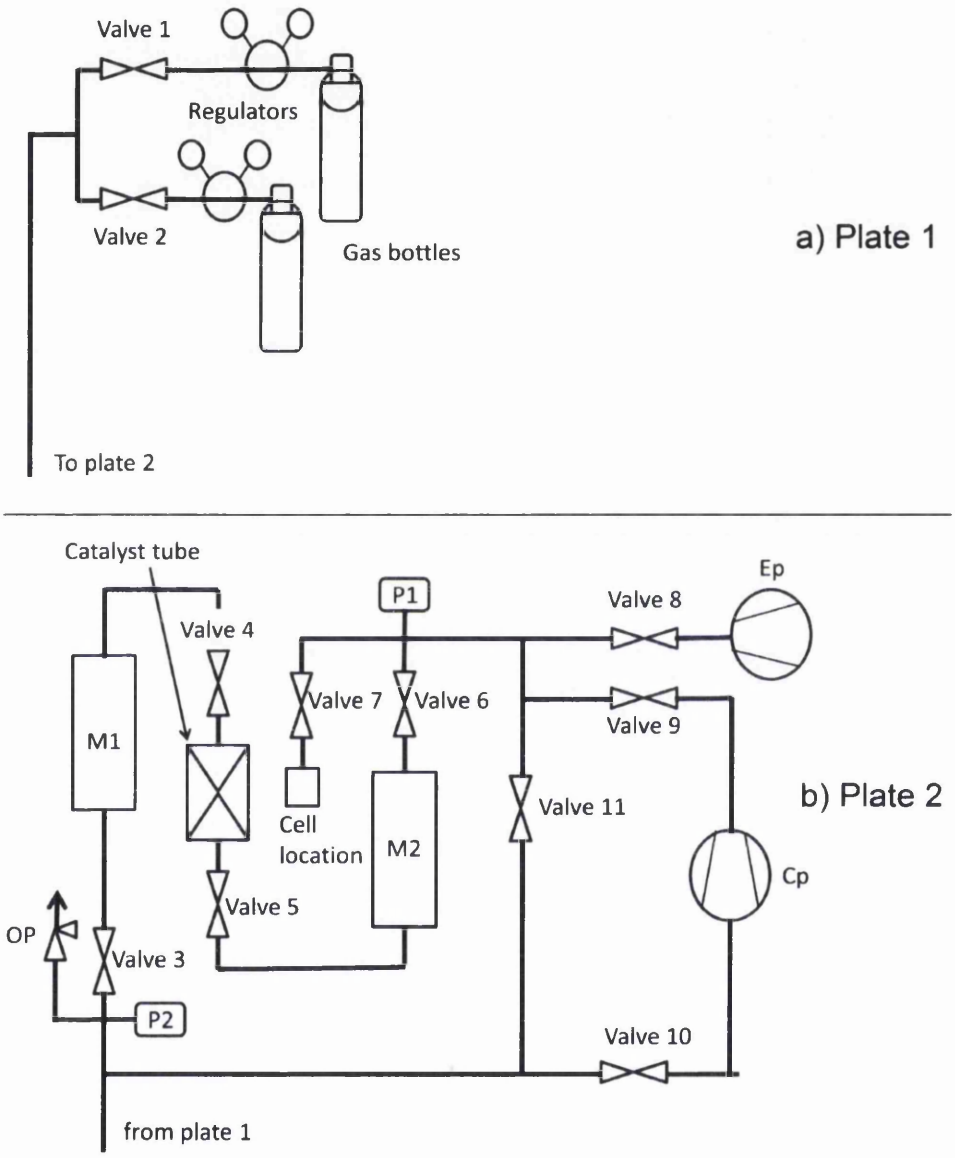

Figure A.7: Circuit diagram of the gas mixing system. a) Plate 1 and b) Plate 2. The labelling is the same as in figures A.5 and A.6.

Institute of Technology (KIT) and is described in its manual [Sch10b]. The two pumps are an oil rotary vane pump (*Edwards* RV5 A65301903) for evacuating the system and a metal bellows pumping unit (*Metal Bellows Corp* MB-158E) for gas circulation. The metal bellows pump is mounted to a metal block to isolate some of the vibrations and has two 1/4" *Swagelok* VCR connectors mounted to the top. These 1/4" VCR connectors are connected to the 6 mm *Swagelok* tubing of the gas mixing system via the VCR connector and 1/4" *Swagelok* flexible tubing (321-4-X-2) to isolate the pump vibrations further. The rotary vane pump is connected to the gas mixing system via flexible hose. When in use the rotary pump should be connected to the outside via flexible tubing (in this case the tubing is placed so that it sticks out of the window). However, when the pump is off the tube is disconnected as it would be a trip hazard. To prevent accidental direct venting into the room an oil filter is placed on top of the pump. The buffer vessels M1 and M2 are made from *Caburn* flange parts with *Swagelok* adapters attached to the front face. The over pressure valve OP is a *Swagelok* low pressure proportional relief valve (SS-RL3) set to release if the pressure exceeds approximately 1.5 bar. The regulators are *Concoa* 302 series (302 2302-01-000) single stage regulators. The system is used to fill the LARA cell with a single gas or to mix deuterium with hydrogen or methane.

A.2.2 Connecting parts to the system

Connecting gas bottles Gas bottles are connected to the gas mixing system on plate 1 (see figure A.5). The connection procedure is as follows.

1. Place seal into thread connector and ensure PTFE tape is wrapped around the thread. This helps improve the seal.

2. Open the two gas bottle brackets. If the M4 screws and nuts are in place remove and keep safe as they will be needed shortly.

3. Ensure the gas mixing system has been brought up to atmospheric pressure and there is space to install the new gas bottle (the system can only hold two bottles at a time).

4. Align gas bottle with connector and hand tighten the connector to ensure the alignment is correct. Keep the gas bottle weight supported whilst this is done.

5. Whilst supporting the gas bottle close the two gas bottle brackets (top followed by the bottom) and secure using the screw and nut. Do not tighten the screws fully until both are in place. Please note this may be easier with the assistance of a second person as the brackets try to spring back open again. Once both brackets are connected tighten the M4 screws.

6. Seal the gas bottle connector using a 19 mm wrench.

7. To verify that the seal does not leak close valve 1 (and/or valve 2) and the regulator and evacuate the system (see section A.2.3). Open the regulator and valve. The pressure on the gauges P1 and P2 (on plate 2) should increase slightly as there will be some air trapped in the gap between the gas bottle and the regulator. It should then stop increasing. If this occurs the gas bottle is connected correctly. Otherwise try reconnecting the bottle using the above steps.

8. Close valve 1 (and/or valve 2) and the regulator then slowly open the gas bottle until the pressure gauge on the right hand side of the regulator reaches $10-20$ bar and close the gas bottle again.

9. The gas bottle is now connected ready for a cell filling.

Disconnecting gas bottles The procedure to disconnect gas bottles from the gas mixing system is as follows.

- Ensure there is not excess pressure of gas inside the regulator. This is determined by the pressure gauge on the right hand side of the regulator going to zero.
- Ensure the gas bottle is closed.
- Bring the gas mixing system up to atmospheric pressure. The procedure for doing this is shown in section A.2.4.
- Ensure valve 1 (and/or valve 2) and the regulator are open.
- Disconnect the gas bottle gas connector using a 19mm wrench. If the system is not up to atmospheric pressure a hissing noise will be heard.
- Whilst supporting the gas bottle, open the gas bottle brackets by removing the M4 screws and nuts.
- Take the gas bottle out of the bracket and remove the internal seal (to go in the replacement bottle if needed) and store in a safe place.

Connecting the LARA cell The LARA cell is connected to the gas mixing system on plate 2 at Cell location (see figure A.6). The connection procedure is as follows.

1. Place the sealing ring inside the VCR connector.

2. Roughly align the cell VCR connector with the gas mixing system connector at Cell location. Then partly secure the cell in place using two M5 screws into the black block at Cell location.

3. Ensure that the seal and VCR connector sides are aligned correctly. Then hand tighten the VCR connector.

4. Tighten the M5 screws to ensure the cell is secure.
5. Seal the VCR connector using a 19 mm wrench on the cell side and a 5/8" wrench on the gas mixing system side. Stop tightening as soon as resistance is felt. This should be approximately 1/4 of a turn beyond finger tight.
6. To complete the link of the cell to the gas system the valve on the cell and valve 7 will need to be opened.
7. If the VCR connector is not sealed correctly it will leak. This will be seen as a slow increase in pressure on P1 when the system is evacuated.

Disconnecting the LARA cell To disconnect the LARA cell from the gas mixing system the procedure is as follows

1. Ensure valve 7 and the cell valves are closed completely.
2. Disconnect the VCR connector using a 19 mm wrench on the cell side and a 5/8" wrench on the gas mixing system side of the connector.
3. Whilst holding the cell remove the M5 screws to disconnect the cell from the black block.
4. Remove the seal from the VCR connector.
5. Place the cell back in the cupboard or into its stand in the LARA setup.

A.2.3 Evacuating the system

To ensure there are no contaminants from the atmospheric gases in the system and to perform leak tests, the system has to be evacuated. This is performed using a rotary oil pump (Ep in figure A.6), which is connected to the system by Valve 8. The rotary pump is then connected via plastic tubing to the outside so that the gases do not enter the room. To avoid a trip hazard this tubing is disconnected when the system is not in use (when the pump is off). To prevent accidental venting into the room an oil filter is placed on top of the pump. The procedure for evacuating the system is as follows

1. Ensure the pump is plugged in and the pump is venting to the outside world.
2. Verify that the black valve on top of the pump is closed (turned fully clockwise) and valve 8 is closed.
3. To evacuate the entire system open all other valves. If there is no cell connected leave valve 7 closed. If set parts of the system want to be evacuated leave the appropriate valves closed i.e. if you want to maintain the mixture in the catalyst loop (valve 3 to valve 6). Then ensure valves 6, 9,10 and 11 are also closed.

4. Switch the pump on using the switch on the side.
5. Slowly open the pump valve. The plastic tube will start to evacuate.
6. Once the pump valve is open, open valve 8. The system will start to evacuate.
7. Monitor sensors P1 and P2 (if applicable). When the system is fully evacuated the reading on the sensors will change to ****. Leave to evacuate as long as required for procedure.
8. When the evacuation process is complete close valve 8. Note if any parts of the system are leaking the sensors P1 and P2 will start to register readings at this point. If this is the case try to isolate the leak and try again.
9. Close the pump valve by turning it in the clockwise direction. Once the valve is completely closed, turn the pump off at the switch and unplug it. Note: If the pump valve is not shut properly oil could get into the system. So ensure the pump valve is fully closed before the pump is switched on or off.

A.2.4 Bringing the system up to atmospheric pressure

There are times when the system will need to be brought up to atmospheric pressure. The procedure for this is as follows

1. Evacuate the system using the procedure above (if not done already).
2. If there is a cell connected, remove it using the procedure in section A.2.2. This is needed as the cell location is used as the atmospheric pressure opening.
3. If the whole system wants to be brought up to atmospheric pressure open all valves except valves 7 and 8. Otherwise, isolate the appropriate part of the system by closing the relevant valves. For example if the system needs to be brought up to air to change a gas bottle but the gas in the catalyst loop doesn't want to be changed open valves 1, 2 and 11.
4. With the appropriate valves opened, open valve 7. This will bring the system up to atmospheric pressure as visualised by sensors P1 and P2 rising to read approximately zero.

A.2.5 Cell filling

Single-gas cell fillings. For single gas fillings the bypass loop is used as the catalyst tube is not needed. The procedure is as follows

1. Ensure the gas bottles and cell are connected to the mixing system as described in section A.2.2.

2. Ensure the entire system (including the cell) is evacuated (see section A.2.3).

3. Close all valves in the system.

4. For single gas cell fillings the only valve that needs to be open on plate 2 is valve 12. On plate 1, valve 1 or valve 2 needs to be open. Only open the valve that is next to the gas bottle containing the gas for the single cell filling. All other valves should be closed.

5. Whilst viewing pressure gauges P1 and P2 slowly open the regulator of the required single gas. The pressure will slowly rise. The pressure gauges are differential gauges so a reading of zero corresponds to 1000 mbar. Once the pressure has reached the required value, close the regulator. Note that that maximum pressure of this system is approximately 1500 mbar. If the pressure exceeds this the over pressure valve OP will open. The over pressure is set at this point to protect the cell from damage.

6. Open valve 8 and the cell valve and the gas will move into the cell. Once the pressure on gauges P1 and P2 is stable, close valve 8 and the cell valve. The cell can now be disconnected as described in section A.2.2.

Gas-mixing cell fillings. For gas mixing the catalyst tube needs to be used. Extra information on the catalyst tube can be found in the catalyst tube manual [Sch10b]. The catalyst tube can be used for mixing hydrogen and deuterium to form the isotopologue HD and for mixing methane and deuterium to form deuteriated methanes. Hydrogen and deuterium mixing can be performed at room temperature. However, after opening up the system to air if the catalyst tube wants to be used it should be baked out whilst evacuating to remove any water vapour that could be in the system. The bake out procedure is described in [Sch10b].

The procedure for gas mixing is as follows

1. Ensure the gas bottles and cell are connected to the mixing system as described in section A.2.2.

2. Ensure the entire system (including the cell) is evacuated (see section A.2.3) and bake out the catalyst if necessary (see [Sch10b]).

3. Close all valves in the system.

4. Heat the catalyst tube to the required temperature (if required).

5. For gas mixing fillings initially the only valve that needs to be open is valve 4 on plate 2.

6. On plate 1 open valve 1 or valve 2. Open the valve that is next to the deuterium gas bottle. All other valves should be closed. Whilst viewing pressure gauge P2 slowly open the regulator of the deuterium gas bottle. The pressure will slowly rise. Close the regulator once the pressure has reached 100 mbar (−0.9 on the gauge) and close the corresponding valve 1 or 2.

7. Open the other valve on plate 1 (valve 1 or 2). Whilst viewing pressure gauge P2 slowly open the regulator of the other (not deuterium) gas bottle. The pressure will slowly rise. Close the regulator once the pressure has increased by 100 mbar. Repeat the previous 2 steps alternating between gas mixtures until the pressure on pressure gauge P2 is approximately 1000 mbar.

8. Open valves 6 and 7. Then slowly open valve 5 until the gas starts to flow slowly over the catalyst tube. Once the pressure on P1 and P2 has equalised close valves 5, 6 and 7 and repeat the above filling process until the pressure on P1 and P2 corresponds to 500 mbar (−0.5 on the gauge).

9. Open valves 5, 6 and 7. Then open valves 10 and 11 and plug the circulation pump Cp in. The pressure on gauge P2 should increase drastically and on P1 should drop. The gas is now circulating through the catalyst tube. Let the gas circulate for at least 5 minutes.

10. When circulation is complete unplug the circulation pump and close valves 5, 10 and 11. Then slowly open valve 5 to allow gas to flow slowly over the catalyst tube.

11. Repeat steps 6,7 and 8 until the pressure on gauges P1 and P2 is just over 1000 mbar (reading of approximately 0.1).

12. Open valve 8 and the cell valve and the gas will move into the cell. Once the pressure on gauges P1 and P2 is stable, close valve 8 and the cell valve. The cell can now be disconnected as described in section A.2.2.

A.3 Synapse CCD detector characterisation

This section contains additional information on the characterisation of the Synapse CCD detector.

A.3.1 LabSpec 5 software and Synapse configuration

As specified in chapter 5 the Synapse camera was delivered with the software "LabSpec 5". It has some problems associated with it, when it is used in acquisition configurations suitable for the KATRIN LARA application.

1. Firstly, the software is designed to be used with analytical Raman spectroscopy of solid samples mounted on an x-y-z stage. This means there are many options in the software that are not needed in our application. In principle, this should not be a problem since according to discussions with *Horiba* engineers the software should be compatible with all *Horiba* CCD detectors.

2. Nowhere in the manual or software itself is the Synapse detector actually addressed; only reference to the Symphony detector is given. This seems to cause problems with the camera drivers and subsequently with operating the detector via the LabSpec software.

3. As a consequence of this, one could not change between the three gain-settings of the detector from within the software. There is an option to select between only two settings, namely "normal" and "high" gain. However, the high gain setting is set up within the config-files, so that it is the same value as the normal gain-thus, no alteration of gain is possible. Whereas, the detector has three different gain settings.

4. The CCD 2D image can only be read out in "real time" i.e. repetitively once started. To initiate capture of a single acquisition 2D image was not possible. For single acquisitions the software produces a spectrum using the on-chip binning procedure (see section 5.3.5). However, this was a non-tuneable version, so the spectra are binned over the entire chip only.

A.3.2 Running the Synapse detector under LabSpec and LabVIEW

After running the detector with the LabVIEW VIs the settings for the gain in the LabSpec config-files have also been changed, and different settings of the detector were encountered. For example, if the detector was last run in "high sensitivity" mode under LabVIEW, it would be in high sensitivity mode when subsequently running under LabSpec.

A.3.3 Detector problems - "dead pixel" phenomenon

During the characterisation and alignment process of the Synapse detector one specific problem was encountered, which will be discussed in this section.

For aligning the detector a white light source was used to enable the tilt of the detector to be adjusted correctly. When the image recorded from the CCD detector was viewed a column of "dead" pixels were observed (see figure A.8).

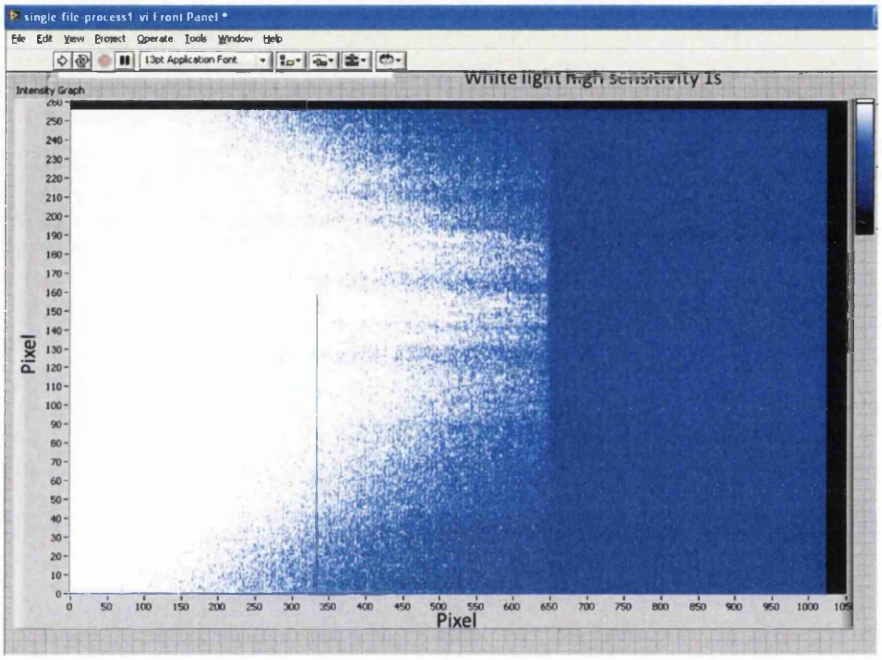

Figure A.8: Image recorded by the Synapse CCD detector, using a white light source for illumination. Settings: high sensitivity mode, 1 s acquisition time. The apparent cut-off pixel $\sim$ 650 is due to the presence of the 532 nm edge filter; the shape of the intensity profile is caused by the (ordered) fibre bundle being illuminated by a light beam with near-Gaussian intensity distribution. Note that the horizontal axis is λ-dependent.

To test whether this strange observation was related to hardware or software problems, a range of white-light acquisitions were taken for different exposure times. When the acquisition time is increased beyond 100 s the number of "dead" pixels apparently reduces (see figure A.9).

To analyse what is happening to this (single) column of pixels, a bespoke LabVIEW routine was used to extract this column, and the variation of intensity was plotted. A plot of the variation of intensity across the column containing the "dead" pixels, namely column 334, is shown in figure A.10 for 10 s, 100 s and 500 s acquisition times, and for high-sensitivity mode. The pixels appear to begin reading out data as the acquisition time, i.e. the overall light exposure, is increased.

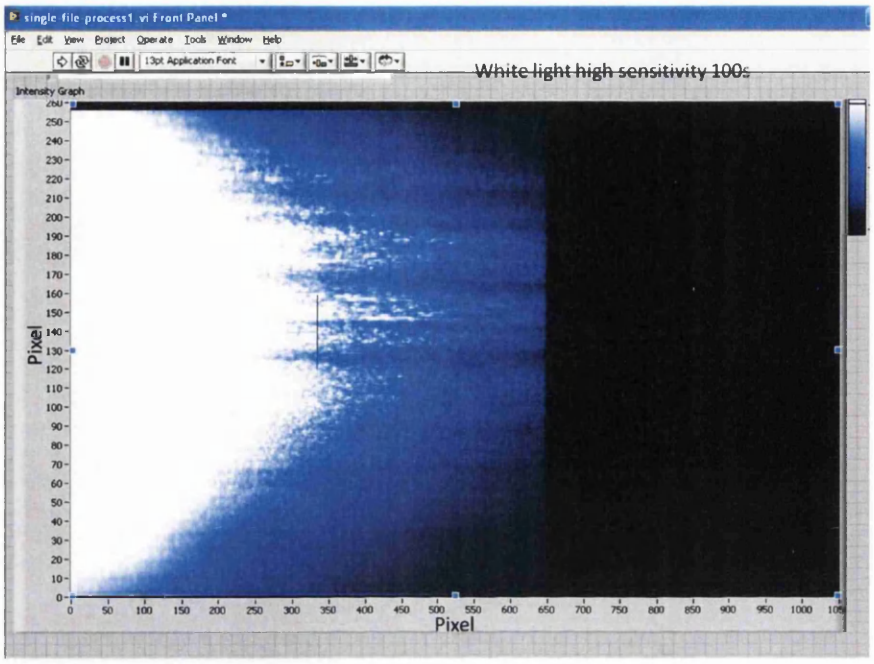

Figure A.9: Image recorded by the Synapse CCD detector using a white light source for illumination. Settings: High sensitivity mode, 100 s acquisition time. Note that the horizontal axis is λ-dependent.

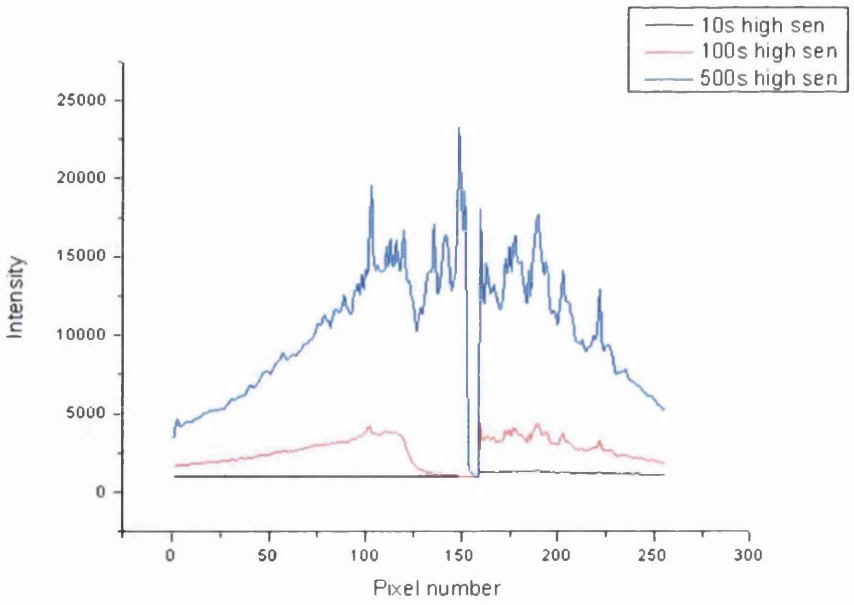

Figure A.10: An plot of the variation of intensity across the column containing the dead pixels. Note that the pixels, in this case, are in the vertical direction (y-axis in figures A.8 and A.9.

To check whether other pixel columns are read out correctly, the adjacent column was also extracted and plotted. This comparison is shown in figure A.11. When comparing

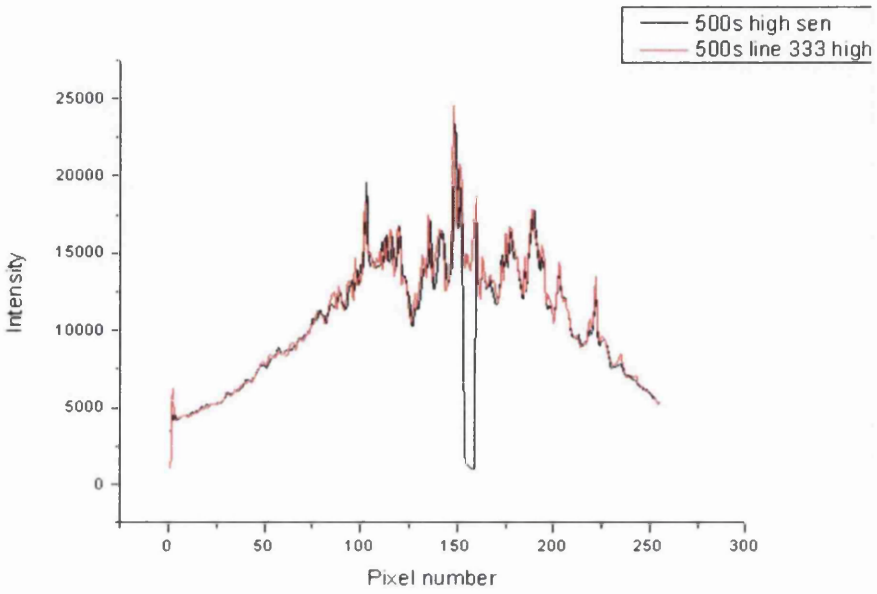

Figure A.11: Comparison between the column containing the dead pixels and the adjacent column. Note that the pixels, in this case, are in the vertical direction (y-axis in figures A.8 and A.9.

the figure to the previous one (for a range of exposures) one observes that the pixels, which are "dead" for shorter acquisition times, appear to be reading out similar data to the adjacent column everywhere, excluding the shortened "dead" region. This behaviour is completely puzzling; it appears to be dependent on the intensity incident on the CCD chip.

After consulting with the manufacturer they informed us that the CCD chip used in the Synapse is a grade 1 CCD and a grade 1 CCD detector can have 1 dead pixel when it is manufactured. Therefore, the detector was not repaired. This means that for all measurements with the Synapse detector the dead pixel data values are replaced with the value from an adjacent pixel.

A.4 Depolarisation measurement data of the hydrogen isotopologues

The depolarisation measurements of the hydrogen isotopologues are described in full in chapter 6. Additional tables that are needed in the chapter are included here, so they do not disrupt the flow of the text.

A.4.1 Polarisability tensors of the hydrogen isotopologues from LeRoy, for 532 nm excitation

The theoretical values of the average polarisability and the anisotropy of the hydrogen isotopologues have been calculated by LeRoy [Roy12] for 532 nm excitation radiation using *ab initio* calculations described in Schwartz and LeRoy [LRoy88]. The calculated values for the Q-branch of the hydrogen isotopologues for $J = 0$ to $J = 9$ are collated in table A.1.

The tabulated values are used as inputs into equation (6.2) to obtain the depolarisation ratio ρ_{SP0SA} in table 6.7 in chapter 6.

A.4.2 Complete corrected depolarisation ratios of the hydrogen isotopologues

The correction procedure described in chapters 3 and 6 to correct the observed depolarisation ratios of the hydrogen isotopologues for comparison with the theoretical values of LeRoy has been applied to all the measured data sets included in table 6.4. The resultant corrected values are shown in table A.2. These values are used to produce the statistical histogram for comparison of the measured data with that of LeRoy. The values are used individually in the calculation of F_d

$$F_d = \frac{\rho_{\mathrm{LeRoy}} - \rho_{\mathrm{SP0SA-cor}}}{\sigma(\rho_{\mathrm{SP0SA-cor}})} \tag{A.68}$$

as described in chapter 6.

Table A.1: Top: Theoretical average polarisability $|\langle v^f|a|v^i\rangle|^2$ of the Q_1 branches of all six hydrogen isotopologues from LeRoy. Bottom: Theoretical anisotropy $|\langle v^f|\gamma|v^i\rangle|^2$ of the Q_1 branches of all six hydrogen isotopologues from LeRoy

	$\|\langle v^f\|a\|v^i\rangle\|^2$ **Isotopologue**					
J	H_2	HD	HT	D_2	DT	T_2
0	0.780260	0.722899	0.700810	0.649723	0.619545	0.584671
1	0.781434	0.723723	0.701523	0.650222	0.619943	0.584671
2	0.783774	0.725367	0.702945	0.651219	0.620740	0.585578
3	0.787269	0.727825	0.705073	0.652712	0.621932	0.586484
4	0.791900	0.731088	0.707899	0.654696	0.623518	0.587689
5	0.797643	0.735143	0.711414	0.657167	0.625495	0.589192
6	0.804469	0.739976	0.715606	0.660120	0.627858	0.590990
7	0.812343	0.745568	0.720462	0.663547	0.630604	0.593081
8	0.821224	0.751898	0.725965	0.667440	0.633726	0.595461
9	0.831067	0.758945	0.732099	0.671790	0.637219	0.598128

	$\|\langle v^f\|\gamma\|v^i\rangle\|^2$ **Isotopologue**					
J	H_2	HD	HT	D_2	DT	T_2
0	0.653379	0.600413	0.580297	0.534351	0.507575	0.476960
1	0.655344	0.601780	0.581476	0.535170	0.508227	0.477452
2	0.659271	0.604513	0.583833	0.536809	0.509531	0.478437
3	0.665153	0.608609	0.587365	0.539267	0.511485	0.479913
4	0.672984	0.614064	0.592071	0.542542	0.514090	0.481882
5	0.682751	0.620874	0.597947	0.546633	0.517344	0.484341
6	0.694440	0.629032	0.604987	0.551538	0.521246	0.487291
7	0.708035	0.638532	0.613189	0.557255	0.525796	0.490731
8	0.723516	0.649363	0.622544	0.563780	0.530991	0.494660
9	0.740859	0.661517	0.633046	0.571112	0.536830	0.499078

Table A.2: Complete corrected depolarisation ratios of the Q_1 branches of all six hydrogen isotopologues used in the comparison with the theoretical values of LeRoy

		$\rho_{Sp0SA-cor}$		
Isotopologue	J	Set 1	Set 2	Set 3
H_2	0	0.0000(6)	0.0000(10)	0.0000(6)
	1	0.0177(6)	0.0190(9)	0.0180(6)
	2	0.0133(6)	0.0141(9)	0.0148(6)
	3	0.0128(6)	0.0133(15)	0.0129(6)
HD	0	0.0000(5)		
	1	0.0177(6)		
	2	0.0126(6)		
	3	0.0121(6)		
HT	0	0.0000(6)		
	1	0.0173(6)		
	2	0.0126(6)		
	3	0.0122(6)		
	4	0.0125(6)		
D_2	0	0.0000(6)	0.0000(10)	0.0000(5)
	1	0.0180(6)	0.0182(10)	0.0174(5)
	2	0.0133(6)	0.0131(9)	0.0118(5)
	3	0.1070(6)	0.0128(15)	0.0111(6)
	4	0.0109(6)	0.0121(17)	0.0110(6)
	5	0.0138(10)		
	6	0.0456(17)		
DT	0	0.0000(6)		
	1	0.0170(6)		
	2	0.0123(6)		
	3	0.0127(6)		
	4	0.0115(6)		
	5	0.0130(6)		
	6	0.0126(9)		
T_2	0	-0.0026(100)	-0.0030(100)	
	1	0.0165(6)	0.0161(6)	
	2	0.0119(6)	0.0115(6)	
	3	0.0111(6)	0.0108(6)	
	4	0.0104(6)	0.0100(6)	
	5	0.0113(6)	0.0109(6)	
	6	0.0115(6)	0.0112(7)	
	7	0.0156(6)	0.0152(8)	

A.5 Derivation of the polarisability matrix elements for nitrogen and oxygen

Buldakov *et al* [Bul03] have performed some calculations so that the polarisability matrix elements can be determined for diatomic molecules from the molecular and spectroscopic constants in the literature (e.g. from NIST [Lah91]). The equations the group state in the paper to describe the depolarisation ratio (depolarisation degree in their case) match the ones used by the KATRIN LARA group discussed in this work. In the next sections the equations used by Buldakov will be stated. For a discussion on the derivation see Buldakov *et al* [Bul03].

A.5.1 Matrix elements of diatomic molecules

The depolarisation ratio used in this work is defined as (see chapters 3 and 6)

$$\rho_{\mathrm{SP0SA}} = \frac{I_{\perp^s,\parallel^i}(\theta=\pi/2,\varphi=0)}{I_{\perp^s,\perp^i}(\theta=\pi/2,\varphi=0)} = \frac{3b^2_{Jf0:Ji0}|\langle v^f|\gamma|v^i\rangle|^2}{45|\langle v^f|a|v^i\rangle|^2 + 4b^2_{Jf0:Ji0}|\langle v^f|\gamma|v^i\rangle|^2} \tag{A.69}$$

This is the depolarisation ratio for $\theta = 90°$. Note that the poalrisability matrix elements $|\langle v^f|a|v^i\rangle|$ and $|\langle v^f|\gamma|v^i\rangle|$ are defined by Buldakov *et al* as $\langle v^i J|a|v^f J\rangle$ and $\langle v^i J|\gamma|v^f J\rangle$ to state that these terms have a dependence on the rotational quantum number J. To avoid confusion with some of the internal terms in their calculation the Buldakov notation will be used for the remainder of this section. The polarisability matrix elements are defined as

$$|\langle v^i J^i|a,\gamma|v^f J^f\rangle|^2 = F^{a,\gamma}_{v^i,v^f}(m)|\langle v^i|a,\gamma|v^f\rangle|^2 \tag{A.70}$$

where in this case the matrix elements $\langle v^f|a,\gamma|v^i\rangle$ are the vibration part of the polarisability matrix element and do not have a J dependence. $F^{a,\gamma}_{v^i,v^f}(m)$ is the Herman-Wallis factor and the term m changes depending on the selection rule of ΔJ for the branch of interest. More information on how the individual terms in this equation are derived is not discussed here. Buldakov *et al* have derived functions for various v^i and v^f scenarios for $F^{a,\gamma}_{v^i,v^f}(m)$, $\langle v^i|a,\gamma|v^f\rangle$ and $|\langle v^i J|a,\gamma|v^f J\rangle|$.

In this work the measurements of interest are for the Q_1-branch as the S_1- and O_1-branches depolarisation ratio is always equal to 0.75, so it is not dependent on the polarisability matrix elements. The Q_1-branch of diatomic molecules has the selection rules of $\Delta J = 0$ and $\Delta\nu = +1$. For these selection rules this sets $m = J(J+1)$, $J^i = J^f = J$, $v^i = v$ and $v^f = v+1$. The resultant equations for these selection rules derived for nitrogen and oxygen are included in the next sections

A.5.2 Matrix elements for the Q-branch of nitrogen (N_2)

The derived equations to obtain the polarisability matrix elements of the Q_1-branch nitrogen are

$$F^a_{v,v+1}(m) = 1 + [1.10(15) \times 10^{-5} - 0.61(28)v \times 10^{-7}]m \tag{A.71}$$

$$F^\gamma_{v,v+1}(m) = 1 + [0.14(10) \times 10^{-4} - 0.12(23)v \times 10^{-6}]m \tag{A.72}$$

$$\langle v|a|v+1\rangle = \left[\frac{v+1}{2}\right]^{0.5} \left(\frac{2B_e}{\omega_e}\right)^{0.5} [1.871(50) + 0.0105(35)v] \tag{A.73}$$

$$\langle v|\gamma|v+1\rangle = \left[\frac{v+1}{2}\right]^{0.5} \left(\frac{2B_e}{\omega_e}\right)^{0.5} [2.25(21) + 0.019(23)v] \tag{A.74}$$

where the numbers in brackets following the number terms indicate the uncertainty in the last digit. B_e and ω_e are spectroscopic constants and are $1.998241\,\mathrm{cm}^{-1}$ and $2358.57\,\mathrm{cm}^{-1}$ respectively for the fundamental branch where $v = 0$ (from NIST [Lah91]). These equations can be used to determine the J dependent polarisability matrix elements with an uncertainty for the fundamental Q_1-branch of nitrogen. The uncertainty is propagated through the formulae using error propagation. The resultant values are collated in table A.3.

Due to the resolution of the measurement of the depolarisation ratio of nitrogen in chapter 7 the individual Q-branch lines are not resolved. This means that the measured signal is a convolution of all the lines and the depolarisation ratio stated in equation (A.69) cannot apply for the SP0SA ratio in this case. The convolution means that the observed intensity is a sum over the individual branches i.e.

$$I_{\mathrm{obs}} = \sum_J I(J) = K\mathcal{I}\sum_J (\tilde{\nu}_s)^4 g_i N_i \Phi(a^2, \gamma^2, \theta) \tag{A.75}$$

Note the assumption has been made that the spectral efficiency of the system is constant over this narrow spectral region. For a description of the individual terms see chapter 3. This leads to a new depolarisation ratio namely

$$\begin{aligned}\rho_{\mathrm{SP0SA-conv}} &= \frac{\sum_J (\tilde{\nu}_s)^4 g_i N_i \Phi_{\perp^s,\parallel^i}(\theta = \pi/2, \varphi = 0)}{\sum_J (\tilde{\nu}_s)^4 g_i N_i \Phi_{\perp^s,\perp^i}(\theta = \pi/2, \varphi = 0)} \\ &= \frac{\sum_J (\tilde{\nu}_s)^4 g_i N_i (3b^2_{Jf0:Ji0} |\langle v^f|\gamma|v^i\rangle|^2)}{\sum_J (\tilde{\nu}_s)^4 g_i N_i (45|\langle v^f|a|v^i\rangle|^2 + 4b^2_{Jf0:Ji0}|\langle v^f|\gamma|v^i\rangle|^2)}\end{aligned} \tag{A.76}$$

To calculate this depolarisation ratio from the polarisability matrix elements the state population, level degeneracy and the wavenumber position need to be taken into account. These terms are discussed in more detail in chapter 3. The input terms needed to perform the calculation are $\tilde{F}_J = BJ(J+1)$, $B = 1.972263\,\mathrm{cm}^{-1}$, $g_i = 3$ for odd J, $g_i = 6$ for even J, $h = 6.626068 \times 10^{-31}$, $c_0 = 2.99792458 \times 10^{10}\,\mathrm{cms}^{-1}$, $k = 1.3806503 \times 10^{-20}\,\mathrm{cm}^2\,\mathrm{kg\,s}^{-2}$

Table A.3: Calculated polarisability matrix elements for the Q-branch of nitrogen (N_2)

J	$\lvert\langle v=0, J\lvert a\rvert v+1=1, J\rangle\rvert$	$\lvert\langle v=0, J\lvert \gamma\rvert v+1=1, J\rangle\rvert$
0	0.05446(146)	0.6549(1375)
1	0.05446(146)	0.6549(1375)
2	0.05446(146)	0.6549(1375)
3	0.05446(146)	0.6550(1375)
4	0.05447(146)	0.6550(1376)
5	0.05447(146)	0.6550(1376)
6	0.05447(146)	0.6551(1376)
7	0.05448(146)	0.6552(1376)
8	0.05448(146)	0.6552(1376)
9	0.05449(146)	0.6553(1376)
10	0.05449(146)	0.6554(1376)
11	0.05450(146)	0.6555(1377)
12	0.05451(146)	0.6556(1377)
13	0.05451(146)	0.6557(1377)
14	0.05452(146)	0.6559(1377)
15	0.05453(146)	0.6560(1378)
16	0.05454(146)	0.6562(1378)
17	0.05455(146)	0.6563(1378)
18	0.05456(146)	0.6565(1379)
19	0.05457(146)	0.6567(1379)
20	0.05459(146)	0.6568(1379)

and $T = 300\,\mathrm{K}$. Using these parameters and performing the appropriate calculation along with error propagation leads to a theoretical depolarisation ratio for nitrogen of $\rho_{\mathrm{SP0SA-conv}} = 0.0241(101)$.

A.5.3 Matrix elements for the Q-branch of oxygen (O_2)

The derived equations to obtain the polarisability matrix elements of the Q_1-branch oxygen are

$$F^{a}_{v,v+1}(m) = 1 + [2.28(16) \times 10^{-5} - 0.24(15)v \times 10^{-6}]m \tag{A.77}$$

$$F^{\gamma}_{v,v+1}(m) = 1 + [2.60(54) \times 10^{-5} - 0.46(25)v \times 10^{-6}]m \tag{A.78}$$

$$\langle v|a|v+1\rangle = \left[\frac{v+1}{2}\right]^{0.5} \left(\frac{2B_e}{\omega_e}\right)^{0.5} [1.779(71) + 0.019(12)v] \tag{A.79}$$

$$\langle v|\gamma|v+1\rangle = \left[\frac{v+1}{2}\right]^{0.5} \left(\frac{2B_e}{\omega_e}\right)^{0.5} [3.25(26) + 0.057(19)v] \tag{A.80}$$

where the numbers in brackets following the number terms indicate the uncertainty in the last digit. B_e and ω_e are spectroscopic constants and are $1.44563\,\mathrm{cm}^{-1}$ and $1580.193\,\mathrm{cm}^{-1}$ respectively for the fundamental branch where $v = 0$ (from NIST [Lah91]). These equations can be used to determine the J dependent polarisability matrix elements with an uncertainty for the fundamental Q_1-branch of oxygen. The uncertainty is propagated through the formulae using error propagation. The resultant values are collated in table A.4.

The individual Q-branch lines of oxygen are not resolved in the measurement of the depolarisation ratio of oxygen in chapter 7. The same convolution equations combining the intensities and obtaining the convoluted depolarisation ratio discussed above can be used to calculate the theoretical depolarisation ratio for oxygen. The equations that can be used are equations (A.75) and (A.76). The input terms needed to perform the calculation for oxygen, which are different to those used in the nitrogen calculation, are $\tilde{F}_J = BJ(J+1)$, $B = 1.972263\,\mathrm{cm}^{-1}$ and $g_i = 1$ for odd J. The even rotational levels are unpopulated; $g_i = 0$ in this case. Using these parameters and performing the appropriate calculation along with error propagation leads to a theoretical depolarisation for oxygen of $\rho_{\mathrm{SP0SA-conv}} = 0.0548(285)$.

Table A.4: Calculated polarisability matrix elements for the Q-branch of oxygen (O_2). Note the calculations have been performed for all rotational levels even though the even levels are unpopulated.

J	$\lvert\langle v=0, J\lvert a\rvert v+1=1, J\rangle\rvert$	$\lvert\langle v=0, J\lvert \gamma\rvert v+1=1, J\rangle\rvert$
0	0.05381(215)	0.9830(2556)
1	0.05381(215)	0.9830(2556)
2	0.05381(215)	0.9831(2556)
3	0.05382(215)	0.9832(2556)
4	0.05382(215)	0.9833(2556)
5	0.05383(215)	0.9834(2557)
6	0.05383(215)	0.9835(2557)
7	0.05384(215)	0.9837(2558)
8	0.05385(215)	0.9839(2558)
9	0.05386(215)	0.9842(2559)
10	0.05388(215)	0.9844(2559)
11	0.05389(215)	0.9847(2560)
12	0.05390(215)	0.9850(2561)
13	0.05392(215)	0.9853(2562)
14	0.05394(215)	0.9857(2563)
15	0.05396(215)	0.9861(2564)
16	0.05397(215)	0.9865(2565)
17	0.05400(216)	0.9869(2566)
18	0.05402(216)	0.9874(2567)
19	0.05404(216)	0.9879(2568)
20	0.05407(216)	0.9884(2570)
21	0.05409(216)	0.9889(2571)
22	0.05412(216)	0.9895(2573)
23	0.05415(216)	0.9900(2574)
24	0.05418(216)	0.9906(2576)
25	0.05421(216)	0.9913(2577)
26	0.05424(216)	0.9919(2579)
27	0.05427(217)	0.9926(2581)
28	0.05430(217)	0.9933(2583)
29	0.05434(217)	0.9941(2585)

A.6 Software and analysis routines

The software and analysis routines used in this work will be discussed here. The analysis procedure is also discussed in [Jam13], [SJLc] and [SJLd] where they are available for download off of Sourceforge.

A.6.1 Detector acquisition software

As stated in chapter 5 the Synapse detector can be run using *National Instruments* LabVIEW. The detector is operated using Active X controls and the LabVIEW VIs for the Symphony CCD detector (version 0.9.4.0) have been modified so that (i) they work with the Synapse detector and (ii) all the settings can be modified from within the LabVIEW VI. The software has been gradually optimised throughout this work. A screenshot of the front panel is shown in figure A.12.

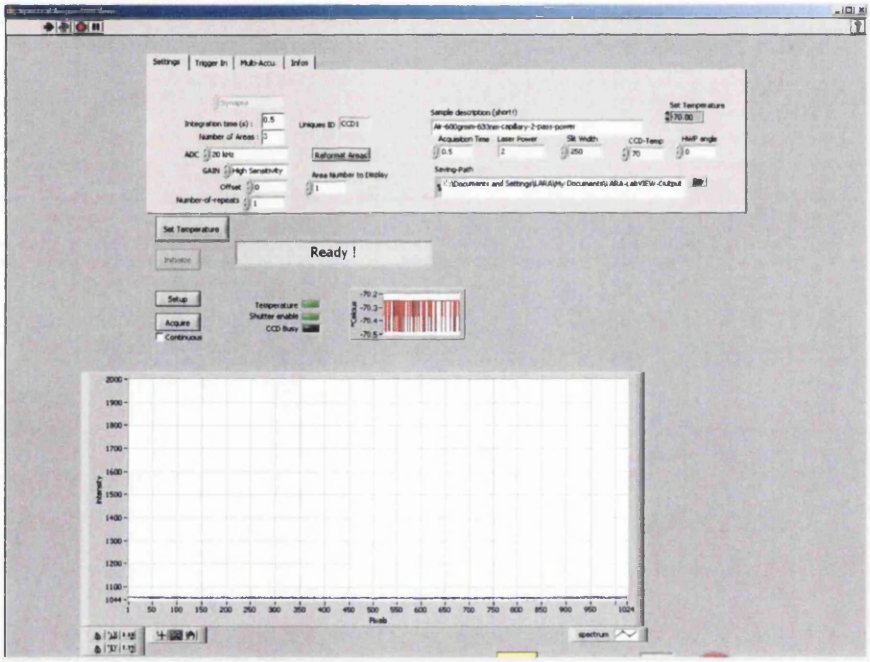

Figure A.12: Screenshot of the front panel of the Synapse detector acquisition software.

Detector initialisation

After the detector has been switched on at its power supply the detector needs to be initialised before it can be used. The procedure for this is as follows:

1. Start the LabVIEW VI.

2. Press "Initialize" to initialise the detector. When a configuration error box appears press ok. It then takes approximately 20 s for the detector to initialise correctly.

3. Wait for the detector head temperature to reach the set-point (default = −70 °C). To change the temperature set-point, change the value in the "Set Temperature" box and select the "Set Temperature" button. The detector temperature is displayed in a plot of temperature vs. time in the front panel.

4. Once the set-point temperature has been reached (within 0.25 °C), set the integration time to 0.5 s, number of areas to 3, ADC to 20 kHz, Gain to High sensitivity, Offset to 0, Number-of-repeats to 1 and Area number to display to 1.

5. Select the "Setup" button then the "Acquire" button. This takes a 0.5 s acquisition using the detector to clear the CCD of any residual charge. After this has completed restart the LabVIEW VI and repeat the steps above.

6. Select the "Setup" button then the "Acquire" button again. If the enclosure, containing the detector, is dark the main intensity plot should show a constant intensity of approximately 1000 counts for all 1024 pixels, as shown in figure A.12.

7. The detector is now ready to use by setting the appropriate acquisition parameters.

Configuring acquisition parameters

The following parameters can be set and adjusted (on the left hand side of the front panel) to use the software to take spectra: integration time, number of on-chip binning areas, ADC, gain, detector offset, number of repeats and area number to display. If any of these are adjusted, the "Setup" button needs to be reselected for the changes to be applied to the detector. If the number of on-chip binning areas are changed the "Reformat Areas" button needs to be selected first. Note: if the "Setup" button is selected when the parameters have not been changed the detector software will crash when trying to read out the data from the detector, after the acquisition has run.

After each spectrum is taken the data is automatically saved as a text file in the directory specified in the "Saving-Path" box on the right hand side of the front panel. The file save structure is:
YYYYMMDDHHmmss.fs_(Sample description)_Laser Power_Slit Width_CCD-temp_Acquisition time-NN.txt
where YYYY is the year, MM is the month, DD is the day, HH is the hour, mm is the minute, ss is the second and .fs is the fraction of the second; taken from the computer clock. The named parts are controlled by the inputs into the relevant boxes on the right hand side of the front panel and NN corresponds to the repeat number starting from zero (i.e. for the first acquisition NN = 00 and for the second acquisition NN = 01).

The details of the block diagram and working code for the detector software will not be included here. For more information the reader is referred to the Symphony detector VI documentation (available from *Horiba*) and the block diagram itself.

A.6.2 Webcam software

A modified webcam has been used as a small 2D position monitoring detector as described in chapter 4. The 2D chip image of the webcam is recorded using call library function nodes within a customised LabVIEW routine. The function nodes call a dynamic link library file (.dll) called capwind.dll (obtained from *National Instruments* discussion forums). The function nodes required to readout the data are shown in figure A.13. Note that this is a simplified version of the utilised program to display the function nodes more clearly.

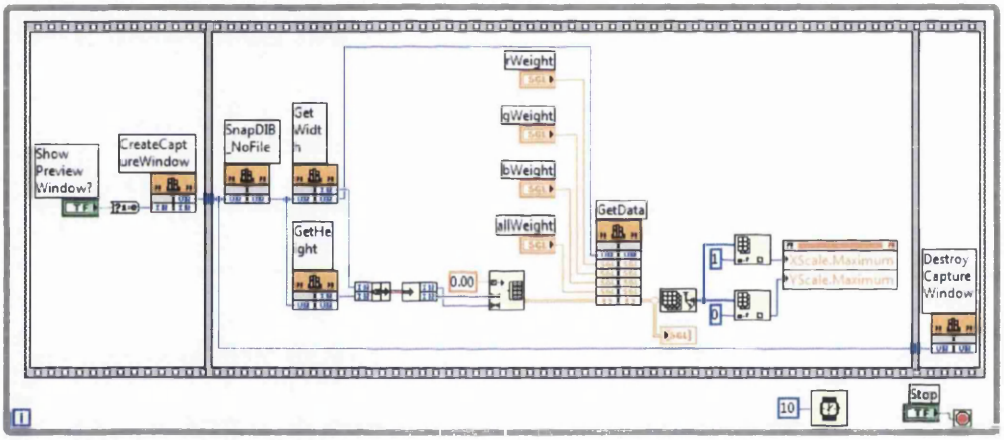

Figure A.13: Screenshot of the block diagram showing the function nodes required to readout the webcam data.

The function node combination outputs the recorded webcam image as a 2D array, which can be analysed to determine the beam position of the incident laser beam spot.

Beam position determination

As stated in chapter 4 the beam position is found by

- Finding the maximum intensity for each row (for the x- and y-directions separately) and output the row number, max index and max value.
- Fit the maximum intensity vs. row number with a Gaussian fit. The centre position of this fit is the pixel co-ordinate in that direction.

These steps are contained within the same customised LabVIEW routine. LabVIEW has the advantage that the maximum value from an array and a Gaussian peak fit are inbuilt functions. The 2D array is read row-by-row using a for loop (to change between the x- and y-directions the 2D array is transposed). The Gaussian fit function in LabVIEW outputs the peak amplitude, peak centre and standard deviation. The peak centre from the x- and y-directions is saved as the pixel co-ordinate determining the beam position. The entire procedure is contained within a timed loop, so that the webcam chip is read out periodically until the stop button is selected.

A.6.3 Analysis procedures

The overall analysis procedure used in this work is described here as a sequence of individual steps, each associated with its own LabVIEW subroutine (subVI). The routines can either be used on their own or as part of the entire analysis procedure, which is needed for the KATRIN experiment. The procedure is discussed relating to KATRIN in James *et al* [Jam13]. The routines that will be discussed here are:

- the cosmic ray removal routine TCRR;
- the background removal routine SCARF;
- and the peak fitting routine ShapeFit.

For on-line applications, all steps are fully incorporated into a program flow which requires only minimal user intervention during the initial set-up; for off-line applications the sequence is overlaid with a graphical front end. By setting option switches in the program flow, individual steps in the sequence may be skipped should they not be required for a particular spectrum analysis.

Cosmic ray removal

The simple technique, to remove cosmic rays, that has been used in this work is "temporal cosmic ray removal" (TCRR). Having sets of spectra recorded over time, like in this work, enables the identification and elimination of cosmic rays by using spectral difference comparison. This concept is implemented by comparing (at least) two consecutive spectra recordings and determining the signal difference pixel-by pixel. If the absolute value of this difference is less than a threshold, the two spectral data points are averaged and this average is taken as the "cleaned" output value; otherwise, the smaller-valued data point is taken. The threshold value has to be set large enough not to be compromised by noise fluctuations, but small enough to efficiently capture the majority of cosmic ray events, which can have a wide range of random amplitudes. This process is repeated for the selected set of rows or binning-segments of the detector chip, and for the full set of spectra.

The TCRR can be programmed as described below. Note that this is the TCRR as performed by the LabVIEW subVIs in this work.

1. Two consecutive two dimensional signal arrays A and B are imported as arrays of double precision values. The arrays rows correspond to the number of on chip binning segments.

2. The arrays are fed into a for loop so each individual row is analysed as a one dimensional array (Ai_j).

3. The arrays are processed using the SCARF routine with a wide radius to ensure the background level of the consecutive arrays is as similar as possible.

4. The difference of the one dimensional arrays (Ai_j and Bi_j) is calculated for each element j where $di_j = Ai_j - Bi_j$.

5. The cleaned array Ci is produced as follows

   (a) If the difference element di_j is less than a threshold value t ($di_j < t$) the cleaned element Ci_j is then $Ci_j = \frac{Ai_j + Bi_j}{2}$.

   (b) Otherwise, the cleaned element Ci_j is then $Ci_j = Ai_j$ if $Ai_j < Bi_j$ and $Ci_j = Bi_j$ if $Ai_j > Bi_j$.

6. The arrays Ci_j are then summed to form the cleaned one dimensional array Ci where $Ci = \sum_j Ci_j$. This array is then passed to the handling VI.

It should be noted that TCRR has certain limitations. TCRR works assuming that cosmic-ray events are random and sparse whereas, the spectral features of interest are static for consecutive spectra. This is no longer valid for very long acquisition times. As the acquisition time expands the probability that cosmic rays will strike the detector in the same place, in consecutive acquisitions, increases. Hence, an acquisition time threshold will be encountered where the simple (two back-to-back acquisitions only) temporal routine will no longer remove all cosmic rays. Above this threshold, more than two consecutive acquisitions will be needed to ensure the spectra are completely clean of cosmic rays.

The routine has been tested on high and low intensity spectra for various acquisition times; for each measurement series cosmic ray events left in the spectra were counted. The number of cosmic rays present in a spectrum will vary depending on the location, shielding and time of day. Based on the test measurements with the Synapse detector in Swansea the TCRR routine removed all cosmic rays with only two consecutive spectra for acquisition times below typically 600 s; this means a combined consecutive-spectra acquisition time for the two spectra of 1200 s. Above this value three or more consecutive

spectra were required. The numbers stated here may change for other detectors and measurement conditions. However, the results show that TCRR can be very successful and that for short acquisition times almost always only two consecutive spectra are needed to remove all cosmic rays.

Background removal

The various background removal methodologies, in the literature, have been considered and the most suitable procedure for background removal, in this work, seems to be the rolling-circle filter (RCF) concept. It requires no further user intervention once parameters have been set for the specific task, but can thereafter cope automatically with nearly any not-too-sudden variation in background/noise during long measurement periods. However, the routine needed to be modified slightly to function correctly for quantitative spectral analysis. The methodology in this work, along with test measurements, is discussed below

The Rolling Circle Filter (RCF)

The Rolling Circle filter (RCF) routine was originally proposed by Mikhailyuk *et al* [Mik03] the associated canonical RCF is described e.g. in Brandt *et al* [Bra06]. The concept of the RCF is visualised in figure A.14. It is broadly equivalent to rolling a

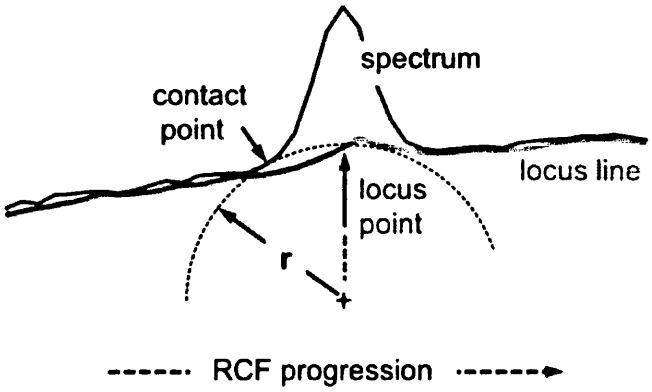

Figure A.14: Action of the Rolling Circle Filter (RCF) on an example spectrum; the filter tends to roll into the peak, overcompensating the background level. This deficiency is overcome by using the SCARF filter routine.

circle of radius r below a measured array of points, treating the array as a rigid surface. As the circle is rolled the vertical locus at the top of the circle is taken as an estimate of the varying background level.

The RCF can be practically realised as summarised below. Note that this is the RCF action as performed by the LabVIEW subVIs in this work.

1. A $(2r + 1)$-element array of double-precision values, C, is generated where each element $C_j = (\sqrt{r^2 - (j - r)^2}) - r$, and $j = 0, 1, \ldots 2r$ is the index of the array, numbered from zero.

2. The M element signal array A is imported as an array of double-precision values A_m, where $m = 0, 1, \ldots (M - 1)$.

3. The sanity check $(2r+1) < M$ is made; the subVI will only execute if this condition is met.

4. The signal array is conditioned by subtracting the minimum (most negative) element value $A^{\min}$ from each element of A, yielding the modified signal array A'. This procedure ensures that the minimum possible value of any element A'_m of A' is zero.

5. A' is windowed with respect to each reference index $m = 0, 1, \ldots (M - 1)$. It is then operated upon with either the entire array C or a subset thereof as described in the next step. The size of the subsets utilised depends on the value of the reference index m as follows:

   (a) In the case where $m < (r + 1)$, A' is sampled from A'_0 to $A'_{(r-m)}$ and C is sampled from $C_{(m+1)}$ to C_{2r}

   (b) In the case where $(M - (r + 1)) \leq m \leq (r + 1)$, A' is sampled from $A'_{(m-r)}$ to $A'_{(m+r)}$, and the entire array is C is utilised

   (c) In the case where $m > (M - (r + 1))$, A' is sampled from A'_{M-r} to A'_M and C is sampled from C_0 to $C_{(M-(m-1))}$

6. By applying the above rules, one obtains two array subsets $A'^{\text{sub},m}$ and $C^{\text{sub},m}$ of equal size for each value of m. For each value of m, the minimum value $D^{\min}_m$, which is the minimum value of the elements of the difference array $D_m = A'^{\text{sub},m} - C^{\text{sub},m}$. The minimum difference array $D^{\min}$ can thus be generated over $m = 0, 1, \ldots M$.

7. The array representing the locus of the rolling circle L is calculated by adding the user-supplied estimate of the signal's intrinsic noise variance σ to the minimum difference array, i.e. $L = D^{\min} + \sigma$

8. The following arrays are passed to the handling VI:

   (a) The original signal array, A

   (b) The locus array, L

   (c) The 'residue' array $R = A' - L$, which represents the 'cleaned' signal

The Savitzky-Golay Coupled Advanced Rolling Circle Filter (SCARF)

The RCF algorithm has a serious deficiency, namely that the baseline level is overestimated if a gap (like a peak or broad unresolved feature) is encountered whose baseline width, w, is larger than double the RCF-circle radius, i.e. $w \geq 2r$. Then the propagating circle "rolls into the gap" (see figure A.14), thus subtracting more than the actual background. Increasing the RCF-circle to much larger values doesn't solve the problem, as will be shown in the examples further below.

This deficiency is overcome by the SCARF algorithm. It works by applying a Savitzky-Golay filtering step to the locus-array generated from a single RCF pass. Two key parameters in the SGF algorithm have to be set appropriately, namely (i) the number of side-points $s \geq r$ to be included and (ii) the polynomial order n of the smoothing process. Note that on all occasions this routine is used this work the polynomial order was always n = 3. Note also that the SGF step is not applied to the spectral data itself but to the background residuals. LabVIEW has an inbuilt Savitzky-Golay filter function where the only tuning parameters are the number of side-points and the polynomial order.

Care should be taken to choose suitable value of r in the RCF segment of the routine and the number of side points s. Specifically, r should be as small as possible in order to capture details in the variation of the baseline level, but normally should not be smaller than the widest spectral peak of interest (i.e. $2r \geq w_{\max}$) whose shape one wishes to preserve, sitting upon the moving baseline. For broad background features within the moving baseline the limit of r may be reduced, to ensure the baseline is followed correctly. But as a consequence of reducing $2r$ to values below $w_{\max}$ the number of side-points needs to be increased. However, decreasing $2r$ too far may have unwanted effects, as shown in the examples below. Finally, for most efficient removal of odd-shaped background from peaks of varying width multiple passes of the routine may be required.

To demonstrate the action of the standard RCF and the advanced SCARF routines we applied them for a range of filter parameters, specifically (i) to a synthetic line spectrum, and (ii) to a real Raman spectrum. In the first instance, a simple synthetic spectrum has been generated, consisting of a pure Gaussian line of FWHM $w = 10$ pixel, sitting on an offset background dressed with random shot noise fluctuations. The amplitude of the spectral line was changed from values just above the noise level to values at which the noise becomes nearly negligible. The default starting parameter for the RCF procedure was $r = 2w$. The results are summarised in figure A.15 and table A.5; note that the entries in the table are the amplitudes, in units of counts, recuperated by peak-fitting of the background-corrected spectra after filter treatment.

Both the figure and table data clearly reveal that selecting the filter parameters too small with respect to the base width of the peak results in the filter rolling into the peak. The width at the base of the peak is responsible for how far the filter rolls into the peak. The application of the SCARF routine with the same width parameter improves this

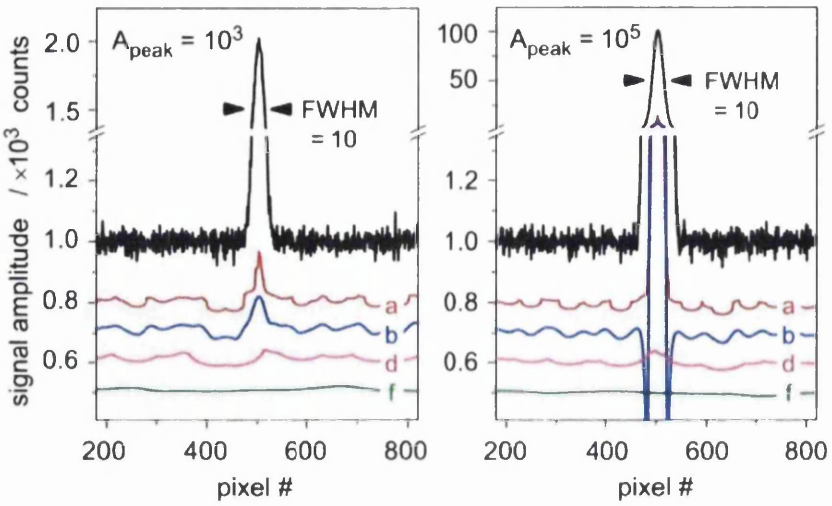

Figure A.15: Background removal for synthetic spectrum of a Gaussian peak, with FWHM = 10 pixel, and different amplitude A_{peak} (left: $A_{\text{peak}} = 10^3$; right: $A_{\text{peak}} = 10^5$). The baseline is offset by 1000 counts, exhibiting random shot-noise background. The background-fit traces (a), (b), (d) and (f) are associated with the various RCF and SCARF parameter entries in table I; for clarity they are consecutively offset downwards.

Table A.5: RCF and SCARF applied to a synthetic Gaussian peak of FWHM w = 10 (see Fig. 5), with different amplitude, and offset by $A_{\text{offset}} = 1000\pm$ random shot noise (in units of counts; median = 33). The parameters r and s of RCF (r) and SCARF (r,s) are in units of pixel. The data entries correspond to the amplitudes obtained by peak-fitting after application of the filter procedure to the spectra (in units of counts), with fitting errors (2σ) in brackets.

	Nominal peak amplitude A_{peak}(counts)			
	100	1000	10000	100000
Peak width at base (pixel)	26(1)	48(1)	62(1)	77(1)
(a) RCF(20)	67(12)	829(17)	8590(30)	86413(35)
(b) SCARF (20, 20)	76(13)	899(27)	9350(67)	94218(98)
(c) 2× SCARF (20, 80) + (20, 40)	82(13)	916(26)	9574(58)	96430(87)
(d) RCF (60)	83(10)	980(15)	9963(22)	99940(25)
(e) SCARF (60, 60)	89(10)	984(14)	9985(20)	99968(22)
(f) 2× SCARF (60, 240) + (60, 120)	98(8)	993(12)	9991(15)	99990(15)

but cannot fully compensate. In fact, one may even complicate things: due to the sharp edges of the RCF(20) signal at the position of the peak, the SCARF routine introduces a negative-going second derivative shape.

The implication is that the underlying RCF algorithm has to start with a sensible value, which needs to account for the width at the base of any peak of interest for quantitative analysis. A nearly "perfect" background removal and baseline correction function is achieved when applying the SCARF routine twice, with staggered number of side points included. Note that in this repetitive application the second SCARF-passage acts on the spectral data from which the result of the first SCARF-run has been subtracted.

The same procedure as above was applied to a real N_2 Raman spectrum, which in addition was superimposed with a non-linear background contribution. In figure A.16 the results from a selected range of filter functions on this spectrum are shown. The original spectral data traces are overlaid with the derived background functions, namely the circle loci for the normal RCF-routine RCF(r) with two different radii r=20 and r=60; the SCARF routine SCARF(r,s) with (r=60,s=60); and the repetitive SCARF-routine with varied Savitzky-Golay parameters (r=60,s=240) followed by (r=60,s=120).

In the standard RCF routine the filter has rolled into the spectral lines for RCF with r=20 pixels; but even for r=60 pixel which is much wider than the narrow S_1- and O_1-branch Raman lines, hints of roll-in are evident. This results in loss of quantifiable spectral information because incorrect amounts of background intensity are subtracted. This may not be critical for the large intensity Q_1-branch of $^{16}N_2$ at $2330\,cm^{-1}$, where the "lost" amount accounts for roughly 10^{-2}, or less for the wider circle radius, the low-intensity Q_1-branch of $^{16}N^{18}N$ near $2285\,cm^{-1}$ suffers a loss of as much as 20 to 30%. This means that incorrect values from the spectra would have been extracted and reliable quantification is lost.

As in the synthetic spectrum case discussed above, applying the SCARF routine has nearly eliminated the problem of roll-in. However, with the larger radii parameters $r = 60$ and $s = 60$ the background trace now does not follow the background curvature correctly, and consequently the actual background is not yet completely removed. Full background compensation is achieved by applying SCARF a second time on the adjusted spectrum from the first run (see the lowest trace in figure A.16).

Finally, for quantitative analysis of spectral lines via peak fitting routines, a flat background with the noise oscillating around zero is required. However, the application of RCF/SCARF for background removal exhibits a minor deficiency. Since the circle always rolls below all data points, this slightly offsets any noise baseline to a minute value above zero. This can be overcome by calculating the median of a (reasonably) flat, noise-only region of the spectrum. This median subtraction routine is included in the Spectrum Processing Suite used in this work [SJLc] and [SJLd].

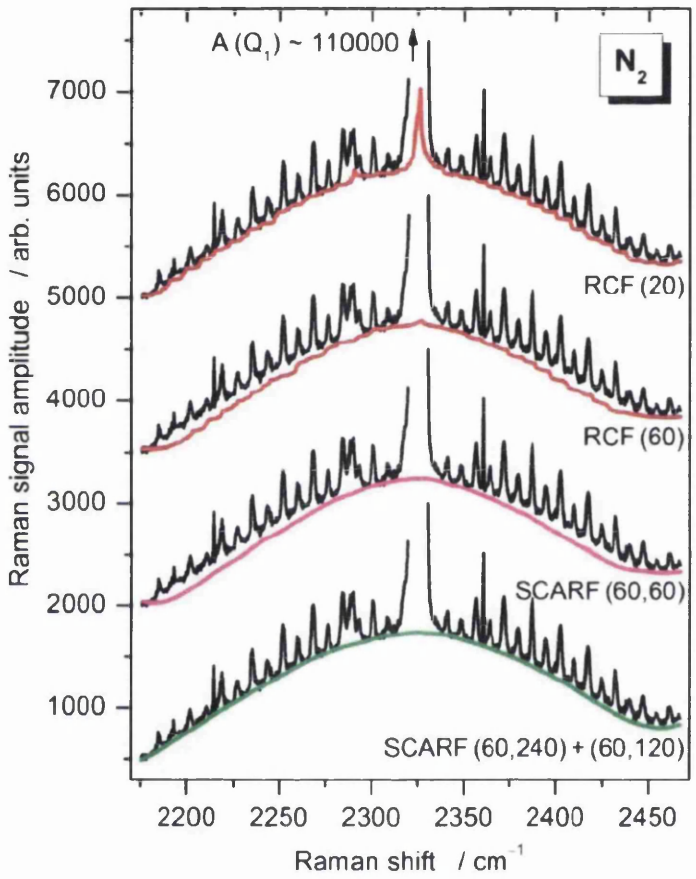

Figure A.16: Background removal test for a Raman spectrum of N_2, overlaid with non-linear background; traces are offset by 1500 units, consecutively from top to bottom. The traces are annotated with the respective filter actions used, RCF(r) and SCARF(r,s). Note that the displayed Raman shift range corresponds to the full detector width of 1024 pixel. For further details and discussion, see text.

Peak fitting

The last step in the post acquisition data treatment is the extraction of peak intensities (or areas). Two types of techniques have been considered for the determination of intensities (or areas).

The first employs integration by simple summing of the intensity of all pixels within a peak profile, arriving at a peak area value. However, the method is unsuitable if one wishes to deconvolute overlapping lines.

The method of choice used throughout in this work is a routine developed by the KATRIN LARA group called ShapeFit (see Schlösser [Sch13] or [SJLd] for more information). The routine works as follows

- In the first step of the routine a line is selected from the spectrum which has sufficient intensity and stands isolated (no convolution with other lines); for example, this could be a line from a spectral calibration lamp. The shape of this peak is stored pixel-by-pixel in an auxiliary data array.

- In the second step, all lines within a spectrum are fitted, using the previously determined digital peak shape function and multiplying it by the appropriate amplitude factor. The process incorporates the Levenberg-Marquart algorithm, in which amplitude and centre-position of each peak are treated as fitting parameters.

- Sub-pixel translation of the peak positions is enabled by interpolation of the numerical peak shape. The baseline of the spectrum can be either fixed, or added as a fitting parameter.

Since the peak-shape is stored numerically, very complicated and odd shapes can be used, while at the same time the number of free parameters per peak is still only two (position and amplitude). The ShapeFit routine was implemented as a LabVIEW subVI, and its principle details are summarised in [Jam13], [SJLc] and [SJLd].

Bibliography

[All70] C. D. Allemand. Depolarization ratio measurements in Raman spectrometry. *Appl. Spectrosc.*, 24(3):348–353, May 1970.

[Als11] A. S. A. Alshahrie. *Raman spectroscopy of hydrogen isotopologues and trace gas detection analysis for KATRIN.* PhD thesis, Swansea University, Swansea, UK, 2011.

[Alt01] R. Altkorn, M. D. Malinsky, R. P. Van Duyne, and I. Koev. Intensity considerations in liquid core optical fiber raman spectroscopy. *Appl. Spectrosc.*, 55(4):373–381, Apr 2001.

[Ama65] G. Amat and M. Pimbert. On Fermi resonance in carbon dioxide. *J. Mol. Spectrosc.*, 16(2):278 – 290, 1965.

[Bar85] J. J. Barrett. Photoacoustic Raman spectroscopy of gases. *Appl. Spectros. Rev.*, 21(4):419–464, 1985.

[Bri64] N. J. Bridge and A. D. Buckingham. Polarization of laser light scattered by gases. *J. Chem. Phys.*, 40(9):2733–2734, 1964.

[Bar79] J. J. Barrett and M. J. Berry. Photoacoustic Raman spectroscopy (PARS) using cw laser sources. *Appl. Phys. Lett.*, 34(2):144–146, 1979.

[Bab12] M. Babutzka, M. Bahr, J. Bonn, B. Bornschein, A. Dieter, G. Drexlin, K. Eitel, S. Fischer, F. Glück, S. Grohmann, M. Hötzel, T. M. James, W. Käfer, M. Leber, B. Monreal, F. Priester, M. Röllig, M. Schlösser, U. Schmitt, F. Sharipov, M. Steidl, M. Sturm, H. H. Telle, and N. Titov. Monitoring of the operating parameters of the KATRIN Windowless Gaseous Tritium Source. *New J. Phys.*, 14(10):103046, 2012.

[Bra06] N. N. Brandt, O. O. Brovko, A. Y. Chikishev, and O. D. Paraschuk. Optimization of the Rolling-Circle Filter for Raman Background Subtraction. *Appl. Spectrosc.*, 60(3):288–293, Mar 2006.

[Bel95] A.I. Belesev, A.I. Bleule, E.V. Geraskin, A.A. Golubev, N.A. Golubev, O.V. Kazachenko, E.P. Kiev, Yu.E. Kuznetsov, V.M. Lobashev, B.M. Ovchinnikov, V.I. Parfenov, I.V. Sekachev, A.P. Solodukhin, N.A. Titov, I.E. Yarykin, Yu.I. Zakharov, S.N. Balashov, and P.E. Spivak. Results of the troitsk experiment on the search for the electron antineutrino rest mass in tritium beta-decay. *Phys. Lett. B*, 350(2):263 – 272, 1995.

[Bur09] M. P. Buric, K. Chen, J. Falk, R. Velez, and S. Woodruff. Raman sensing of fuel gases using a reflective coating capillary optical fiber. In *Proc. SPIE 7316, Fiber Optic Sensors and Applications VI*, pages 731608–731608–8, 2009.

[Bur10] M. P. Buric, K. P. Chen, J. Falk, and S. D. Woodruff. Multimode metal-lined capillaries for raman collection and sensing. *J. Opt. Soc. Am. B*, 27(12):2612–2619, Dec 2010.

[Bul03] M.A. Buldakov, V.N. Cherepanov, B.V. Korolev, and I.I. Matrosov. Role of intramolecular interactions in Raman spectra of N_2 and O_2 molecules. *J. Mol. Spectrosc.*, 217(1):1 – 8, 2003.

[Bon09] M. Bonn, M. Müller, H. A. Rinia, and K. N.J. Burger. Imaging of chemical and physical state of individual cellular lipid droplets using multiplex CARS microscopy. *J. Raman Spectros.*, 40(7):763–769, 2009.

[Bor05] L. Bornschein. The KATRIN experiment - a direct measurement of the electron antineutrino mass in the sub-eV region. *Nucl. Phys. A*, 752(0):14 – 23, 2005.

[Bou06] V. Boudon, M. Rey, and M. Lote. The vibrational levels of methane obtained from analyses of high-resolution spectra. *J. Quant. Spectrosc. Radiat. Transfer*, 98(3):394 – 404, 2006.

[Ber11] M. Berglund and M. E. Wieser. Isotopic compositions of the elements 2009 (IUPAC Technical Report). *Pure Appl. Chem.*, 83:397–410, 2011.

[Car72] R.W. Carlson and W.R. Fenner. Absolute Raman scattering cross-section of molecular hydrogen. *Astrophys. J.*, 178:551–556, December 1972.

[Kat12] KATRIN collaboration. KATRIN web page. `http://www.katrin.kit.edu/`.

[Col05] E. Collett. *Field Guide to Polarization.* SPIE Field Guides. SPIE Press, 2005.

[Dic29] R. G. Dickinson, R. T. Dillon, and F. Rasetti. Raman Spectra of Polyatomic Gases. *Physical Review*, 34:582–589, August 1929.

[Dem96] W. Demtröder. *Laser spectroscopy: basic concepts and instrumentation.* Number v. 2 in Advanced Texts in Physics. Springer-Verlag, Berlin-Heidelberg, Germany, 1996.

[Den40] D. M. Dennison. The infra-red spectra of polyatomic molecules. part ii. *Rev. Mod. Phys.*, 12:175–214, Jul 1940.

[Dan81] S. A. Danichkin, A. A. Eliseev, T. N. Popova, O. V. Ravodina, and V. V. Stenina. Raman scattering parameters for gas molecules (survey). *J. Appl. Spectrosc.*, 35:1057–1066, 1981.

[dla] 532 nm *Dream laser* data sheet. `http://www.dreamlasers.com/products/laser/532nm.htm`.

[Dow01] A. Downes, R. Mouras, P. Bagnaninchi, and A. Elfick. Raman spectroscopy and CARS microscopy of stem cells and their derivatives. *J. Raman Spectrosc.*, 42(10):1864–1870, 2011.

[Dro07] M. Drosg. *Dealing With Uncertainties: A Guide to Error Analysis.* Springer, 2007.

[Dos06] N. Doss, J. Tennyson, A. Saenz, and S. Jonsell. Molecular effects in investigations of tritium molecule β decay endpoint experiments. *Phys. Rev. C*, 73:025502, Feb 2006.

[Egu03] K. Eguchi, S. Enomoto, K. Furuno, J. Goldman, H. Hanada, H. Ikeda, K. Ikeda, K. Inoue, K. Ishihara, W. Itoh, T. Iwamoto, T. Kawaguchi, T. Kawashima, H. Kinoshita, Y. Kishimoto, M. Koga, Y. Koseki, T. Maeda, T. Mitsui, M. Motoki, K. Nakajima, M. Nakajima, T. Nakajima, H. Ogawa, K. Owada, T. Sakabe, I. Shimizu, J. Shirai, F. Suekane, A. Suzuki, K. Tada, O. Tajima, T. Takayama, K. Tamae, H. Watanabe, J. Busenitz, Z. Djurcic, K. McKinny, D.-M. Mei, A. Piepke, E. Yakushev, B. E. Berger, Y. D. Chan, M. P. Decowski, D. A. Dwyer, S. J. Freedman, Y. Fu, B. K. Fujikawa, K. M. Heeger, K. T. Lesko, K.-B. Luk, H. Murayama, D. R. Nygren, C. E. Okada, A. W. P. Poon, H. M. Steiner, L. A. Winslow, G. A. Horton-Smith, R. D. McKeown, J. Ritter, B. Tipton, P. Vogel, C. E. Lane, T. Miletic, P. W. Gorham, G. Guillian, J. G. Learned, J. Maricic, S. Matsuno, S. Pakvasa, S. Dazeley, S. Hatakeyama, M. Murakami, R. C. Svoboda, B. D. Dieterle, M. DiMauro, J. Detwiler, G. Gratta, K. Ishii, N. Tolich, Y. Uchida, M. Batygov, W. Bugg, H. Cohn, Y. Efremenko, Y. Kamyshkov, A. Kozlov,

Y. Nakamura, L. De Braeckeleer, C. R. Gould, H. J. Karwowski, D. M. Markoff, J. A. Messimore, K. Nakamura, R. M. Rohm, W. Tornow, A. R. Young, and Y.-F. Wang. First Results from KamLAND: Evidence for Reactor Antineutrino Disappearance. *Phys. Rev. Lett.*, 90:021802, Jan 2003.

[Eck62] G. Eckhardt, R. W. Hellwarth, F. J. McClung, S. E. Schwarz, D. Weiner, and E. J. Woodbury. Stimulated Raman scattering from organic liquids. *Phys. Rev. Lett.*, 9:455–457, Dec 1962.

[Edw78] H. G. M. Edwards, D. A. Long, and H. R. Mansour. Pure rotational and vibration-rotational Raman spectra of tritium, $^3H_2$. *J. Chem. Soc., Faraday Trans. 2*, 74:1203–1207, 1978.

[Eva05] C. L. Evans, E. O. Potma, M. Puoris'haag, D. Ct, C. P. Lin, and X. S. Xie. Chemical imaging of tissue in vivo with video-rate coherent anti-Stokes Raman scattering microscopy. *PNAS*, 102(46):16807–16812, 2005.

[Ete] *Newport Corp* tutorial: light collection and system throughput. `http://www.newport.com/Tutorial-Light-Collection-and-Systems-Throughput/381845/1033/content.aspx`.

[Fuk98] Y. Fukuda, T. Hayakawa, E. Ichihara, K. Inoue, K. Ishihara, H. Ishino, Y. Itow, T. Kajita, J. Kameda, S. Kasuga, K. Kobayashi, Y. Kobayashi, Y. Koshio, M. Miura, M. Nakahata, S. Nakayama, A. Okada, K. Okumura, N. Sakurai, M. Shiozawa, Y. Suzuki, Y. Takeuchi, Y. Totsuka, S. Yamada, M. Earl, A. Habig, E. Kearns, M. D. Messier, K. Scholberg, J. L. Stone, L. R. Sulak, C. W. Walter, M. Goldhaber, T. Barszczxak, D. Casper, W. Gajewski, P. G. Halverson, J. Hsu, W. R. Kropp, L. R. Price, F. Reines, M. Smy, H. W. Sobel, M. R. Vagins, K. S. Ganezer, W. E. Keig, R. W. Ellsworth, S. Tasaka, J. W. Flanagan, A. Kibayashi, J. G. Learned, S. Matsuno, V. J. Stenger, D. Takemori, T. Ishii, J. Kanzaki, T. Kobayashi, S. Mine, K. Nakamura, K. Nishikawa, Y. Oyama, A. Sakai, M. Sakuda, O. Sasaki, S. Echigo, M. Kohama, A. T. Suzuki, T. J. Haines, E. Blaufuss, B. K. Kim, R. Sanford, R. Svoboda, M. L. Chen, Z. Conner, J. A. Goodman, G. W. Sullivan, J. Hill, C. K. Jung, K. Martens, C. Mauger, C. McGrew, E. Sharkey, B. Viren, C. Yanagisawa, W. Doki, K. Miyano, H. Okazawa, C. Saji, M. Takahata, Y. Nagashima, M. Takita, T. Yamaguchi, M. Yoshida, S. B. Kim, M. Etoh, K. Fujita, A. Hasegawa, T. Hasegawa, S. Hatakeyama, T. Iwamoto, M. Koga, T. Maruyama, H. Ogawa, J. Shirai, A. Suzuki, F. Tsushima, M. Koshiba, M. Nemoto, K. Nishijima, T. Futagami, Y. Hayato, Y. Kanaya, K. Kaneyuki, Y. Watanabe, D. Kielczewska, R. A. Doyle,

J. S. George, A. L. Stachyra, L. L. Wai, R. J. Wilkes, and K. K. Young. Evidence for Oscillation of Atmospheric Neutrinos. *Phys. Rev. Lett.*, 81:1562–1567, Aug 1998.

[Fen73] W. R. Fenner, H. A. Hyatt, J. M. Kellam, and S. P. S. Porto. Raman cross section of some simple gases. *J. Opt. Soc. Am.*, 63(1):73–77, Jan 1973.

[Fer06] J. M. Fernàndez, A. Punge, G. Tejeda, and S. Montero. Quantitative diagnostics of a methane/air mini-flame by Raman spectroscopy. *Journal of Raman Spectroscopy*, 37(1-3):175–182, 2006.

[Fis11] S. Fischer, M. Sturm, M. Schlösser, B. Bornschein, G. Drexlin, F. Priester, R. J. Lewis, and H. H. Telle. Monitoring of tritium purity during long-term circulation in the KATRIN test experiment LOOPINO using laser Raman spectroscopy. *Fusion Sci. Technol.*, 60(3):976 – 981, 2011.

[Gol62] D. M. Golden and Jr. B. Crawford. Absolute Raman intensities. i. method for molecules in the gas phase. *J. Chem. Phys.*, 36(6):1654–1661, 1962.

[Gar80] Y. Garrabos, R. Tufeu, B. Le Neindre, G. Zalczer, and D. Beysens. Rayleigh and Raman scattering near the critical point of carbon dioxide. *J. Chem. Phys.*, 72(8):4637–4651, 1980.

[Gon12] A. G. Gonzálvez and Á. González Ureña. Transmission Resonance Raman Spectroscopy: Experimental Results Versus Theoretical Model Calculations. *Appl. Spectrosc.*, 66(10):1163–1170, Oct 2012.

[Hol73] W. Holzer, Y. Le Duff, and K. Altmann. J dependence of the depolarization ratio of the rotational components of the Q branch of the H_2 and D_2 Raman band. *J. Chem. Phys.*, 58(2):642–643, 1973.

[Hec02] E. Hecht. *Optics.* Pearson Education. Addison-Wesley, 2002.

[Her50] G. Herzberg. *Molecular Spectra and Molecular Structure: I. Spectra of Diatomic Molecules Second Edition.* Molecular Spectra and Molecular Structure. Van Nostrand Reinhold Company Inc., New York, N.Y., 1950.

[Her89] G. Herzberg. *Molecular Spectra and Molecular Structure: II. Infrared and Raman Spectra of Polyatomic Molecules.* Molecular Spectra and Molecular Structure. R.E. Krieger Pub. Co., 1989.

[Her11] P. Herwig. Kalibrierung des KATRIN Laser-Raman-Systems mit nichttritiierten Wassstoffisotopolgen. Master's thesis, Karlsruhe Institute of Technology, Karlsruhe, Germany, 2011.

[HLo71] H. E. Howard-Lock and B.P. Stoicheff. Raman intensity measurements of the Fermi diad ν_1, $2\nu_2$ in $^{12}CO_2$ and $^{13}CO_2$. *J. Mol. Spectrosc.*, 37(2):321 – 326, 1971.

[Hos75] L. C. Hoskins. Pure rotational Raman spectroscopy of diatomic molecules. *J. Chem. Educ.*, 52(9):568, 1975.

[Hun84] J. L. Hunt, J. D. Poll, and L. Wolniewicz. Ab initio calculation of properties of the neutral diatomic hydrogen molecules H_2, HD, D_2, HT, DT, and T_2. *Can. J. Phys.*, 62(12):1719–1723, 1984.

[Her63] J. Herranz and B.P. Stoicheff. High-resolution Raman spectroscopy of gases: Part XVI. The ν_3 Raman band of methane. *J. Mol. Spectrosc.*, 10(16):448 – 483, 1963.

[Ini03] J.C.T. Iniesta. *Introduction to Spectropolarimetry.* Cambridge University Press, 2003.

[Jam09] T. M. James. Cooling Upgrade and Characterisation of Swansea University's Gas Raman Spectroscopy System, and Initial Investigations into the Raman Scattering Intensity Dependence on Laser Excitation Polarisation. Master's thesis, Swansea University, Swansea, U.K., 2009.

[Jou05] E. Jourdanneau, F. Chaussard, R. Saint-Loup, T. Gabard, and H. Berger. The methane Raman spectrum from 1200 to 5500 cm^1: A first step toward temperature diagnostic using methane as a probe molecule in combustion systems. *J. Mol. Spectrosc.*, 233(2):219 – 230, 2005.

[Joh35] M. Johnston and D. M. Dennison. The Interaction Between Vibration and Rotation for Symmetrical Molecules. *Phys. Rev.*, 48:868–883, Dec 1935.

[McG94] Jr. J. P. McGuire and R. A. Chipman. Polarization aberrations. 1. rotationally symmetric optical systems. *Appl. Opt.*, 33(22):5080–5100, Aug 1994.

[Jam12a] T. M. James, M. Schlösser, S. Fischer, M. Sturm, B. Bornschein, R. J. Lewis, and H. H. Telle. Precise and accurate depolarization ratio measurements for all diatomic hydrogen isotopologues. *submitted to J. Raman. Spectrosc.*, 2012.

[Jam13] T. M. James, M. Schlösser, R. J. Lewis, S. Fischer, B. Bornschein, and H. H. Telle. Automated quantitative spectroscopic analysis combining cosmic-ray removal, background subtraction and peak fitting. *Submitted to, at revision stage, Appl. Spectrosc.*, 2013.

[Jul09] *Julabo* F34 data sheet. `http://www.julabo.de/us/p_datasheet.asp?Produkt=F34-MC`.

[Kra05] Ch Kraus, B. Bornschein, L. Bornschein, J. Bonn, B. Flatt, A. Kovalik, B. Ostrick, E.W. Otten, J.P. Schall, Th Thümmler, and Ch Weinheimer. Final results from phase II of the Mainz neutrino mass searchin tritium β decay. *Eur. Phys. J. C*, 40:447–468, 2005.

[Kit09] N. Kita. Technique to manage polarization aberrations. *Opt. Rev.*, 16(3):305 – 312, 2009.

[Lew07] R. J. Lewis. *Development of a Raman system for in-line monitoring of tritium at the Karlsruhe tritium neutrino (KATRIN) experiment.* PhD thesis, Swansea University, Swansea, UK, 2007.

[Lah91] R. R. Laher and F. R. Gilmore. Improved fits for the vibrational and rotational constants of many states of nitrogen and oxygen. *J. Phys. Chem. Ref. Data*, 20(4):685–712, 1991.

[Lan34] A. Langseth and J. Rud Nielsen. Polarization and intensity measurements in the Raman spectrum of carbon dioxide. *Phys. Rev.*, 46:1057–1058, Dec 1934.

[Lob03] V.M. Lobashev. The search for the neutrino mass by direct method in the tritium beta-decay and perspectives of study it in the project KATRIN. *Nucl. Phys. A*, 719(0):C153 – C160, 2003.

[Lon02] D.A. Long. *The Raman Effect: A Unified Treatment of the Theory of Raman Scattering by Molecules.* Wiley, 2002.

[LQu09] *Laser Quantum* Excel data sheet. `http://www.laserquantum.com/lasers/excel.html`.

[Log94] J.E. Logan, N.A. Robertson, and J. Hough. Measurements of birefringence in a suspended sample of fused silica. *Opt. Commun.*, 107(56):342 – 346, 1994.

[Lew08] R.J. Lewis, H.H. Telle, B. Bornschein, O. Kazachenko, N. Kernert, and M. Sturm. Dynamic Raman spectroscopy of hydrogen isotopomer mixtures in-line at TILO. *Laser Phys. Lett.*, 5(7):522–531, 2008.

[McC02] R.L. McCreery. *Photometric Standards for Raman Spectroscopy.* John Wiley & Sons Ltd, Chichester, UK, 2002.

[McCam03] D. W. McCamant, P. Kukura, and R. A. Mathies. Femtosecond broadband stimulated Raman: A new approach for high-performance vibrational spectroscopy. *Appl. Spectrosc.*, 57(11):1317–1323, Nov 2003.

[Mik03] I.K. Mikhailyuk and A.P. Razzhivin. Background Subtraction in Experimental Data Arrays Illustrated by the Example of Raman Spectra and Fluorescent Gel Electrophoresis Patterns. *Instrum. Exp. Tech.*, 46(6):765, Nov 2003.

[May03] W. Mayer, J. Telaar, R. Branam, G. Schneider, and J. Hussong. Raman measurements of cryogenic injection at supercritical pressure. *Heat and Mass Transfer*, 39:709–719, 2003.

[Nap12] S. Napoli. Absolute calibration of Laser Raman Signals for the Karlsruhe Tritium Neutrino (KATRIN) experiment. Master's thesis, Swansea University, Swansea, UK, 2012.

[Nag96] V. Nagali, S. I. Chou, D. S. Baer, R. K. Hanson, and J. Segall. Tunable diode-laser absorption measurements of methane at elevated temperatures. *Appl. Opt.*, 35(21):4026–4032, Jul 1996.

[Nea09] J. Neauport, P. Cormont, P. Legros, C. Ambard, and J. Destribats. Imaging subsurface damage of grinded fused silica optics by confocal fluorescence microscopy. *Opt. Express*, 17(5):3543–3554, Mar 2009.

[new] *Newport Corp* tutorial on focussing and collimating light. `http://www.newport.com/Focusing-and-Collimating/141191/1033/content.aspx`.

[NPL12] *Tables of Physical & Chemical Constants (16th edition 1995). 3.1.4 Composition of the Earths atmosphere).* Kaye & Laby Online. Version 2.0, 2012.

[Okit10] Y. Okita, T. Katagiri, and Y. Matsuura. A Raman cell based on hollow optical fibers for breath analysis. In *Proc. SPIE 7559, Optical Fibers and Sensors for Medical Diagnostics and Treatment Applications X*, pages 755908–755908–5, 2010.

[Ott08] E W Otten and C Weinheimer. Neutrino mass limit from tritium decay. *Rep. Prog. Phys.*, 71(8):086201, 2008.

[Owy78] A. Owyoung. High-resolution cw stimulated Raman spectroscopy in molecular hydrogen. *Opt. Lett.*, 2(4):91–93, Apr 1978.

[Oki99] Y. Oki, J. Yakafuji, M. Maeda, and N. Kawada. Nonlinear Raman spectroscopies with Raman shifter for sensitive gas detection. In *Lasers and*

Electro-Optics, 1999. CLEO/Pacific Rim '99. The Pacific Rim Conference on, volume 4, pages 1192 –1193 vol.4, 1999.

[Pou77] S. K. Poultney, M. L. Brumfield, and Jr. J. H. Siviter. Quantitative remote measurements of pollutants from stationary sources using Raman lidar. *Appl. Opt.*, 16(12):3180–3182, Dec 1977.

[Pea08] W. F. Pearman, J. C. Carter, S. M. Angel, and J. W-J. Chan. Quantitative measurements of CO_2 and CH_4 using a multipass Raman capillary cell. *Appl. Opt.*, 47(25):4627–4632, Sep 2008.

[Pid06] M. Pidwirny. Atmospheric Composition. Fundamentals of Physical Geography, 2nd Edition. `http://www.physicalgeography.net/fundamentals/7a.html`, 2006.

[Pin76] A. S. Pine. High-resolution methane ν_3-band spectra using a stabilized tunable difference-frequency laser system. *J. Opt. Soc. Am.*, 66(2):97–108, Feb 1976.

[Pix09] *Princeton Instruments* PIXIS:400 data sheet. `http://www.roperscientific.de/datasheets/Princeton_Instruments_PIXIS_400_RevC0.pdf`.

[Plo07] E. Ploetz, S. Laimgruber, S. Berner, W. Zinth, and P. Gilch. Femtosecond stimulated Raman microscopy. *Appl. Phys. B*, 87:389–393, 2007. 10.1007/s00340-007-2630-x.

[Pra12] M Prall, P Renschler, F Glück, A Beglarian, H Bichsel, L Bornschein, Z Chaoui, G Drexlin, F Fränkle, S Grhardt, S Mertens, M Steidl, Th Thmmler, S Wstling, C Weinheimer, and S Zadorozhny. The KATRIN prespectrometer at reduced filter energy. *New J. Phys.*, 14(7):073054, 2012.

[Pri12] *Princeton Instruments* Etaloning in Back-Illuminated CCDs. `http://www.princetoninstruments.com/Uploads/Princeton/Documents/Whitepapers/etaloning.pdf`, December 2012.

[Ros95] K.M. Rosso and R.J. Bodnar. Microthermometric and Raman spectroscopic detection limits of CO_2 in fluid inclusions and the Raman spectroscopic characterization of CO_2. *Geochim. Cosmochim. Ac.*, 59(19):3961 – 3975, 1995.

[Hit04] L.S. Rothman, D. Jacquemart, A. Barbe, D. Chris Benner, M. Birk, L.R. Brown, M.R. Carleer, C. Chackerian Jr., K. Chance, L.H. Coudert, V. Dana, V.M. Devi, J.-M. Flaud, R.R. Gamache, A. Goldman, J.-M. Hartmann,

K.W. Jucks, A.G. Maki, J.-Y. Mandin, S.T. Massie, J. Orphal, A. Perrin, C.P. Rinsland, M.A.H. Smith, J. Tennyson, R.N. Tolchenov, R.A. Toth, J. Vander Auwera, P. Varanasi, and G. Wagner. The HITRAN 2004 molecular spectroscopic database. *J. Quant. Spectrosc. Radiat. Transfer*, 96(2):139 – 204, 2005.

[ROO] Open source software package "ROOT - A Data Analysis Framework". `root.cern.ch`.

[Roy12] R. J. Le Roy. Recalculation of Raman transition matrix elements of all hydrogen isotopologues for 532nm laser excitation. private communication, 2012.

[Rup12] S. Rupp. Proof of concept of a calibration method for the laser Raman system for KATRIN based on the determination of the system's spectral sensitivity. Master's thesis, Karlsruhe Institute of Technology, Karlsruhe, Germany, 2012.

[Str01] K.A. Stroud and D.J. Booth. *Engineering Mathematics*. Industrial Press, 2001.

[Sch09] M. Schlösser. First Laser Raman measurements with tritium for KATRIN and studies of systematic effects of the LARA-setup. Master's thesis, Karlsruhe Institute of Technology, Karlsruhe, Germany, 2009.

[Sch10a] M. Schlösser. Characterization of the PIXIS CCD. Internal report for the KATRIN LARA group, 2010.

[Sch10b] M. Schlösser. Description of custom made catalyst bed for hydrogen deuterium equilibration. Internal report for the KATRIN LARA group, 2010.

[Sch13] M. Schlösser. *TBC*. PhD thesis, Karlsruhe Institute of Technology, Karlsruhe, Germany, 2013.

[Sto51] B. P. Stoicheff, C. Cumming, G. E. St. John, and H. L. Welsh. Rotational structure of the ν_3 Raman band of methane. *Phys. Rev.*, 84:592–592, Nov 1951.

[Sch11] M. Schlösser, S. Fischer, M. Sturm, B. Bornschein, R. J. Lewis, and H. H. Telle. Design implications for laser Raman measurement systems for tritium sample-analysis, accountancy or process-control applications. *Fusion Sci. Technol.*, 60(3):976 – 981, 2011.

[Shu12] W. Shu. Raman Spectroscopy for the ITER Tritium Plant Analytical System. private communication, 2012.

[Sil04] W.T. Silfvast. *Laser Fundamentals 2nd Edition.* Cambridge University Press, Cambridge, U.K., 2004.

[Shr02] M. Shribak, S. Inoue, and R. Oldenbourg. Polarization aberrations caused by differential transmission and phase shift in high-numerical-aperture lenses: theory, measurement, and rectification. *Opt. Eng.*, 41(5):943–954, 2002.

[Sch12a] M. Schlösser, T. M. James, S. Fischer, R. J. Lewis, B. Bornschein, and H. H. Telle. Evaluation method for Raman depolarization measurements including geometrical effects and polarization aberrations. *J. Raman Spectrosc.*, 2012. doi: 10.1002/jrs.4201.

[SJLa] M. Schlösser, T. M. James, and R. J. Lewis. Depol Tools additional information. `http://depoltools.sourceforge.net`.

[SJLb] M. Schlösser, T. M. James, and R. J. Lewis. Depol Tools application on Sourceforge. `http://sourceforge.net/projects/depoltools`.

[SJLc] M. Schlösser, T. M. James, and R. J. Lewis. Spectools application on Sourceforge. `http://sourceforge.net/projects/spectools`.

[SJLd] M. Schlösser, T. M. James, and R. J. Lewis. Spectrum Processing Suite additional information. `http://spectools.sourceforge.net`.

[LRoy88] C. Schwartz and R. J. Le Roy. Nonadiabatic eigenvalues and adiabatic matrix elements for all isotopes of diatomic hydrogen. *J. Mol. Spectrosc.*, 121(2):420 – 439, 1987.

[Sch12b] M. Schlösser, S. Rupp, H. Seitz, S. Fischer, B. Bornschein, T. M. James, and H. H. Telle. Accurate calibration of the laser Raman system for the Karlsruhe Tritium Neutrino experiment. *J. Mol. Struct.*, 2012. doi: 10.1016/j.molstruc.2012.11.022.

[Stu09] M. Sturm, M. Schlösser, R.J. Lewis, B. Bornschein, G. Drexlin, and H.H. Telle. Monitoring of all hydrogen isotopologues at tritium laboratory Karlsruhe using Raman spectroscopy. *Laser Phys.*, 20:493–507, 2010.

[Sch12c] M. Schlösser, H. Seitz, S. Rupp, P. Herwig, C. Alecu, C. Sturm, and B. Bornschein. In-Line Calibration of Raman Systems for Analysis of Gas Mixtures of Hydrogen Isotopologues with Sub-Percent Accuracy. *submitted to Anal. Chem.*, 2012.

[Syn09] *Horiba* Synapse 1024 × 256 FIOP CCD detector data sheet and manual. `http://www.horiba.com/fileadmin/uploads/Scientific/Documents/OSD/OSD0057256FIOP.pdf`.

[Tec09] LC-035 data sheet. `http://www.tetech.com/Liquid-Coolers/LC-035.html`.

[Tay01] D. J. Taylor, M. Glugla, and R. D. Penzhorn. Enhanced Raman sensitivity using an actively stabilized external resonator. *Rev. Sci. Instrum.*, 72(4):1970–1976, 2001.

[tla] *ThorLabs* web pages containing technical information on their products. `http://www.thorlabs.com`.

[Tel07] H.H. Telle, A.G. Ureña, and R.J. Donovan. *Laser Chemistry: Spectroscopy, Dynamics and Applications.* John Wiley & Sons, 2007.

[Val10] K. Valerius. The wire electrode system for the KATRIN main spectrometer. *Prog. Part. Nucl. Phys.*, 64(2):291 – 293, 2010.

[Wav12] *CVI Melles Griot* Etaloning in Back-Illuminated CCDs. `http://www.cvimellesgriot.com/products/Documents/TechnicalGuide/Waveplates.pdf`, December 2012.

[Wes09] R. C. Westhoff, B. E. Burke, H. R. Clark, A. H. Loomis, D. J. Young, J. A. Gregory, and R. K. Reich. Low dark current, back-illuminated charge coupled devices. In *Proc. SPIE 7249, Sensors, Cameras, and Systems for Industrial/Scientific Applications X.*

[Wan11] X. Wang, I.-M. Chou, W. Hu, R. C. Burruss, Q. Sun, and Y. Song. Raman spectroscopic measurements of CO_2 density: Experimental calibration with high-pressure optical cell (HPOC) and fused silica capillary capsule (FSCC) with application to fluid inclusion observations. *Geochim. Cosmochim. Ac.*, 75(14):4080 – 4093, 2011.

[Weh92] J. A. Wehrmeyer, T. S. Cheng, and R. W. Pitz. Raman scattering measurements in flames using a tunable KrF excimer laser. *Appl. Opt.*, 31(10):1495–1504, Apr 1992.

[Wei05] C. Weinheimer. Direct determination of the neutrino masses. *C. R. Phys.*, 6(7):768 – 777, 2005.

[Wue10] S. Wuestling, F. Fraenkle, F. Habermehl, P. Renschler, and M Steidl. Results from a 64-pixel PIN-diode detector system for low-energy beta-electrons. *Nucl. Instrum. Methods Phys., Sect. A*, 624(2):295 – 302, 2010.

[Witt00] M. Wittmann, A. Nazarkin, and G. Korn. New regime of fs-pulse stimulated Raman scattering. *Appl. Phys. B*, 70:S261–S267, 2000.

[Wei98] M. Weisser, F. Thoma, B. Menges, U. Langbein, and S. Mittler-Neher. Fluorescence in ion exchanged BK7 glass slab waveguides and its use for scattering free loss measurements. *Opt. Commun.*, 153(13):27 – 31, 1998.

[Yu07] Y. Yu, K. Lin, X. Zhou, H. Wang, S. Liu, and X. Ma. Precise measurement of the depolarization ratio from photoacoustic Raman spectroscopy. *J. Raman Spectrosc.*, 38(9):1206–1211, 2007.

[Zha11] H. Zhang, Z. Yuan, J. Zhou, J. Dong, Y. Wei, and Q. Lou. Laser-induced fluorescence of fused silica irradiated by ArF excimer laser. *J. Appl. Phys.*, 110(1), 2011.